AAA Workshop Series Volume 12
Asociación Argentina de Astronomía

Proceedings of the VIII La Plata International School

Pulsations Along Stellar Evolution

La Plata, Argentina, November 11-22, 2019

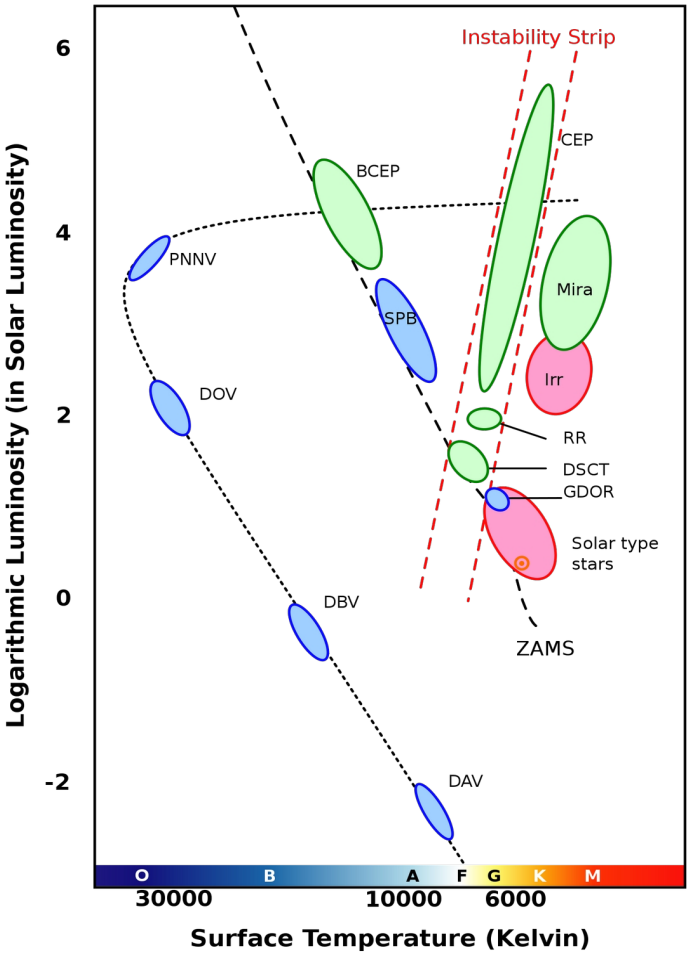

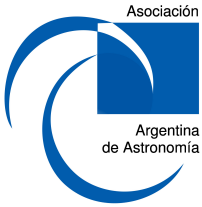

Asociación Argentina de Astronomía

Pulsations Along Stellar Evolution

Proceedings of the VIII La Plata International School

La Plata, Argentina, November 11–22, 2019

Michaela Kraus & Andrea F. Torres, eds.

Credits

Cover picture: HR Diagram for pulsating stars from Wikimedia Commons.
The Editors thank Leonardo Pellizza for providing a LaTeX macro for the edition of this volume.

Only electronic format – September 2021

Kraus, Michaela
Pulsations Along Stellar Evolution : Proceedings of the VIII La Plata International School / Michaela Kraus ; Andrea F. Torres. - 1a ed. - La Plata : Asociación Argentina de Astronomía, 2021.
Libro digital, PDF - (AAA Workshop Series ; 12)

Archivo Digital: descarga
ISBN 978-987-24948-7-2

1. Astrofísica. 2. Astronomía. I. Torres, Andrea F. II. Título.
CDD 523.01

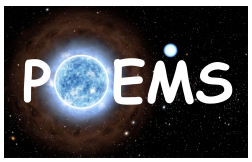

Asociación Argentina de Astronomía

Fundada en 1958

Personería Jurídica (Legajo 21.459 - Matr. 1.421), Pcia. de Buenos Aires

Comisión Directiva

(2017–2020)

Presidente:	Dr. Leonardo J. Pellizza
Vicepresidente:	Dra. Susana E. Pedrosa
Secretario:	Dr. Rodrigo F. Díaz
Tesorero:	Dr. Daniel D. Carpintero
Vocal 1ro:	Dra. Andrea V. Ahumada
Vocal 2do:	Dra. Andrea P. Buccino
Vocal Sup. 1ro:	Dra. Georgina Coldwell
Vocal Sup. 2do:	Dra. Hebe Cremades

Comisión Revisora de Cuentas

Titulares:	Dra. Sofía A. Cora
	Dr. Gerardo Juan M. Luna
	Dr. Luis R. Vega

Comité Nacional de Astronomía

Secretaria:	Dra. Cristina Mandrini
Miembros:	Dra. Lydia Cidale
	Dra. Hebe Cremades
	Dr. Federico González
	Dr. Hernán Muriel

Asociación Argentina de Astronomía

Proceedings of the VIII La Plata International School Pulsations Along Stellar Evolution

La Plata, Argentina, November 11–22, 2019

Scientific Organizing Committee

Chair: M. Kraus (Astronomical Institute, Czech Academy of Sciences, Czech Republic)
Co-chair: L. Cidale (Universidad Nacional de La Plata, Argentina)
Members: O. Benvenuto (Universidad Nacional de La Plata, Argentina)
W. Glatzel (Georg-August-Universität Göttingen, Germany)
M. Vučković (Universidad de Valparaíso, Chile)

Local Organizing Committee

Chair: Andrea F. Torres (FCAG - IALP)
Members: Lydia Cidale (FCAG - IALP)
Yanina Cochetti (FCAG - IALP)
Betina Fregenal (FCAG)
Maximiliano Haucke (FCAG - IALP)
Romina Miculán (FCAG - IALP)
Jorge Panei (FCAG - IALP)
Julieta Sánchez Arias (FCAG - IALP)
Rodolfo Vallverdú (FCAG - IALP)

Editorial Committee

Members: Michaela Kraus
Andrea F. Torres

Foreword

The VIII La Plata International School was successfully held in the period 2019 November 11 – 22 on the campus of the Universidad Nacional de La Plata. The school was organized by the research group Modelos de Estrellas Peculiares (MEP) of the Facultad de Ciencias Astronómicas y Geofísicas (FCAG).

The subject of this school was *Pulsations Along Stellar Evolution*. The offered lectures covered a wide range of topics such as stellar evolution, theoretical concepts of stellar pulsations, observing and data analysis techniques, along with practical courses for the analysis of selected pulsating stars. The ultimate goal of the Summer School was that the participants deepen their understanding of the physics of stellar pulsations and learn relevant techniques to analyze and properly interpret observational data of pulsating stars. This was achieved by the active participation in a number of courses dealing with theoretical exercises and practical computer-based exercises. This volume provides a comprehensive summary of the lectures that were presented during the school.

The topics offered by the school attracted 58 participants from 13 different countries all over the world. The majority of participants came from Latin-America (Argentina, Brazil, Chile, Peru, and Nicaragua), but we also had participants from several European countries (Czech Republic, Estonia, Spain, and United Kingdom) as well as from Asia (Georgia), Africa (Egypt), Australia, and the United States of America. By chance, the genders of the participants were extremely well balanced, with 29 male and 29 female astronomers, physicists and mathematicians, in divers states of their studies (majority within their Master or PhD studies) along with a few post-docs and more advanced researchers.

The organization of the school has received funding from the FCAG of the Universidad Nacional de La Plata, and from the European Union's Framework Programme for Research and Innovation Horizon 2020 (2014-2020) under the Marie Skłodowska-Curie Grant Agreement No. 823734 (POEMS).

We wish to thank the members of the Scientific Organizing Committee for their excellent selection of teachers and preparation of the program. Furthermore, we wish to express our deepest thanks to the members of the Local Organizing Committee and those students who helped with the organization. And finally, we are grateful to all teachers for their fantastic classes and to all participants that helped making this school an event to be remembered.

Michaela Kraus
Andrea F. Torres

School group photo.

Contents

Theory of Stellar Evolution and Pulsations

Pulsations Along Stellar Evolution
VIII LAPIS Summer School
AAA Workshop Series 12, 2021
M. Kraus & A.F. Torres, eds.

A Brief Introduction to Stellar Evolution

Omar G. Benvenuto[1], †

[1]*Facultad de Ciencias Astronómicas y Geofísicas, Universidad Nacional de La Plata, and Instituto de Astrofísica de La Plata (CCT-CONICET-UNLP), La Plata, Argentina*
Email: obenvenu@fcaglp.unlp.edu.ar

Abstract. With the aim of providing a reference frame for the study of stellar pulsations we describe the process known as stellar evolution. Evolution and pulsations are deeply related and the knowledge gained in one of them has an immediate impact on the other. First we describe the observational basis, presenting the Hertzsprung-Russell Diagram and other fundamental concepts. Then we describe the physical context of stellar evolution in which, quite fortunately, matter is very close to (but not in) thermodynamic equilibrium. This allows for a simplification of the problem of paramount importance. We describe the equation of state of stellar matter, paying attention on when we should expect the occurrence of partial and full ionization (fundamental for pulsations), and electron degeneracy. Then, we present the concept of hydrostatic equilibrium. As a natural consequence we consider barotropic structures, like polytropic spheres and cold white dwarfs, discussing the existence of the Chandrasekhar's mass limit. As realistic stars are not cold but at finite temperature (they radiate energy in space!), in general they are non-barotropic. So, we need to consider the conservation of energy and also its transport by radiation, convection and conduction. As it is well known, the engine of stars is nuclear reactions. We present the proton-proton and carbon-nitrogen-oxygen cycles of hydrogen burning and also the main helium burning reactions. Then, we make some brief comments on the methods for solving the full set of non-linear, partial differential equations of stellar evolution and also those needed for computing the changes of chemical composition. At this point we are in conditions to present stellar evolution as a direct consequence of these physical ingredients. We discuss the main stages of stellar evolution for a variety of objects: pre-main sequence, low and intermediate mass, white dwarfs, and finally massive stars. In this paper we restricted ourselves to the case of isolated and non-rotating objects evolving during their long lived stages. In our opinion, this provides a general basis for most of the usually considered pulsating

stars.
Key words: stars: evolution — stars: interiors

†Member of the Carrera del Investigador Científico, Comisión de Investigaciones Científicas de la Provincia de Buenos Aires (CIC PBA), La Plata, Argentina

1. Introduction

In these lectures we shall present the classical problem of stellar evolution with emphasis on the properties of stars that determine the variety of pulsations they suffer. This is a vast field of research. Because of lack of space here we are not in conditions to make an in deep description of each of the addressed topics. These have been presented in several textbooks. Especially relevant are those of Chandrasekhar (1939); Cox & Giuli (1968); Clayton (1968); Kippenhahn & Weigert (1990); Arnett (1996); and Maeder (2009). The reader may be somewhat surprised because the main references of these lectures have been published sometime ago. The reason is very simple, the most fundamental processes occurring in stars are well understood. Several facts converged to make it possible. For example, the engine of stars (nuclear reactions) was identified almost a century ago, and the stellar interiors are extremely close to thermodynamic equilibrium. This provides a solid basis to investigate this problem. Of course, this means in no way that the study of stars is over. Definitively this is *not* the case.

We shall present the theory of stellar structure and evolution paying special attention to the relevant physical ingredients that determine their lives. In our opinion, this is essential in order to understand the oscillation properties of stars from a theoretical point of view. These oscillations carry very valuable information about the structure of stellar interiors. Thus, structure and evolution are intimately related to oscillations and the study of these aspects of stars are largely complimentary.

Perhaps the most famous diagram related to stars is the Hertzsprung-Russell Diagram (or simply HRD) in which we plot (for example) their luminosities versus effective temperatures. There are several versions of the HRD in which in place of luminosity astronomers employed absolute magnitude and a colour index (or even the spectral type) replaces the effective temperature. If we collect intrinsic data quantities from field stars we can construct an HRD where the distribution of objects is *not uniform*. In this case, it has a statistical meaning. There are regions of the diagram where we find a large density of objects. This is due to the fact that at these regions stars evolve slowly. The so-called *"Main Sequence"* (MS), on which we find most of the objects, is due to the strong energy release by core hydrogen burning occurring in these stars. The MS is the longest stage of evolution for objects undergoing intense nuclear reactions. The red giant branch has less stars and is a shorter stage of evolution, etc.

If we collect data from a stellar cluster, all stars are essentially at the same distance, have approximately the same chemical composition and usually it is considered that have been born simultaneously. Thus, all stars have the same age and because they have a mass distribution they are on an *isochrone* in the HRD.

As an example of typical HRDs, in Figure (1) we show them for the open cluster NGC 2516 and the globular cluster NGC 1261. These diagrams are of colour index (B-V) (that has a direct relation with effective temperature) versus the apparent visual magnitude V without the correction for reddening. These are not intrinsic data since they have to be converted to absolute magnitudes by means of the distance modulus; but, this is the same for all stars belonging to a cluster. Consequently, these HRD have the same structure as those with intrinsic quantities.

Apart from the contamination due to faint field stars that do not belong to these clusters, the MS is clearly visible in the HRD of the open cluster. In the case of the globular cluster it is possible to see the lower MS (higher mass stars evolved off the MS in the far past), the red giant branch (RGB), horizontal branch (HB), and asymptotic giant branch (AGB).

Usually, the width of stellar atmospheres is far smaller than stellar radii; and the effective temperature corresponds to a layer in which most photons escape from the star. As a first, rough approximation, the spectrum of a star may be considered as a Planckian curve with $T = T_{eff}$. Since we are interested on the intrinsic properties of stars, in the following Sections we shall consider the version of the HRD defined by the plane $\log\left(L/L_{\odot}\right)$ versus $\log\left(T_{eff}/K\right)$ where L is the bolometric luminosity, $L_{\odot} = 3.828 \times 10^{33}\, erg\, s^{-1}$ is the solar value, T_{eff} is the effective temperature and K denotes Kelvin degrees. These quantities are related by $L = 4\pi R^2 \sigma T_{eff}^4$ where R is the radius of the star and σ is the Stefan-Boltzmann constant. Evidently, $\log\left(L/L_{\odot}\right) = 2\log\left(R/R_{\odot}\right) + 4\log\left(T_{eff}/T_{eff,\odot}\right)$ where $T_{eff,\odot} = 5780$ K is the effective temperature of the Sun, that has a mass $M_{\odot} = 1.989 \times 10^{33}$ g and a radius of $R_{\odot} = 6.96 \times 10^{10}$ cm.

Here we shall restrict ourselves to the case of non-rotating, isolated stars. We feel it is not possible to present all topics in two lectures. We prefer to discuss the most relevant stages related with stellar pulsations. Also, we shall not treat the case of neutron stars and its related physics since it is outside the scope of this School. Here we shall not try to make a detailed description of the state-of-the-art of each addressed topic. We consider it more useful to review established results.

A fundamental assumption is that *oscillations do not have any secular effect on stellar evolution.* This means that we do not need to take care of the details of stellar pulsations to compute stellar evolution. Otherwise we would have faced (in the language of numerical analysis) an extremely stiff problem since there occur quite different and relevant timescales. For pulsations, timescales may be of the order of days or less, whereas stellar evolution proceeds on millions of years.

The remainder of this article is organised as follows. In Section (2) we describe the equation of state of matter inside stars. Section (3) is dedicated to describe hydrostatic equilibrium, where we also briefly describe the theory of polytropic spheres (§ 3.1) and cold White Dwarfs (WDs) (§ 3.2). In Section (4) we describe the conservation of energy in the stellar interior. Then, in Section (5) we present the problem of the transport of energy in stellar interiors, making a description of the main characteristics of radiative (§ 5.1), convective (§ 5.2), and conductive (§ 5.3) transport mechanisms. The Section (6) is devoted to describe the fundamental characteristics of nuclear reactions in stellar interiors. Then

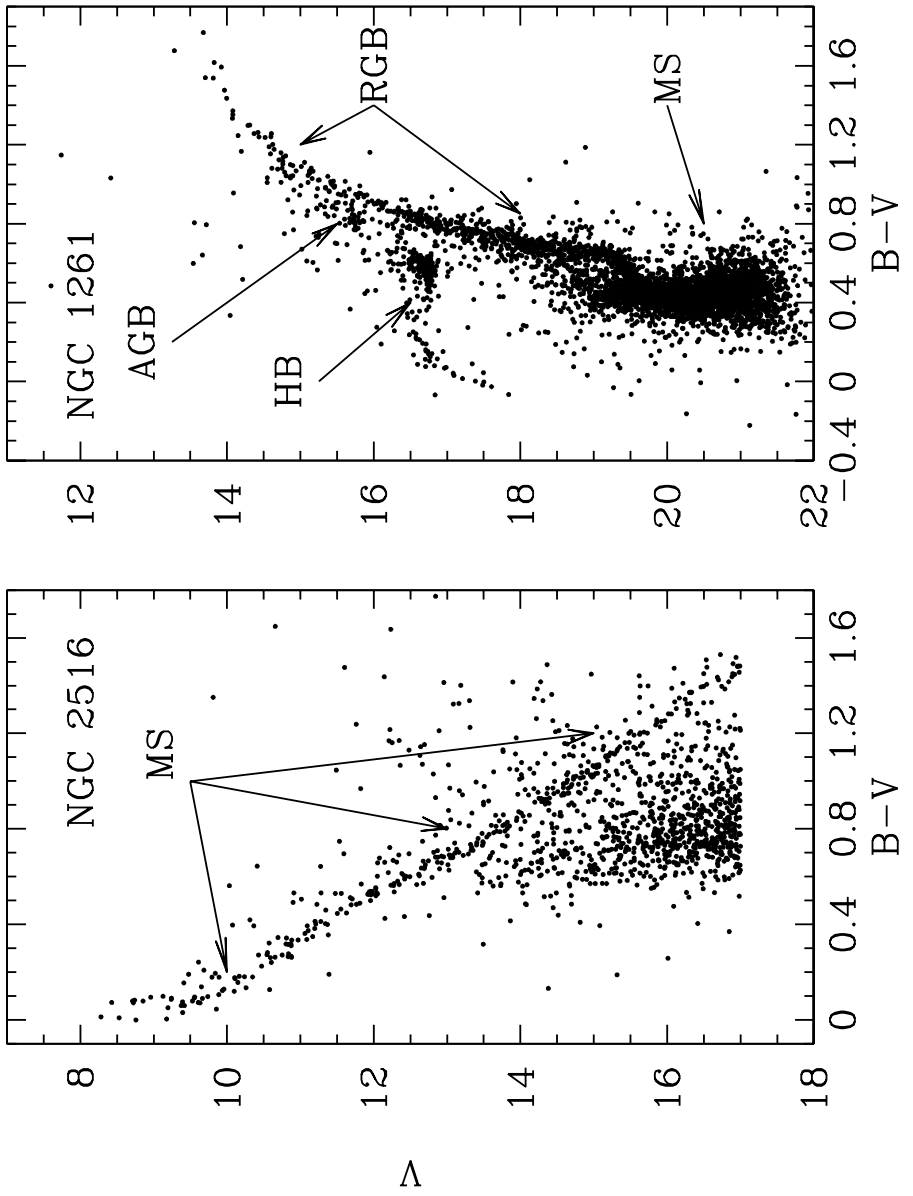

Figure 1. The HRD of the open cluster NGC 2516 (Sung et al., 2002b) (data available at Sung et al. 2002a) and the globular cluster NGC 1261 (Kravtsov et al., 2010b) (data available at Kravtsov et al. 2010a). For details see text.

we describe in some detail the Proton-Proton (§ 6.1), Carbon-Nitrogen-Oxygen (§ 6.2) and Helium burning (§ 6.3) cycles. In Section (7) we briefly describe the full system of differential equations that describe stellar evolution together with the method of solution for the equations of structure (§ 7.1) and chemical evolution (§ 7.2). Then, in Section (8) we describe stellar evolution. Subsection (§ 8.1) is devoted to describe the main characteristics of Pre-MS evolution. (§ 8.2) is dedicated to the case of the evolution of our Sun and low mass stars. (§ 8.3) is devoted to the case of intermediate mass while in (§ 8.4) we describe the main characteristics of WDs evolution. Closing this section, in (§ 8.5) we address the case of massive stars. Finally, in Section (9) we give some concluding remarks.

2. The Equation of State

For describing stars one of the most relevant physical ingredients is the behaviour of matter. This is described by the so-called "Equation Of State", or EOS. Inside stars, matter can be found on an extremely wide variety of conditions. Apart from its chemical composition, the density and temperature vary from $\rho = 10^{-12}\, g\, cm^{-3}$ and $T \approx 10^3$ K in the photosphere of a giant to $\rho = 10^{11}\, g\, cm^{-3}$ and $T \approx 10^{10}$ K in the core of a pre-supernova near core collapse. So, matter can be non, partially, or fully ionized, electrons may be degenerate, and even there may appear pairs electron-positron at very high temperatures ($T \gtrsim 5 \times 10^9$ K). Also, in conditions of low density and high temperature, radiation pressure is relevant.

A fundamental approximation, fully justified in stellar interiors is the so-called *"Local Thermodynamic Equilibrium"* or LTE. It is quite obvious that stars are not in thermodynamic equilibrium, simply because they irradiate. However, variations of T, ρ, etc. in stellar interior are not very steep. As a consequence, the radiation field is anisotropic but only to 1 part in $\approx 10^{11}$ (see, e.g., Clayton 1968). So, the state of matter is extremely close to equilibrium. Thus, LTE is valid and so, to describe the EOS we can employ the thermodynamics of equilibrium.

Another fundamental fact is that the energy of interaction between particles use to be far smaller than their kinetic energy. Thus, we may consider the material as composed by non-interacting particles. Interactions, e.g., electrostatic or Coulomb, are considered only for constructing very detailed stellar models (see below§ 3.2).

Taking into account that particles that compose matter are *fermions* (their spins are $\hbar/2$, where $\hbar$ is the Planck constant h over 2π.), they obey the Fermi-Dirac statistics. Then, we can write the EOS of fermionic non-interacting particles as (Chandrasekhar, 1939)

$$P_{gas} = \frac{8\pi}{3h^3} \int_0^\infty \frac{p^3 v_p}{1 + exp\big[\beta\big(E(p) - \mu\big)\big]} dp, \tag{1}$$

$$\frac{E_{gas}}{V} = \frac{8\pi}{h^3} \int_0^\infty \frac{p^2 E(p)}{1 + exp\big[\beta\big(E(p) - \mu\big)\big]} dp, \tag{2}$$

$$\frac{N}{V} = n = \frac{8\pi}{h^3} \int_0^\infty \frac{p^2}{1 + exp\big[\beta\big(E(p) - \mu\big)\big]} dp. \tag{3}$$

Here, $\beta = 1/kT$, P_{gas} is the pressure due to particles and E_{gas} is their kinetic energy, V is the volume, N is the total particle number, n is their number density, k the Boltzmann constant, p is the momentum of the particles, $E(p)$ is the energy of the particles of mass m and impulse p given by $E(p) = \sqrt{p^2c^2 + m^2c^4} - mc^2$, v_p is its velocity, and c is the speed of light. This represents a parametric EOS where the parameter is the chemical potential μ.

If density is low enough, quantum mechanical effects are negligible and the gas behaves as non-degenerate (Maxwell-Boltzmann statistics). Then, we immediately arrive to the famous and simplest EOS: $P_{gas} = \frac{\rho kT}{\mu H}$, where μ is the mean molecular weight (this is a misleading name since in most cases there are no molecules). For *full ionization* we have $1/\mu = \sum X_i(Z_i + 1)/A_i$ where X_i is the mass fraction of the i- component of the plasma, Z_i is its electric charge and A_i is its atomic weight. In this case, the mean kinetic energy of each particle is $3kT/2$ and the contribution to the specific heat per particle is $3k/2$, i.e., a *constant*.

Frequently, the abundances of hydrogen and helium are denoted by X and Y respectively, while Z denotes the heavier elements fraction; they verify $X + Y + Z = 1$

If temperature is not so high to provide full ionization, in order to consider the EOS properly we have to solve for the ionic mixture. Because of the validity of LTE we can do it by employing thermodynamic equilibrium that leads to the so-called Saha's law. For the case of the ionization of hydrogen it reads (we ignore corrections due to internal partition functions)

$$\frac{n_{H^+} n_e}{n_H} = \left(\frac{2\pi m_e kT}{h^2}\right)^{3/2} \exp\left(-\frac{\chi_H}{kT}\right) \tag{4}$$

where n_i are the particle number densities, $\chi_H = 13.59$ eV is the ionization potential, and m_e is the electron mass. While here we present only the expression for hydrogen, we need to consider all the elements present in the mixture (see, e.g., Baker & Kippenhahn 1961). It leads to a non-trivial system of equations. *Considering ionizations in detail is of central relevance for stellar pulsations.*

The effect of ionizations on the gas pressure is rather obvious, since it affects the amount of free particles. Ionization is a way of storing heat that largely affects the specific heats. For example, for a pure hydrogen plasma, when the fraction of ionized atoms is of 50%, the specific heat at constant volume C_v is ≈ 20 times the C_v without considering ionizations (Clayton, 1968).

If the gas has a much higher density, due to its very low mass compared to that of nucleons ($\approx$ 1830 times lower), electrons depart from the classical behaviour. Electrons provide a strong pressure P_e due to the Pauli's exclusion principle (there can be only one fermion per energy level). If thermal effects are negligible ($kT \ll \mu$) we may set $T = 0$. In this case, the distribution of occupied levels goes up to the Fermi impulse p_f, which is related to the chemical potential by $\mu = \sqrt{p_f^2c^2 + m_e^2c^4} = m_ec^2\sqrt{x^2 + 1}$ (where $x = p_f/m_ec$). In this case, the particle number density is $n \propto x^3$ whereas, if density is not too high (see below), electron will behave as non-relativistic and then $P_e \propto x^5$. On the contrary, if density is higher and electrons are very relativistic we have $P_e \propto x^4$. In this case

the integrals in Equations (1)-(3) extend on the interval of impulses $[0, p_f]$, the denominator is 1 and the EOS is (Chandrasekhar, 1939)

$$P_e = A\big[x(2x^2-3)\sqrt{x^2+1} - 3\ln\left(\sqrt{x^2+1}-x\right)\big] \tag{5}$$

and

$$\rho/\mu_e = Bx^3, \tag{6}$$

where $A = (8\pi/3)m_e c^2\big(m_e c/h\big)^3$, $B = 8\pi\big(m_e c/h\big)^3$ and μ_e is the mean molecular weight per electron. For full ionization we have $1/\mu_e = \sum X_i Z_i/A_i$. Another very important characteristic of degenerate electron gas is that it is not efficient for storing heat. It can be shown that $C_v \propto T$ (Chandrasekhar, 1939) which is characteristic of fermionic excitations.

Notice that here we have assumed full ionization even at $T = 0$. This is due to the so-called *ionization by pressure*. The reason for this to occur is that particles are so close each other that the wave function corresponding to bound states has no room to accommodate. Consequently, bound states cannot be occupied.

Another very important source of pressure is photons. Photons are massless Bosons (they have spin $\hbar$) and follow the so-called Bose-Einstein statistics[1]. As the number of photons is not defined, *the chemical potential of photons is zero*. This leads to the Planck function B_ν

$$B_\nu = \frac{2h\nu^3}{c^2}\frac{1}{e^{h\nu/kT}-1}, \tag{7}$$

where ν is the frequency of radiation. Photons provide the *radiation pressure* that is given by the very simple expression

$$P_{rad} = \frac{1}{3}aT^4, \tag{8}$$

where a is the constant of radiation.

In Figure (2) we present the typical thermodynamic conditions for stellar interiors. We describe the regions in which the different sources of pressure dominate over the others. For example, the division between the regions dominated by gas and radiation pressure is given by $P_{rad} = P_{gas}$, etc. Also we included the structure of several stellar interiors. For the star of 20 $M_\odot$, radiation pressure is important, whereas this is not the case for a 1 $M_\odot$ object. Also, we show the structure of a 0.8 $M_\odot$ carbon-oxygen WD. While its outer layers are non-degenerate, the deep interior is at very high densities reaching relativistic conditions.

As we shall see below, the equations of stellar evolution include a temporal derivative of the entropy S; so, it is useful to write down the differential of S. If we consider P and T as independent variables, this differential is

---

[1] An even number of fermions may be together in a bound state, e.g., a ^4He nucleus. These compound objects have a spin value that is an integer multiple of $\hbar$; so, they are bosons too. However, these particles are so massive that are non-degenerate in normal (not neutron) stars and the quantum effects are negligible for their description.

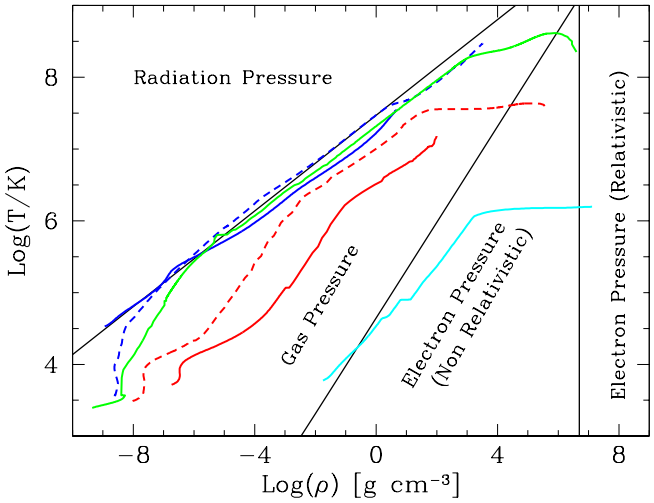

Figure 2. The conditions at which dominates each of the four basic sources of pressure. Black solid lines divide each region. As examples of stellar structures we included several relevant cases. In blue lines we plot the structure of a 20 $M_{\odot}$ star on the Zero Age MS (solid) and the conditions at helium core exhaustion (dashed). The structure of a 1 $M_{\odot}$ is denoted with red lines for the case of the present Sun (solid) and when reached red giant conditions (dashed) previous to the helium flash (see below § 8.2). Solid green line depicts the structure of a 5 $M_{\odot}$ star well after helium core exhaustion. Finally, in solid cyan line we show the structure of a cool 0.8 $M_{\odot}$ carbon-oxygen WD. All these states of evolution are described below in Section (8).

$$dS = C_P dT - \frac{\delta}{\rho} dP. \tag{9}$$

Here C_P is the specific heat at constant pressure and δ is the thermodynamic derivative $\delta = -\left(\partial \ln \rho / \partial \ln T\right)_P$.

The problem of the stellar EOS is treated in all textbooks cited above and also in several papers, the interested reader may consult for example those of Kippenhahn et al. (1967); Cox & Giuli (1968); and Timmes & Arnett (1999).

3. Hydrostatic Equilibrium

Stellar evolution proceeds so slowly on time that we can consider it as a continuous sequence of structures in hydrostatic equilibrium. For non-rotating, Newtonian objects, the equations that describe this condition are[2]

$$\frac{dP}{dr} = \frac{GM_r}{r^2}\rho, \tag{10}$$

and

$$\frac{dM_r}{dr} = 4\pi r^2 \rho. \tag{11}$$

Here P is the total pressure, r is the radius, G is the Gravitational constant, M_r is the mass enclosed inside a sphere of radius r, and ρ is the density. The boundary conditions are $M_r = 0$ at $r = 0$ and the surface is defined by zero gas pressure $P_{gas} = 0$; there $r = R$.

Equations (10) and (11) can be solved if the EOS of material behaves as barotropic, i.e., $P = P(\rho)$. This is the topic of the next two subsections.

3.1. Polytropic Spheres

Let us consider a particular barotropic form for the EOS: $P = K\rho^{1+1/n}$ where n is the polytropic index and K is a constant. If we define $\rho = \rho_c \theta^n$ where ρ_c is the central density and θ is the polytropic function; and $r = \alpha\xi$, where $\alpha^2 = \frac{(n+1)K}{4\pi G}\rho_c^{1/n-1}$ we find the Lane-Emden equation

$$\frac{1}{\xi^2}\frac{d}{d\xi}\left(\xi^2 \frac{d\theta}{d\xi}\right) = -\theta^n. \tag{12}$$

The corresponding boundary conditions are $\theta(\xi = 0) = 1$, $d\theta/d\xi|_{\xi=0} = 0$ and the surface is defined by $\theta(\xi = \xi_s) = 0$; thus, the radius R is $R = \alpha\xi_S$. The mass of the whole sphere is given by $M = 4\pi\alpha^3\rho_c(-\xi^2 d\theta/d\xi)_{\xi=\xi_s}$. The solution of the Lane-Emden equation and the density profile is shown in Figure (3) for some values of the polytropic index. Analytic solutions for Equation (12) are known for $n = 0, 1$, and 5.

---

[2]These equations are not applicable to neutron stars. In this case we need to consider the Tolman-Oppenheimer-Volkoff equations that correspond the case of gravitation described by General Relativity (see Shapiro & Teukolsky 1983).

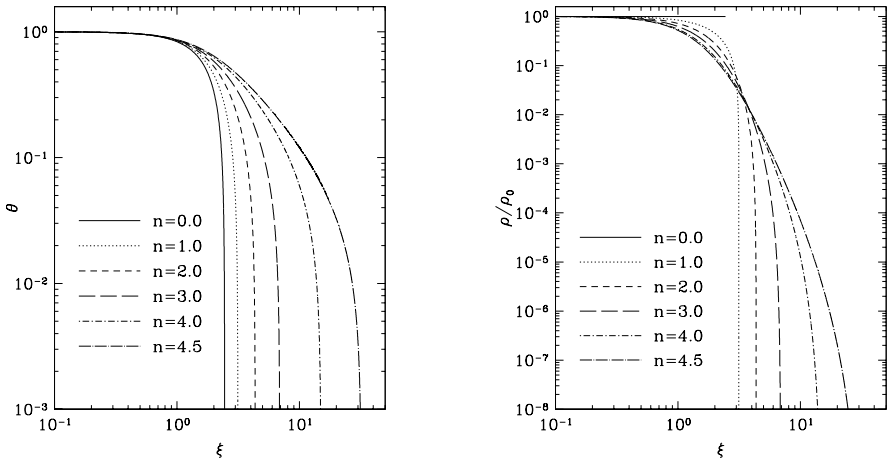

Figure 3. The polytropic function (left panel) and the density profile (right panel) for few values of the polytropic index.

Polytropes with $n = 3/2$ are a good approximation for fully convective stars at the Hayashi Track during the Pre-MS evolution (§ 8.1) and also for low mass WDs (§ 3.2). The case of $n = 3$ nicely represents the case of very massive WDs (§ 3.2) and sometimes is employed as a rough approximation to the structure of MS stars (Arnett, 1996).

3.2. Cold White Dwarf Stars

The simplest way to study the structure of WDs is to consider them to be chemically homogeneous at zero temperature with the EOS described by Equation (5). This EOS is *not* polytropic but equations may be handled in a similar way to find the equation that describes the structure of WDs. Indeed, as quoted above, its polytropic index is 3/2 at low densities and 3 at high densities (relativistic degeneracy). This was done by Chandrasekhar (1939) who found one of the most relevant results of stellar astrophysics: a degenerate star can be in hydrostatic equilibrium only if its mass is below a value currently known as the Chandrasekhar's Mass Limit

$$M_{Ch} = \frac{5.75}{\mu_e^2} M_\odot. \tag{13}$$

Because of evolutionary reasons, WDs with masses $M > 10^{-2} M_\odot$ can have a little amount of hydrogen located in the outermost layers. This has a minor effect on the total mass of the WD. If we neglect it, for objects composed by matter that has symmetric nuclei (these are nuclei with the same number of

protons and neutrons, e.g., ^4He, ^{12}C, ^{16}O, etc.) $\mu_e = 2$ and $M_{Ch} = 1.4 M_\odot$[3]. Observations to measure the masses and radii of WDs are difficult, in any case they are in nice agreement with the predictions of this theory. S. Chandrasekhar awarded the Nobel Prize of Physics in 1983 for this work.

Remarkably, the WD with $M = M_{Ch}$ has infinite density and zero radius! Evidently, this indicates that some basic hypotheses have to be improved, at least for very massive WDs. This was done by Hamada & Salpeter (1961) who applied the EOS derived by Salpeter (1961). They considered Coulomb and other interactions for the cold degenerate plasma. These corrections represent a negative correction to the pressure of free electrons. So, for a given pressure the gas is denser compared with the value corresponding to the free particle treatment given by Equation (5).

At very high densities ($\rho > 10^9\, g\, cm^{-3}$) the electron chemical potential becomes so high that it is energetically favourable their capture by nuclei. This phenomenon is usually known as *"electron capture"*. Thus, at such high densities an increase in density makes the pressure to grow slower (the EOS softens). This induces the occurrence of a gravitational instability at a mass similar to the value found by Chandrasekhar, but *at finite stellar radius*.

An important result is related to very low mass objects ($M < 10^{-2} M_\odot$): the corrections to the free particle EOS become proportionally larger the lower the object mass is. Then, it is found that there is a maximum radius for such low mass objects. This result is absent in the treatment by Chandrasekhar, who found that the lower the mass the larger the radius. Because of the complexity of its EOS (see, e.g., Saumon et al. 1995), very low mass WDs are not simple objects. They are deeply related to the Solar System's gaseous giant planets[4].

The mass radius relation for cold WDs is presented in Figure (4) (see also Hamada & Salpeter 1961).

Among other phenomena, the theory of WDs has a direct impact for example in the theory of Type Ia supernova explosions. Further details on the physics of cold WDs can be found in Shapiro & Teukolsky (1983).

Let us remark that, apart from the great success of this theory, this is *not* enough for considering the non-radial pulsation of WDs. For such purpose the zero temperature hypothesis must be relaxed and WDs should be constructed as consequence of stellar evolution as it will be described below in § (8.4).

4. Conservation of Energy in Stellar Interiors

In order to study non-barotropic structures we have to consider the conservation and transport of energy in stellar interiors. The equation of energy conservation can be written as

$$\frac{\partial L_r}{\partial r} = 4\pi r^2 \rho \left(\varepsilon_n - \varepsilon_\nu - T \frac{\partial S}{\partial t}\bigg|_{M_r} \right). \tag{14}$$

[3]However, for an iron ^{56}Fe composition, $\mu_e = 2.153$ and $M_{Ch} = 1.24 M_\odot$

[4]This is especially true for Jupiter and Saturn because their structures are mostly gaseous.

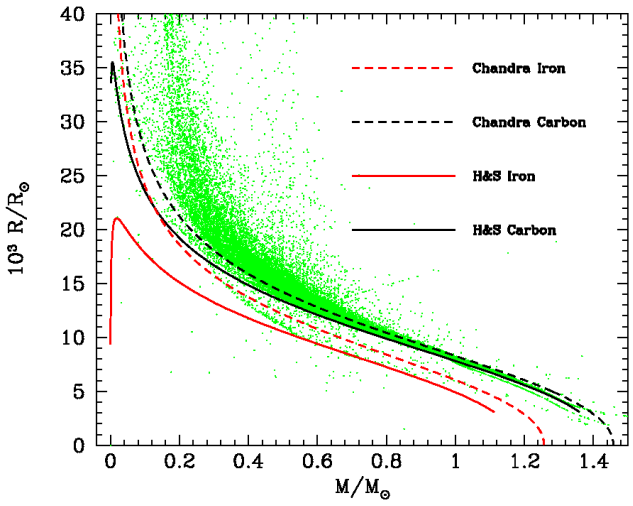

Figure 4. Mass radius relation for cold WDs. Solid lines represent sequences that consider the Salpeter (1961) EOS and are similar to those presented by Hamada & Salpeter (1961). Dashed lines denote the Chandrasekhar WDs. We considered models of carbon and iron. Green dots represent the data given in Dufour et al. (2017). Notice that massive WDs ($M \gtrsim 0.6 M_{\odot}$) are in excellent agreement with the theoretical results. Lower mass objects have larger radii due to thermal effects (See below, Figure (12)).

Here L_r is the luminosity that emerges from a spherical surface of radius r, ε_n (ε_ν) is the energy release (loss) due to nuclear reactions (neutrino emission) per gram and second, and S is the entropy per mass unit. We should remark that the derivative of the entropy is computed for a fixed mass element (Lagrangian) since it is the element that exchanges energy. ε_n and ε_ν are functions strongly dependent on the temperature, density and the chemical composition. So, it is unavoidable to compute the chemical evolution of the stellar interior to compute stellar evolution.

The boundary condition is $L_r = 0$ at the stellar centre. Since there occurs a partial derivative with respect to time, this indicates that the star at time $t + \Delta t$ is connected with its structure at t.

There may occur (for example in the case of cold WDs) that $\varepsilon_n = 0$, $\varepsilon_\nu = 0$ and $L_r > 0$. So, the star is releasing entropy. This does *not* violate the second principle of thermodynamics, since radiation carries away entropy and in such case the isolated system in which total entropy cannot diminish is the star and the surrounding space.

5. Transport of Energy in Stellar Interiors

Because of the variety of thermodynamic conditions, it is not surprising that all possible processes of energy transport play a rôle in stellar interiors. These processes are radiation, convection and conduction.

Radiation is the dominant process for transporting energy when material is transparent enough. Material may be considered at rest and the transport is driven by electromagnetic radiation. When matter is not so transparent, energy is transported by convection. Convection can be roughly described as two currents of matter moving, one outwards and the other inwards without net mass flux. If the outward flux carries more energy than the inward one it renders a net energy flux. Convection is one of the most uncertain ingredients of stellar interiors. This is especially important for the case of the outer layers of cold stars. Indeed, the uncertainties in the treatment of convection (usually the Mixing Length Theory MLT) prevent us to get a fully predictive theory in the red part of the HRD. Finally, conduction is important in conditions of very high densities.

Most of the stars have radiative and convective layers. For example, our Sun has a convective envelope and radiative interior, massive stars on the upper MS have convective cores and radiative envelopes, etc. Conduction is important in conditions of very high densities attained in the core of red giant stars and WDs. Indeed, conduction is usually considered so efficient that it is able to transport energy with a very small temperature gradient. In other words, conduction usually lead to structures nearly isothermal.

There is another physical process capable of transporting energy. This is the emission of neutrinos. In the context of normal stars, this is fundamentally different from the other three processes quoted above. Neutrinos have a so small interaction cross section with matter that their mean free path is by far larger than star sizes. So, neutrino emission acts as a local cooling process. The only contexts in which neutrinos have to be transported are core collapse supernovae (Janka et al., 2016) and the birth of neutron stars (Burrows & Lattimer, 1986).

5.1. Radiative Transport and the Opacity

The opacity is due to interactions that remove photons from a given direction of propagation. There are of two types of opacity sources qualitatively different. One can be defined as *true absorption* in which a photon is destroyed and its energy is employed to excite some degree of freedom of the plasma. The other process does not destroy the radiation but changes the direction of propagation; this is the *scattering*.

True absorption is due to

- *Bound-Bound transitions:* An electron jumps from a discrete level to another at higher energy. It leads to discrete absorption opacity.
- *Bound-Free transitions:* An electron jumps from a discrete level to the continuum. It leads to continuous opacity with a sharp cut off edge at wavelength corresponding to photons with the ionization energy.
- *Free-Free transition:* An electron jumps from two states of the continuum in the Coulomb field of a neighbouring ion. It also leads to continuum opacity.

At conditions of full ionization of the material, the only possible process is scattering. This due to the well known fact that *free particles cannot absorb photons*. It is easy to verify that the absorption of a photon by a free particle cannot fulfil energy and impulse conservation simultaneously.

As stated above, the stellar interior is in LTE. Thus, the radiation field is almost a black body spectrum given by Equation (7). It can be shown (see, e.g. Clayton 1968) that the opacity relevant for stellar interiors is the *Rosseland mean opacity*, defined as

$$\frac{1}{\kappa_R} = \left[\int_0^\infty \frac{dB_\nu}{dT} d\nu\right]^{-1} \int_0^\infty \frac{1}{\kappa^*_{\nu,a} + \kappa_{\nu,s}} \frac{dB_\nu}{dT} d\nu \tag{15}$$

where $\kappa^*_{\nu,a}$ is the true absorption coefficient $\kappa_{\nu,a}$ corrected by induced emission $\kappa^*_{\nu,a} = \kappa_{\nu,a}\big(1 - \exp\left(-h\nu/kT\right)\big)$, and $\kappa_{\nu,s}$ is the scattering coefficient.

Considering the number of species, the different degrees of ionization and the population of the energy levels of each of them it is easy to conclude that the amount of possible transitions is quite large. Also, in order to apply the theory of interaction of matter with radiation it is necessary to know the wave function of the present ions and the perturbations due to mean field effects that were not essential for the treatment of the EOS here are unavoidable. This makes radiative opacity calculations among the most difficult in astrophysics. Notice that in most cases the results are hardly testable in laboratory. This is not a minor difficulty.

The first opacity tables were computed assuming that all wave functions correspond to hydrogen like ions (ions with charge Z and one bound electron) which represents a poor approximation to reality. Since computational facilities were powerful enough, opacities were largely improved. Now, the OPAL project Iglesias & Rogers (1996); Rogers & Iglesias (1992) published tables of Rosseland

opacities[5] that cover a large portion of the conditions present in stellar interiors and virtually all chemical mixtures expected to occur in stars. For a given chemical composition these tables are presented as functions of the logarithms of T and R, with the latter defined as[6] $R \equiv \rho/T_6^3$ (where T_6 is the temperature in millions of Kelvins). These tables cover temperatures from $6 \times 10^3 K \leq T \leq 5 \times 10^8 K$ and $10^{-8} \leq R \leq 10^1$.

OPAL calculations neglect the presence of molecules. For temperatures below few thousands of Kelvins molecules have to be included. Classical calculations of opacities considering the molecular contributions have been presented by Alexander & Ferguson (1994) who tabulated opacities for a variety of chemical compositions, temperatures in the interval $2.7 \leq \log(T/K) \leq 4.5$ and the same values of R as in OPAL tables.

A typical result is presented in Figure (5) where we show the values of opacity for a Solar mixture ($X = 0.70$, $Y = 0.28$, $Z = 0.02$) as function of the temperature for different values of R. For low temperatures, κ_R has a deep minimum and tends to increase with T up to values at which molecules are broken. The maximum opacity values correspond to conditions of partial ionization of the species that dominate the composition (in this case hydrogen and helium). At higher T, κ_R decreases being dominated by bound-free and free-free transitions. For even higher T, and especially for low R values, κ_R shows a remarkable minimum. It corresponds to fully ionized matter that has a Thompson scattering opacity which corresponds to a value of $\kappa_R = 0.19(1+X)\, cm^2\, g^{-1}$.

In spite of the great efforts devoted to improve stellar opacities, still there are conditions for which they are not accurately known. This is so especially since for low mass objects interactions are strong and the perturbative expansion employed become poor approximations. This is the case found for the envelope of WDs and also very low mass stars and substellar objects.

It cannot overstated the relevance of the opacity. It appears in the equations of stellar evolution and oscillations. However, there is a quite remarkable difference: while opacity derivatives play no rôle in stellar evolution, they are essential for non-adiabatic pulsation calculations. So, it is not only necessary to know opacities accurately but also their derivatives (see *carefully* Figure (5)).

If radiative transport prevails, the gradient of temperature is given by

$$\nabla_{rad} = \left(\frac{d\ln T}{d\ln P}\right)_{rad} = \frac{3}{16\pi acG}\frac{\kappa_R P L_r}{M_r T^4} \tag{16}$$

5.2. Convective Transport

In convective zones we need to compute the temperature gradient ∇_{conv}. The treatment usually employed is that given by the Mixing Lenght Theory (MLT). This theory assumes (see, e.g., Cox & Giuli 1968; Kippenhahn & Weigert 1990) that bubbles carry heat that is exchanged with the surroundings after travelling

---

[5]These are available at `https://opalopacity.llnl.gov/existing.html`. Also, they provide interpolation routines tailored to handle these tables.

[6]This quantity has been chosen because of numerical convenience since in stellar interiors R vary on a much narrower interval than ρ, that was employed in older tabulations.

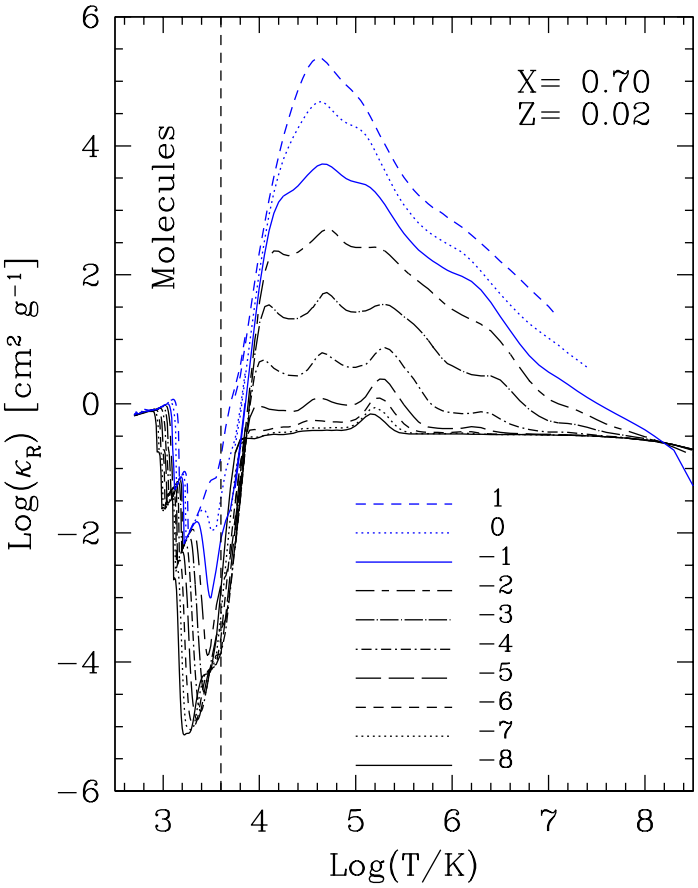

Figure 5. The Rosseland mean opacity for a Solar mixture. At low temperatures ($Log(T/K) \leq 3.7$) opacities include the contributions due to molecules whereas for higher temperatures they are due to atoms, ions, and electrons. Different lines are labelled with the corresponding value of $Log(R)$. For further details see text.

a distance ℓ. Remarkably, this critical parameter is *not* provided by the theory. This is a serious shortcoming since the temperature gradient ∇_{conv} is strongly dependent on this parameter. Frequently, ℓ is adjusted to fit the radius of the Sun and then is applied to any star. Certainly, this procedure is not free of objections. There are in the literature a large number of proposals of how to improve the treatment of energy transport by convection. However, there is no consensus on what is the best way to do it. Clearly, this problem is still open. Despite these limitations, MLT is used in stellar modelling because of its simplicity.

The temperature gradient ∇_{conv} can be expressed as a function of two dimensionless parameters: U and W defined as

$$U = \frac{3acT^3}{C_P \rho^2 \kappa_R \ell^2} \sqrt{\frac{8H_P}{g\delta}} \tag{17}$$

and

$$W = \nabla_{rad} - \nabla_{ad} \tag{18}$$

where g is the gravitational acceleration, and H_P is the pressure scale height. U is proportional to the ratio of the time for free falling a distance ℓ and the thermal adjustment timescale. Usually, ℓ is written as $\ell = \alpha_{mlt} H_P$ where α_{mlt} is a free parameter and H_P is given by

$$H_P = -\frac{dr}{dlogP} = \frac{P}{g\rho} = \frac{r^2 P}{GM_r \rho}. \tag{19}$$

Notice that $H_P \to \infty$ at the stellar centre, while near surface it is $H_P \ll R$. With these quantities we have to solve the cubic equation

$$\left(\xi - U\right)^3 + \frac{8U}{9}\left(\xi^2 - U^2 - W\right) = 0 \tag{20}$$

and then, we compute the temperature gradient with

$$\nabla_{conv} = \nabla_{ad} + \xi^2 - U^2. \tag{21}$$

Due to the rough description of convection made by the MLT, ∇_{conv} is a rather uncertain quantity. In convective cores this uncertainty has no impact on the structure of the star, since ∇_{conv} differs from ∇_{ad} typically only in $\approx 10^{-8}$. In other words, at these conditions convection is almost adiabatic since the heat exchanged is far smaller than the heat content of the material. However, this is *not* the case for convective envelopes. In outer layers, convection is appreciably non-adiabatic (the difference $\nabla_{conv} - \nabla_{ad}$ is non-negligible) and the uncertainties in ∇_{conv} make the outer structure of these stars to be poorly known. This fact is sometimes forgotten but it is very relevant for a correct interpretation of the observational data based on theoretical models that employ this theory.

5.3. Conductive Transport

As already quoted, conduction is important at high densities. In these conditions electrons are largely inhibited to undergo Coulomb scattering because most quantum states are occupied (and then, they are not available as final state for scattering because of the Pauli's exclusion principle). Thus, electrons use to have

a very large mean free path and carry information of temperature differences over long distances. This process has been studied in many papers, e.g., Itoh et al. (1983); Itoh et al. (1984).

Conduction is usually handled to define a conductive opacity equivalent to the Rosseland mean opacity. Then, radiative and conductive opacities are added as parallel resistances in electric circuits:

$$\frac{1}{\kappa} = \frac{1}{\kappa_R} + \frac{1}{\kappa_{cond}}. \tag{22}$$

Evidently, the dominant opacity is the lowest of them.

As stated above, there are thermodynamic conditions at which κ_R is not accurately known and we cannot apply Equation (22). Fortunately, in most situations this does not represent a serious shortcoming since in these cases we have $\kappa_{cond} \ll \kappa_R$ and then, $\kappa = \kappa_{cond}$

6. Nuclear Reactions

At present, it is clear that the main source of energy that allow stars to shine on very long times is nuclear reactions.

Nuclei are objects formed by protons and neutrons that remain bound by *strong interactions*. Usually, the numbers of protons and neutrons are denoted by Z and N respectively while the total baryon number of a nucleus is $A = N + Z$. The radius of nuclei is approximately $1.2 \times 10^{-13} A^{1/3}\, cm = 1.2 A^{1/3}\, Fm$. Let us define the binding energy $B(A,Z)$ as $B(A,Z)/c^2 = M(A,Z) - Zm_p - (A-Z)m_n$. Here $M(A,Z)$ is the mass of the nucleus (A,Z) and m_p (m_n) is the mass of the proton (neutron). A nucleus can exist if $B(A,Z) < 0$, i.e., to disintegrate it is necessary to add an amount of energy greater or equal to $|B(A,Z)|$. Notice that the condition $B(A,Z) < 0$ does not imply the stability of nucleus (A,Z); it may be stable or decay by several channels (e.g., by the emission of a photon, proton, neutron, electron, ^4He, etc.).

It is well known that the most tightly bound nuclei are those with Z values close to iron: vanadium, manganese, chromium, cobalt, nickel, copper, etc. If a fusion reaction occurs between light nuclei and produces a nucleus lighter than iron peak isotopes, in general it will be exothermic. This is the way stars release energy: they continuously undergo reactions that produce more tightly bound nuclei. As energy conserves, a part of it may be stored in its interior and the rest is released as luminosity.

As in any combustion process, nuclear reactions modify the composition of the stellar interior and slowly change the mean molecular weight. So, the stellar structure has to accommodate to the continuously changing distribution of elements, modifying its characteristics (radius, luminosity, etc.). *This, and the energy released as luminosity are the very reasons why stars evolve.*

At the conditions present in stellar interiors, protons, neutrons and nuclei are non-degenerate particles that obey the Maxwell-Boltzmann distribution of velocities

$$\phi(v) d^3v = 4\pi \left(\frac{h^2}{2\pi\mu kT} \right)^{3/2} v^2 \exp\left(-\frac{\mu v^2}{2kT} \right) dv \tag{23}$$

where μ is the reduced mass of the reacting particles[7], and v is their relative velocity. This fact is of enormous relevance, since the particles that undergo the reactions are in the high energy tail of the distribution.

Nuclear reactions in astrophysics occur at very low energy. Let us imagine that two positively charged nuclei approach each other. Since typical energies are low (≈KeVs) and the potential barriers are much higher (≈MeVs), classical physics predicts the occurrence of a turning point of the trajectories that prevents nuclei to get close enough to feel their structures, inhibiting any reaction. However, the correct treatment is given by quantum mechanics which allows the occurrence of the *tunnel effect* that provides a way for nuclei to go across the potential barrier and allows the reaction to occur.

The fundamental quantity to go further is the nuclear reaction cross section σ, usually is defined as

$$\sigma(v) = \frac{S(E)}{E} \exp\left(- \frac{2\pi Z_0 Z_1 e^2}{\hbar v} \right). \tag{24}$$

The exponential factor is the so-called *Gamow Factor* that describes the tunnelling across the repulsive Coulomb potential, $E = \mu v^2/2$ is the energy at the reference frame in which the centre of mass is at rest, Z_0 and Z_1 are the charges of the reacting nuclei, and e is the electric charge unit. In the case in which the energy of the projectile does not coincide with any energy level of the nuclei $S(E)$ is a smooth function and the reaction proceed as *non-resonant*.

In the case in which particles reach the energy level of the compound nucleus, σ is described by the Breit-Wigner cross section

$$\sigma = \frac{(2\ell + 1)}{4\pi} \lambda^2 \frac{\Gamma_a(\Gamma - \Gamma_a)}{(E - E_r)^2 + \Gamma^2}. \tag{25}$$

Here ℓ is the quantum number of angular momentum corresponding to the resonance, E_r is the energy of the resonance, Γ is the width of the energy level, Γ_a is the width due to the resonance channel, and λ is the De Broglie wavelength of the particle.

The factor $S(E)$ in Equation (24) cannot be measured in laboratory directly for the range of energies at which non-resonant reactions occur in stars. At these energies, reaction cross sections use to be too low for such purpose. So, it is a common practice to measure the reactions at energies much higher at which resonances occur and reactions are by far more frequent. Then, employing expressions like Equation (25) the cross section is *extrapolated* to stellar energies. This procedure leads to uncertainties in the knowledge of the factor $S(E)$.

In order to compute the energy release due to nuclear reactions as well as the change of chemical abundances we have to compute their reaction rates. This is given by an integral over the distribution of velocities of the particles

$$r = \frac{N_0 N_1}{1 + \delta_{0,1}} \int_0^\infty \sigma(v)\ v\ \phi(v) d^3 v \tag{26}$$

---

[7]Do not confound with the mean molecular weight defined in the treatment of the equation of state.

where N_0 and N_1 are the particle number densities of the reacting nuclei. The Kroenecker's delta takes into account that if particles are identical, the number of different pairs has to be corrected by a factor of one half.

In the case of non-resonant reactions the rate is

$$r_{nr} = \frac{2.62 \times 10^{29}}{(1+\delta_{0,1})AZ_0Z_1}\rho^2 \frac{X_0X_1}{A_0A_1} S_0 \tau^2 \exp\big(-\tau\big)\, cm^{-3}\, s^{-1}, \tag{27}$$

where A_0 and A_1 are the masses of the reacting nuclei, X_0 and X_1 are their abundances by mass, and A the reduced mass ($1/A = 1/A_0 + 1/A_1$). S_0 is the value of $S(E)$ at the energy of maximum efficiency of the reactions (Clayton, 1968) given in units of KeV barn (1 barn$= 10^{-24}\, cm^2$), and τ is

$$\tau = 42.48\left(\frac{Z_0^2 Z_1^2 A}{T_6}\right)^{1/3}. \tag{28}$$

For the case of resonant reactions the expression is

$$r_r = \frac{2.94 \times 10^{36}}{1+\delta_{0,1}}\rho^2 \frac{X_0X_1}{A_0A_1}\frac{1}{AT_6}\frac{\Gamma_1(\Gamma-\Gamma_1)}{\Gamma}\exp\left(-11.61\frac{E_r}{T_6}\right) cm^{-3}\, s^{-1}, \tag{29}$$

where E_r is the energy of the resonance in KeV units and Γ_1 is the energy width of the resonance employed by the reaction.

The energy release due to nuclear reactions is given by

$$\varepsilon_{nuc} = \frac{1}{\rho}\sum_i r_i Q_i \tag{30}$$

where Q_i is the energy released and the sum goes over all the reactions.

6.1. The Proton-Proton Cycle

The Proton-Proton cycle is the following sequence of reactions

$$\begin{aligned}
{}^1H + {}^1H &\rightarrow {}^2D + e^+ + \nu_e, && (31)\\
{}^2D + {}^1H &\rightarrow {}^3He, && (32)\\
{}^3He + {}^3He &\rightarrow {}^4He + 2\,{}^1H, && (33)\\
{}^3He + {}^4He &\rightarrow {}^7Be, && (34)\\
{}^7Be + e^- &\rightarrow {}^7Li + \nu_e, && (35)\\
{}^7Li + {}^1H &\rightarrow 2\,{}^4He, && (36)\\
{}^7Be + {}^1H &\rightarrow {}^8B, && (37)\\
{}^8B &\rightarrow {}^8Be + e^+ + \nu_e, && (38)\\
{}^8Be &\rightarrow 2\,{}^4He. && (39)
\end{aligned}$$

The key Reaction (31) of the Proton-Proton cycle was identified by Hans Bethe. Two protons encounter each other; then, one becomes a neutron and

get bounded as a deuteron. This is a *weak interaction* that has an extremely low cross section. The deuteron is the simplest composed nucleus with a low binding energy. Considering it as bounded in a spherical potential well, the wave function occupies an appreciable volume in space, even outside the well. This has the important consequence that Reaction (32) has a cross section larger than Reaction (31) by a factor of $\approx 10^{18}$. Then, in the deep solar interior, the ratio of the abundances of deuterium to hydrogen is $\left(D/H\right)_{\odot} \approx 10^{-18}$. However, remarkably, on Earth this ratio is much larger: $\left(D/H\right)_{\oplus} \approx 10^{-4}$. This fact is easily accounted for if we assume that the deuterium present on Earth is due to Big Bang nucleosynthesis and that the matter forming the Earth has never been in the solar interior. Evidently, it imposes a fundamental condition to any theory of the formation of our Solar System.

The deuteron captures another proton and produces a ^3He (Reaction 32). Then, two ^3He nuclei fuse to give a ^4He and two ^1H (Reaction (33)). This is the PP I subcycle. When there is ^4He, it is possible the occurrence of Reaction (34), and the cycle goes through subcycles PP II (Reactions (31), (32), (34), (35), and (36)) or PP III (Reactions (31), (32), (34), (37), (38), and (39))

Because in this cycle the reactions involve the lightest nuclei, the Coulomb barriers are the lowest possible. So, the PP-cycle is the dominating energy source at low temperatures (see below Figure (6)). Of course, there are reactions that can occur at lower temperatures. For example, Reaction (32) is the only one that occurs in substellar objects with masses of $\gtrsim 10^{-2} M_{\odot}$. For the case of Solar composition objects, it dominates for stars with $M \leq 1.2 M_{\odot}$.

The rate of energy release for the PP-cyle in stationary conditions[8] is given by

$$\varepsilon_{pp} = 2.38 \times 10^6 \frac{\rho X^2}{T_6^{2/3}} \exp\left(- \frac{33.80}{T_6^{1/3}} \right) erg\, g^{-1}\, s^{-1}. \tag{40}$$

The PP-cycle is self starting. It needs no other isotope but hydrogen present for it to occur (of course, if there is no ^4He, the only possible subcycle is the PP I). This is in sharp contrast with the next cycle to be presented, the Carbon-Nitrogen-Oxygen cycle

6.2. The Carbon-Nitrogen-Oxygen Cycle

The other way to burn hydrogen in stellar interiors is the Carbon-Nitrogen-Oxygen (or CNO) cycle:

[8]This corresponds to the case in which deuterium and the isotopes of lithium, beryllium and boron have low abundances that remain almost constant on the timescale of hydrogen burning.

$$
\begin{aligned}
{}^{12}C + {}^{1}H &\rightarrow {}^{13}N, && (41)\\
{}^{13}N &\rightarrow {}^{13}C + e^{+} + \nu_e, && (42)\\
{}^{13}C + {}^{1}H &\rightarrow {}^{14}N, && (43)\\
{}^{14}N + {}^{1}H &\rightarrow {}^{15}O, && (44)\\
{}^{15}O &\rightarrow {}^{15}N + e^{+} + \nu_e, && (45)\\
{}^{15}N + {}^{1}H &\rightarrow {}^{12}C + {}^{4}He, && (46)\\
{}^{15}N + {}^{1}H &\rightarrow {}^{16}O, && (47)\\
{}^{16}O + {}^{1}H &\rightarrow {}^{17}F, && (48)\\
{}^{17}F &\rightarrow {}^{17}O + e^{+} + \nu_e, && (49)\\
{}^{17}O + {}^{1}H &\rightarrow {}^{14}N + {}^{4}He. && (50)
\end{aligned}
$$

The CNO cycle does need for the presence of ${}^{12}C$ or ${}^{14}N$. This is very different from the PP-cycle. In this cycle protons are captured on heavier nuclei that produce β-unstable isotopes that decay on a timescales of few minutes. Protons are converted to neutrons in such decays (Reactions (42), (45), and (49)). This cycle is usually divided in two subcycles, the CN (Reactions (41)-(46)) and ON (Reactions (44), (45), and (47)-(50)). In the CN (ON) subcycle the ${}^{12}C$ (${}^{14}N$) acts as a catalyst because it is destroyed and then produced during the subcycle.

Compared to the PP-cycle, since proton captures occur on heavier nuclei, the CNO cycle is possible for higher temperatures. The mean energy release in stationary conditions is given by

$$\varepsilon_{cno} = 8.67 \times 10^{27} \frac{\rho X X_{CN}}{T_6^{2/3}} \exp\left(- \frac{152.28}{T_6^{1/3}} \right) erg\, g^{-1}\, s^{-1} \qquad (51)$$

where X_{CN} is the abundance of ${}^{12}C$ and ${}^{14}N$.

6.3. The Helium Burning

-

The main helium burning reactions are

$$
\begin{aligned}
{}^{4}He + {}^{4}He &\leftrightarrow {}^{8}Be, && (52)\\
{}^{8}Be + {}^{4}He &\leftrightarrow {}^{12}C^{*}, && (53)\\
{}^{12}C^{*} &\rightarrow {}^{12}C, && (54)\\
{}^{12}C + {}^{4}He &\rightarrow {}^{16}O, && (55)\\
{}^{16}O + {}^{4}He &\rightarrow {}^{20}Ne, && (56)\\
{}^{20}Ne + {}^{4}He &\rightarrow {}^{24}Mg. && (57)
\end{aligned}
$$

Considering that the species present at the end of hydrogen burning are helium and traces of hydrogen, a fundamental difficulty for burning helium is

that there are no stable nuclei with $A = 5$ or 8 in Nature. The 3α cycle[9] is formed by Reactions (52)-(54). This has been proposed by Salpeter and Hoyle. Salpeter recognised that this had to be at least a two step cycle. Hoyle proposed that Reaction (53) must be resonant reactions in order to account for the amount of ^{12}C present in the Universe. In particular, he postulated the existence of an excited energy level of the ^{12}C for allowing the resonant reaction to occur. In a landmark discovery of nuclear astrophysics, the existence of this energy level was confirmed experimentally by W. A. Fowler. In few words, two ^4He fuse to produce a highly unstable ^8Be (decay time $2.6 \times 10^{-16}\, s$) that, before decaying, captures another ^4He to produce an excited $^{12}C^*$. As a final reaction, very few times the excited carbon nucleus $^{12}C^*$ decays by means of two forbidden radiative transitions to become ^{12}C; but, by far, the most probable end of $^{12}C^*$ is to split back in three helium nuclei. Reactions (52) and (53) are resonant and endothermic, and the remaining (54) is by far more exothermic. Reactions (55)-(57) are other important reactions during the helium burning stage.

The energy release due to the 3α cycle is

$$\varepsilon_{3\alpha} = 5.09 \times 10^{11} \frac{\rho^2 Y^3}{T_8^3} \exp\left(-\frac{44.027}{T_8} \right) erg\, g^{-1}\, s^{-1} \tag{58}$$

where $T_8 = T/10^8 K$ and Y is the abundance of ^4He.

A comparison of the energy release of the main nuclear reaction cycles (PP, CNO, and 3α) is presented in Figure (6).

7. The Equations of Structure

The full set of partial differential equations of stellar evolution is

$$\frac{\partial r}{\partial M_r} = \frac{1}{4\pi r^2 \rho}, \tag{59}$$

$$\frac{\partial P}{\partial M_r} = -\frac{G M_r}{4\pi r^4}, \tag{60}$$

$$\frac{\partial L_r}{\partial M_r} = \varepsilon_n - \varepsilon_\nu - T\frac{\partial S}{\partial t}, \tag{61}$$

$$\frac{\partial T}{\partial M_r} = -\frac{G M_r T}{4\pi r^4 P} \nabla. \tag{62}$$

Two boundary conditions are imposed at the centre ($M_r = 0$), we have $r = 0$ and $L_r = 0$. The others are set at the outermost layers ($M_r = M$), where $T = T_{atm}$ and $P = P_{atm}$; T_{atm} and P_{atm} are the temperature (usually the effective one) and the total pressure at the stellar atmosphere.

In order to find the value of the temperature gradient ∇ we have to consider its stability against convection. Let us consider the Schwarzschild criterium that states that if $\nabla_{rad} \leq \nabla_{ad}$, $\nabla = \nabla_{rad}$, if $\nabla_{rad} > \nabla_{ad}$, $\nabla = \nabla_{conv}$, where $\nabla_{ad} = \left(\frac{\partial \ln T}{\partial \ln P}\right)_S$.

---

[9]Its name is due that sometimes ^4He nuclei are referred to as α particles.

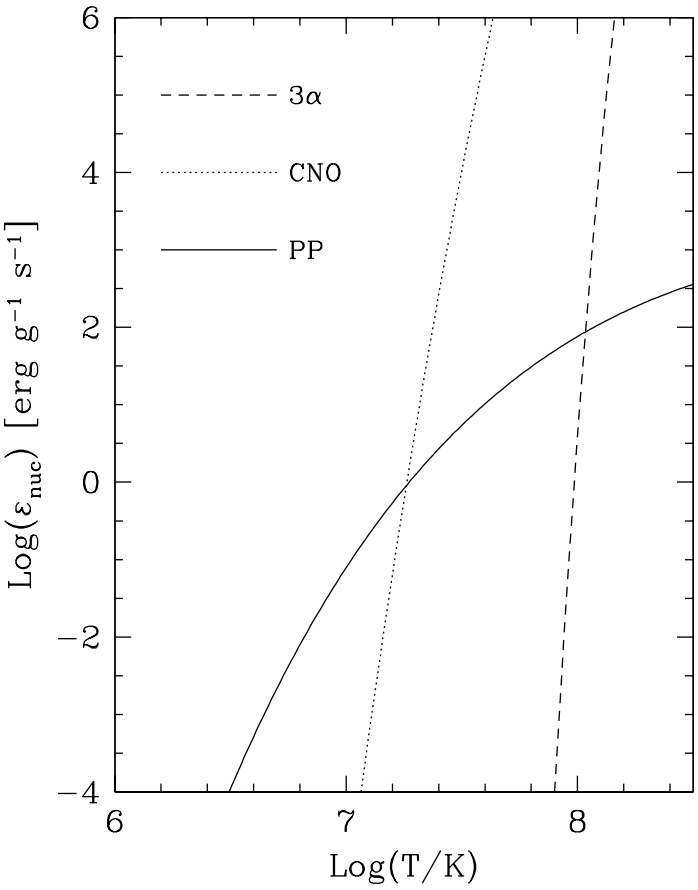

Figure 6. The rates of energy release due to the Proton-Proton, Carbon-Nitrogen-Oxygen, and Triple Alpha cycles (PP, CNO, and 3α respectively). For the PP and CNO cycles we assumed $X = 1$, $\rho = 1\, g\, cm^{-3}$, and $X_{CN} = 0.01$. For the case of the 3α we considered $Y = 1$, $\rho = 10^4\, g\, cm^{-3}$ which are typical values for helium burning.

Here we have written the system of equations as a function of M_r. This is usually referred to as *Lagrangian variable*, in contrast to the Eulerian variable r. This is more adequate because of numerical reasons.

As the constitutive physics is strongly dependent on the chemical composition, it is necessary to simultaneously solve the equations for the evolution of the abundances.

7.1. Solution of the Structure Equations

Computing stellar evolution is possible only by means of numerical simulations. The method usually employed for such purpose has been devised by Louis Henyey (Henyey et al., 1964) in the end of fifties. Henyey proposed to employ a finite differences method with an implicit algorithm, writing temporal derivatives as backward differences. This has been masterfully described by Kippenhahn et al. (1967). The key advantage of such algorithm compared to others is its *numerical stability*. With this method it is possible to handle stellar models with few thousand of concentric shells and to compute its evolution even with an average personal computer.

7.2. Solution of the Chemical Evolution Equations

When computing stellar models, one possibility is to study them paying special attention to the evolution. In this case it may be enough to consider a *nuclear reaction network* (the name usually employed when referring to the system of differential equations that provide the chemical evolution of the stellar interior) with few tens of carefully chosen isotopes. When models are constructed to be applied to study stellar oscillations this strategy is adequate.

On the contrary, if we construct stellar models to compute the nucleosynthesis products, things are far harder. In this case, the number of isotopes to be considered may be of thousands and the number of reactions connecting them can be an order of magnitude larger. A key property of these reaction networks is that they include reaction rates that operate on very disparate timescales, making the problem very stiff. A classical example of this difficulty is in the solution of the detailed reaction network of PP cycle when we consider deuterium explicitly, the rates of Reactions (31) and (32) differ in a factor of 10^{18}. The implicit method of Bader & Deuflhard is strongly recommended (Press et al., 1992). A very nice account of the difficulties of nucleosynthesis calculations can be found in Timmes (1999).

When nuclear burning occurs in convective layers, convective currents have a characteristic timescale by far shorter than that of nuclear reactions. Thus, the entire convective zone is continuously mixed and burned. An extreme assumption is to consider that mixing is infinitely fast (instantaneous mixing). So, the entire convective zone remains homogeneous. Also, convective boundaries use to move, and this has to be considered in detail. Instantaneous mixing is not valid during the latest stages of massive stellar evolution close to the final core collapse.

8. The Evolution of Stars

8.1. The Pre-Main Sequence of Low Mass Stars

Here we describe the stage usually called *Pre-MS* or PMS. We shall restrict ourselves to the case of low mass objects. For the case of higher mass objects the problem is far more complex.

Essentially, the PMS is the stage in which stars evolve from the initial establishment of hydrostatic equilibrium up to core hydrogen burning ignition. At the very beginning of the PMS the stellar matter is so opaque that the object is entirely convective up to its photosphere. This kind of structure is said to correspond to the *Hayashi Line* along which the stars initially evolve (see, e.g., Kippenhahn & Weigert 1990). For a given mass value, the Hayashi line is a very steep line that defines the red edge of the region of the HRD at which stars can be located. To the right side of this line hydrostatic equilibrium is not possible. In this initial stage the stellar structure is well approximated by a polytropic sphere with n=3/2 (see § 3.1). The object shines thanks to the release of gravitational energy due to contraction. This effect increases the internal temperature which, in turn, makes the opacity to decrease (see Figure (5)) and the centre of the star becomes radiative. So, the *evolutionary track* departs from the Hayashi line bending in the HRD to higher effective temperatures.

Here we have just introduced the fundamental concept of evolutionary track. This is generally referred to the path followed by a star in the HRD during its evolution[10].

The PMS ends when hydrogen burning establishes and the star arrives to the *quite inappropriately called* Zero Age MS (or simply ZAMS). These ages, defined in this case when the star has burned 1% of the original hydrogen content are given in Table (1). A typical PMS evolution on the HRD is presented in Figure (7). These tracks have been calculated with our evolutionary code for this lecture notes (Benvenuto & De Vito, 2003)

8.2. The Evolution of Low Mass Stars

Usually we call *star* an object that at some stage of its evolution shines with a luminosity fully provided by nuclear reactions. For Solar composition, stars have masses $M \geq 0.08 M_{\odot}$. Sub-stellar objects with $0.016 M_{\odot} \leq M \leq 0.08 M_{\odot}$ release energy by nuclear reactions and gravitational contraction. These are the *brown dwarfs*. For even lower masses, $M \leq 0.016 M_{\odot}$, temperature is so low that the objects cannot undergo any nuclear reaction and are fed only by gravitational contraction (Burrows et al., 1995). These are the *gaseous giant planets*. For sub-stellar objects usually it is very important the burning of primordial deuterium by Reaction (32) but the PP cycle is not completed because the higher Coulomb barrier inhibits the occurrence of Reaction (33).

In Figure (8) (Sackmann et al., 1993) we show the evolution of our Sun. Its PMS is denoted by a dashed line and the object reaches the ZAMS at point

[10]Of course, it is possible to call this way the path that describe the change of other quantities, e.g., the evolution of the central conditions of the star: $Log\, T_c$ versus $Log\, \rho_c$, but this is not the standard case.

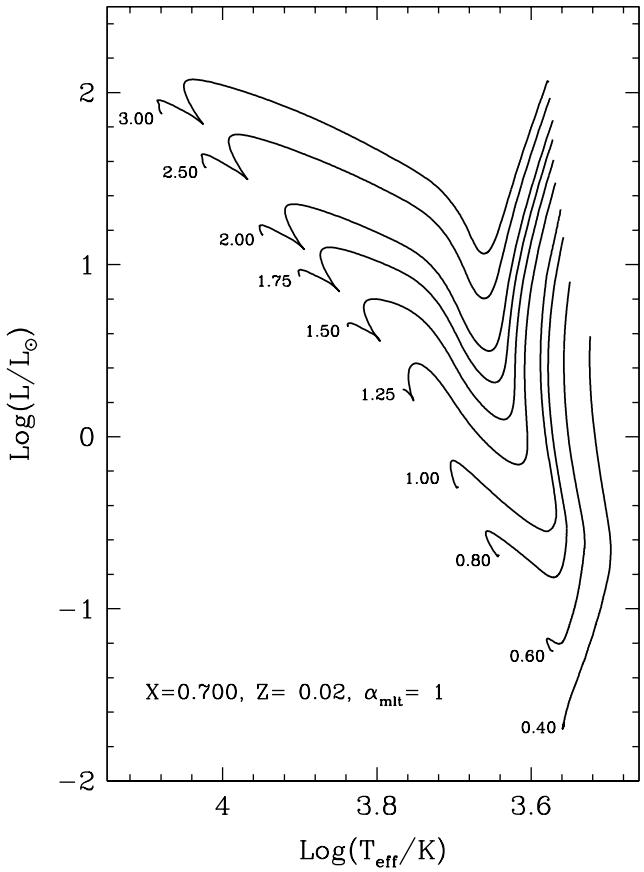

Figure 7. The PMS evolution for a set of stellar masses. Calculations start from a polytropic structure ($n = 1.5$) on their respective Hayashi tracks and are followed up to the onset of core hydrogen burning. Each curve is labelled with the corresponding mass given in solar units. These tracks have been computed by ourselves employing our stellar code.

Table 1. Conditions at the end of the Pre-MS. Columns indicate the mass of the object in solar units, the age in million years and the decimal logarithms of the effective temperature in Kelvins, the luminosity in solar units, the central temperature in Kelvins and the central density in $g\ cm^{-3}$.

M	Age	$Log\ T_{eff}$	$Log\ L$	$Log\ T_c$	$Log\ \rho_c$
0.40	10244	3.557	-1.657	6.906	1.812
0.60	1391	3.571	-1.241	6.968	1.824
0.80	522.2	3.641	-0.686	7.051	1.857
1.00	331.9	3.694	-0.288	7.101	1.855
1.25	117.2	3.765	0.278	7.205	1.909
1.50	73.4	3.837	0.646	7.260	1.893
1.75	49.3	3.900	0.937	7.296	1.850
2.00	32.6	3.948	1.177	7.320	1.793
2.50	19.8	4.021	1.569	7.353	1.683
3.00	11.1	4.078	1.881	7.376	1.586

A. There, the star is burning hydrogen in its radiative core. B corresponds to the present Sun and E denotes the core hydrogen exhaustion that corresponds to the age of 10.91 Gyr. At that moment the star leaves the MS and starts to undergo hydrogen shell burning that dominates its energy balance, evolves to lower effective temperatures and develops a deep outer convective zone, ascending on the *Red Giant Branch* (or RGB, points F to H). The stellar core is strongly degenerate and undergoes heavy neutrino losses that make the maximum temperature to be located off-centre. Helium is suddenly ignited at point H on the track when the hottest stellar layers reach $T_8 \approx 1$. These layers are strongly degenerate, which makes the pressure of matter to be weakly dependent on temperature. In these conditions, helium ignition is initially unstable. This is the so-called *helium flash*. Helium burning ignition leads to an energy release that increases the temperature[11] but, since the EOS is weakly dependent on temperature, the structure is only slightly modified but nuclear reactions are strongly accelerated. The flash progressively removes the degeneracy and the burning tends to stabilise. On a short timescale the object finds a new, long lived evolutionary stage called *horizontal branch* (or HB, corresponding to point K on the track). Helium is burned stably on the HB and after its exhaustion on the core, it develops a helium shell burning and evolves to the red region in the HRD again, now on the *Asymptotic Giant Branch* or AGB. At these conditions the star begins simultaneously to suffer mass loss and thermal pulses. Thermal pulses are due to the interaction between the shells burning hydrogen and helium and have a timescale of $\approx 10^5$ y, far longer than the timescale in which a sound wave goes across the star. When the star has lost a large amount of mass, starts to evolve bluewards to become a carbon-oxygen WD star of $0.541 M_\odot$.

[11] At these conditions the pressure is dominated by degenerate, non-relativistic electrons while the specific heat is dominated by the non-degenerate gas of nuclei.

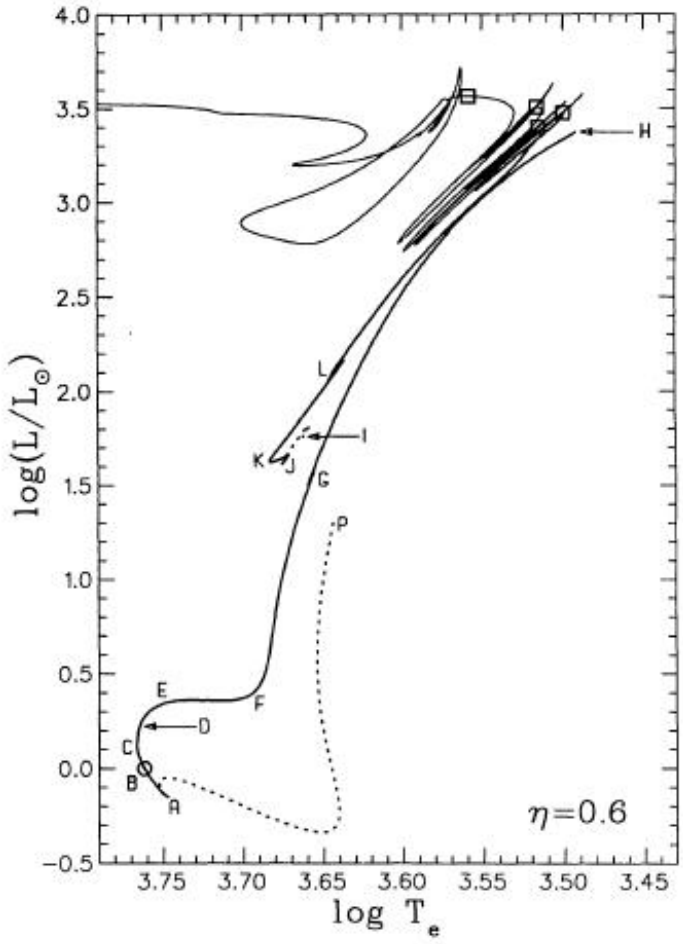

Figure 8. The evolutionary track of our Sun. For details, see text. Reprinted from Sackmann, Boothroyd & Kraemer, "Our Sun. III. Present and Future", ApJ, 418, 457, 1993, `https://ui.adsabs.harvard.edu/abs/1993ApJ...418..457S`, ©AAS. Reproduced with permission.

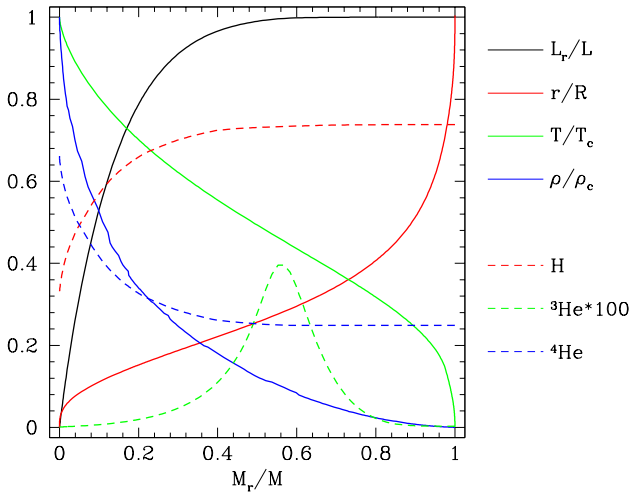

Figure 9. The structure and composition of the present Sun. The values used for scaling are $T_c = 1.54 \times 10^7$ K and $\rho_c = 162\, g\, cm^{-3}$; also $L = L_\odot$ and $R = R_\odot$. These results have been computed by ourselves employing our stellar code.

It is interesting to discuss the present structure of the Sun. Its main characteristics are shown in Figure (9). Most of the luminosity (dominated by the PP cycle, although the CNO reactions give some contribution) is released in the inner 40% of mass. Remarkably, the profiles of temperature, density and hydrogen and helium abundances are monotonous. However, this is not the case for the profile of ^3He abundance (enhanced by a factor of 100). This is due to the differences in the Coulomb barriers of the Reactions (31) and (32), compared to those occurring in the case of Reactions (33) and (34). In the core of the Sun the temperature is high enough to produce and burn ^3He. However this is not the case in outer layers; there ^3He burning is not so efficient.

8.3. The Evolution of Intermediate Mass Stars

Usually, we consider as intermediate mass stars those objects that ignite helium in non-degenerate conditions (they do not suffer a helium flash) and develop a degenerate carbon oxygen core after helium core exhaustion. This sets the mass interval for these objects in the range of $1.8 - 2.2 < M/M_\odot < 8 - 9$ (Chiosi, 1997).

Typical tracks of intermediate mass stars are shown in Figure (10) and some relevant characteristics of the models are presented in Table (2).

The ZAMS for stars in this range of masses is at temperatures appreciably higher than those of lower mass objects. As consequence, they have radiative outer layers while the deep interior has to be convective to transport the large amount of energy released by the CNO cycle. Due to the occurrence of convection in the deep interior, the stars burn the available hydrogen in the entire convective zone.

The meaning of points A-I given in Table (2) is presented in Figure (11) for the case of a $4M_{\odot}$ object. This is valid for the rest of the evolutionary tracks presented in this subsection; notice that all of them have a similar morphology. Evolution begins at point A that corresponds to the ZAMS, where we set age to zero. Point B corresponds to the minimum effective temperature during core hydrogen burning MS while point C denotes the end of the latter. From that stage on, stars develop a shell burning hydrogen and the evolutionary track goes across the HRD in a relatively short timescale (as compared to MS duration) becoming red giant (point D). Because of the relative shortness of this timescale, finding stars at this stage is not frequent and because of this reason this region of the HRD is known as the *Hertzsprung gap*. The star begins to develop a deep outer convective zone while the core has not reached temperatures of hundred million Kelvins, necessary to ignite helium, yet. Such ignition occurs when the stars reach a luminosity maximum (point E). Remarkably, the rise of another source of energy forces the stars to rearrange to a structure that evolves towards lower luminosities[12] (up to point F). Most of core helium is burnt out in convective conditions during a loop (from points F to H) in which the star spends an appreciable timescale. At these conditions, helium core is almost exhausted and the star develops a deep convective zone and evolves towards higher luminosities up to the end of the calculation (point I). This is consequence of the outward motion of the shells burning hydrogen and helium.

After these stages, while the objects are still in the red part of the HRD, the mentioned shells become closer and closer forcing the stars to undergo thermal pulses in a way similar as mentioned for the case of low mass objects. However, in this case the timescale of pulses is at least an order of magnitude shorter (10^4 y). Simultaneously, during thermal pulses, stars undergo mass loss. When most of the hydrogen rich envelope has been lost, the star evolves on a short timescale (comparable to that of a thermal pulse) to a compact structure reaching effective temperatures much higher than those corresponding to the ZAMS at the same range of luminosities. Then, the evolutionary track star bends down starting the pre-WD stage. At this moment the star is composed by a carbon-oxygen core surrounded by a helium shell that has $\approx 1\%$ of the stellar mass, and an even less massive outermost hydrogen layer.

8.4. The Evolution of White Dwarfs

As discussed above, WDs represent the final state of evolution of low and intermediate mass stars. This kind of objects is very important for asteroseismology since it is well known that they undergo non-radial pulsations. Because of this reason, we present some characteristics of these objects when considered as consequence of stellar evolution. Here we shall not discuss the WD composition in details but consider a very simple case to show the general trend of their evolution.

In Figure (12) we show a typical set of cooling tracks of WDs for different masses from rather low ($0.3M_{\odot}$) to high ($1.2M_{\odot}$) values. Here we have assumed that all models have the same homogeneous chemical composition of carbon and

[12]This occurs in a similar way to the case of low mass objects at the onset of the helium flash.

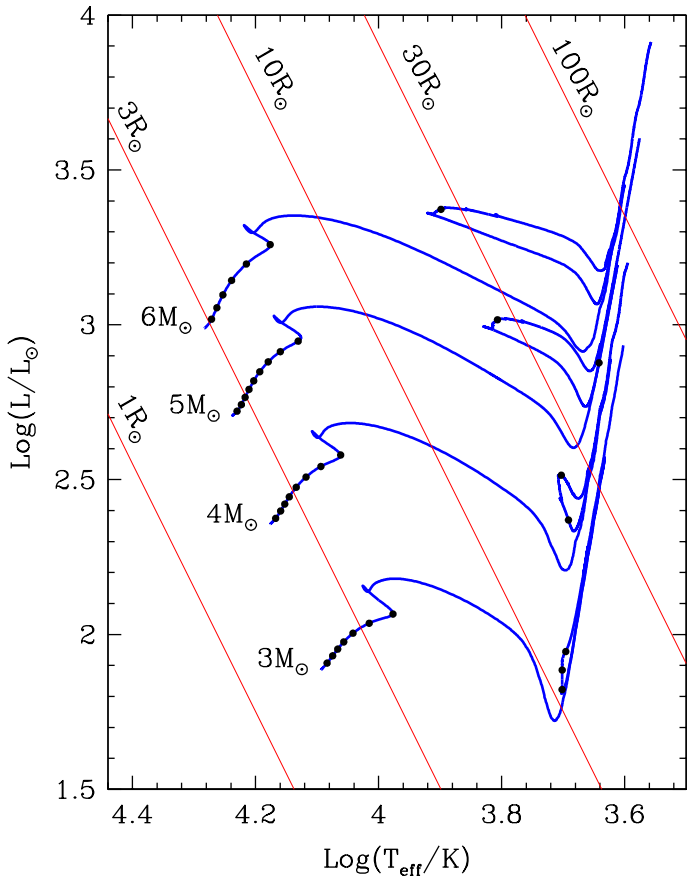

Figure 10. Typical HRD for the case of intermediate mass, Solar composition stars. The masses corresponding to each evolutionary tracks, shown in solid blue lines, are indicated in solar units. Lines of constant radii are shown in thin red lines. On the tracks, dots indicate age intervals. These are of 5×10^7 yr for $3M_\odot$, of 2×10^7 yr for $4M_\odot$ and of 10^7 yr for $5M_\odot$ and $6M_\odot$. These tracks have been computed by ourselves employing our stellar code.

Table 2. Selected stages of evolution of the intermediate mass stars presented in Figure (10). Columns indicate the point on the respective track, the age in million years, the decimal logarithms of the luminosity in solar units, effective temperature and central temperature in Kelvins, and central density in $g\ cm^{-3}$. The last two columns present the central abundances of hydrogen and helium. For the position of the points A-I on the tracks, see Figure (11).

$3M_{\odot}$

Point	Age	*Log L*	*Log* T_{eff}	*Log* T_c	*Log* ρ_c	X_c	Y_c
A	0.00	1.885	4.093	7.380	1.635	0.7293	0.2568
B	351.75	2.069	3.976	7.462	1.805	0.0417	0.9453
C	359.46	2.157	4.025	7.533	2.207	0.0003	0.9867
D	370.44	1.722	3.712	7.750	4.040	0.0000	0.9871
E	374.48	2.570	3.632	8.042	4.819	0.0000	0.9854
F	389.24	1.808	3.702	8.059	4.448	0.0000	0.8937
G	476.99	1.909	3.701	8.114	4.304	0.0000	0.3333
H	519.99	2.002	3.685	8.231	4.496	0.0000	0.0080
I	523.38	2.933	3.602	8.078	5.980	0.0000	0.0000

$4M_{\odot}$

Point	Age	*Log L*	*Log* T_{eff}	*Log* T_c	*Log* ρ_c	X_c	Y_c
A	0.00	2.356	4.176	7.413	1.479	0.7294	0.2566
B	159.32	2.576	4.061	7.491	1.620	0.0485	0.9386
C	163.39	2.656	4.108	7.573	2.035	0.0003	0.9868
D	167.08	2.207	3.697	7.818	3.909	0.0000	0.9871
E	168.07	2.887	3.623	8.075	4.468	0.0000	0.9845
F	177.83	2.333	3.681	8.100	4.120	0.0000	0.7969
G	194.75	2.510	3.708	8.142	4.081	0.0000	0.3384
H	213.84	2.439	3.675	8.239	4.251	0.0000	0.0215
I	214.71	3.200	3.594	8.270	5.713	0.0000	0.0000

$5M_{\odot}$

Point	Age	*Log L*	*Log* T_{eff}	*Log* T_c	*Log* ρ_c	X_c	Y_c
A	0.00	2.705	4.236	7.435	1.359	0.7369	0.2492
B	92.13	2.957	4.126	7.517	1.494	0.0466	0.9405
C	94.39	3.026	4.169	7.599	1.956	0.0001	0.9870
D	96.03	2.602	3.682	7.876	3.833	0.0000	0.9871
E	96.46	3.191	3.611	8.095	4.160	0.0000	0.9817
F	102.57	2.735	3.663	8.128	3.921	0.0000	0.7155
G	105.49	2.994	3.828	8.142	3.911	0.0000	0.5459
H	115.84	2.863	3.649	8.303	4.222	0.0000	0.0038
I	118.37	3.602	3.575	8.380	5.777	0.0000	0.0000

$6M_{\odot}$

Point	Age	*Log L*	*Log* T_{eff}	*Log* T_c	*Log* ρ_c	X_c	Y_c
A	0.00	2.988	4.282	7.454	1.259	0.7284	0.2576
B	59.70	3.255	4.176	7.536	1.394	0.0469	0.9402
C	61.22	3.321	4.218	7.630	1.823	0.0002	0.9869
D	62.04	2.913	3.668	7.927	3.769	0.0000	0.9871
E	62.27	3.449	3.600	8.110	3.978	0.0000	0.9805
F	66.32	3.068	3.647	8.151	3.762	0.0000	0.6585
G	68.25	3.360	3.919	8.168	3.757	0.0000	0.4755
H	73.50	3.182	3.632	8.323	4.078	0.0000	0.0044
I	74.81	3.912	3.557	8.460	5.927	0.0000	0.0000

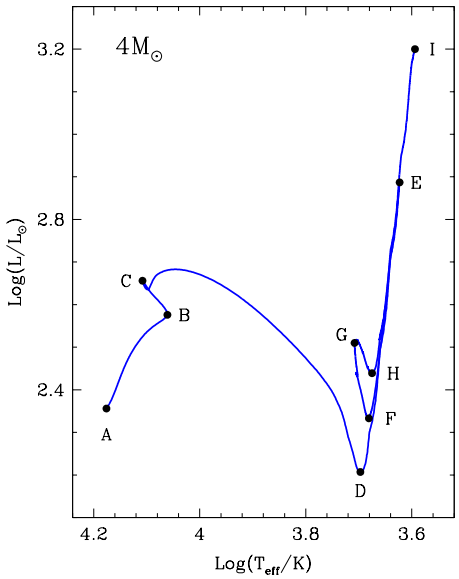

Figure 11. The track corresponding to the $4M_{\odot}$ object, indicating the position of the points A-I on the tracks presented in Figure (10) whose characteristics are given in Table (2).

oxygen ($X_c = X_o = 0.5$) representative of the case of intermediate mass WDs and neglected the presence of lighter elements in their outer layers. At present it is currently accepted that low mass WDs ($M < 0.4M_{\odot}$) are due to binary evolution and should be made up by helium, while the most massive ones ($M \gtrsim 1.0M_{\odot}$) are expected to be composed by oxygen, neon and magnesium. In Figure (13) we show the luminosity evolution of the same set of models. Ages have been set to zero at the beginning of the tracks shown in Figure (12); so, they correspond only to cooling evolution.

WDs are simple and well understood objects; so, they can be considered as cosmic clocks for the stellar population where they belong. Also, the most massive objects are expected to undergo *crystallization*. This is expected to occur when the Coulomb interactions are strong enough. For a one component plasma it occurs when $\Gamma \approx 171$, where

$$\Gamma = \frac{(Ze)^2}{kT\langle r_i \rangle}. \tag{63}$$

Here Z is the charge of the ions, and $\langle r_i \rangle$ is the ionic mean distance. Γ is the ratio between Coulomb and thermal energy. Crystallization changes the specific heat of the WD interior and even releases a latent heat. This has some impact on the cooling evolution of these objects.

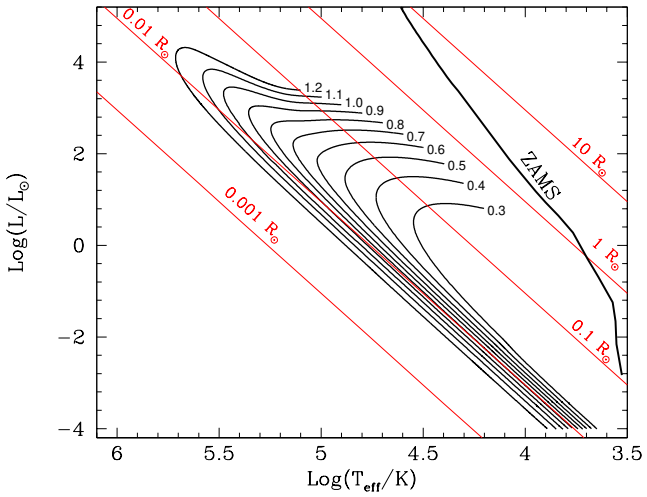

Figure 12. The evolutionary tracks for carbon-oxygen WDs. We assumed an homogeneous composition of $X_c = X_o = 0.5$. Solid black lines are labelled with their corresponding masses given in solar units. For comparison, we show the ZAMS and constant radii lines. Notice that, as it is shown in Figure (4), the larger the mass the smaller the radius. After reaching the maximum luminosity in each track, the WD cools down with decreasing radius. This is especially noticeable for the case of low mass objects and nicely accounts for the apparent discrepancy between the theoretical mass radius relation for *cold* WDs and observations. These tracks have been computed by ourselves employing our stellar code.

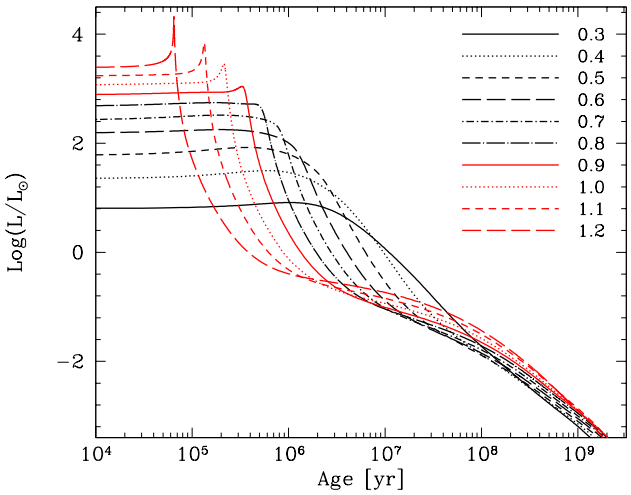

Figure 13. The evolution of the luminosity for the WDs considered in Figure (12). Types of lines are labelled with the corresponding mass values, given in solar units. The zero age has been set at the beginning of the tracks shown in Figure (12); so, the evolutionary scale corresponds only to the cooling evolution of the objects. Crystallization is not included.

8.5. The Evolution of Massive Stars

Usually massive stars refer to objects that end their lives in a catastrophic way by an implosion and (at least in some cases) a subsequent supernova explosion. Although they undergo strong mass loss, at the end of their lives they have masses well above the Chandrasekhar limit. Thus these stars cannot end their lives as WDs. For this to occur it is usually considered that their initial masses should be $M \geq 8-9M_{\odot}$. These objects are capable to undergo all the main thermonuclear burning cycles: hydrogen, helium, carbon, neon, oxygen, and silicon. Due to their high mass values they are very bright, allowing them to be detected far from us.

There are few facts that make the evolution of massive stars appreciably uncertain. Perhaps the most important is that massive stars are not numerous, and due to their short lives they are difficult to observe. Another relevant sources of uncertainty are mass loss, overshooting and rotation.

It is well known that massive stars undergo heavy mass loss. This is detectable in detailed spectroscopic observations from which we can deduce the value of the mass loss rate $\dot{M}$, which is rather uncertain. If τ is the timescale of stellar lives and we multiply it by $\dot{M}$ we find that $\dot{M}\tau$ is comparable to M. In other words, massive stars lose a non-negligible portion of their masses. This brings the possibility to detect material that has already undergone nuclear reactions emerging at their photospheres.

Overshooting is another phenomenon usually considered in massive stars. The physical reason for its occurrence is simple. Let us imagine, as discussed

above, that convection is the upwards and downwards motion of bubbles. It can be shown that when bubbles reach the position of the convective boundary indicated by the Schwarzschild criterium what goes to zero is not the velocity but the acceleration. So, at that position the bubble begins to brake down, moving beyond the classical boundary. This is still an open problem that has been not fully solved. So, astronomers use to consider overshooting in a parametric way in order to fit observational data, in particular the width of the upper MS band (sacrificing predictivity). The new parameter is α_{ov} which provides the extension l_{ov} of the convective zone beyond the standard edge as $l_{ov} = \alpha_{ov} H_P$.

Perhaps the most difficult phenomenon to treat properly is rotation. Rotation is fundamental in binary systems since orbital angular momentum can be transferred to stars by mass exchange making them to be spin up[13]. But it is also important for isolated objects, especially for massive stars that are known since long ago to be fast rotators (their rotation rate can be a non-negligible fraction of the breakup velocity). Rotation not only makes the figure of equilibrium to depart from spherical shape but more importantly, it gives rise to currents of meridional circulation that advect material, changing the composition of the stellar interior in a way that does not occur in non-rotating objects. On Earth, rotation is responsible for the existence of sea currents that advect heat and modify the weather in a quite noticeable way (due to the Gulf Current, Norway is not so cold as Alaska or Siberia). The problem is that the equations to handle shellular rotation (Zahn, 1992) (rotation velocity constant on isobars[14]) are of fourth order in space, making it very difficult from a numerical point of view.

In Figure (14) (Maeder & Meynet, 1987) we show a typical theoretical upper HRD with the evolution of a set of massive stars. The MS widens for $M \approx 40 M_\odot$ while for even more massive objects it narrows because of heavy mass loss and overshooting. After hydrogen core exhaustion, while stars with $M \lesssim 40 M_\odot$ burn helium as red objects, those more massive do it in the blue region at the left of the ZAMS. They are located there since they have lost a large fraction of the hydrogen rich outer layers, becoming Wolf-Rayet stars.

The evolution of the internal structure of the $60 M_\odot$ object (Maeder & Meynet, 1987) is presented in Figure (15) where it can be seen the changes of the surface chemical composition as consequence of the interplay of convection and mass loss. This is very important, since these abundances should be in agreement with the predictions of the CNO cycle.

In Table (3) we give some important quantities that describe the evolution of these massive stars. As in the previous ranges of masses, the main characteristic is that, since luminosity grows with mass faster than linear, and the fuel available goes with the mass, *the timescale of evolution is a steep decreasing function of the stellar mass.*

---

[13]This is the standard mechanism considered for the existence of recycled millisecond pulsars.

[14]This is considered because the diffusion coefficient of angular momentum is expected to be strongly anisotropic: it should be very large in the direction of isobars and much smaller in vertical direction. See, e.g., Maeder (2009) for further details.

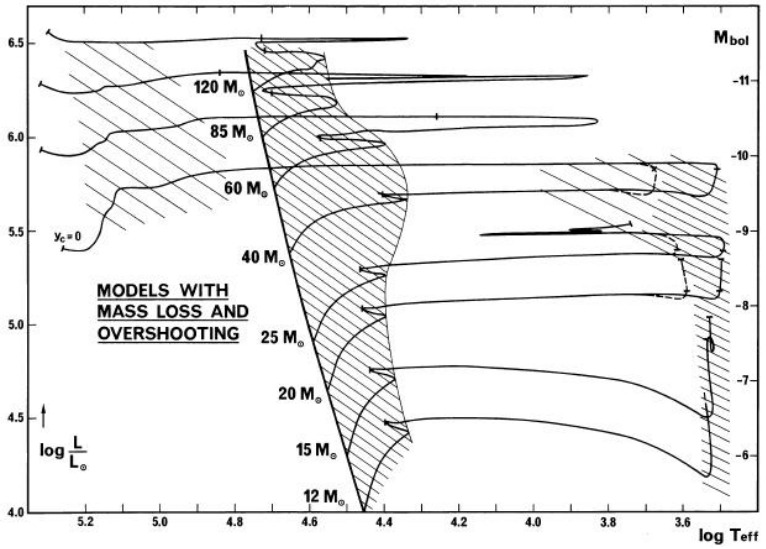

Figure 14. Typical upper HRD for Solar composition massive stars with mass loss and overshooting. Hatched areas indicate hydrogen core burning stage (MS band), and core helium burning as red objects for $M \leq 40 M_{\odot}$ but as blue for more massive ones (to the left of the ZAMS). Here the parameter of MLT is $\alpha_{mlt} = 1.5$ and for overshooting it has been assumed $\alpha_{ov} = 0.3$. For further details see text. Reprinted from Maeder & Meynet, A&A, 182, 243, reproduced with permission ©ESO.

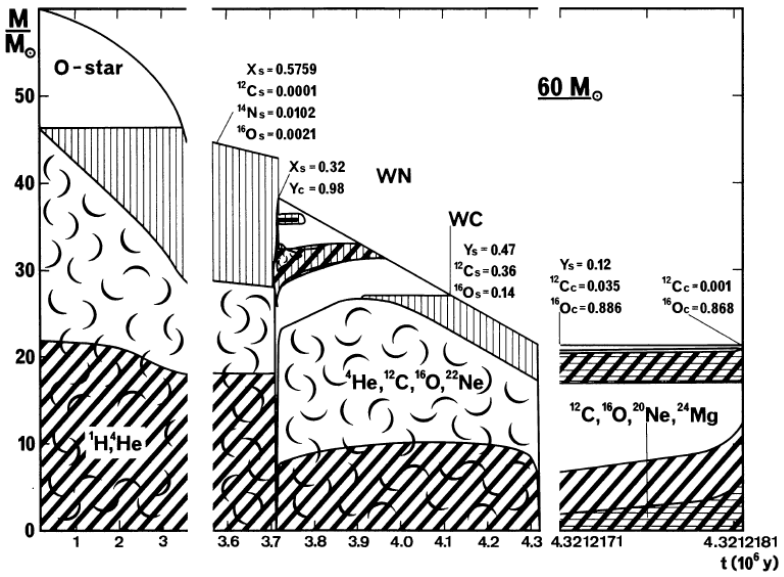

Figure 15. The internal evolution of a $60 M_{\odot}$ object subject to mass loss and overshooting. Tilted hatch indicates active nuclear burning, vertical lines denote the presence of a gradient of chemical composition, whereas curls depict convective zones. The upper solid line indicates the mass coordinate of the photosphere. Notice that due to mass loss, nuclearly processed material emerges to the stellar surface and should be detected by observations. Reprinted from Maeder & Meynet, A&A, 182, 243, reproduced with permission ©ESO.

Table 3. Selected stages of evolution of the massive stars presented in Figures (14) and (15). Columns indicate different important evolutionary stages: A, B, C, and D correspond to the conditions near the ZAMS, hydrogen core exhaustion, core helium ignition, and its exhaustion, respectively. We give the age in million years, the mass in solar units, the logarithm of the mass loss rate in solar masses per year, the logarithm of the luminosity in solar units, the logarithm of the effective temperature given in Kelvins, and the central abundances of hydrogen, helium and carbon (YC_c).

$20M_\odot$

Point	Age	M	$Log\ \dot{M}$	$Log\ L$	$Log\ T_{eff}$	X_c	Y_c	YC_c
A	0.24	19.996	-7.844	4.643	4.552	0.692	0.288	0.0001
B	8.79	19.098	-6.448	5.064	4.438	0.000	0.980	0.0002
C	8.82	19.084	-6.085	5.147	3.980	0.000	0.979	0.0007
D	10.06	14.311	-5.280	5.339	3.601	0.000	0.000	0.1167

$40M_\odot$

Point	Age	M	$Log\ \dot{M}$	$Log\ L$	$Log\ T_{eff}$	X_c	Y_c	YC_c
A	0.21	39.899	-6.345	5.374	4.652	0.684	0.295	0.0001
B	4.79	32.357	-5.286	5.679	4.375	0.000	0.980	0.0002
C	4.80	31.777	-3.924	5.825	3.673	0.000	0.976	0.0008
D	5.43	9.975	-4.553	5.404	5.268	0.000	0.000	0.0977

$60M_\odot$

Point	Age	M	$Log\ \dot{M}$	$Log\ L$	$Log\ T_{eff}$	X_c	Y_c	YC_c
A	0.17	59.757	-5.864	5.731	4.693	0.685	0.295	0.0001
B	3.71	42.999	-5.157	5.999	4.583	0.000	0.981	0.0002
C	3.72	42.959	-5.000	6.034	4.267	0.000	0.980	0.0003
D	4.32	21.384	-4.553	5.928	5.313	0.000	0.000	0.0432

$120M_\odot$

Point	Age	M	$Log\ \dot{M}$	$Log\ L$	$Log\ T_{eff}$	X_c	Y_c	YC_c
A	0.12	119.456	-5.398	6.254	4.739	0.685	0.294	0.0001
B	2.92	80.916	-5.114	6.449	4.720	0.000	0.980	0.0002
C	2.94	80.724	-4.551	6.511	4.503	0.000	0.979	0.0005
D	3.45	64.019	-4.553	6.552	5.292	0.000	0.000	0.0124

9. Concluding Remarks

In these lectures we have presented a brief description of the most important characteristics of stellar evolution in order to provide a basis for the understanding of the properties of the most frequently studied stellar pulsators. In doing so, we have made a description of the main physical ingredients that play a central rôle in stars and then, the fundamental characteristics of the process of stellar evolution.

It is important to remark that in this work we have not been able to refer to many important processes that occur in stars, that are relevant for a correct understanding of these objects. For example we did not describe semiconvection and diffusion that are also important for the determination of the internal chemical profiles. We have only made a brief reference to binary evolution and did not quote the neutron capture processes that are considered as responsible for the existence of elements heavier than those of the iron peak in Nature. Most of them are described in the textbooks cited in the Introduction. Also, we did not discuss the solar neutrino emission.

We hope that this work will be useful for the reader that intends to enter in the exciting realm of stellar astronomy.

The author wants to acknowledge the SOC of this School for inviting him to deliver these lectures. Also, he wants to acknowledge Dr. Gabriel Ferrero for his help in the preparation of Figure (1).

This work has made use of the VizieR catalogue access tool, CDS, Strasbourg, France (DOI: 10.26093/cds/vizier). The original description of the VizieR service was published in 2000, A&AS 143, 23.

References

Alexander D. R., Ferguson J. W., 1994, *ApJ*, **437**, 879

Arnett D., 1996, *Supernovae and Nucleosynthesis: An Investigation of the History of Matter from the Big Bang to the Present*, Princeton University Press

Baker N., Kippenhahn R., 1961, *AJ*, **70**, 278

Benvenuto O. G., De Vito M. A., 2003, *MNRAS*, **342**, 50

Burrows A., Lattimer J. M., 1986, *ApJ*, **307**, 178

Burrows A., Saumon D., Guillot T., Hubbard W. B., Lunine J. I., 1995, *Nature*, **375**, 299

Chandrasekhar S., 1939, *An introduction to the study of stellar structure*, University of Chicago Press

Chiosi C., 1997, T. R. Bedding, A. J. Booth, and J. Davis (eds.), *IAU Symposium*, Vol. 189 of *IAU Symposium*, pp 323–330

Clayton D. D., 1968, *Principles of stellar evolution and nucleosynthesis*, Wiley

Cox J. P., Giuli R. T., 1968, *Principles of stellar structure*, Gordon and Breach

Dufour P., Blouin S., Coutu S., Fortin-Archambault M., Thibeault C., Bergeron P., Fontaine G., 2017, *The Montreal White Dwarf Database: A Tool for*

the Community, Vol. 509 of *Astronomical Society of the Pacific Conference Series*, p. 3, Astronomical Society of the Pacific
Hamada T., Salpeter E. E., 1961, *ApJ*, **134**, 683
Henyey L. G., Forbes J. E., Gould N. L., 1964, *ApJ*, **139**, 306
Iglesias C. A., Rogers F. J., 1996, *ApJ*, **464**, 943
Itoh N., Kohyama Y., Matsumoto N., Seki M., 1984, *ApJ*, **285**, 758
Itoh N., Mitake S., Iyetomi H., Ichimaru S., 1983, *ApJ*, **273**, 774
Janka H.-T., Melson T., Summa A., 2016, *Annual Review of Nuclear and Particle Science*, **66**, 341
Kippenhahn R., Weigert A., 1990, *Stellar Structure and Evolution*, Springer Verlag
Kippenhahn R., Weigert A., Hofmeister E., 1967, *Methods in Computational Physics*, **7**, 129
Kravtsov V., Alcaino G., Marconi G., Alvarado F., 2010a, *VizieR Online Data Catalog*, pp J/A+A/516/A23
Kravtsov V., Alcaíno G., Marconi G., Alvarado F., 2010b, *A&A*, **516**, A23
Maeder A., 2009, *Physics, Formation and Evolution of Rotating Stars*, Springer Verlag
Maeder A., Meynet G., 1987, *A&A*, **182**, 243
Press W. H., Teukolsky S. A., Vetterling W. T., Flannery B. P., 1992, *Numerical recipes in FORTRAN. The art of scientific computing*, Cambridge University Press
Rogers F. J., Iglesias C. A., 1992, *ApJS*, **79**, 507
Sackmann I. J., Boothroyd A. I., Kraemer K. E., 1993, *ApJ*, **418**, 457
Salpeter E. E., 1961, *ApJ*, **134**, 669
Saumon D., Chabrier G., van Horn H. M., 1995, *ApJS*, **99**, 713
Shapiro S. L., Teukolsky S. A., 1983, *Black holes, white dwarfs, and neutron stars : the physics of compact objects*, Wiley
Sung H., Bessell M., Lee B.-W., Lee S.-G., 2002a, *VizieR Online Data Catalog: UBVI CCD photometry of NGC 2516*
Sung H., Bessell M. S., Lee B.-W., Lee S.-G., 2002b, *AJ*, **123**, 290
Timmes F. X., 1999, *ApJS*, **124**, 241
Timmes F. X., Arnett D., 1999, *ApJS*, **125**, 277
Zahn J. P., 1992, *A&A*, **265**, 115

Pulsations Along Stellar Evolution
VIII LAPIS Summer School
AAA Workshop Series 12, 2021
M. Kraus & A.F. Torres, eds.

Low Amplitude Adiabatic Non-radial Stellar Oscillations

Omar G. Benvenuto[1,†]

[1]*Facultad de Ciencias Astronómicas y Geofísicas, Universidad Nacional de La Plata, and Instituto de Astrofísica de La Plata (CCT-CONICET-UNLP), La Plata, Argentina*
Email: obenvenu@fcaglp.unlp.edu.ar

Abstract.

We present the problem of low amplitude, adiabatic non-radial oscillations starting from first principles. We describe the perturbations imposed to the models, assuming that its non-perturbed structure is spherical. Then, we restrict ourselves to the case of adiabatic oscillations, presenting the equations written in terms of the Dziembowski variables. We describe a numerical method for solving these equations based on finite differences and apply it for the simple case of polytropic spheres. A computer code based on this algorithm is available at the web page of the school. This method can be easily generalised for computing the case of low amplitude, non-adiabatic, non-radial pulsations.

Key words: asteroseismology — stars: oscillations — stars: interiors

[†]Member of the Carrera del Investigador Científico, Comisión de Investigaciones Científicas de la Provincia de Buenos Aires (CIC PBA), La Plata, Argentina

1. Introduction

In this lecture we shall present the problem of low amplitude, adiabatic non-radial stellar oscillations starting from first principles. We shall derive the equations that describe these oscillations and also present a numerical scheme to solve them. Because these are low amplitude oscillations, they are linear in the amplitude of the perturbation but non-linear with respect to the eigenfrequency. This is a classical problem treated in the books presented by Cox (1980) and Unno et al. (1989) and more recently by Aerts et al. (2010).

The remainder of this work is organised as follows. In Section (2), starting from first principles, we derive the equations of non-radial oscillations corresponding to a non-rotating model in hydrostatic and thermal equilibrium. In Section (3) we restrict ourselves to the case of adiabatic oscillations and write the equations in the Dziembowski variables. Then, in Section (4) we present a finite differences algorithm devised to solve these equations including some comments on how to construct an initial approximate solution to be relaxed by iterations. In Section (5) we apply this algorithm to the particularly simple case of polytropic spheres. Finally, in Section (6) we give some general comments about the applicability of this method to the case of non-adiabatic oscillations and also to compute the oscillations of realistic stellar models.

2. The Equations of Oscillations

Let us begin by writing the equations of continuity (1), of Euler (2) (we neglect viscous stress), conservation of energy (3), Laplace (4), and energy flux (5)

$$\frac{\partial \rho}{\partial t} + \vec{\nabla}.\left(\rho \vec{v}\right) = 0, \tag{1}$$

$$\rho\left(\frac{\partial}{\partial t} + \vec{v}.\,\vec{\nabla}\right)\vec{v} = -\vec{\nabla}P - \rho\vec{\nabla}\Phi, \tag{2}$$

$$T\left(\frac{\partial}{\partial t} + \vec{v}.\,\vec{\nabla}\right)S = -\rho\big(\varepsilon_n + \varepsilon_v\big) - \vec{\nabla}.\,\vec{F}, \tag{3}$$

$$\nabla^2\Phi = 4\pi G\rho, \tag{4}$$

$$\vec{F} = -K\vec{\nabla}T = -\frac{4ac}{3\kappa\rho}T^3\vec{\nabla}T. \tag{5}$$

The symbols have their usual meaning: ρ is the density, $\vec{v}$ is the velocity, P is the pressure, Φ is the gravitational potential, G is the gravitational constant, T is the temperature, S is the entropy, ε_n (ε_ν) is the energy release (loss) due to nuclear reactions (neutrino emission), $\vec{F}$ is the energy flux, K is the conductivity, a is the radiation constant, c is the velocity of light and κ is the opacity. For simplicity here we shall ignore convection.

In the case of non-rotating objects in hydrostatic and thermal equilibrium these equations reduce to

$$\frac{dP}{dr} = -\frac{GM_r}{r^2}\rho, \tag{6}$$

$$\frac{dM_r}{dr} = 4\pi r^2\rho, \tag{7}$$

$$\frac{dL_r}{dr} = 4\pi r^2\rho(\varepsilon_n - \varepsilon_\nu), \tag{8}$$

$$\frac{dT}{dr} = -\frac{3\kappa\rho}{4ac}\frac{1}{T^3}\frac{L_r}{4\pi r^2}, \tag{9}$$

where M_r is the mass enclosed by a sphere of radius r and $L_r = 4\pi r^2 F$ is the luminosity emerging from its surface.

There are two ways of considering perturbations to any attribute of the stellar interior, these are the Eulerian and Lagrangian perturbations. At a given point the attribute changes from $f_0(\vec{r})$ to $f(\vec{r},t)$ (Equation 10) due to an Eulerian perturbation

$$f(\vec{r},t) = f_0(\vec{r}) + f^{'}(\vec{r},t). \tag{10}$$

If a portion of the star undergoes a displacement $\vec{\xi} = \vec{r} - \vec{r}_0$, the attribute changes from $f_0(\vec{r}_0)$ to $f(\vec{r},t)$ due to a Lagrangian perturbation (Equation (11))

$$f(\vec{r},t) = f_0(\vec{r}_0) + \delta f(\vec{r}_0,t). \tag{11}$$

These formulations are related by Equation (12)

$$\delta f(\vec{r},t) = f^{'}(\vec{r},t) + \vec{\xi}.\vec{\nabla} f_0(\vec{r}). \tag{12}$$

We shall consider that the non-perturbed structure is at rest, in hydrostatic and thermal equilibrium (so $\vec{v} = 0$) and write the perturbed equations to the lowest order. These are

$$\frac{\partial \rho^{'}}{\partial t} + \vec{\nabla}.\left(\rho_0\vec{v}\right) = 0, \tag{13}$$

$$\rho_0\frac{\partial \vec{v}}{\partial t} + \vec{\nabla}P^{'} + \rho_0\vec{\nabla}\Phi^{'} + \rho^{'}\vec{\nabla}\Phi_0 = 0, \tag{14}$$

$$\rho_0 T_0\frac{\partial}{\partial t}\left(S^{'} + \vec{\xi}.\vec{\nabla}S_0\right) = \left[\rho\left(\varepsilon_n - \varepsilon_\nu\right)\right]^{'} - \vec{\nabla}.\vec{F'}, \tag{15}$$

$$\nabla^2\Phi^{'} = 4\pi G\rho^{'}, \tag{16}$$

$$\vec{F'} = -K_0\vec{\nabla}T^{'} - K^{'}\vec{\nabla}T. \tag{17}$$

If the non-perturbed structure is spherically symmetric, we have $\rho_0 = \rho_0(r)$, $T_0 = T_0(r)$, $\Phi_0 = \Phi_0(r)$, etc. We apply a perturbation considering

that all quantities are proportional to $\exp(i\sigma t)$. Then, the operator $\frac{\partial}{\partial t}$ can be replaced by $i\sigma$ and the perturbations are written as $\vec{\xi} = (\xi_r, \xi_\theta, \xi_\phi)$, where the normal part is $\vec{\xi}_\perp = (0, \xi_\theta, \xi_\phi)$. Also, it is convenient to define the normal part of the gradient and the Laplacian operators as

$$\vec{\nabla}_\perp = \frac{1}{r}\left(0, \frac{\partial}{\partial\theta}, \frac{1}{\sin\theta}\frac{\partial}{\partial\phi}\right), \tag{18}$$

$$\nabla_\perp^2 = \frac{1}{r^2\sin^2\theta}\left[\sin\theta\frac{\partial}{\partial\theta}\left(\sin\theta\frac{\partial}{\partial\theta}\right) + \frac{\partial^2}{\partial\phi^2}\right]. \tag{19}$$

$$\tag{20}$$

It is straightforward to verify that the angular part of the equations of motion are diagonal in the base of the spherical harmonics, defined as

$$Y_\ell^m(\theta,\phi) = (-1)^{(m+|m|)/2}\left[\frac{2\ell+1}{4\pi}\frac{(\ell-|m|)!}{(\ell+|m|)!}\right]^{1/2} P_\ell^{|m|}(\cos\theta)e^{im\phi} \tag{21}$$

where $P_\ell^{|m|}(\cos\theta)$ are the associated Legendre polynomials that fulfil the differential equation

$$\frac{d}{d\mu}\left[(1-\mu^2)\frac{dP_\ell^m(\mu)}{d\mu}\right] + \left(\ell(\ell+1) - \frac{m^2}{1-\mu^2}\right)P_\ell^m(\mu) = 0, \tag{22}$$

where $\mu = \cos\theta$. Let us remind the fundamental property that spherical harmonics are orthogonal and normalised

$$\int_0^{2\pi}\int_0^{\pi} Y^*_{\ell',m'}(\theta,\phi)Y_{\ell,m}(\theta,\phi)\sin\theta d\theta d\phi = \delta_{\ell,\ell'}\delta_{m,m'}. \tag{23}$$

Let us write the perturbation as

$$\vec{\xi} = \left[\xi_r(r), \xi_h(r)\frac{\partial}{\partial\theta}, \frac{\xi_h(r)}{\sin\theta}\frac{\partial}{\partial\phi}\right]Y_\ell^m(\theta,\phi)e^{i\sigma t}. \tag{24}$$

Applying it, together with the thermodynamic relation

$$\frac{\delta\rho}{\rho} = \frac{1}{\Gamma_1}\frac{\delta P}{P} - \nabla_{ad}\frac{\rho T}{P}\delta S \tag{25}$$

where

$$\nabla_{ad} = \left.\frac{\partial\log T}{\partial\log P}\right|_S, \tag{26}$$

and

$$\Gamma_1 = \left.\frac{\partial \log P}{\partial \log \rho}\right|_S, \tag{27}$$

we find the equations of motion

$$\frac{1}{\rho}\frac{dP'}{dr} + \frac{g}{\rho c_s^2}P' + \left(N^2 - \sigma^2\right)\xi_r + \frac{d\Phi'}{dr} = g\nabla_{ad}\frac{\rho T}{P}\delta S, \tag{28}$$

$$\frac{1}{r^2}\frac{d}{dr}\left(r^2\xi_r\right) + \frac{1}{\Gamma_1}\frac{d\ln P}{dr}\xi_r + \left(1 - \frac{L_\ell^2}{\sigma^2}\right)\frac{P'}{\rho c_s^2} - \frac{\ell(\ell+1)}{\sigma^2 r^2}\Phi' = \nabla_{ad}\frac{\rho T}{P}\delta S, \tag{29}$$

$$\frac{1}{r^2}\frac{d}{dr}\left(r^2\frac{d\Phi'}{dr}\right) - \frac{\ell(\ell+1)}{r^2}\Phi' - 4\pi G\rho\left(\frac{P'}{\rho c_s^2} + \frac{N^2}{g}\xi_r\right) = -4\pi G\nabla_{ad}\frac{\rho^2 T}{P}\delta S, \tag{30}$$

$$K\frac{dT'}{dr} = -F_r' - K'\frac{dT}{dr}, \tag{31}$$

$$i\sigma\rho T\delta S = \left[\rho\left(\varepsilon_n - \varepsilon_\nu\right)\right]' - \frac{1}{r^2}\frac{d}{dr}\left(r^2 F_r'\right) - \frac{\ell(\ell+1)}{r^2}KT'. \tag{32}$$

There,

$$L_\ell^2 = \ell(\ell+1)\frac{c_s^2}{r^2}, \tag{33}$$

$$N^2 = -gA = g\left(\frac{1}{\Gamma_1}\frac{d\ln P}{dr} - \frac{d\ln\rho}{dr}\right) \tag{34}$$

are the Lamb and Brunt-Väisälä frequencies, respectively. Also $c_s^2 = P\Gamma_1/\rho$ is the adiabatic velocity of sound, and $g = GM_r/r^2$ is the acceleration of gravity.

3. The Adiabatic Oscillations

We shall restrict ourselves to the case of adiabatic oscillations. So, we assume that $\delta S = 0$ and the equations are

$$\frac{1}{\rho}\frac{dP'}{dr} + \frac{g}{\rho c_s^2}P' + \left(N^2 - \sigma^2\right)\xi_r + \frac{d\Phi'}{dr} = 0, \tag{35}$$

$$\frac{1}{r^2}\frac{d}{dr}\left(r^2\xi_r\right) + \frac{1}{\Gamma_1}\frac{d\ln P}{dr}\xi_r + \left(1 - \frac{L_\ell^2}{\sigma^2}\right)\frac{P'}{\rho c_s^2} - \frac{\ell(\ell+1)}{\sigma^2 r^2}\Phi' = 0, \tag{36}$$

$$\frac{1}{r^2}\frac{d}{dr}\left(r^2\frac{d\Phi'}{dr}\right) - \frac{\ell(\ell+1)}{r^2}\Phi' - 4\pi G\rho\left(\frac{P'}{\rho c_s^2} + \frac{N^2}{g}\xi_r\right) = 0. \tag{37}$$

If we neglect the perturbations on the gravitational potential (Cowling approximation), it is possible to make a simple qualitative analysis usually called "Local Analysis". Let us assume that the coefficients of the oscillation equations are far smoother than the eigenfunctions. If we assume that they are proportional to $\exp(ik_r r)$, it can be shown that

$$k_r^2 = \frac{(\sigma^2 - L_\ell^2)(\sigma^2 - N^2)}{c_s^2 \sigma^2}. \tag{38}$$

For the mode to be oscillating, it has to fulfil $\sigma^2 > L_\ell^2$ and $\sigma^2 > N^2$, or $\sigma^2 < L_\ell^2$ and $\sigma^2 < N^2$, see below, Figure (8).

Let us define the variables

$$y_1 = \frac{\xi_r}{r};\ y_2 = \frac{1}{gr}\left(\frac{P'}{\rho} + \Phi'\right);\ y_3 = \frac{1}{gr}\Phi';\ y_4 = \frac{1}{g}\frac{d\Phi'}{dr}. \tag{39}$$

These correspond to

$$\xi_r = r y_1;\ P' = \rho g r (y_2 - y_1);\ \Phi' = g r y_3;\ \frac{d\Phi'}{dr} = g r y_4 \tag{40}$$

Then, we arrive to the Dziembowski's form of the equations of adiabatic oscillation

$$x\frac{dy_1}{dx} = \big(V_g - 3\big)y_1 + \left[\frac{\ell(\ell+1)}{C_1\omega^2} - V_g\right]y_2 + V_g y_3, \tag{41}$$

$$x\frac{dy_2}{dx} = \big(C_1\omega^2 - A^*\big)y_1 + \big(A^* - U + 1\big)y_2 - A^* y_3, \tag{42}$$

$$x\frac{dy_3}{dx} = \big(1 - U\big)y_3 + y_4, \tag{43}$$

$$x\frac{dy_4}{dx} = UA^* y_1 + UV_g y_2 + \Big[\ell(\ell+1) - UV_g\Big]y_3 - U y_4. \tag{44}$$

Here there appear the auxiliary variables that describe the effects of stellar structure on the oscillations and also the dimensionless frequency. These are

$$V_g = \frac{V}{\Gamma_1} = -\frac{1}{\Gamma_1}\frac{dln\ P}{dln\ r} = \frac{gr}{c_s^2}, \tag{45}$$

$$U = \frac{dln\ M_r}{dln\ r} = \frac{4\pi\rho r^2}{M_r}, \tag{46}$$

$$C_1 = \left(\frac{r}{R}\right)^3\left(\frac{M}{M_r}\right), \tag{47}$$

$$A^* = -rA = \frac{r}{g}N^2 = \frac{1}{\Gamma_1}\frac{dln\ P}{dln\ r} - \frac{dln\ \rho}{dln\ r}, \tag{48}$$

$$\omega^2 = \sigma^2\frac{R^3}{GM}. \tag{49}$$

The inner boundary conditions can be found taking into account that $V \to 3$, $U \to 0$, $A^* \to 0$. The conditions are

$$\frac{C_1\omega^2}{\ell}y_1 - y_2 = 0, \tag{50}$$

$$\ell y_2 - y_4 = 0. \tag{51}$$

The other two equations necessary to close the system are imposed on the outer layers of the star. There we have $V_g \to V_g(x = 1)$; $U \to 0$; $A^* \to A^*(x = 1)$. The conditions are

$$(\ell + 1)y_3 - y_4 = 0, \tag{52}$$

$$\left[1 + \left(\frac{\ell(\ell+1)}{\omega^2} - 4 - \omega^2\right)\frac{1}{V}\right]y_1 - y_2 + \left[1 + \left(\frac{\ell(\ell+1)}{\omega^2} - \ell - 1\right)\frac{1}{V}\right]y_3 = 0. \tag{53}$$

Due to the linearity of these equations with respect to the dependent variables y_i, they do not provide the amplitude of the oscillations. Then, we have to add an *arbitrary* normalisation condition that is usually taken at the stellar surface as $y_1(r = R) = 1$.

4. A Finite Differences Method of Solution

Let us now consider a method for solving these equations. This has been presented by Córsico & Benvenuto (2002) and is a generalisation of the scheme presented by Kippenhahn et al. (1967) to compute stellar evolution. The equations of low amplitude, adiabatic non-radial oscillations have the form

$$\frac{dy_i}{dx} = f_i(y_1, y_2, y_3, y_4, \omega), \qquad i = 1, ..., 4. \tag{54}$$

We shall divide the star in several concentric layers and write these equations in finite differences. We shall define the values of the dependent variables as $y_{i,j}$ where the first subscript indicates the variable and the second denotes the point at which it is evaluated. Among the variety of possible ways to adopt (for further details see, e.g., Press et al. 1992), we shall employ

$$G_i^j = \frac{y_{i,j+1} - y_{i,j}}{x_{j+1} - x_j} - f_i\left(y_{1,j+\frac{1}{2}}, y_{2,j+\frac{1}{2}}, y_{3,j+\frac{1}{2}}, y_{4,j+\frac{1}{2}}, \omega\right) = 0; \\ i = 1, \cdots, 4; j = 1, \cdots, N-1 \tag{55}$$

where

$$y_{i,j+\frac{1}{2}} = \frac{y_{i,j} + y_{i,j+1}}{2}. \tag{56}$$

Also, the boundary conditions $B_i = 0, i = 1, 2, 3$ (outer) and $C_i = 0, i = 1, 2$ (inner) are written in a similar way.

Notice that these equations are local with respect to the eigenmodes, since their derivatives are dependent on their values at the same point. The eigenvalue is "non-local" in the sense that it is present in these equations regardless where you are computing the derivatives.

To solve the difference equations let us employ a Newton-Raphson technique. We have to provide an approximate solution of a particular oscillation mode and improve it by successive iterations. So, the algorithm is devised to find the corrections necessary for the initially proposed solution to be relaxed to an accurate solution of the mode, fully consistent with the stellar structure of the non-perturbed model.

Notice that while the Equations (41)-(44) and (50)-(53) are linear in the functions y_i, they are *non-linear* with respect to the eigenfrequency.

$$\frac{\partial B_k}{\partial y_{1,1}}\ \delta y_{1,1} + \cdots + \frac{\partial B_k}{\partial y_{4,1}}\ \delta y_{4,1} + \frac{\partial B_k}{\partial \omega}\ \delta\omega = -B_k;\ k = 1, 2, 3, \tag{57}$$

$$\frac{\partial G_i^j}{\partial y_{1,j}}\ \delta y_{1,j} + \cdots + \frac{\partial G_i^j}{\partial y_{4,j}}\ \delta y_{4,j} + \frac{\partial G_i^j}{\partial y_{1,j+1}}\ \delta y_{1,j+1} + \cdots + \frac{\partial G_i^j}{\partial y_{4,j+1}}\ \delta y_{4,j+1} + \\ \frac{\partial G_i^j}{\partial \omega}\ \delta\omega = -G_i^j;\ \ i = 1, \ldots, 4;\ j = 1, 2, \ldots, N-1, \tag{58}$$

$$\frac{\partial C_m}{\partial y_{1,N}}\ \delta y_{1,N} + \cdots + \frac{\partial C_m}{\partial y_{4,N}}\ \delta y_{4,N} + \frac{\partial C_m}{\partial \omega}\ \delta\omega = -C_m;\ m = 1, 2, \tag{59}$$

These expressions can be written as a matrix equation. This is a sparse matrix (most of the elements are zero) which, with the exception of the first and last blocks, has the non-zero elements in blocks of four rows and eight columns. The first block can be written as

$$\begin{bmatrix} \frac{\partial B_1}{\partial y_{1,1}} & \cdots & \cdots & \frac{\partial B_1}{\partial y_{4,1}} & 0 & 0 & 0 \\ \frac{\partial B_2}{\partial y_{1,1}} & \cdots & \cdots & \frac{\partial B_2}{\partial y_{4,1}} & 0 & 0 & 0 \\ \frac{\partial B_3}{\partial y_{1,1}} & \cdots & \cdots & \frac{\partial B_3}{\partial y_{4,1}} & 0 & 0 & 0 \\ \frac{\partial G_1^1}{\partial y_{1,1}} & \cdots & \cdots & \frac{\partial G_1^1}{\partial y_{4,1}} & \frac{\partial G_1^1}{\partial y_{1,2}} & \frac{\partial G_1^1}{\partial y_{2,2}} & \frac{\partial G_1^1}{\partial y_{3,2}} \\ \vdots & \ddots & & \vdots & \vdots & \vdots & \vdots \\ \vdots & & \ddots & \vdots & \vdots & \vdots & \vdots \\ \frac{\partial G_4^1}{\partial y_{1,1}} & \cdots & \cdots & \frac{\partial G_4^1}{\partial y_{4,1}} & \frac{\partial G_4^1}{\partial y_{1,2}} & \frac{\partial G_4^1}{\partial y_{2,2}} & \frac{\partial G_4^1}{\partial y_{3,2}} \end{bmatrix} \cdot \begin{bmatrix} \delta y_{1,1} \\ \delta y_{2,1} \\ \delta y_{3,1} \\ \delta y_{4,1} \\ \delta y_{1,2} \\ \delta y_{2,2} \\ \delta y_{3,2} \end{bmatrix} = \begin{bmatrix} 0 & -\frac{\partial B_1}{\partial \omega} & -B_1 \\ 0 & -\frac{\partial B_2}{\partial \omega} & -B_2 \\ 0 & -\frac{\partial B_3}{\partial \omega} & -B_3 \\ -\frac{\partial G_1^1}{\partial y_{4,2}} & -\frac{\partial G_1^1}{\partial \omega} & -G_1^1 \\ \vdots & \vdots & \vdots \\ \vdots & \vdots & \vdots \\ -\frac{\partial G_4^1}{\partial y_{4,2}} & -\frac{\partial G_4^1}{\partial \omega} & -G_4^1 \end{bmatrix} \cdot \begin{bmatrix} \delta y_{4,2} \\ \delta \omega \\ 1 \end{bmatrix}. \tag{60}$$

Introducing the auxiliary vectors U, V, and W, their first seven components are defined by

$$\begin{bmatrix} \delta y_{1,1} \\ \delta y_{2,1} \\ \delta y_{3,1} \\ \delta y_{4,1} \\ \delta y_{1,2} \\ \delta y_{2,2} \\ \delta y_{3,2} \end{bmatrix} = \begin{bmatrix} U_1 & V_1 & W_1 \\ U_2 & V_2 & W_2 \\ \vdots & \vdots & \vdots \\ \vdots & \vdots & \vdots \\ \vdots & \vdots & \vdots \\ \vdots & \vdots & \vdots \\ U_7 & V_7 & W_7 \end{bmatrix} \cdot \begin{bmatrix} \delta y_{4,2} \\ \delta \omega \\ 1 \end{bmatrix} \tag{61}$$

and are the solution of the matrix equation

$$\begin{bmatrix} \frac{\partial B_1}{\partial y_{1,1}} & \cdots & \cdots & \frac{\partial B_1}{\partial y_{4,1}} & 0 & 0 & 0 \\ \frac{\partial B_2}{\partial y_{1,1}} & \cdots & \cdots & \frac{\partial B_2}{\partial y_{4,1}} & 0 & 0 & 0 \\ \frac{\partial B_3}{\partial y_{1,1}} & \cdots & \cdots & \frac{\partial B_3}{\partial y_{4,1}} & 0 & 0 & 0 \\ \frac{\partial G_1^1}{\partial y_{1,1}} & \cdots & \cdots & \frac{\partial G_1^1}{\partial y_{4,1}} & \frac{\partial G_1^1}{\partial y_{1,2}} & \frac{\partial G_1^1}{\partial y_{2,2}} & \frac{\partial G_1^1}{\partial y_{3,2}} \\ \vdots & \ddots & & \vdots & \vdots & \vdots & \vdots \\ \vdots & & \ddots & \vdots & \vdots & \vdots & \vdots \\ \frac{\partial G_4^1}{\partial y_{1,1}} & \cdots & \cdots & \frac{\partial G_4^1}{\partial y_{4,1}} & \frac{\partial G_4^1}{\partial y_{1,2}} & \frac{\partial G_4^1}{\partial y_{2,2}} & \frac{\partial G_4^1}{\partial y_{3,2}} \end{bmatrix} \cdot \begin{bmatrix} U_1 & V_1 & W_1 \\ U_2 & V_2 & W_2 \\ \vdots & \vdots & \vdots \\ \vdots & \vdots & \vdots \\ \vdots & \vdots & \vdots \\ \vdots & \vdots & \vdots \\ U_7 & V_7 & W_7 \end{bmatrix} = \begin{bmatrix} 0 & -\frac{\partial B_1}{\partial \omega} & -B_1 \\ 0 & -\frac{\partial B_2}{\partial \omega} & -B_2 \\ 0 & -\frac{\partial B_3}{\partial \omega} & -B_3 \\ -\frac{\partial G_1^1}{\partial y_{4,2}} & -\frac{\partial G_1^1}{\partial \omega} & -G_1^1 \\ \vdots & \vdots & \vdots \\ \vdots & \vdots & \vdots \\ -\frac{\partial G_4^1}{\partial y_{4,2}} & -\frac{\partial G_4^1}{\partial \omega} & -G_4^1 \end{bmatrix}. \tag{62}$$

The other components of the auxiliary vector are defined by

$$\begin{bmatrix} \delta y_{4,j} \\ \delta y_{1,j+1} \\ \delta y_{2,j+1} \\ \delta y_{3,j+1} \end{bmatrix} = \begin{bmatrix} U_{4j} & V_{4j} & W_{4j} \\ U_{4j+1} & V_{4j+1} & W_{4j+1} \\ U_{4j+2} & V_{4j+2} & W_{4j+2} \\ U_{4j+3} & V_{4j+3} & W_{4j+3} \end{bmatrix} \cdot \begin{bmatrix} \delta y_{4,j+1} \\ \delta\omega \\ 1 \end{bmatrix}, \tag{63}$$

and computed by the expression

$$\begin{bmatrix} \alpha_1^j & \frac{\partial G_1^j}{\partial y_{1,j+1}} & \frac{\partial G_1^j}{\partial y_{2,j+1}} & \frac{\partial G_1^j}{\partial y_{3,j+1}} \\ \alpha_2^j & \frac{\partial G_2^j}{\partial y_{1,j+1}} & \frac{\partial G_2^j}{\partial y_{2,j+1}} & \frac{\partial G_2^j}{\partial y_{3,j+1}} \\ \alpha_3^j & \frac{\partial G_3^j}{\partial y_{1,j+1}} & \frac{\partial G_3^j}{\partial y_{2,j+1}} & \frac{\partial G_3^j}{\partial y_{3,j+1}} \\ \alpha_4^j & \frac{\partial G_4^j}{\partial y_{1,j+1}} & \frac{\partial G_4^j}{\partial y_{2,j+1}} & \frac{\partial G_4^j}{\partial y_{3,j+1}} \end{bmatrix} \cdot \begin{bmatrix} U_{4j} & V_{4j} & W_{4j} \\ U_{4j+1} & V_{4j+1} & W_{4j+1} \\ U_{4j+2} & V_{4j+2} & W_{4j+2} \\ U_{4j+3} & V_{4j+3} & W_{4j+3} \end{bmatrix} = \begin{bmatrix} -\frac{\partial G_1^j}{\partial y_{4,j+1}} & -\beta_1^j & -\gamma_1^j \\ -\frac{\partial G_2^j}{\partial y_{4,j+1}} & -\beta_2^j & -\gamma_2^j \\ -\frac{\partial G_3^j}{\partial y_{4,j+1}} & -\beta_3^j & -\gamma_3^j \\ -\frac{\partial G_4^j}{\partial y_{4,j+1}} & -\beta_4^j & -\gamma_4^j \end{bmatrix}, \tag{64}$$

where we have employed the auxiliary vectors

$$\alpha_i^j = \frac{\partial G_i^j}{\partial y_{4,j}} + U_{4j-3}\,\frac{\partial G_i^j}{\partial y_{1,j}} + U_{4j-2}\,\frac{\partial G_i^j}{\partial y_{2,j}} + U_{4j-1}\,\frac{\partial G_i^j}{\partial y_{3,j}}, \tag{65}$$

$$\beta_i^j = \frac{\partial G_i^j}{\partial \omega} + V_{4j-3}\,\frac{\partial G_i^j}{\partial y_{1,j}} + V_{4j-2}\,\frac{\partial G_i^j}{\partial y_{2,j}} + V_{4j-1}\,\frac{\partial G_i^j}{\partial y_{3,j}}, \tag{66}$$

$$\gamma_i^j = G_i^j + W_{4j-3}\,\frac{\partial G_i^j}{\partial y_{1,j}} + W_{4j-2}\,\frac{\partial G_i^j}{\partial y_{2,j}} + W_{4j-1}\,\frac{\partial G_i^j}{\partial y_{3,j}}. \tag{67}$$

With these expressions we reduce the information necessary to solve for the corrections and find the last block of the matrix. This is written as

$$\begin{bmatrix} \alpha_1^{N-1} & \frac{\partial G_1^{N-1}}{\partial y_{1,N}} & \frac{\partial G_1^{N-1}}{\partial y_{2,N}} & \frac{\partial G_1^{N-1}}{\partial y_{3,N}} & \frac{\partial G_1^{N-1}}{\partial y_{4,N}} & \beta_1^{N-1} \\ \alpha_2^{N-1} & \frac{\partial G_2^{N-1}}{\partial y_{1,N}} & \frac{\partial G_2^{N-1}}{\partial y_{2,N}} & \frac{\partial G_2^{N-1}}{\partial y_{3,N}} & \frac{\partial G_2^{N-1}}{\partial y_{4,N}} & \beta_2^{N-1} \\ \alpha_3^{N-1} & \frac{\partial G_3^{N-1}}{\partial y_{1,N}} & \frac{\partial G_3^{N-1}}{\partial y_{2,N}} & \frac{\partial G_3^{N-1}}{\partial y_{3,N}} & \frac{\partial G_3^{N-1}}{\partial y_{4,N}} & \beta_3^{N-1} \\ \alpha_4^{N-1} & \frac{\partial G_4^{N-1}}{\partial y_{1,N}} & \frac{\partial G_4^{N-1}}{\partial y_{2,N}} & \frac{\partial G_4^{N-1}}{\partial y_{3,N}} & \frac{\partial G_4^{N-1}}{\partial y_{4,N}} & \beta_4^{N-1} \\ 0 & \frac{\partial C_1}{\partial y_{1,N}} & \frac{\partial C_1}{\partial y_{2,N}} & \frac{\partial C_1}{\partial y_{3,N}} & \frac{\partial C_1}{\partial y_{4,N}} & \frac{\partial C_1}{\partial \omega} \\ 0 & \frac{\partial C_2}{\partial y_{1,N}} & \frac{\partial C_2}{\partial y_{2,N}} & \frac{\partial C_2}{\partial y_{3,N}} & \frac{\partial C_2}{\partial y_{4,N}} & \frac{\partial C_2}{\partial \omega} \end{bmatrix} \cdot \begin{bmatrix} \delta y_{4,N-1} \\ \delta y_{1,N} \\ \delta y_{2,N} \\ \delta y_{3,N} \\ \delta y_{4,N} \\ \delta\omega \end{bmatrix} = \begin{bmatrix} -\gamma_1^{N-1} \\ -\gamma_2^{N-1} \\ -\gamma_3^{N-1} \\ -\gamma_4^{N-1} \\ -C_1 \\ -C_2 \end{bmatrix}. \tag{68}$$

This expression allows us to find the corrections to the quantities corresponding to the central part of the model together with that for the eigenfrequency. Employing them in Equations (61) and (63) backwards we find the rest of the corrections that are applied to the proposed solution.

$$\omega \to \omega + \delta\omega, \tag{69}$$

$$y_{i,j} \to y_{i,j} + \delta y_{i,j};\ i = 1, \cdots, 4;\ j = 1, \cdots, N \tag{70}$$

This completes an iteration that can be repeated up to when corrections are small enough.

The way of solving for the modes and the eigenfrequency is similar to the method we employ for computing binary stellar evolution. In this case, the "non-local" quantity is the mass transfer rate, that is computed simultaneously with the structure of the donor star. For details see Benvenuto & De Vito (2003).

4.1. Approximate Solution: the Discriminant

In order to look for the approximate solutions of the equations we have to explore the frequency interval of interest. To do so, we relax one of the physical boundary conditions (not the normalisation condition!) and look for the solution of oscillation equations for a given frequency. If at a given frequency the boundary condition is fulfilled, it corresponds to an approximate eigenmode, otherwise not. So, we store in the memory of the computer the approximate frequency and modes to be improved iteratively, as described above.

4.2. On the Distribution of Mesh Points

One of the most difficult problems on finite difference solution of differential equations is how to choose the distribution of mesh points. Here we cannot present a detailed discussion of this issue but we shall give few general comments.

Usually it is considered that a good description of a function is attained if it is defined on a large number of mesh points. However, obviously, this cannot be very large because both, the memory and the speed of the computer are finite. For example, it can be assumed that a function is well represented if between neighbouring mesh points it does not vary more than (say) 1% of the maximum amplitude in all the interval. In general, the solution of the equations of oscillations will have several nodes. Evidently, these functions do need more mesh points to be well defined as compared with the zoning necessary for stellar evolution. Thus, in general a good zoning for stellar evolution calculations may be completely inadequate for pulsation calculations.

5. A Particular Case: Polytropic Spheres

Let us now apply the above described numerical scheme to a particular case. If the equation of state is of the form $P = K\rho^{1+1/n}$, where K is a constant, the structure of the object is a polytropic sphere. If we define $\rho = \rho_c\theta^n$ and $r = \alpha\xi$ where ρ_c is the central density, θ is the polytropic function, and $\alpha^2 = \frac{(n+1)K}{4\pi G}\rho_c^{1/n-1}$, we find the Lane-Emden equation

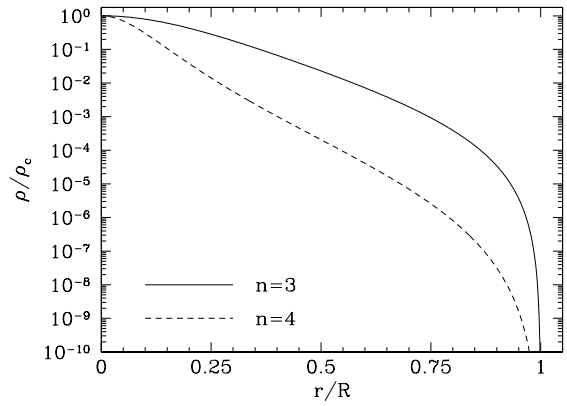

Figure 1. The density profile for polytropic spheres of $n = 3$ and 4.

$$\frac{1}{\xi^2}\frac{d}{d\xi}\left(\xi^2\frac{d\theta}{d\xi}\right) = -\theta^n. \tag{71}$$

The boundary conditions are $\theta(\xi = 0) = 1$, $d\theta/d\xi|_{\xi=0} = 0$ and the surface is defined by $\theta(\xi = \xi_s) = 0$. The radius of the sphere is $R = \alpha\xi_s$ and its mass is given by $M = 4\pi\alpha^3\rho_c(-\xi_s^2 d\theta/d\xi)_{\xi=\xi_s}$.

All the results shown below have been computed with the codes provided during the school[1], `politro.for` and `NR_AD_School.for`. First you have to compile and execute `politro.for`. After choosing the polytropic index the code will provide a file with the structure coefficients necessary to compute the oscillations. `NR_AD_School.for` will ask you for the value of ℓ of the oscillations and the range of values of the square of the dimensionless frequency ω^2. Automatically this code will store the discriminant and the modes in the required range.

Compilations and executions are fairly standard:

> gfortran xxx.for -o xxx

> ./xxx

Analytical solutions of Equation (71) are known only for n=0, 1, and 5. Let us here consider the cases of $n = 3$ and 4 and that the gas has an adiabatic coefficient Γ_1 corresponding to the monoatomic case: $\Gamma_1 = 5/3$. For this case, the density profiles are shown in Figure (1) and the coefficients given by Equations (49) are shown in Figure (2).

Having available these coefficients, we can now compute the modes. The first step is to calculate the discriminant. In this case we have employed Equation (52) for such purpose. The results are shown in Figure (3).

---

[1]For interested readers, the codes can be obtained from the author upon request.

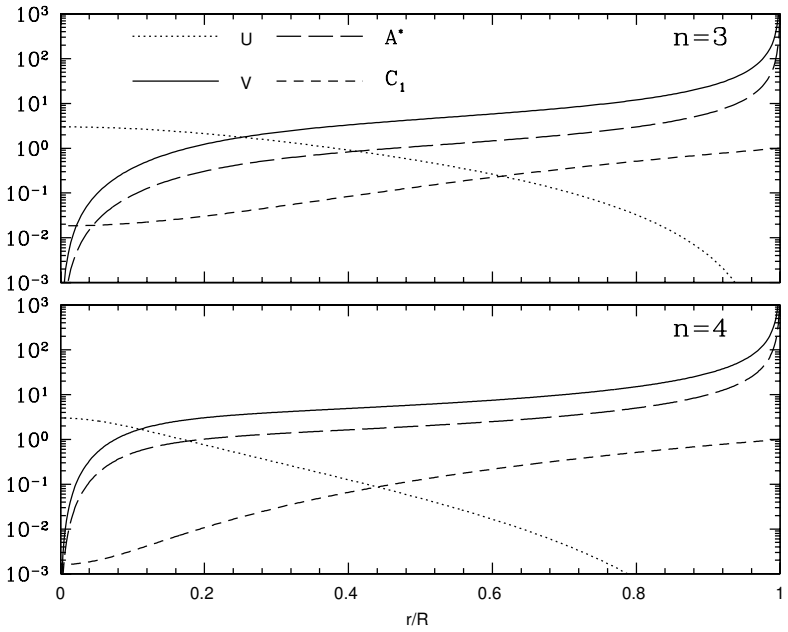

Figure 2. The coefficients given by Equations (45)-(48) that describe the structure of the polytropic spheres of $n = 3$ and 4.

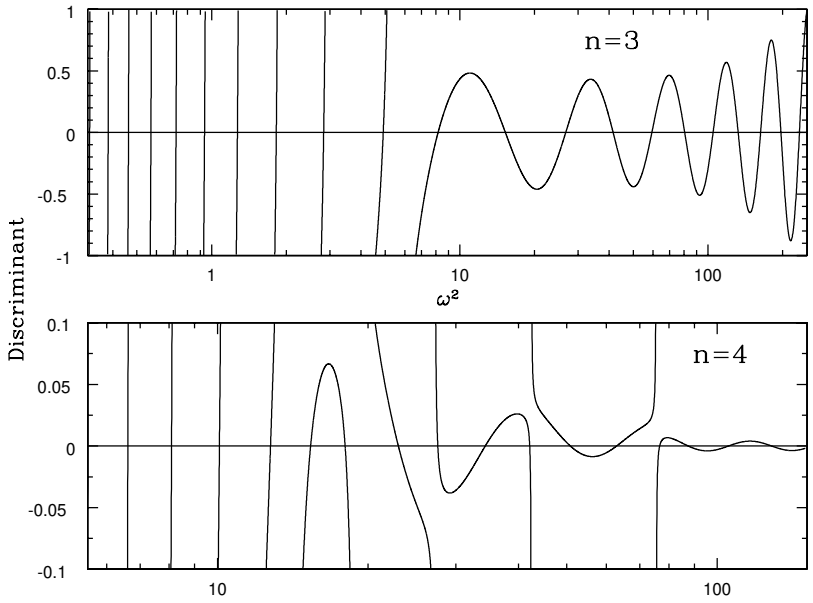

Figure 3. Discriminant for $\ell = 2$ modes for polytropic spheres of $n = 3$ and 4.

The modes correspond to the frequencies at which the discriminant is zero. Modes for both polytropic indices are shown in Figures (4)-(7).

Another interesting way to have a global view of the properties of the modes is to employ the so-called "Propagation Diagram" which is based on Equation (38). This is an useful tool for polytropes, but also for stellar models in general. The Propagation Diagrams for the cases of polytropic spheres of $n = 3$ and 4 are shown in Figure (8).

6. Conclusions

In this lecture we have presented the classical problem of low amplitude, adiabatic non-radial pulsations. We have derived the equation of oscillations starting from first principles. The formulation is based on the Equations (41)-(44) and boundary conditions (50)-(53) written in the Dziembowski variables.

In order to solve the equations we have presented a finite differences scheme. In order to look for the modes we have relaxed one of the boundary conditions and considered the values of this condition as a discriminant. When it has the physical value, this frequency corresponds to an oscillation

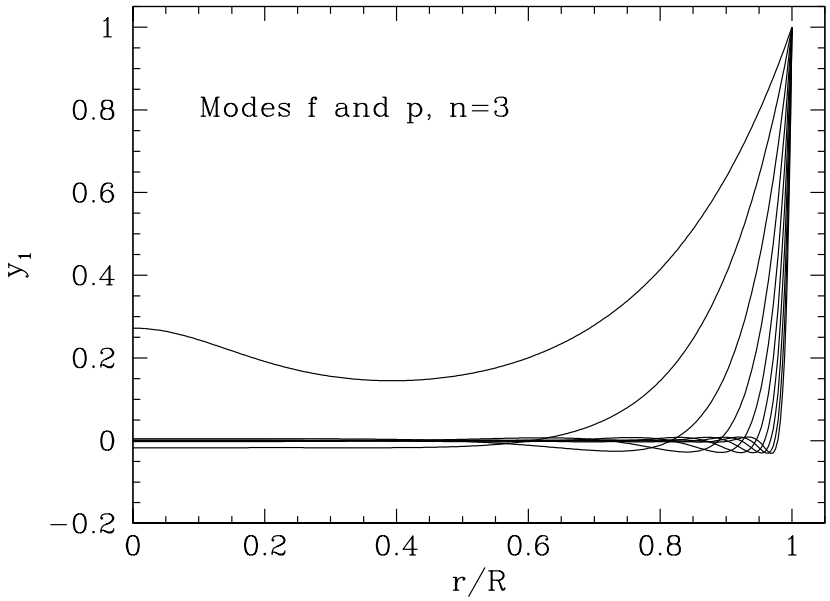

Figure 4. The first p-modes and the f-mode (without nodes) for a $n = 3$ polytropic sphere

mode. Then, we imposed the correct boundary condition and computed the eigenmodes and eigenfrequencies by relaxation.

Although here we have restricted ourselves to the case of adiabatic oscillations, the numerical scheme can be immediately generalised to the case of non-adiabatic oscillations. In this case we have to handle not four real but six complex first order differential equations.

In order to compute the modes of a simple stellar model, we applied it to the case of polytropic spheres with indices n=3 and 4. This is straightforward and is the first step we recommend to do before trying to compute the oscillatory modes of realistic stellar models. Of course, the numerical scheme is adequate for such a purpose if you are able to provide the coefficients given by Equations (45)-(48). In the case of realistic models a point to be taken with care is that the derivative of the density has to be computed numerically since it is *not* provided by the equations of stellar evolution.

The author wants to acknowledge the SOC of this School for inviting him to deliver these lectures.

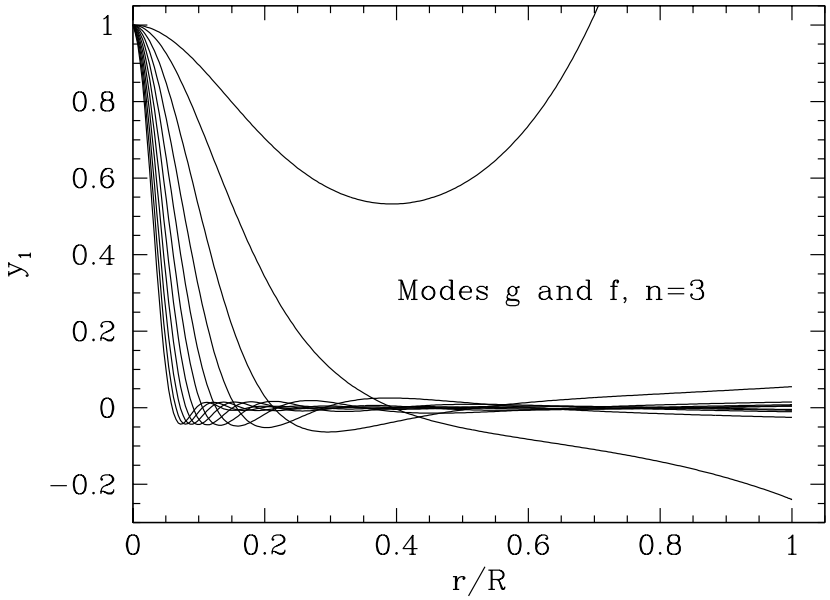

Figure 5. The first g-modes and the f-mode (without nodes) for a $n = 3$ polytropic sphere. Here the normalisation condition has been imposed at the centre of the model.

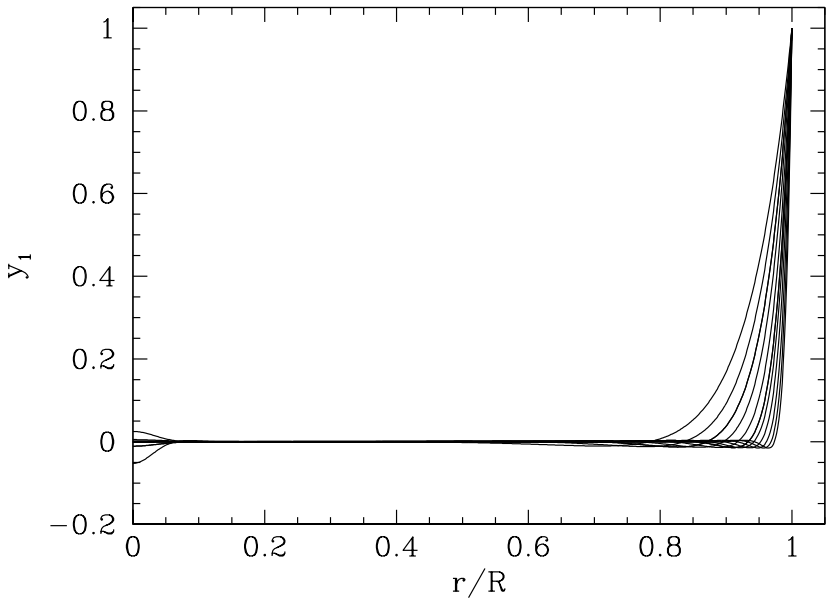

Figure 6. p-modes for a $n = 4$ polytropic sphere

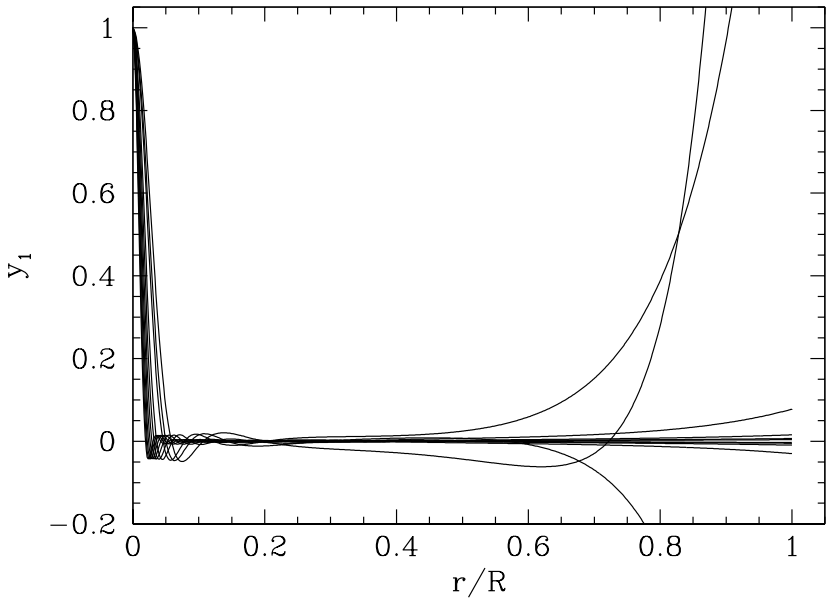

Figure 7. g-modes for a $n = 4$ polytropic sphere. Here the normalisation condition has been imposed at the centre of the model.

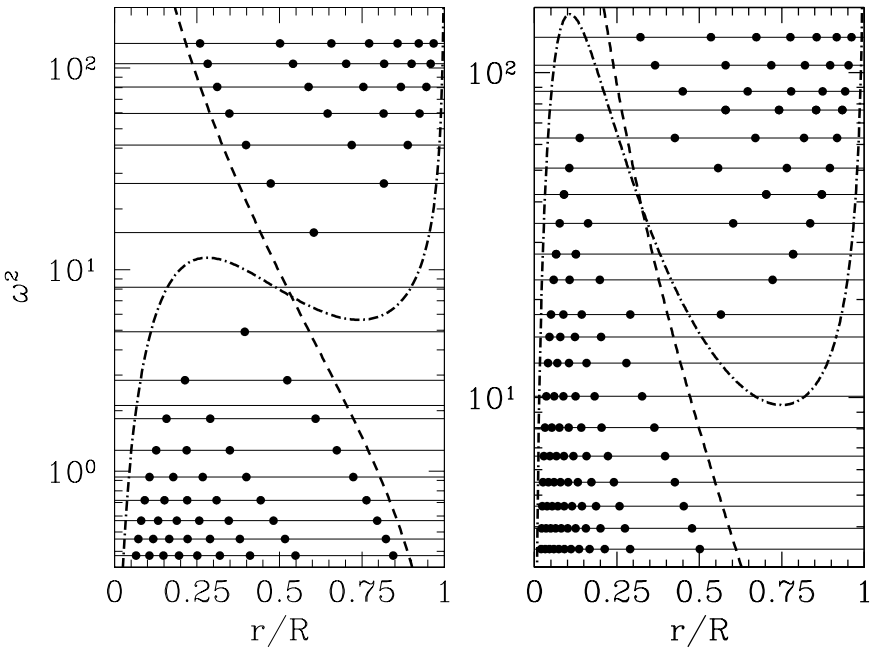

Figure 8. The propagation diagrams for $\ell = 2$ oscillations for polytropic spheres of $n = 3$ and 4 (corresponding to the left and right panels respectively). The squares of the characteristic Lamb (L_ℓ, defined in Equation (33)) and Brunt-Väisälä (N, defined in Equation (34)) frequencies are represented with dashed and dash dot lines respectively. Horizontal lines correspond to the frequencies and filled dots represent the coordinates at which each mode has a node in the y_1 eigenfunction. For the case of $n = 3$ there are p-modes oscillating with nodes in the outer resonant cavity and g-modes oscillating in the inner one, separated by the so-called fundamental mode that has no node. On the contrary, for the case of $n = 4$ there also exist the two resonant cavities, but the p and g modes are not so clearly separated since there are modes with nodes in both cavities. These figures can be qualitatively understood in terms of the local analysis based on Equation (38).

References

Aerts C., Christensen-Dalsgaard J., Kurtz D. W., 2010, *Asteroseismology*, Springer

Benvenuto O. G., De Vito M. A., 2003, *MNRAS*, **342**, 50

Córsico A. H., Benvenuto O. G., 2002, *Ap&SS*, **279**, 281

Cox J. P., 1980, *Theory of stellar pulsation*, Princeton University Press

Kippenhahn R., Weigert A., Hofmeister E., 1967, *Methods in Computational Physics*, **7**, 129

Press W. H., Teukolsky S. A., Vetterling W. T., Flannery B. P., 1992, *Numerical recipes in FORTRAN. The art of scientific computing*, Cambridge University Press

Unno W., Osaki Y., Ando H., Saio H., Shibahashi H., 1989, *Nonradial oscillations of stars*, University of Tokyo Press

Pulsations Along Stellar Evolution
VIII LAPIS Summer School
AAA Workshop Series 12, 2021
M. Kraus & A.F. Torres, eds.

Theoretical Description and Basic Physics of Stellar Pulsations

W. Glatzel[1]

[1]*Institut für Astrophysik, Georg-August-Universität Göttingen, Friedrich-Hund-Platz 1, D-37077 Göttingen, Germany*

Abstract.

As an introduction to the subject basic properties of stellar pulsations are derived using simple intuitive estimates. With respect to a theoretical description of pulsating stars the physical principles governing stellar structure and dynamics are discussed. The associated equations are simplified by the assumption of spherical symmetry thus providing the basis for the study of radial pulsations.

Key words: asteroseismology — hydrodynamics — radiative transfer — stars: oscillations

1. Preliminary Considerations

Variability of stars, observed either by photometric or spectral methods, can originate from various effects. It could be caused by eclipses in binaries, by disks in cataclysmic variables, by nuclear explosions in Novae and Supernovae, by star spots associated with magnetic fields, or by oscillations of the star around its equilibrium, i.e., by stellar pulsations, which are the subject of the current series of lectures. In order to distinguish them from other sources of variability we define them in a first attempt as an intrinsic property of a single, isolated star exhibiting (possibly multiple) periodic variability of its effective temperature, radius and luminosity.

Pulsating stars are of fundamental importance for astrophysics, since the properties of the pulsations allow for reliable estimates of stellar parameters, and certain classes of pulsating stars (e.g., Cepheids) can be used for distance determinations. In asteroseismology direct information on stellar structure and interiors is obtained from the spectrum of observed oscillation frequencies. Historically, the hypothesis, that stellar pulsations or oscillations may be responsible for observed stellar variability was first raised by Shapley in 1914 and considered theoretically by Eddington in 1918 (see Cox, 1980). For further reading we recommend the article by Ledoux & Walraven (1958) and the textbooks by Cox (1980) and Unno et al. (1989).

In order to identify the stellar parameters governing the observed timescale of pulsation-induced variability we consider the various timescales occurring in stellar physics.

The mechanical or dynamical timescale is determined by the acceleration of a mass element under the action of gravity. Denoting the radial position of a

mass element with r, the time with t, the mass of the star with M, and the gravitational constant with G, we estimate the acceleration as

$$\frac{d^2r}{dt^2} \propto -\frac{GM}{r^2} \tag{1}$$

Using the stellar radius R as an estimate for r and the dynamical timescale τ_{Dyn} as an estimate for t we are left with

$$\frac{R}{\tau_{Dyn}^2} \propto \frac{GM}{R^2} \tag{2}$$

Solving for τ_{Dyn} we obtain

$$\tau_{Dyn} \propto (G\rho)^{-1/2} \tag{3}$$

where ρ denotes the mean density of the star. Thus the dynamical timescale of a star is entirely determined by its mean density and varies between milliseconds for compact neutron stars and some 100 days for giants.

The thermal (Kelvin - Helmholtz) timescale τ_{KH} of a star may be defined by the time needed to radiate its thermal energy content $E_{thermal}$ at its current luminosity L:

$$\tau_{KH} \propto \frac{E_{thermal}}{L} \tag{4}$$

Due to the virial theorem the thermal and gravitational potential energy E_{Grav} of a star are of the same order of magnitude ($E_{thermal} \propto E_{Grav} \propto \frac{GM^2}{R}$) and we obtain

$$\tau_{KH} \propto \frac{GM^2}{LR} \propto 10^7 years \frac{(M/M_\odot)^2}{(L/L_\odot)(R/R_\odot)} \tag{5}$$

Similar to the thermal timescale the nuclear timescale τ_{nuc} of a star may be defined by the time needed to radiate its nuclear energy content E_{nuc} at its current luminosity L. Since the nuclear energy content of a star is proportional to its mass we are left with

$$\tau_{nuc} \propto \frac{E_{nuc}}{L} \propto \frac{M}{L} \propto 10^{10} years \frac{M/M_\odot}{L/L_\odot} \tag{6}$$

Comparing the nuclear, thermal and mechanical timescales of a star with the observed timescale of stellar pulsations of at most a few hundred days we conclude that the mechanical timescale is relevant for stellar pulsations. Moreover, the physics governing pulsations should be dominated by the mechanics of the system. The pulsation - induced variability of stellar parameters is usually small compared to their mean time independent values. Thus pulsations may be regarded as oscillations around the mechanical (hydrostatic) equilibrium, where the perturbed equilibrium is readjusted on the dynamical timescale.

Oscillations require a restoring force. In a star, two types of restoring forces are available: Stellar matter is compressible and the perturbation of the density of a mass element will be associated with a perturbation of its pressure implying

forces which counteract the density perturbation and tend to restore the unperturbed configuration. In a continuous medium this restoring force gives rise to the existence of sound waves. Since pressure is the restoring force, standing sound waves in a star are denoted as p - modes. Buoyancy is the origin of a second restoring force. For its action it requires a non vanishing acceleration (the gravity g in a star) and a finite density gradient $\frac{d\rho}{dr}$. An aspherical displacement of a mass element will then induce a restoring buoyancy force proportional to the gravity and the density gradient ($\propto g \cdot \frac{d\rho}{dr}$). In a continuous medium it leads to the existence of gravity waves. Since gravity is an essential ingredient in buoyancy, standing gravity waves in a star are denoted as g - modes.

With respect to the geometry we distinguish radial from nonradial pulsations. For radial pulsations the perturbations preserve the spherical geometry of the hydrostatic star, whereas nonradial pulsations allow for non - spherically deformed perturbations. Since buoyancy cannot act in spherical geometry, radial g - modes do not exist and radial pulsations do consist of p - modes only. For the same reason pure gravity modes - should they exist - have to be nonradial. Nonradial pulsations contain both g - and p - modes, where the strict classification of a given mode as g - or p - mode is not always meaningful, since there are modes with a mixed character, where both restoring forces act simultaneously.

On the basis of the hypothesis that stellar pulsations may be regarded as standing waves in a star we would like to provide a simple intuitive estimate of their pulsation periods, restricting ourselves to considering radial acoustic p - modes. As a guidance the analogue of an organ pipe as an acoustic resonator turns out to be helpful. The acoustic frequency spectrum of an organ pipe is obtained by considering the wavelengths λ of standing waves which a pipe with length L and rigid boundaries at the top and at the bottom (corresponding to nodes of standing acoustic waves) allows for. If $n-1$ denotes the number of nodes within the pipe of the standing sound wave, $\lambda/2$ can take the infinite number of discrete values L/n. Assuming now that a star can be regarded as an acoustic resonator similar to an organ pipe with nodes of standing waves at the center ($r=0$) and the surface ($r=R$) we identify the length L of the organ pipe with the stellar radius R and obtain from $\lambda \propto L/n$ by analogy as an order of magnitude estimate for the wavelengths of standing sound waves in a star $\lambda \propto R/n$. Wavelengths and associated frequencies ν are in both cases related by

$$\nu\lambda = c_{Sound} \tag{7}$$

where the sound speed c_{Sound} is given by

$$c^2{}_{Sound} = \gamma p/\rho \propto p/\rho \tag{8}$$

p, ρ and γ denote pressure, density and the adiabatic exponent, respectively. Thus the spectrum of acoustic frequencies of an organ pipe is estimated as

$$\nu = c_{Sound}/\lambda \propto n\frac{\sqrt{p/\rho}}{L} \tag{9}$$

For the (radial) acoustic spectrum of a star we obtain the estimate

$$\nu = c_{Sound}/\lambda \propto n\frac{\sqrt{p/\rho}}{R} \tag{10}$$

For a star, the ratio p/ρ can be estimated from the condition of hydrostatic equilibrium:

$$\frac{1}{\rho}\frac{\partial p}{\partial r} = -\frac{GM_r}{r^2} \tag{11}$$

where M_r denotes the mass within a sphere of radius r. Using $\frac{p}{R}$ as an estimate for $\frac{\partial p}{\partial r}$, M as an estimate for M_r and R as an estimate for r we obtain

$$\frac{1}{\rho}\frac{p}{R} \propto \frac{GM}{R^2} \tag{12}$$

Thus the ratio p/ρ is given by

$$\frac{p}{\rho} \propto \frac{GM}{R} \tag{13}$$

and the radial acoustic spectrum of a star (see equation 10) is estimated as

$$\nu \propto n\sqrt{\frac{GM}{R^3}} \propto n\sqrt{G\rho} \tag{14}$$

Replacing the frequency by the pulsation period $\Pi = 1/\nu$ we obtain for the radial fundamental mode ($n = 1$):

$$\Pi\sqrt{\rho} = constant \tag{15}$$

Equation 15 represents the period - density - relation for the radial fundamental mode of stellar pulsations. Note that according to our estimates the density occurring in equation 15 has to be regarded as the mean density of the star. A familiar form of the period - density - relation (see, e.g., Cox, 1980) reads:

$$\Pi(\rho/\rho_\odot)^{1/2} = Q \quad with \quad 0.03d \lesssim Q \lesssim 0.12d \tag{16}$$

The variation of Q is caused by the influence on the pulsation period of different stellar structures, which was not accounted for by our simple estimates. Note that the period - density relation is consistent with our initial findings that the timescale of pulsations is given by the dynamical timescale (equation 3).

2. Physics of Stellar Structure and Dynamics

For continuous systems like stars two kinds of descriptions are common. In the Eulerian framework fixed positions in space are considered, position vectors $\vec{r}$ and time t are used as independent variables. Accordingly, the Eulerian time derivative $\frac{\partial}{\partial t}|_{\vec{r}}$ is defined at constant position vector $\vec{r}$. In the Lagrangean framework fixed mass elements are considered, the initial position vector $\vec{r_0}$ of a mass element and the time t are used as independent variables. Accordingly, the Lagrangean time derivative $\frac{d}{dt}|_{\vec{r_0}}$ is defined at constant initial position vector $\vec{r_0}$ of the mass element considered. Note that in the Lagrangean description the actual

position vector $\vec{r} = \vec{r}(\vec{r_0}, t)$ is a (time dependent) dependent variable. For the definition of the velocity $\vec{v}$ the Lagrangean description is adopted:

$$\vec{v} = \frac{d\vec{r}}{dt} \tag{17}$$

Using the relation

$$\frac{d}{dt} = \frac{\partial}{\partial t} + (\vec{v}\nabla) \tag{18}$$

between the Lagrangean and the Eulerian time derivatives the acceleration $\frac{d\vec{v}}{dt}$ can be written as

$$\frac{d\vec{v}}{dt} = \frac{\partial \vec{v}}{\partial t} + (\vec{v}\nabla)\vec{v} \tag{19}$$

Depending on which of the equivalent descriptions is more convenient for the particular situation studied, either the Eulerian or the Lagrangean approach (or even a combination of them) is used.

The physical principles governing stellar structure and dynamics comprise the conservation laws for mass, momentum and energy together with Poisson's equation for the gravity and a prescription for the energy transport. In its differential form mass conservation is described by the continuity equation

$$\frac{d\rho}{dt} + \rho\nabla\vec{v} = 0 \tag{20}$$

Alternatively, the continuity equation in the Eulerian approach may be written as

$$\frac{\partial \rho}{\partial t} + \nabla(\rho\vec{v}) = 0 \tag{21}$$

By definition, an incompressible motion is characterized by a vanishing Lagrangean time derivative of the density ($\frac{d\rho}{dt} = 0$). According to equation 20 this condition is equivalent to $\nabla\vec{v} = 0$, i.e., to a vanishing divergence of the velocity field. Incompressibility and homogeneity, which would correspond to a vanishing gradient of the density ($\nabla\rho = 0$), must not be confused.

In the absence of viscosity and magnetic fields, momentum conservation is described by Euler's equation:

$$\rho\frac{d\vec{v}}{dt} = \rho(\frac{\partial \vec{v}}{\partial t} + (\vec{v}\nabla)\vec{v}) = -\nabla p - \rho\nabla\phi \tag{22}$$

The left hand side of equation 22 describes the inertial forces in either the Lagrangean or the Eulerian framework, the first term on the right hand side corresponds to forces induced by pressure gradients, the second refers to the gravitational force where ϕ is the gravitational potential. It is determined by Poisson's equation:

$$\triangle\,\phi = 4\pi G\rho \tag{23}$$

The solution of Poisson's equation 23 may be represented as:

$$\phi(\vec{r},t) = -G \int \frac{\rho(\vec{x},t)}{|\vec{x}-\vec{r}|} d^3x \tag{24}$$

Based on the first law of thermodynamics energy conservation may be expressed as

$$\rho \frac{du}{dt} = -p\nabla\vec{v} + \rho\varepsilon - \nabla\vec{F} \tag{25}$$

where u, $\vec{F}$ and ε denote the specific internal energy, the heat flux and the specific energy generation rate, respectively. The variation with time of the internal energy of a mass element is given by the mechanical work done by the element (first term on the r.h.s. of equation 25), the (nuclear) energy generation within the element (second term) and the heat deposited in it, expressed in terms of the divergence of the heat flux (third term). With $V = 1/\rho$, the continuity equation 20 and some basic thermodynamics two terms of equation 25 may be rearranged to yield:

$$\rho \frac{du}{dt} + p\nabla\vec{v} = \rho(\frac{du}{dt} + p\frac{dV}{dt}) = \rho T \frac{ds}{dt} \tag{26}$$

where T and s denote temperature and specific entropy, respectively. Thus an alternative form of energy conservation (equation 25) is given by

$$\rho T \frac{ds}{dt} = \rho\varepsilon - \nabla\vec{F} \tag{27}$$

In stellar interiors energy transport is usually approximated by a diffusion type process, where the heat flux is proportional and opposite to the temperature gradient:

$$\vec{F} = -D\nabla T \tag{28}$$

The particular transport process enters through the diffusion coefficient D. In the optically thick regime (e.g., in stellar interiors) radiation transport can be treated in the diffusion approximation with D given by:

$$D = \frac{4ac}{3\kappa\rho} T^3 \tag{29}$$

where a, c and κ are the radiation constant, the speed of light and the Rosseland mean of the opacity, respectively.

If nuclear processes are of interest, the system of equations has to be complemented by the variation with time of the chemical composition (X_i denotes the mass fraction of nucleus i) induced by nuclear reactions:

$$\frac{dX_i}{dt} = \frac{dX_i}{dt}(X_j, p, T) \tag{30}$$

The specific dependence on chemical composition, pressure and temperature of the reaction rate entering equation 30 is provided by nuclear physics.

A closure of the system of equations given above is accomplished by the prescription of a thermal and a caloric equation of state (EOS) provided by

thermodynamics and atomic physics. Depending on the thermodynamic basis adopted it may formally be written as, e.g.,

$$p = p(\rho, T) \quad or \quad \rho = \rho(p, T) \quad or \quad s = s(p, T) \tag{31}$$

Moreover, the Rosseland mean of the opacity $\kappa = \kappa(p, T)$ and the nuclear energy generation rate $\varepsilon = \varepsilon(p, T)$ have to be provided by atomic and nuclear physics either in parametrized or in tabular form.

The problem posed by the system of equations introduced here consists of their application to stellar structure and dynamics and their mathematical solution. Concerning the latter, a numerical treatment of the equations with subsequent numerical simulations seems to be an appropriate strategy. However, concerning stellar pulsations reliable nonlinear 3D simulations satisfying the necessary accuracy requirements are still not yet feasible. Therefore the theoretical study of stellar pulsations still relies on simplifications and approximations.

3. Radial Pulsations

As an attempt to reduce the mathematical complexity of the problem we simplify its geometry by assuming spherical symmetry, i.e., we restrict our studies to radial pulsations. However, according to the preliminary considerations in section 1 this assumption does not only simplify the mathematics, it also leads to a loss of physical effects, such as buoyancy. As a consequence, e.g., g - modes are excluded in this approach. Therefore the interpretation and generalisation of results based on a radial analysis has to be dealt with caution. For convenience, we introduce spherical polar coordinates (r, θ, φ) and adopt the Lagrangean description. Then the mass M_r contained within a sphere of radius r is given by (subscripts 0 refer to initial quantities in the Lagrangean sense):

$$M_r = \int_0^{r(r_0,t)} \rho(r', t) 4\pi r'^2 dr' = \int_0^{r_0} \rho(r_0') 4\pi r_0'^2 dr_0' = M_{r_0} \tag{32}$$

With this definition the conservation of mass is expressed as

$$M_r = M_{r_0} \quad ; \quad \frac{dM_r}{dt} = 0 \tag{33}$$

and $M_r = M_{r_0}$ is chosen as a new Lagrangean variable replacing r_0. Thus M_r (and t) have become independent Lagrangean variables, whereas $r(M_r, t)$ is a dependent variable. The relation between r and M_r is obtained by differentiation of the definition of M_r (equation 32):

$$\frac{\partial M_r}{\partial r} = 4\pi r^2 \rho \quad or \quad \frac{\partial r}{\partial M_r} = \frac{1}{4\pi r^2 \rho} \tag{34}$$

Note that in equation 34 the derivatives have to be interpreted in the Lagrangean sense. In spherical symmetry the gravitational force occurs in Euler's equation 22 in terms of the gradient $\frac{\partial \phi}{\partial r}$ of the potential ϕ. It is determined by Poisson's equation 23 which in spherical symmetry is given by:

$$\frac{\partial^2\phi}{\partial r^2} + \frac{2}{r}\frac{\partial\phi}{\partial r} = \frac{1}{r^2}\frac{\partial}{\partial r}(r^2\frac{\partial\phi}{\partial r}) = 4\pi G\rho \tag{35}$$

By multiplication of equation 35 with r^2 and integration we obtain:

$$r^2\frac{\partial\phi}{\partial r} = \int 4\pi G\rho r^2 dr = GM_r \tag{36}$$

For the gravity we are thus left with

$$\frac{\partial\phi}{\partial r} = \frac{GM_r}{r^2} \tag{37}$$

Note that the particular choice of the Lagrangean variables allows for an algebraic representation of the gravitational force. No further integration is required.

To present the equations governing radial pulsations in their conventional form, some transformations and definitions have to be introduced: The radial component F_r of the heat flux is replaced by the luminosity $L(r)$ through

$$L(r) = 4\pi r^2 F_r \tag{38}$$

Choosing pressure p and temperature T as the thermodynamic basis we write the differential of the specific entropy $s = s(p,T)$ as

$$Tds = c_p dT - \frac{\delta}{\rho}dp \tag{39}$$

where c_p denotes the specific heat at constant pressure and the coefficients α and δ of the differential form of the equation of state $\rho = \rho(p,T)$ are defined as

$$\alpha = \left.\frac{\partial\log\rho}{\partial\log p}\right|_T \quad ; \quad \delta = -\left.\frac{\partial\log\rho}{\partial\log T}\right|_p \tag{40}$$

The transformation from r to M_r as an independent variable is accomplished by using equation 34 in the form

$$\frac{\partial}{\partial r} = 4\pi r^2\rho\frac{\partial}{\partial M_r} \tag{41}$$

We are thus left with the following system of equations describing the spherically symmetric structure and dynamics of a star ($\frac{\partial}{\partial t}$ refers to the Lagrangean time derivative):

Mass conservation

$$\frac{\partial r}{\partial M_r} = \frac{1}{4\pi r^2\rho} \tag{42}$$

Momentum conservation

$$\frac{\partial p}{\partial M_r} = -\frac{GM_r}{4\pi r^4} - \frac{1}{4\pi r^2}\frac{\partial^2 r}{\partial t^2} \tag{43}$$

Energy conservation

$$\frac{\partial L}{\partial M_r} = \varepsilon - c_p\frac{\partial T}{\partial t} + \frac{\delta}{\rho}\frac{\partial p}{\partial t} \tag{44}$$

Energy transport

$$\frac{\partial T}{\partial M_r} = -\frac{3\kappa L}{64\pi^2 acr^4 T^3} \tag{45}$$

Change of chemical composition by nuclear processes

$$\frac{\partial X_i}{\partial t} = \frac{\partial X_i}{\partial t}(X_j, p, T) \tag{46}$$

This system of five partial differential equations needs to be closed by the prescription of an equation of state and by specifying the nuclear energy generation rate ε and the opacity κ. We note that energy transport processes other than radiation diffusion are not taken into account in equation 45. In particular, energy transport by convection is disregarded.

Three terms involving a time derivative occur in equations 42 — 46, each of them being related to one of the characteristic stellar timescales discussed in section 1: The acceleration term in equation 43 is associated with the dynamical timescale, the time derivative of the entropy in equation 44 (expressed by the time derivatives of temperature and pressure, respectively) with the thermal timescale and the time derivatives of the mass fractions in equation 46 with the nuclear timescale.

Stellar evolution relies on hydrostatic equilibrium ($\frac{\partial^2 r}{\partial t^2} = 0$) and is governed by the nuclear and the thermal timescales. Thus the description of standard stellar evolution is included in equations 42 — 46 as the special case of vanishing acceleration.

On the other hand, the study of pulsations requires deviations from hydrostatic equilibrium ($\frac{\partial^2 r}{\partial t^2} \neq 0$), whereas on the timescale of pulsations the nuclear changes of the chemical composition may be ignored. Thus nuclear processes, i.e., equations 46 are usually ignored and the chemical composition in terms of the mass fractions X_i is assumed to be constant on the dynamical timescale of pulsations. Thus pulsations are governed by the dynamical and thermal timescales. Under certain conditions for pulsations even the change of the entropy (i.e., its time derivative in equation 44) may be neglected. Then the energy equations can be disregarded altogether and we are left with a mechanical system, where pulsations are completely determined by the dynamical timescale.

Acknowledgments. I would like to thank the organisers of the VIII LAPIS summer school for the perfect performance and the warm hospitality at La Plata.

References

Cox J. P., 1980, *Theory of stellar pulsation*
Ledoux P., Walraven T., 1958, *Handbuch der Physik*, **51**, 353
Unno W., Osaki Y., Ando H., Saio H., Shibahashi H., 1989, *Nonradial oscillations of stars*

Pulsations Along Stellar Evolution
VIII LAPIS Summer School
AAA Workshop Series 12, 2021
M. Kraus & A.F. Torres, eds.

Linear Analysis

W. Glatzel[1]

[1]*Institut für Astrophysik, Georg-August-Universität Göttingen, Friedrich-Hund-Platz 1, D-37077 Göttingen, Germany*

Abstract.

We discuss the general strategy of the theoretical description of stellar stability and pulsations. The initial construction of a spherically symmetric stellar model in hydrostatic equilibrium is followed by considering small perturbations around the equilibrium. Both for radial and nonradial disturbances the linear equations governing these small perturbations are derived. The influence of the thermal and the dynamical timescale on the properties of linear pulsations is discussed in detail. For unstable stellar models the last step of the general approach consists of following the evolution of an instability into the nonlinear regime by numerical simulation.

Key words: asteroseismology — hydrodynamics — radiative transfer — stars: oscillations

1. General Strategy

In the present paper, we will adopt the same notation as in the previous lecture in this volume on "Theoretical Description and Basic Physics of Stellar Pulsations" (hereafter referred to as paper I). Moreover, we shall make use of the results obtained there.

Most of the pulsating stars maintain their mean properties (such as luminosities and effective temperatures) while pulsating. Moreover, the pulsational variability of the stellar parameters is in general small compared to their stationary mean values. Thus pulsations may be regarded as "small" time dependent perturbations superimposed on a stationary star in hydrostatic equilibrium. For a theoretical treatment these findings suggest to start with a hydrostatic stellar model subsequently considering time dependent perturbations of the equilibrium, which are small compared to the equilibrium values. As a consequence, in an expansion around the equilibrium only terms linear in the perturbations will be significant while higher order terms in the perturbations can be neglected. Thus the approach will lead to a system of linear equations for the perturbations.

The construction of a (spherical) hydrostatic stellar model as the first step of the analysis can be accomplished by standard stellar evolution calculations leading to models with the desired (or observed) parameters. Alternatively, for prescribed (observed) stellar parameters hydrostatic envelope models can be calculated by integration of the equation of mass conservation (see equation 42 of paper I):

$$\frac{\partial r}{\partial M_r} = \frac{1}{4\pi r^2 \rho} \tag{1}$$

the equation of hydrostatic equilibrium (the equation of momentum conservation with vanishing acceleration, see equation 43 of paper I):

$$\frac{\partial p}{\partial M_r} = -\frac{GM_r}{4\pi r^4} \tag{2}$$

and the equation of energy transport (see equation 45 of paper I):

$$\frac{\partial T}{\partial M_r} = -\frac{3\kappa L}{64\pi^2 acr^4 T^3} \tag{3}$$

For prescribed chemical composition, luminosity L, effective temperature T_{eff} and mass M the integration of equations 1 — 3 can be performed as an initial value problem starting at the photosphere. Initial values for r and p are obtained from Stefan - Boltzmann's law and an estimate for the photospheric pressure, respectively (see, e.g. Kippenhahn & Weigert, 1990). In case of energy transport by convection equation 3 needs to be modified. In a stellar envelope nuclear processes do not occur ($\varepsilon = 0$). As a consequence, the chemical composition is constant and integration of the stationary form of the equation of energy conservation (see equation 44 of paper I) shows the luminosity to be constant there. We are thus left with the three ordinary differential equations 1 — 3 posing an initial value problem.

Assuming that a hydrostatic stellar model has been constructed either by stellar evolution calculations or by envelope integrations in the way discussed above, any physical variable Q, where Q stands for, e.g., pressure, temperature and density, will be known for this model as a function of M_r. Hereafter, quantities referring to time independent hydrostatic models will be indicated by the subscript 0, i.e., for further studies we can assume the physical variables $Q_0(M_r)$ of a hydrostatic model to be given. Considering spherically symmetric time dependent perturbations around the hydrostatic equilibrium we may decompose a variable $Q(M_r, t)$ in the following way:

$$Q(M_r, t) = Q_0(M_r) + Q_1(M_r, t) \tag{4}$$

where the perturbation Q_1 (like Q) depends on both M_r and t. In the next step, the decomposition 4 is inserted in the system of equations describing the spherically symmetric structure and dynamics of a star (equations 42 — 45 of paper I) to obtain a system of equations for the perturbations Q_1. In accordance with the general strategy we shall assume in this procedure that Q_0 satisfies equations 42 — 45 of paper I separately and that the perturbations Q_1 are "small" compared to their hydrostatic counterparts Q_0:

$$\frac{Q_1}{Q_0} \ll 1 \quad \Longrightarrow \quad \left(\frac{Q_1}{Q_0}\right)^2 \ll \frac{Q_1}{Q_0} \tag{5}$$

Thus terms of higher order than linear in the perturbations can be neglected and we are left with a system of linear equations for the perturbations Q_1. As

a consequence of the linearisation of the problem achieved in this way the solutions of the linear differential equations may be superposed and multiplied by an arbitrary complex constant to yield further solutions of the system. Thus the amplitude of the perturbations remains a free parameter and cannot be determined in the linear approach. If pulsation amplitudes are to be determined, a nonlinear treatment of the problem is inevitable.

Should a stellar model turn out to be unstable according to the linear treatment its final fate might be determined – as a last step of the general strategy – by following the evolution of the instability into the nonlinear regime by numerical simulation of the complete set of nonlinear equations (equations 42 — 45 of paper I). This approach would then also allow for a determination of pulsation amplitudes, if finite amplitude pulsations are the result of a stellar instability.

2. Linear Radial Stability and Pulsations

In this section the equations governing "small" spherically symmetric perturbations of a star in hydrostatic equilibrium will be discussed. The analysis and notation closely follows the paper by Baker & Kippenhahn (1962), see also Gautschy & Glatzel (1990). Adopting the general strategy described in section 1 a hydrostatic model is assumed to be provided in terms of the physical variables $Q_0(M_r)$. The variables Q are decomposed according to equation 4 and inserted into equations 42 — 45 of paper I. Assuming $\frac{Q_1}{Q_0} \ll 1$ all terms are expanded around Q_0 retaining only stationary terms and expressions linear in the perturbations. For illustration, the linearisation of the expression $\frac{1}{r^2}$ (r is a dependent variable) and the equation of state $\rho = \rho(p,T)$ is performed explicitly:

$$\frac{1}{r^2} = \frac{1}{{r_0}^2(1+r_1/r_0)^2} = \frac{1}{{r_0}^2}(1-2r_1/r_0) = \frac{1}{{r_0}^2} - 2\frac{r_1}{{r_0}^3} \tag{6}$$

$$\begin{aligned} \rho &= \rho_0 + \rho_1 = \rho(p,T) = \rho(p_0+p_1, T_0+T_1) \\ &= \rho(p_0,T_0) + \left(\left.\frac{\partial\rho}{\partial p}\right|_T\right)_0 p_1 + \left(\left.\frac{\partial\rho}{\partial T}\right|_p\right)_0 T_1 + O({p_1}^2, {T_1}^2) \\ &= \rho_0 + \left(\left.\frac{\partial\rho}{\partial \log p}\right|_T\right)_0 p_1/p_0 + \left(\left.\frac{\partial\rho}{\partial \log T}\right|_p\right)_0 T_1/T_0 \end{aligned} \tag{7}$$

Hence

$$\rho_1/\rho_0 = \left(\left.\frac{\partial\log\rho}{\partial\log p}\right|_T\right)_0 p_1/p_0 + \left(\left.\frac{\partial\log\rho}{\partial\log T}\right|_p\right)_0 T_1/T_0 = \alpha_0 p_1/p_0 - \delta_0 T_1/T_0 \tag{8}$$

Taking into account that the variables Q_0 satisfy the time independent version of equations 42 — 45 of paper I separately the linearisation process finally yields the following system of equations:

Mass conservation

$$\frac{\partial r_1}{\partial M_r} = -\frac{2}{4\pi\rho_0 {r_0}^3} r_1 - \frac{1}{4\pi {r_0}^2 \rho_0}(\alpha_0 p_1/p_0 - \delta_0 T_1/T_0) \tag{9}$$

Momentum conservation

$$\frac{\partial p_1}{\partial M_r} = 4\frac{GM_r}{4\pi {r_0}^5} r_1 - \frac{1}{4\pi {r_0}^2}\frac{\partial^2 r_1}{\partial t^2} \tag{10}$$

Energy conservation

$$\frac{\partial L_1}{\partial M_r} = -c_{p0}\frac{\partial T_1}{\partial t} + \frac{\delta_0}{\rho_0}\frac{\partial p_1}{\partial t} + \varepsilon_0(\varepsilon_{p0} p_1/p_0 + \varepsilon_{T0} T_1/T_0) \tag{11}$$

Energy transport

$$\frac{\partial T_1}{\partial M_r} = \frac{T_0}{p_0}\frac{\partial p_0}{\partial M_r}\nabla_0 \left(\frac{L_0}{{L_0}^{rad}} L_1/L_0 - 4r_1/r_0 + \kappa_{p0} p_1/p_0 - (3 - \kappa_{T0}) T_1/T_0 \right) \tag{12}$$

where ∇_0, ε_p, ε_T, κ_p and κ_T are defined as:

$$\nabla_0 = \frac{\frac{\partial \log T_0}{\partial M_r}}{\frac{\partial \log p_0}{\partial M_r}} \tag{13}$$

$$\varepsilon_p = \left.\frac{\partial \log \varepsilon}{\partial \log p}\right|_T \quad ; \quad \varepsilon_T = \left.\frac{\partial \log \varepsilon}{\partial \log T}\right|_p \tag{14}$$

$$\kappa_p = \left.\frac{\partial \log \kappa}{\partial \log p}\right|_T \quad ; \quad \kappa_T = \left.\frac{\partial \log \kappa}{\partial \log T}\right|_p \tag{15}$$

On the timescale of pulsations the change of chemical composition by nuclear processes can be ignored (see section 46 of paper I). Therefore equation 46 of paper I has been disregarded in deriving equations 9 — 12. Equation 12 is not only valid for energy transport by radiation diffusion. In the form given, it is also valid, if energy transport is partially provided by convection and if the coupling between convection and pulsation can be treated according to the "frozen - in approximation" (see, e.g., Baker & Kippenhahn, 1965). The latter consists of assuming the convective flux to be constant during pulsations, i.e., the perturbation of the convective flux is required to vanish. It is applied, if convection contributes a minor fraction to the entire energy transport, and holds, if the turnover timescale of convection is much larger than the pulsation timescale. In the presence of convection ${L_0}^{rad}$ refers to the energy transported by radiation diffusion, whereas L_0 corresponds to the total flux consisting of both the radiative and the convective flux. (In the absence of convection we have ${L_0}^{rad} = L_0$.) Within the "frozen - in approximation" the consideration of convection implies the coefficient $\frac{L_0}{{L_0}^{rad}} \geq 1$ of L_1/L_0 in equation 12.

For the numerical treatment of equations 9 — 12 we introduce relative perturbations Q_1/Q_0 by

$$\zeta = r_1/r_0 \quad ; \quad t = T_1/T_0 \quad ; \quad p = p_1/p_0 \quad ; \quad l = L_1/L_0 \tag{16}$$

For improvement of the numerical resolution in the outer stellar envelope we change the independent variable from M_r to $\log p_0$ by the transformation provided by the equation of hydrostatic equilibrium:

$$\frac{\partial p_0}{\partial M_r} = -\frac{GM_r}{4\pi {r_0}^4} \tag{17}$$

$$\frac{\partial}{\partial M_r} = -\frac{GM_r}{4\pi p_0 {r_0}^4}\frac{\partial}{\partial \log p_0} \tag{18}$$

Hereafter, the derivative with respect to $\log p_0$ will be denoted with $'$. Times will be measured in units of the dynamical timescale, i.e., we introduce a dimensionless time τ by:

$$\tau = t\sqrt{4\pi G\bar{\rho}} \tag{19}$$

where $\bar{\rho}$ is the mean density of the star. We thus arrive at a system of dimensionless differential equations appropriate for a LNA analysis, i.e., a numerical analysis of radial linear nonadiabatic stellar stability and pulsations (see also Baker & Kippenhahn, 1962):
Mass conservation

$$\zeta' = c_4(3\zeta + \alpha p - \delta t) \tag{20}$$

Momentum conservation

$$p' = -p - 4\zeta + c_3\frac{\partial^2\zeta}{\partial\tau^2} \tag{21}$$

Energy conservation

$$l' = c_1\left(\frac{1}{\nabla_{ad}}\frac{\partial t}{\partial\tau} - \frac{\partial p}{\partial\tau}\right) \tag{22}$$

Energy transport

$$t' = \nabla_0\left(\frac{L_0}{{L_0}^{rad}}l - 4\zeta + \kappa_p p - (4-\kappa_T)t\right) \tag{23}$$

In equations 20 — 23 the dependent variables ζ, p, l and t depend on $\log p_0$ (or M_r) and τ, whereas their coefficients are completely determined by the hydrostatic model, i.e., they depend on $\log p_0$ (or M_r) only. Since the risk of confusion is small, subscripts 0 at the coefficients have been omitted and will be omitted hereafter. As the influence on stellar pulsations of nuclear processes is expected to be extremely small (see section 3 of paper I) terms associated with the nuclear energy generation rate ε have been disregarded in equation 22. The coefficient ∇_{ad} occurring in equation 22 and defined as

$$\nabla_{ad} = \left.\frac{\partial\log T}{\partial\log p}\right|_s \tag{24}$$

is without any reference to a particular stellar model completely determined by the equation of state as the logarithmic derivative of temperature with respect to pressure at constant entropy (hence the subscript "adiabatic"). The dimensionless coefficients c_i are obtained as

$$c_3 = \frac{4\pi {r_0}^3 \bar{\rho}}{M_r} \tag{25}$$

$$c_4 = \frac{p_0 r_0}{G M_r \rho_0} \propto 1/{r_0}^2 \quad for \quad r_0 \longrightarrow 0 \tag{26}$$

$$c_1 = \frac{4\pi {r_0}^4 {p_0}^2 \delta_0}{M_r L_0 \rho_0} \sqrt{\frac{4\pi\bar{\rho}}{G}} \propto 1/{r_0}^2 \quad for \quad r_0 \longrightarrow 0 \tag{27}$$

Except for c_1 which will be discussed in detail later all coefficients in equations 20 — 23 are of order unity. For $r_0 \to 0$ c_1 and c_4 diverge like $\propto 1/{r_0}^2$ (since $M_r \propto {r_0}^3$ and $L_0 \propto {r_0}^3$ for $r_0 \to 0$).

Since the coefficients of the linear partial differential system 20 — 23 do not depend on time it can be transformed into an ordinary differential system by separating the time dependence of the dependent variables Q according to

$$Q(\log p_0, \tau) = \hat{Q}(\log p_0) \exp(i\sigma\tau) \tag{28}$$

where the complex constant $\sigma = \sigma_r + i\sigma_i$ denotes the dimensionless complex eigenfrequency or eigenvalue. Thus time derivatives in equations 20 — 23 reduce to a multiplication with $i\sigma$ ($\frac{\partial}{\partial\tau} \to i\sigma$ and $\frac{\partial^2}{\partial\tau^2} \to -\sigma^2$) and the time dependence in terms of the common coefficient $\exp(i\sigma\tau)$ is eliminated from equations 20 — 23 leaving an ordinary differential system for the dependent variables $\hat{Q}$ with σ as a free parameter and $\log p_0$ as the independent variable. In the following we shall consider only the time independent parts $\hat{Q}$ of the dependent variables and omit superscripts $\hat{}$ for simplicity. Rewriting the time dependence of Q as

$$Q = \hat{Q} \exp(i\sigma_r\tau - \sigma_i\tau) = \hat{Q} \exp(-\sigma_i\tau)(\cos(\sigma_r\tau) + i \sin(\sigma_r\tau)) \tag{29}$$

we observe that a finite real part of the eigenfrequency implies an oscillation with frequency σ_r, whereas a finite imaginary part is associated with exponential decay (for $\sigma_i > 0$) or exponential growth (for $\sigma_i < 0$) of a perturbation. Thus positive imaginary parts of the eigenfrequency indicate stability, negative imaginary parts correspond to an instability of the star.

The solution of equations 20 — 23, now regarded as a forth order ordinary differential system with σ as a free parameter, requires the specification of four boundary conditions. At the photosphere ($r_0 = R$) being the outer boundary of the stellar models Stefan - Boltzmann's law

$$L = \sigma_{SB} R^2 {T^4}_{eff} \tag{30}$$

holds by definition (σ_{SB} is Stefan - Boltzmann's constant). Its linearised form in terms of the dependent variables of equations 20 — 23 is obtained as

$$l = 2\zeta + 4t \quad for \quad r_0 = R \tag{31}$$

A second boundary condition at $r_0 = R$ might be given by the requirement of a force - free outer boundary implying the pressure perturbation to vanish there:

$$p = 0 \quad for \quad r_0 = R \tag{32}$$

The photosphere is the boundary of the stellar model, but not the physical outer boundary of the star. As a consequence, there is a variety of physically reasonable requirements which might be imposed as boundary conditions at $r_0 = R$. In particular the condition 32 is a matter of debate, since the pressure at the photosphere is finite. Thus the outer boundary conditions at $r_0 = R$ are ambiguous and the influence of their choice on the results of the LNA analysis needs to be studied.

For complete stellar models the inner boundary corresponds to the center of the star ($r_0 = 0$). Rewriting the equations 20 and 22 of mass and energy conservation as

$$\frac{1}{c_4}\zeta' = 3\zeta + \alpha p - \delta t \tag{33}$$

$$\frac{1}{c_1}l' = i\sigma\left(\frac{1}{\nabla_{ad}}t - p\right) \tag{34}$$

we deduce from equations 33 and 34 that the coefficients of the derivatives vanish at the inner boundary $r_0 = 0$, since according to equations 26 and 27 $\frac{1}{c_4} \propto {r_0}^2$ and $\frac{1}{c_1} \propto {r_0}^2$ holds for $r_0 \to 0$. Thus $r_0 = 0$ is a singular point of the differential system enabling diverging solutions for $r_0 \to 0$. For the physical interpretation regular solutions are needed, i.e., contributions from singular solutions have to be excluded by appropriate boundary conditions. If ζ, p, l, t and their derivatives are required to remain finite at $r_0 = 0$, the l.h.s. of equations 33 and 34 vanishes there. As a consequence, also the r.h.s. of equations 33 and 34 has to vanish at $r_0 = 0$ implying two boundary conditions for the differential system 20 — 23 at $r_0 = 0$:

$$3\zeta + \alpha p - \delta t = 0 \quad ; \quad r_0 = 0 \tag{35}$$

$$t - \nabla_{ad} p = 0 \quad ; \quad r_0 = 0 \tag{36}$$

$r_0 = 0$ is a regular singular point of the differential system 20 — 23 providing the boundary conditions 35 and 36, if the solutions of the system (for physical reasons) are required to remain regular. We emphasize that (in contrast to the outer boundary) these boundary conditions are unambiguous. Any other choice will induce singular contributions to the solutions.

The fourth order differential system 20 — 23 together with the two boundary conditions 31 and 32 at $r_0 = R$, the two boundary conditions 35 and 36 at $r_0 = 0$ and the free complex parameter σ poses a boundary value problem. In contrast to initial value problems boundary value problems in general do not have a solution. However, an adjustment of the free parameter σ such that a solution of the differential equations matches all boundary conditions may be used to generate a solution of the complete system (differential equations together

with the boundary conditions). Thus the strategy consists of identifying and determining those values of σ which allow for a solution of the boundary value problem. (For stellar pulsations there is an infinite number of discrete values of σ satisfying this requirement.) According to its mathematical character the problem discussed is also addressed as boundary eigenvalue problem with σ being the eigenvalue or eigenfrequency.

3. Local Definition of Dynamical and Thermal Timescales

The global dynamical and thermal timescales of a star have been introduced in section 1 of paper I. Here we are interested, whether and how these timescales may be defined in a local way, i.e., not for the entire star but for a thin mass shell within a star extending between the radii r and $r + \Delta r$. The global dynamical timescale may be estimated as the time needed by a sound wave to cross the entire star. Accordingly, its local analogon is the time needed by a sound wave to cross a mass shell with thickness Δr. Estimating the sound speed as $c^2{}_{Sound} \propto p/\rho$ it is given by:

$$\tau_{Dyn} \propto \Delta r \sqrt{\rho/p} \tag{37}$$

Similar to the global thermal timescale, the local thermal timescale of a mass shell with mass Δm is defined as the time needed to radiate its thermal energy content at the local luminosity, where the thermal energy content might be expressed as the product of the specific heat c_p, the temperature T and the mass Δm. Rewriting the latter in terms of the density ρ and the volume of the mass shell we finally obtain for the local thermal timescale:

$$\tau_{Thermal} \propto \frac{c_p T \Delta m}{L} = \frac{c_p T \rho 4\pi r^2 \Delta r}{L} \tag{38}$$

Both the local dynamical and the local thermal timescale depend on the thickness Δr of the mass shell considered. Unless there are further arguments how to choose Δr, they can be given any value since the choice of Δr is ambiguous. Thus the local dynamical and thermal timescales given by equations 37 and 38 are ill-defined quantities without any physical relevance. However, their ratio being independent of Δr is well defined and given by:

$$\frac{\tau_{Thermal}}{\tau_{Dyn}} \propto \frac{4\pi r^2 \rho c_p T}{L} \sqrt{p/\rho} \tag{39}$$

For any stellar model the ratio of the local thermal and dynamical timescale increases from values of the order of unity (or even below) at the photosphere to the stellar center by many orders of magnitude. As an example it is shown as a function of relative radius r/R in Figure 1 for two stellar models having different masses but the same luminosity $L = 7.25 \times 10^5 L_\odot$ and effective temperature $T_{eff} = 18600K$.

For $\tau_{Thermal}/\tau_{Dyn} \gg 1$ the time for a mass element needed to exchange heat with its surroundings significantly is much longer than any dynamical event such as, e.g., a sound wave passing the element. As a consequence, the heat content of the mass element may be considered to be constant in this situation, i.e., the

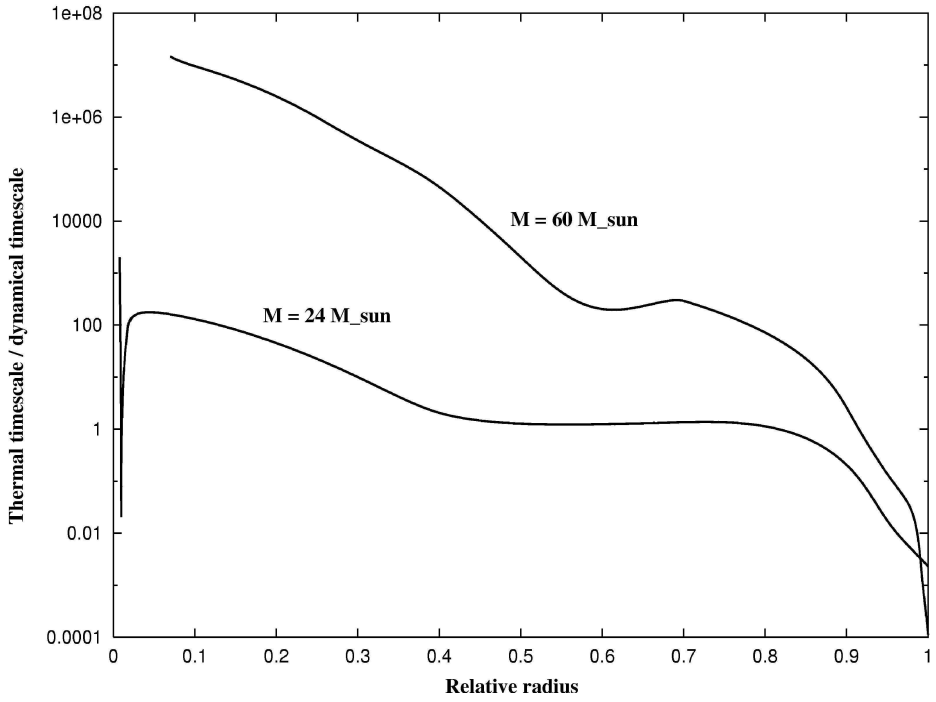

Figure 1. The ratio of the local thermal and dynamical timescale as a function of relative radius r/R for two stellar models with the masses indicated having the same luminosity $L = 7.25 \times 10^5 L_\odot$ and effective temperature $T_{eff} = 18600K$.

changes of state of the mass element occur at constant entropy and are adiabatic. Together with an equation of state this condition implies an algebraic relation between temperature and pressure and leads to the following linear equation for the relative perturbations of temperature and pressure:

$$t - \nabla_{ad} p = 0 \tag{40}$$

From Figure 1 we conclude that the condition 40 of adiabatic changes of state is highly satisfied in the deep interior of a star. For reasons of regularity (see equation 36) it holds even exactly at the very center ($r_0 = 0$). Thus at sufficiently deep layers within a star pulsations can be regarded to be adiabatic satisfying the relation 40. Nonadiabatic effects have to be taken into account close to the stellar surface, where the range in terms of the radial extent of significant deviations from adiabatic behaviour sensitively depends on the stellar model considered. For the model with $M = 60 M_\odot$ shown in Figure 1 it covers the outermost ≈ 20 per cent of the stellar envelope, whereas the adiabatic relation is a poor approximation for the major fraction of the envelope of the $M = 24 M_\odot$ model. Accordingly, studies on pulsations based on the adiabatic approximation 40 are expected to provide results comparable with those of the complete analysis, if the range of radii with $\tau_{Thermal}/\tau_{Dyn} \leq 1$ is sufficiently small. For the $M = 24 M_\odot$ model discussed the latter does not seem to hold and a fully nonadiabatic treatment will be necessary.

Comparing the ratio 39 of the local thermal and dynamical timescales with the definition 27 of the coefficient c_1 we deduce that except for a factor of order unity the expressions are identical, i.e., c_1 occurring in equation 22 as the coefficient of the time derivative of the entropy perturbation is essentially given by the ratio of the local thermal and dynamical timescales and reaches extremely high values when the stellar center is approached (see Figure 1). A large value of c_1 (or rather the vanishing of $1/c_1$ as the coefficient of l' in a suitably rewritten form of equation 22) implies equation 22 to approach singularity with the result that the time derivative of the entropy perturbation should vanish. Separating the time dependence according to equation 28 we are left with the final consequence that the expression $\frac{1}{\nabla_{ad}} t - p$ is required to vanish when c_1 diverges. In this way large values of c_1 naturally lead to adiabatic changes of state and imply the adiabatic relation 40 to hold without the necessity to impose the condition of adiabatic changes of state additionally. Thus our physical considerations concerning the various timescales and their consequences for the properties of pulsations within a star completely agree with the mathematical analysis of the perturbation equations. Through the relation between the timescales and the coefficients of the perturbation equations the physical and mathematical approach implies the same predictions concerning the properties of stellar pulsations.

Motivated by the fact that for many stars the fraction of the envelope with $\tau_{Thermal}/\tau_{Dyn} \leq 1$ is negligible implying adiabatic changes of state for the major part of the star an approximate treatment of the perturbation problem 20 — 23 consists of requiring the adiabatic relation 40 to be valid for the entire stellar model. As a consequence the mechanical and the thermal parts of equations 20 — 23 are decoupled and we are left with the mechanical equations of mass and momentum, where the temperature perturbation is replaced by the pressure perturbation using the adiabatic relation 40:

Mass conservation

$$\zeta' = c_4 \left(3\zeta + (\alpha - \delta\nabla_{ad})p\right) \tag{41}$$

Momentum conservation

$$p' = -p - 4\zeta - \sigma^2 c_3 \zeta \tag{42}$$

Thus the fourth order boundary eigenvalue problem is reduced to a second order problem where the (ambiguous) mechanical outer boundary condition 32 remains unchanged

$$p = 0 \quad ; \quad r_0 = R \tag{43}$$

and the regularity condition at $r_0 = 0$ implied by $c_4 \propto 1/{r_0}^2$ for $r_0 \to 0$ can either be read off directly from equation 41 or is obtained by replacing the temperature perturbation in equation 35 using the adiabatic relation 40. It is given by

$$3\zeta + (\alpha - \delta\nabla_{ad})p = 0 \quad ; \quad r_0 = 0 \tag{44}$$

Equations 41 and 42 together with the boundary conditions 43 and 44 describe linear radial stellar stability and pulsations within the adiabatic approximation.

4. Linear Nonradial Stability and Pulsations

As discussed in section 1 we assume a spherically symmetric hydrostatic stellar model to be provided in terms of physical variables $Q_0(M_r)$. Considering now nonspherical perturbations around the equilibrium it is more convenient to adopt an Eulerian description with the position vector $\vec{r}$ as an independent variable rather than the Lagrangean approach where for spherical symmetry M_r was used as independent variable. Accordingly we express the stationary physical variables in terms of the radial coordinate r as $Q_0(r)$. Adopting spherical polar coordinates (r, θ, φ) any physical variable $Q(r, \theta, \varphi, t)$ is — similar to the procedure described in section 1 — decomposed as

$$Q(r, \theta, \varphi, t) = Q_0(r) + Q_1(r, \theta, \varphi, t) \tag{45}$$

where Q_1 denotes the Eulerian perturbation of Q. (Note that the decomposition 4 refers to the Lagrangean perturbation of Q.) The decomposition 45 is then inserted into the equations of mass conservation (equation 21 of paper I), momentum conservation (equation 22 of paper I) and energy conservation (equation 27 of paper I), the diffusion equation for energy transport (equations 28 and 29 of paper I) and Poisson's equation for the gravitational potential (equation 23 of paper I). In accordance with the discussion in section 3 of paper I the variation with time of the chemical composition (see equation 30 of paper I) is ignored when considering pulsations. In contrast to radial pulsations, where an appropriate choice of Lagrangean variables together with an analytical integration supersedes the complete solution of Poisson's equation, the latter needs to be considered explicitly in the case of nonradial perturbations. In accordance with the general strategy (see section 1) we assume the stationary variables Q_0 to satisfy the system of equations separately and the perturbations Q_1 to be "small" compared to their hydrostatic counterparts Q_0, i.e., we have $Q_1/Q_0 \ll 1$. Neglecting terms of higher order than linear in the perturbations we thus arrive at a

system of homogeneous linear partial differential equations for the perturbations Q_1.

We emphasize that perturbations of a physical variable Q defined either in the Eulerian or Lagrangean approach are different and must not be confused. Eulerian perturbations (in the following denoted with $\tilde{Q}$) refer to a fixed position in space whereas Lagrangean perturbations (in the following denoted with ΔQ) refer to a fixed mass element. The Lagrangean perturbation of the position vector $\vec{r}$ (a dependent Lagrangean variable) for a fixed mass element (an independent Lagrangean variable) is denoted as Lagrangean displacement $\Delta\vec{r}$. For any physical variable Q the Lagrangean and Eulerian perturbations are related by:

$$\Delta Q = \tilde{Q} + \Delta\vec{r}\nabla Q_0 \tag{46}$$

Some authors use both Lagrangean and Eulerian perturbations and variables simultaneously. Therefore it seems useful to note some commutation rules:

$$\frac{d}{dt}\Delta Q = \Delta\frac{dQ}{dt} \quad ; \quad \frac{\partial}{\partial t}\tilde{Q} = \frac{\partial\tilde{Q}}{\partial t} \quad ; \quad \nabla\tilde{Q} = \tilde{\nabla Q} \tag{47}$$

$$\frac{d\tilde{Q}}{dt} = \frac{d}{dt}\tilde{Q} + \tilde{\vec{v}}\nabla Q_0 \tag{48}$$

$$\tilde{\vec{v}} = \frac{\partial}{\partial t}\Delta\vec{r} + (\vec{v_0}\nabla)\Delta\vec{r} - (\Delta\vec{r}\nabla)\vec{v_0} \tag{49}$$

The system of linear partial differential equations for the perturbations Q_1 contains the derivatives $\frac{\partial}{\partial\theta}$ and $\frac{\partial}{\partial\varphi}$ only in the combination

$$\frac{\partial^2}{\partial\theta^2} + \frac{1}{\sin^2\theta}\frac{\partial^2}{\partial\varphi^2} + \cot\theta\frac{\partial}{\partial\theta} =: \vec{L}^2 \tag{50}$$

Spherical harmonics $Y_{lm}(\theta,\varphi)$ with integer harmonic indices $l = 0, 1, 2, ...$ and $m = -l, ..., l$ are eigenfunctions of the operator $\vec{L}^2$ with eigenvalues $l(l+1)$:

$$\vec{L}^2 Y_{lm} = l(l+1)Y_{lm} \tag{51}$$

They provide a complete orthonormal system in terms of the variables θ and φ which suggests an expansion of the perturbations Q_1 in terms of spherical harmonics:

$$Q_1(r,t,\theta,\varphi) = \sum_{l,m}\hat{Q}_{1lm}(r,t)Y_{lm}(\theta,\varphi) \tag{52}$$

Inserting the expansion 52 in the perturbation equations and multiplying them with $Y_{l'm'}$ we take advantage of the orthonormality of the spherical harmonics Y_{lm} thus removing the angular dependence and achieving a separation of the angular variables θ and φ. We are left with a system of partial differential equations (with independent variables r and t only) for the coefficients $\hat{Q}_{1lm}(r,t)$ containing only the harmonic degree l as a parameter. As m does not appear explicitly as a parameter in the equations, the solutions are $2l+1$ - fold degenerate. The

spherical symmetry of the hydrostatic model described in terms of $Q_0(r)$ both enables the separation of the angular variables by expansion in terms of spherical harmonics and induces the degeneracy with respect to the harmonic index m. Finally, a separation of the time dependence of the perturbations Q_1 (enabled by the time independence of Q_0) is achieved similar to the radial case (see equation 28) by

$$\hat{Q}_{1lm}(r,t) = \hat{\hat{Q}}_{1lm}(r)\exp(i\omega t) \tag{53}$$

where ω denotes the complex eigenfrequency. Thus the perturbation equations are reduced to an ordinary differential system with r as an independent variable and the harmonic degree l and the eigenfrequency ω as parameters. Keeping in mind that its solutions depend on these parameters, superscripts and indices are usually omitted at the perturbations.

As the main physical and mathematical aspects of the ordinary differential system describing linear nonradial stability and pulsations are similar to those discussed in connection with the corresponding radial issue (see sections 2 and 3) we shall not explicitly present it here. Rather we shall comment only on the specifics of the nonradial problem and refer to Glatzel & Gautschy (1992) for further details. As its radial counterpart (equations 20 — 23) the nonradial perturbation equations consist of three equations associated with mass, momentum and energy conservation and one equation related to energy transport. Except for an additional term in the mass conservation equation which is proportional to $l(l+1)/\sigma^2$ and gives rise to the existence of gravity waves they exhibit the same structure and properties as the radial perturbation equations 20 — 23. In contrast to the radial problem Poisson's equation (second order) needs to be solved explicitly when considering nonradial perturbations which implies two additional first order equations for the perturbation of the potential and its derivative. Accordingly, nonradial stability and pulsations correspond to a sixth order boundary eigenvalue problem while radial stability and pulsations lead to a fourth order problem.

For the sixth order differential system three unambiguous boundary conditions are provided at the stellar center by the fact that $r = 0$ is a regular singular point of the equations implying a regularity condition for each type of variables (thermal, mechanical and potential variables). For the numerical treatment a transformation of variables according to $Q \rightarrow Q/r^l$ is needed (see Glatzel & Gautschy, 1992) to avoid numerical ambiguities in the formulation of the inner ($r = 0$) boundary conditions. At the outer boundary (photosphere) only the condition involving the potential variables is unique: It is obtained by the requirement that the potential and its derivative is continuously connected to the vacuum solution of Poisson's equation which decays at infinity. Similar to the radial case both the thermal and mechanical boundary conditions at the photosphere are ambiguous, since the photosphere is the outer boundary of the stellar model but not the physical outer boundary of the star. A possible choice of boundary conditions consists of assuming Stefan - Boltzmann's law to hold and the (Lagrangean!) pressure perturbation to vanish there (force - free boundary), see also equations 31 and 32.

Acknowledgments. I would like to thank the organisers of the VIII LAPIS summer school for the perfect performance and the warm hospitality at La Plata.

References

Baker N., Kippenhahn R., 1962, *ZAp*, **54**, 114
Baker N., Kippenhahn R., 1965, *ApJ*, **142**, 868
Gautschy A., Glatzel W., 1990, *MNRAS*, **245**, 597
Glatzel W., Gautschy A., 1992, *MNRAS*, **256**, 209
Kippenhahn R., Weigert A., 1990, *Stellar Structure and Evolution*

Pulsations Along Stellar Evolution
VIII LAPIS Summer School
AAA Workshop Series 12, 2021
M. Kraus & A.F. Torres, eds.

Numerical Treatment of Linear and Nonlinear Stellar Pulsations

W. Glatzel[1]

[1]*Institut für Astrophysik, Georg-August-Universität Göttingen, Friedrich-Hund-Platz 1, D-37077 Göttingen, Germany*

Abstract.

The linear stability analysis of stellar models poses a linear fourth or sixth order boundary eigenvalue problem. Methods for its numerical solution are reviewed, most of which face severe problems, if the ratio of the thermal and dynamical timescale falls below unity for a significant fraction of the stellar envelope considered. The extremely robust and highly accurate Riccati method is introduced and shown to be applicable to stellar stability problems with success even in these cases of strong deviations from adiabaticity. Numerical simulations of the evolution of a stellar instability into the nonlinear regime are still restricted to spherical geometry. We address the basic requirements for and problems connected with the simulation of radial pulsations. How violent artificial initial perturbations may be avoided and the extremely high accuracy requirements posed by the differences between the various energy forms can be met by strictly conservative numerical schemes is discussed.

Key words: asteroseismology — hydrodynamics — methods: numerical — stars: mass loss — stars: oscillations

1. Numerical Solution of the Linear Stability Problems

In the present paper, we will adopt the same notation as in the previous lectures in this volume on "Theoretical Description and Basic Physics of Stellar Pulsations" and on the "Linear Analysis" (hereafter referred to as papers I and II). We shall make use of the results obtained there.

1.1. Matrix Methods and Shooting Methods

We consider the boundary eigenvalue problems emerging from the study of linear stability and pulsations and discussed in sections 2 and 4 of paper II for radial and nonradial perturbations respectively. They consist of four (radial perturbations) or six (nonradial perturbations) homogeneous ordinary differential equations supplemented by two (radial case) or three (nonradial case) homogeneous boundary conditions on each end of the integration interval. A solution of the boundary value problem is accomplished by adjusting the complex parameter σ properly. The values of σ which allow for a solution are denoted as eigenvalues (or eigenfrequencies).

The solution of the boundary eigenvalue problems using a matrix method relies on a discretization of the integration interval by N grid points where x_i denotes the position of grid point i in the integration interval. The value of a dependent variable u at x_i is denoted by u_i: $u_i = u(x_i)$. Derivatives can then be expressed in terms of $\{u_i\}$ and $\{x_i\}$. For example, a simple possibility to represent the derivative $\frac{du}{dx}$ of the variable u would be given by:

$$\frac{du}{dx} = \frac{u_{i+1} - u_i}{x_{i+1} - x_i} \tag{1}$$

By the boundary conditions some values of the dependent variables at the boundaries of the integration interval are fixed. As a result of this approach we finally obtain a linear homogeneous algebraic system of equations which might be written as:

$$\mathbf{A}(\sigma)\mathbf{u} = 0 \tag{2}$$

In equation 2 $\mathbf{u}$ is for the radial problem a $(4 \times 2 \times N - 4 \times 2)$ - dimensional real vector containing all dependent variables $\{u_i\}$. (For the nonradial problem it is a $(6 \times 2 \times N - 6 \times 2)$ - dimensional real vector.) The coefficient 4 (or 6) stands for the number of dependent continuous variables, i.e., the number of differential equations, the coefficient 2 accounts for the fact that the variables are complex. The subtraction of 4×2 (or 6×2) corresponds to the consideration of the boundary conditions. $\mathbf{A}$ is a matrix having the same dimension as $\mathbf{u}$ which contains the information on the hydrostatic stellar model and depends on the eigenvalue σ (and the harmonic degree l as a parameter). The linear homogeneous system of equations 2 has a solution, if the determinant of $\mathbf{A}$ vanishes, i.e., if

$$\det \mathbf{A}(\sigma) = 0 \tag{3}$$

Thus the eigenvalues σ are provided by the zeros of the determinant of the matrix $\mathbf{A}$.

For the solution of equations 2 and 3 posing a standard problem in linear algebra a variety of – mainly iterative – numerical algorithms is available. However, an iterative solution requires initial guesses both for the eigenvalues and the eigenfunctions which are usually taken from the result of a numerically less difficult approximate treatment of the problem, e.g., from the adiabatic approximation. As a consequence, eigensolutions which significantly differ from their approximation or do not have a counterpart in the approximation at all, cannot be identified. Moreover, the convergence of an algorithm towards a pretended solution does not prove it to be a true solution of equation 2. Whether the procedure has converged towards a true or a numerically induced spurious solution is often difficult to decide. The dimension of the matrix $\mathbf{A}$ is proportional to the number N of the grid points used. Thus the resolution of the method is limited by the maximum dimension of $\mathbf{A}$, for which the iteration algorithm provides reliable results and which can be handled by the available computational device. As the optimum distribution of grid points depends both on the hydrostatic model and the eigensolution to be calculated, it is not known a priori. Accordingly, for

a given number of grid points the resolution will suffer from their unfavourable distribution.

The solution of the boundary eigenvalue problems using a shooting method relies on the integration of the differential equations as an initial value problem which guarantees a unique solution for any initial condition (and any value of the parameter σ). Starting at one of the boundaries, four (radial problem) or six (nonradial problem) initial conditions have to be specified only half of which are given. The remaining two (or three) initial conditions in addition to the eigenvalue σ have to be guessed. Once with these initial conditions (and the value of σ chosen) the integration (using any standard algorithm for initial value integration) arrives at the other boundary the solution is compared with the two (or three) boundary conditions prescribed there. The discrepancy between the solution and the boundary conditions forms the basis for the iteration of the unknown initial conditions and the eigenvalue σ until solution and boundary conditions match.

Shooting methods do not require any estimates for the eigenfunctions. Moreover, the stepsize of the initial value integration can be adapted locally to match any prescribed accuracy requirement and to resolve any detail of the eigenfunction and the hydrostatic model. There are no limitations concerning computer storage and the maximum dimension of any matrices involved. A severe problem is associated with the iteration of the unknown initial conditions. For boundary eigenvalue problems of higher than second order the ambiguity in the initial conditions in general introduces the parasitic growth problem, i.e., exponentially growing particular solutions of the initial value problem induced by improperly chosen initial conditions will eventually dominate the entire solution and prevent a solution of the boundary value problem. Thus the numerical instability associated with parasitic growth caused by ambiguous initial conditions is the reason, why simple shooting methods in general fail when applied to boundary value problems of higher than second order. In the next section we shall show how the ambiguity in the initial conditions can be avoided and, as a consequence, a numerically stable shooting method is obtained which may be used successfully to solve high order boundary eigenvalue problems.

1.2. The Riccati Method

The system of differential equations governing linear stability and pulsations may be rewritten in terms of vectors $\mathbf{u}$ and $\mathbf{v}$ and matrices $\mathbf{A}$, $\mathbf{B}$, $\mathbf{C}$ and $\mathbf{D}$ as

$$\begin{aligned} \mathbf{u}' &= \mathbf{A}\mathbf{u} + \mathbf{B}\mathbf{v} \\ \mathbf{v}' &= \mathbf{C}\mathbf{u} + \mathbf{D}\mathbf{v} \end{aligned} \tag{4}$$

where $\mathbf{u}$ and $\mathbf{v}$ are twodimensional (radial perturbations) or threedimensional (nonradial perturbations) vectors each of them containing two (or three) dependent variables. The elements of the 2×2 (or 3×3) matrices correspond to the coefficients of the differential systems and can be read off from the equations directly. They depend on the hydrostatic model, the eigenfrequency σ and – for nonradial perturbations – on the harmonic degree l. As an example, for radial perturbations (see equations 20 — 23 of paper II) $\mathbf{u}$ and $\mathbf{v}$ may be defined as

$$\mathbf{u} = \begin{pmatrix} \zeta \\ t \end{pmatrix} \qquad \mathbf{v} = \begin{pmatrix} l \\ p \end{pmatrix} \tag{5}$$

The matrix $\mathbf{A}$ is then read off from equations 20 and 23 of paper II as

$$\mathbf{A} = \begin{pmatrix} 3c_4 & -\delta c_4 \\ -4\nabla_0 & -\nabla_0(4-\kappa_T) \end{pmatrix} \tag{6}$$

The 2×2 (or 3×3) complex Riccati matrix $\mathbf{R}$ is now defined by

$$\mathbf{u} = \mathbf{R}\mathbf{v} \tag{7}$$

Differentiating 7 and using 4 and 7 to replace $\mathbf{u}'$, $\mathbf{v}'$ and $\mathbf{u}$ we obtain

$$\begin{aligned} \mathbf{u}' &= \mathbf{R}'\mathbf{v} + \mathbf{R}\mathbf{v}' \\ \mathbf{A}\mathbf{u} + \mathbf{B}\mathbf{v} &= \mathbf{R}'\mathbf{v} + \mathbf{R}(\mathbf{C}\mathbf{u} + \mathbf{D}\mathbf{v}) \\ \mathbf{A}\mathbf{R}\mathbf{v} + \mathbf{B}\mathbf{v} &= \mathbf{R}'\mathbf{v} + \mathbf{R}(\mathbf{C}\mathbf{R}\mathbf{v} + \mathbf{D}\mathbf{v}) \end{aligned} \tag{8}$$

and finally

$$(\mathbf{R}' + \mathbf{R}\mathbf{C}\mathbf{R} + \mathbf{R}\mathbf{D} - \mathbf{A}\mathbf{R} - \mathbf{B})\mathbf{v} = 0 \tag{9}$$

Since equation 9 must hold for any arbitrary vector $\mathbf{v}$ we are left with the Riccati equation for the (complex) Riccati matrix $\mathbf{R}$:

$$\mathbf{R}' = \mathbf{B} + \mathbf{A}\mathbf{R} - \mathbf{R}\mathbf{D} - \mathbf{R}\mathbf{C}\mathbf{R} \tag{10}$$

Note that equation 10 is a nonlinear matrix differential equation involving only the Riccati matrix and the coefficient matrices $\mathbf{A}$, $\mathbf{B}$, $\mathbf{C}$ and $\mathbf{D}$. The boundary conditions for the primary linear system 4 can now be rewritten as initial conditions for the integration of the Riccati equation 10. As an example, we consider the boundary conditions for radial perturbations at $r_0 = 0$ (see equations 35 and 36 of paper II):

$$3\zeta + \alpha p - \delta t = 0 \tag{11}$$

$$t - \nabla_{ad} p = 0 \tag{12}$$

They are equivalent to the two equations

$$\zeta = \left(-\frac{\alpha}{3} + \frac{\delta}{3}\nabla_{ad}\right) p \tag{13}$$

$$t = \nabla_{ad} p \tag{14}$$

which may be rewritten in terms of the vectors $\mathbf{u}$ and $\mathbf{v}$ defined by equation 5:

$$\mathbf{u} = \begin{pmatrix} \zeta \\ t \end{pmatrix} = \begin{pmatrix} 0 & \left(-\frac{\alpha}{3} + \frac{\delta}{3}\nabla_{ad}\right) \\ 0 & \nabla_{ad} \end{pmatrix} \begin{pmatrix} l \\ p \end{pmatrix} = \mathbf{R}(r_0 = 0)\mathbf{v} \tag{15}$$

The matrix relating $\mathbf{u}$ and $\mathbf{v}$ by definition (see equation 7) corresponds to the Riccati matrix $\mathbf{R}$ at the boundary $r_0 = 0$. It is denoted by $\mathbf{R}(r_0 = 0)$ in equation 15. From equation 15 we deduce that the boundary conditions unambiguously determine the value of the Riccati matrix at the boundary $r_0 = 0$, i.e., they provide unambiguous initial conditions for the integration of the Riccati equation 10. With the modification that the inverse of the Riccati matrix is determined uniquely this result also holds for the outer boundary (photosphere). In general the boundary conditions for the linear boundary value problem 4 imply unique initial conditions (in terms of unambiguous initial values for the Riccati matrix or its inverse) for the integration of the nonlinear Riccati matrix equation considered as an initial value problem.

Equivalently, a complex matrix $\mathbf{S}$ relating $\mathbf{u}$ and $\mathbf{v}$ may be defined by

$$\mathbf{v} = \mathbf{S}\mathbf{u} \tag{16}$$

instead of the definition 7 for $\mathbf{R}$. From equations 7 and 16 we deduce that $\mathbf{S} = \mathbf{R}^{-1}$ (provided that $\mathbf{R}^{-1}$ does exist). Similar to $\mathbf{R}$ its inverse matrix $\mathbf{S}$ satisfies the Riccati equation 10, however with $\mathbf{A}$ substituted by $\mathbf{D}$ (and vice versa) and $\mathbf{B}$ substituted by $\mathbf{C}$ (and vice versa). During integration $\mathbf{R}$ (or $\mathbf{S}$) may become singular. In this case we can switch from the integration of $\mathbf{R}$ to the integration of $\mathbf{S}$ (or vice versa). Experiments suggest that switching from integrating $\mathbf{R}$ to integrating $\mathbf{S}$ (or vice versa) is appropriate, if $|\det \mathbf{R}|$ (or $|\det \mathbf{S}|$) exceeds a conveniently chosen threshold (> 1).

Thus the Riccati approach consists of a transformation of the linear boundary value problem into a nonlinear initial value problem with unambiguous initial conditions for the integration of the Riccati matrix $\mathbf{R}$ (or its inverse $\mathbf{S}$). Being a shooting method it benefits from all associated advantages in particular concerning reliability, resolution and accuracy. Simultaneously it does not suffer from the problem of unknown initial conditions which is typical for shooting methods applied to high order differential systems. The Riccati method is based on an initial value problem with unique initial conditions. There is no need to iterate a priori unknown initial conditions. As a consequence, the Riccati method is numerically stable and does not suffer from the parasitic growth problem.

Using the Riccati method the stability problem is characterized by unique initial conditions at both boundaries of the integration interval and the coefficient matrices $\mathbf{A}$, $\mathbf{B}$, $\mathbf{C}$ and $\mathbf{D}$. They depend on the stellar model considered, the harmonic degree l and the complex eigenfrequency σ, which is the only free parameter of the problem. For arbitrary values of σ a solution of the boundary eigenvalue problem posed by the stability analysis does not exist (see section 1.1). In order to determine those values which allow for a solution of the problem by using the Riccati method the Riccati equation is integrated for some prescribed value of σ from both boundaries (unique initial conditions!) to some intermediate point x_{fit} within the integration interval. As a result, we obtain two Riccati matrices at x_{fit} determined by the "inner" integration from the bottom boundary to x_{fit} and the "outer" integration from the top boundary to x_{fit}. We denote them by $\mathbf{R}_{in}$ and $\mathbf{R}_{out}$.

For a solution of the boundary eigenvalue problem the eigenfunctions need to be continuous all over the integration interval, i.e., $\mathbf{u}$ and $\mathbf{v}$ have to be continuous

in the integration interval, in particular at x_{fit}. This condition may be written as

$$\begin{aligned} \mathbf{u}_{in} &= \mathbf{u}_{out} \\ \mathbf{v}_{in} &= \mathbf{v}_{out} \end{aligned} \tag{17}$$

where $\mathbf{u}_{in}$ and $\mathbf{v}_{in}$ denote solutions for $\mathbf{u}$ and $\mathbf{v}$ at x_{fit} obtained by integration between the bottom boundary and x_{fit}. $\mathbf{u}_{out}$ and $\mathbf{v}_{out}$ denote solutions for $\mathbf{u}$ and $\mathbf{v}$ at x_{fit} obtained by integration between the top boundary and x_{fit}. Using the general definition 7 of the Riccati matrix $\mathbf{R}$ we obtain from the requirement of continuity at x_{fit} (equation 17)

$$\mathbf{u}_{in} = \mathbf{R}_{in}\mathbf{v}_{in} = \mathbf{u}_{out} = \mathbf{R}_{out}\mathbf{v}_{out} = \mathbf{R}_{out}\mathbf{v}_{in} \tag{18}$$

and

$$(\mathbf{R}_{in} - \mathbf{R}_{out})\mathbf{v}_{in} = 0 \tag{19}$$

A necessary condition for the existence of a solution of the linear homogeneous equation 19 is given by

$$\det(\mathbf{R}_{in} - \mathbf{R}_{out}) = 0 \tag{20}$$

The condition 20 involves $\mathbf{R}_{in}$ and $\mathbf{R}_{out}$ which only depend on the eigenfrequency σ but otherwise have been uniquely determined by integration of the Riccati equation. Thus $\det(\mathbf{R}_{in} - \mathbf{R}_{out})$ is a complex valued function of the complex variable σ and its zeros correspond to a solution of the boundary eigenvalue problem. I.e., those values of σ, for which the determinant in equation 20 vanishes, are the eigenfrequencies of the system we have been searching for. Their determination has thus been reduced to finding the complex zeros of a complex valued function, which can be done using standard numerical techniques (e.g., the Newton - Raphson method). We emphasize that for the determination of the determinant function in equation 20 neither the auxiliary solution of an approximate problem nor estimates for eigenvalues and eigenfunctions are required. The determinant function is entirely based on the unrestricted stability problem without reference to any additional approximation or estimate.
In general numerical algorithms used for the precise determination of the zeros of a function require initial guesses for the position of the zero to start an iterative process. They can be obtained simply by tabulating $\det(\mathbf{R}_{in} - \mathbf{R}_{out})$ as a function of the complex variable σ. Note that even these estimates are based on the unrestricted stability problem and do not rely on any auxiliary approximative treatment. Thus the danger to miss unexpected eigenvalues which are not present in approximative treatments of the problem is considerably reduced. Moreover, by tabulating the determinant function in the vicinity of a value of σ, to which an iterative root finding process has converged, it is possible to check whether this value corresponds to a spurious or a true eigenvalue of the system. The eigenvalues of the stability problem do not (and must not) depend on the choice of x_{fit} which is a free parameter of the Riccati method. However, the run of the determinant function may sensitively depend on the position of x_{fit} within the

integration interval and a suitable choice of x_{fit} can considerably facilitate the search for eigenvalues and their iteration.

Once an eigenvalue σ and the associated Riccati matrix $\mathbf{R}(x)$ as a function of the independent variable x has been determined, also the corresponding eigenfunctions $\mathbf{u}(x)$ and $\mathbf{v}(x)$ can be calculated. First of all $\mathbf{v}_{in}$ is obtained from the linear homogeneous continuity condition 19. With $\mathbf{v}_{in} = \mathbf{v}_{out} = \mathbf{v}(x_{fit})$ we thus have initial conditions for the integration of the eigenfunction component $\mathbf{v}$ from x_{fit} both to the bottom and the top boundary using equation 4 together with the definition 7 of the Riccati matrix:

$$\mathbf{v}' = \mathbf{C}\mathbf{u} + \mathbf{D}\mathbf{v} = (\mathbf{C}\mathbf{R} + \mathbf{D})\mathbf{v} \tag{21}$$

Note that for the integration of equation 21 the predetermined values for the Riccati matrix $\mathbf{R}$ have to be used, the Riccati equation and equation 21 must not be solved simultaneously. Finally, the eigenfunction component $\mathbf{u}$ is obtained using the definition 7 of the Riccati matrix as $\mathbf{u} = \mathbf{R}\mathbf{v}$.

For more details on the application of the Riccati method to stellar stability problems we refer to Gautschy & Glatzel (1990), further discussions of it may be found in Scott (1973), Davey (1977) and Sloan (1977).

2. Numerical Simulation of Pulsations in the Nonlinear Regime

Similar to the previous section we shall adopt the same notation as in papers I and II and shall make use of the results obtained there.

2.1. Basic Assumptions and Equations

Once a stellar model has been found to be unstable according to a linear stability analysis the final result of the instability (e.g., finite amplitude pulsations, mass loss, disruption of the stellar envelope) needs to be determined. A possible approach consists of following the time development of the instability by numerical simulation from hydrostatic equilibrium through the linear phase of exponential growth into the nonlinear regime. At this stage the amplitude of the perturbation is defined and the growth may enter saturation, if the instability leads to finite amplitude pulsations. Should these pulsations be associated with mass loss, or should the envelope become disrupted, the results of the simulation will then provide corresponding evidence.

Since a suitable numerical procedure, satisfying the necessary requirements concerning accuracy and resolution (see below) is not available so far, the nonlinear simulation of nonradial pulsations and intrinsically threedimensional effects (magnetic fields, rotation) is not yet feasible. Therefore numerical simulations of nonlinear pulsations are so far still restricted to onedimensional studies in spherical geometry.

In accordance with our previous discussions the outer boundary of the models will be taken to be the stellar photosphere, i.e., the atmosphere and optically thin parts of the star will be disregarded. As a consequence, radiation transport can be described on the basis of the diffusion approximation. In the absence of a satisfactory description of convection in a pulsating star we adopt, similar to the treatment of convection in the linear analysis (see section 2 of paper II), the

"frozen - in approximation" (see, e.g., Baker & Kippenhahn, 1965). It consists of assuming the convective flux to be constant (and equal to its value in the initial hydrostatic model) during pulsations. This assumption is to be understood in the Lagrangean framework, i.e., the convective flux is required to be constant in time at any value of the Lagrangean coordinate M_r given. For further discussions of the "frozen - in approximation" we refer to section 2 of paper II.

Using the assumptions discussed the equations governing nonlinear radial pulsations may now be derived directly from sections 2 and 3 of paper I. Their analysis and notation closely follows that adopted in the study of Grott et al. (2005). For further details we refer to this paper. Adopting a Lagrangean description with time t and mass M_r as independent variables mass conservation (equation 20 of paper I) may be expressed as

$$\frac{\partial}{\partial t}\left(\frac{1}{\rho}\right) = \frac{\partial}{\partial M_r}\left(4\pi r^2 v\right) \tag{22}$$

where v denotes the radial component of the velocity and $\nabla\vec{v}$ has been rewritten using equation 42 of paper I as

$$\nabla\vec{v} = \frac{1}{r^2}\frac{\partial}{\partial r}\left(r^2 v\right) = \rho\frac{\partial}{\partial M_r}\left(4\pi r^2 v\right) \tag{23}$$

With the definition of v

$$\frac{\partial r}{\partial t} = v \tag{24}$$

the equation of momentum conservation (equation 43 of paper I) is written as

$$\frac{\partial v}{\partial t} = -4\pi r^2\frac{\partial p}{\partial M_r} - \frac{GM_r}{r^2} - \lambda_Q \tag{25}$$

Using 23 for $\nabla\vec{v}$ (together with a corresponding relation for $\nabla\vec{F}$) we obtain for the equation of energy conservation from equation 25 of paper I:

$$\frac{\partial u}{\partial t} = -p\frac{\partial}{\partial M_r}\left(4\pi r^2 v\right) - \frac{\partial}{\partial M_r}\left(4\pi r^2 F_{rad}\right) - \frac{\partial}{\partial M_r}\left(4\pi r^2 F_{conv}\right) - \mu_Q \tag{26}$$

where the radial component F of the total heat flux is given by the radial components of the radiative and convective fluxes, F_{rad} and F_{conv}, through $F = F_{rad} + F_{conv}$. In deriving equation 26 nuclear energy generation has been disregarded ($\varepsilon = 0$), since for the models considered pulsations are restricted to the stellar envelopes, where nuclear processes are irrelevant.
Finally, we obtain for the radiative energy transport in the diffusion approximation from equation 45 of paper I:

$$F_{rad} = -4\pi r^2\frac{c}{\kappa}\frac{\partial p_{rad}}{\partial M_r} \tag{27}$$

where the radiative luminosity has been replaced by the radiative flux and the temperature T has been expressed in terms of the radiation pressure p_{rad}.

Equations 22, 24, 25, 26 and 27 together with a thermal and a caloric equation of state form a closed system for the determination of the dependent variables r, v, F_{rad}, u, p, ρ and p_{rad} (instead of T). Note that F_{conv} is fixed in the frozen - in approximation. The quantities λ_Q and μ_Q occurring in the momentum and energy conservation equations account for the artificial (numerical) viscosity needed to treat shock waves, which typically occur during the evolution of a stellar instability. For more information on this issue, see Grott et al. (2005).

The momentum and energy conservation equations 25 and 26 provide the energy balance of the system by using a familiar procedure: Equation 25 is multiplied with the velocity v and integrated over a mass element. Then equation 26 is integrated over the same mass element and added to the result. We obtain

$$\frac{d}{dt}\left(E_{kin} + E_{therm} + E_{grav}\right) + \Delta L_{therm} + \Delta L_{acoustic} = 0 \tag{28}$$

or, alternatively, after integrating equation 28 over the time and subtracting the initial values of E_{kin}, E_{therm} and E_{grav}:

$$E_{kin} + E_{therm} + E_{grav} + \int \Delta L_{therm} dt + \int \Delta L_{acoustic} dt = 0 \tag{29}$$

Equations 28 and 29 represent the energy balance of the system. They are valid for any mass element and therefore also for the entire stellar envelope. Here, E_{kin}, E_{therm} and E_{grav} refer to the kinetic, thermal and gravitational potential energy content of the mass element, respectively. ΔL_{therm} denotes the difference of the total thermal (radiative and convective) luminosity between the top and the bottom boundary of the mass element, and $\Delta L_{acoustic}$ describes its analogue for the acoustic luminosity $L_{acoustic}$. The latter is defined as

$$L_{acoustic} = 4\pi r^2 v p \tag{30}$$

and represents the luminosity which is associated with the mechanical (acoustic) energy flux given by the product of velocity and pressure. E.g., sound waves and shock waves imply an energy flux and an acoustic luminosity which is described by equation 30.

2.2. Demands on the Numerical Treatment

Apart from standard tests for the numerical scheme (e.g., validation of the code with respect to the correct representation of shock waves according to Noh (1987)) we require the numerical simulation to start from hydrostatic equilibrium and to reveal the physical instability without any additional action or external perturbation. If the numerical scheme is too dissipative, the model remains in equilibrium and an external perturbation would be required to initiate any motion, which is not necessarily related to the physical instability. For low numerical dissipation the system often exhibits violent initial perturbations with amplitudes in the nonlinear regime. As a consequence, the linear phase of exponential growth of the physical instability is not represented and the question remains, whether the result of the simulation is a numerical artefact caused by initial perturbations rather than by the physical instability. For a validation of the code we therefore require that the simulation covers the linear phase. Then

growth rates and periods of unstable modes derived from the simulation can be compared with their independently predetermined counterparts from the linear analysis.

To overcome the unphysical initial perturbations artificial dissipation and viscosity or a pseudo time evolution of the grid (see, e.g., Dorfi & Drury (1987) and Dorfi & Feuchtinger (1991)) have been introduced. As a consequence, the physical instability then has to be triggered by an external perturbation which is undesirable as discussed above. The unwanted initial perturbations were found by Grott et al. (2005) to be caused by a mismatch of the prescribed initial model and the numerical scheme used for the simulation, i.e., the initial model is not in hydrostatic equilibrium with respect to the numerical scheme. A deviation from equilibrium (as defined on the basis of the difference scheme used) implies accelerations and thus initial perturbations which may reach the nonlinear regime. A solution of the problem proposed by Grott et al. (2005) therefore consists of adjusting the prescribed initial model to the numerical scheme such that the slightly modified initial model represents a perfect hydrostatic equilibrium with respect to it.

Adopting - with vanishing accelerations - the numerical scheme used for the subsequent simulations a new hydrostatic initial model is constructed by an iterative relaxation procedure where the original initial model is taken as an initial guess. As a result, the artificial initial perturbations in fact disappear without the necessity to introduce artificial dissipation. Moreover, due to minimal numerical dissipation the code picks up the physical instability from numerical noise without any further action or external perturbation. The time evolution of the instability then enters the linear phase of exponential growth, where - for validation of the code - the pulsation period and the growth rate determined from the simulation can be compared with the corresponding predetermined values from the independent linear analysis.

For illustration the time evolution of the instability of a stellar model corresponding to a mass of $M = 45 M_\odot$, the luminosity $L = 5.37 \times 10^5 L_\odot$, the effective temperature $T_{eff} = 33890K$ and the chemical composition $(X, Y, Z) = (0.7, 0.28, 0.02)$ is shown in Figure 1, where the velocity at the outermost grid point of the model is given as a function of time. It starts from hydrostatic equilibrium with velocity perturbations of the order of $10^{-5} cm/sec$ which correspond to the numerical noise level. Then the code picks up (without any further action or external perturbation) an unstable mode with a period of $0.62d$ and a growth rate of $0.64/d$ which differ from their counterparts determined by the linear analysis by less than 5 per cent. After $\sim 45d$ the linear phase of exponential growth comes to an end and the evolution enters the nonlinear regime where the velocity amplitude saturates at a value corresponding to 19 per cent of the escape velocity. Thus finite amplitude pulsations are the final result of the instability of the model considered.

Apart from validation of the code in the linear regime by comparison with the results of an independent linear analysis the compliance with the energy balance 29 of the simulation provides an essential criterion for its quality. As an example, the various energy terms occurring in equation 29 are given as a function of time in Figures 2, 3 and 4 for the simulation of the unstable model considered above in a time interval covering some pulsation periods in the nonlinear regime.

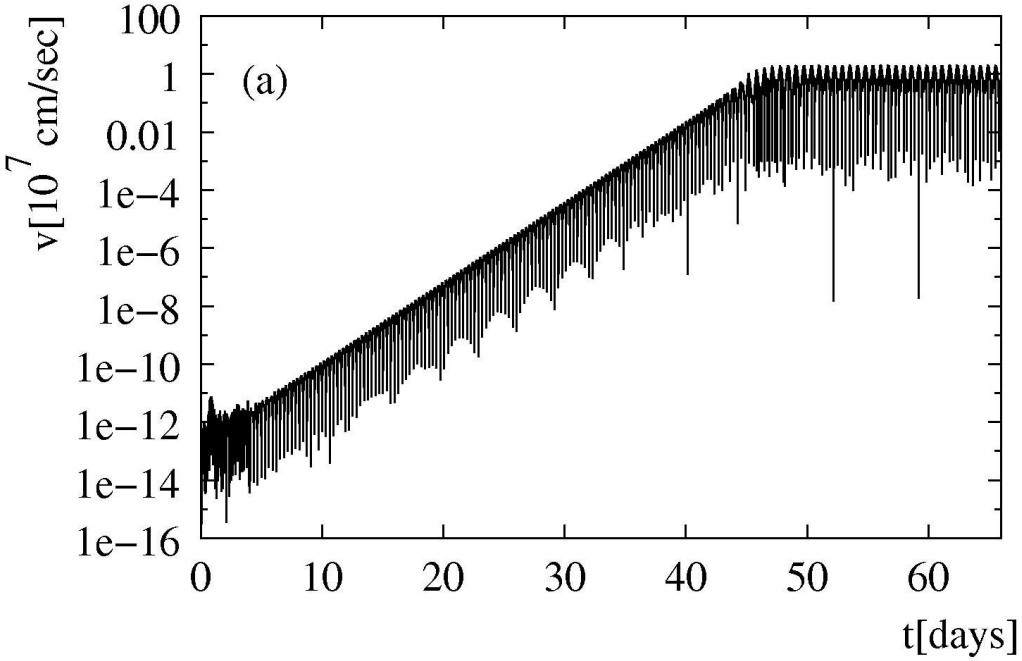

Figure 1. The velocity at the outermost grid point as a function of time for an unstable stellar model with the mass $M = 45M_{\odot}$, the luminosity $L = 5.37 \times 10^5 L_{\odot}$, the effective temperature $T_{eff} = 33890K$ and the chemical composition $(X, Y, Z) = (0.7, 0.28, 0.02)$ (from Figure 1 of Grott et al. (2005)). The evolution starts from hydrostatic equilibrium with velocity perturbations of the order of $10^{-5} cm/sec$ (numerical noise), enters the linear phase of exponential growth of the instability and finally reaches the nonlinear regime where the velocity amplitude saturates at a value corresponding to 19 per cent of the escape velocity. Finite amplitude pulsations are the final result of the instability in this case.

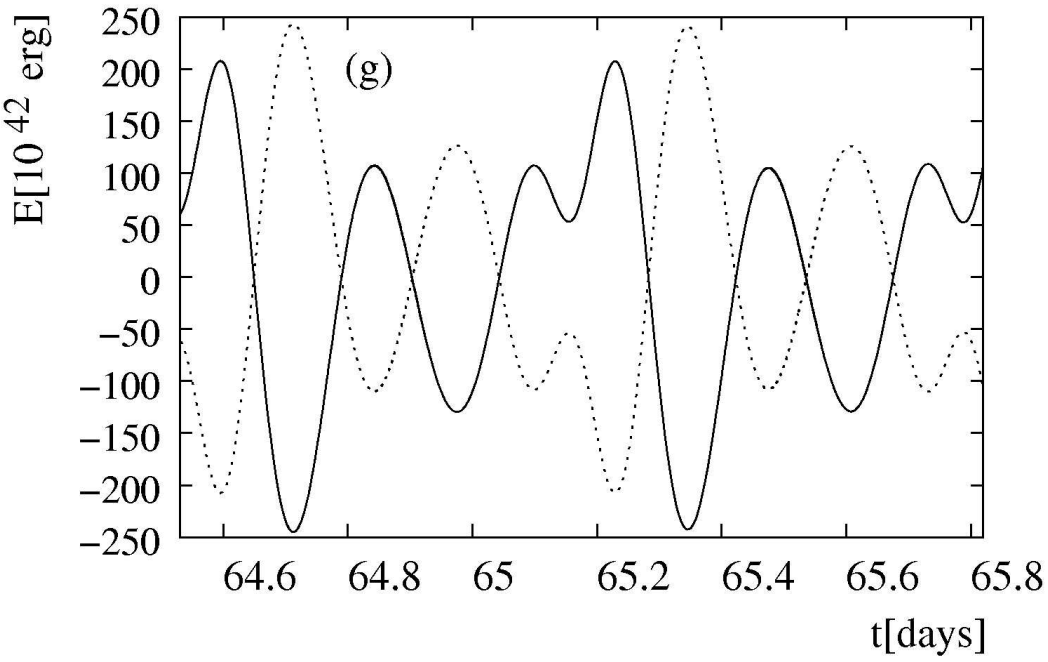

Figure 2. The thermal energy (solid line) and the gravitational potential energy (dotted line) of the stellar envelope (initial hydrostatic values are subtracted) as a function of time for the same unstable stellar model as in Figure 1 (from Figure 1 of Grott et al. (2005)).

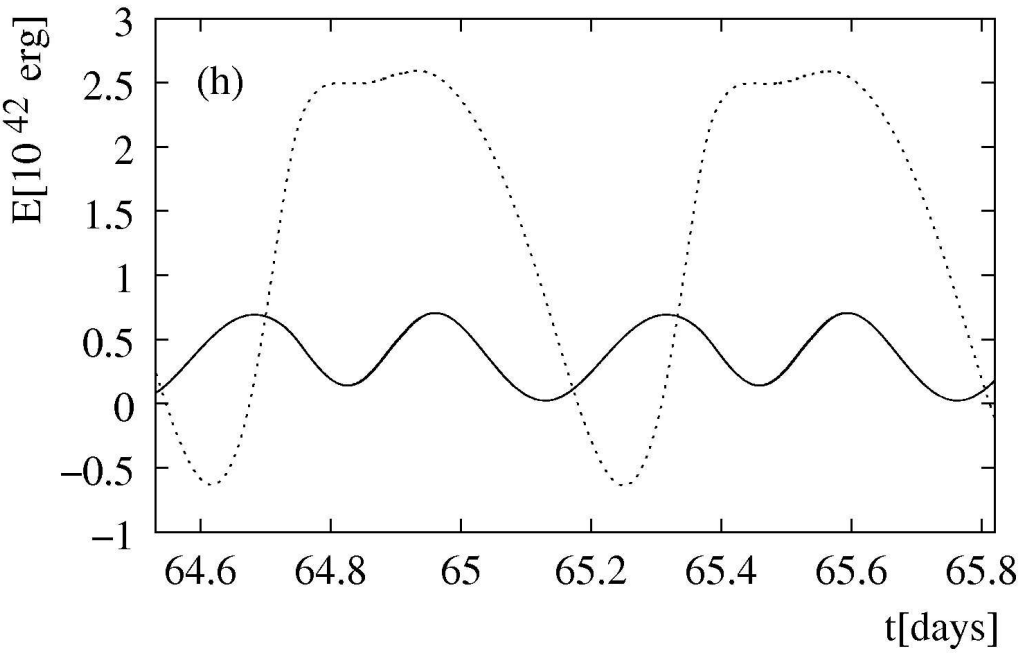

Figure 3. The kinetic energy of the stellar envelope (solid line) and the time integral of the difference between top and bottom boundary of the envelope of the thermal luminosity (dotted line) as a function of time for the same unstable stellar model as in Figure 1 (from Figure 1 of Grott et al. (2005)).

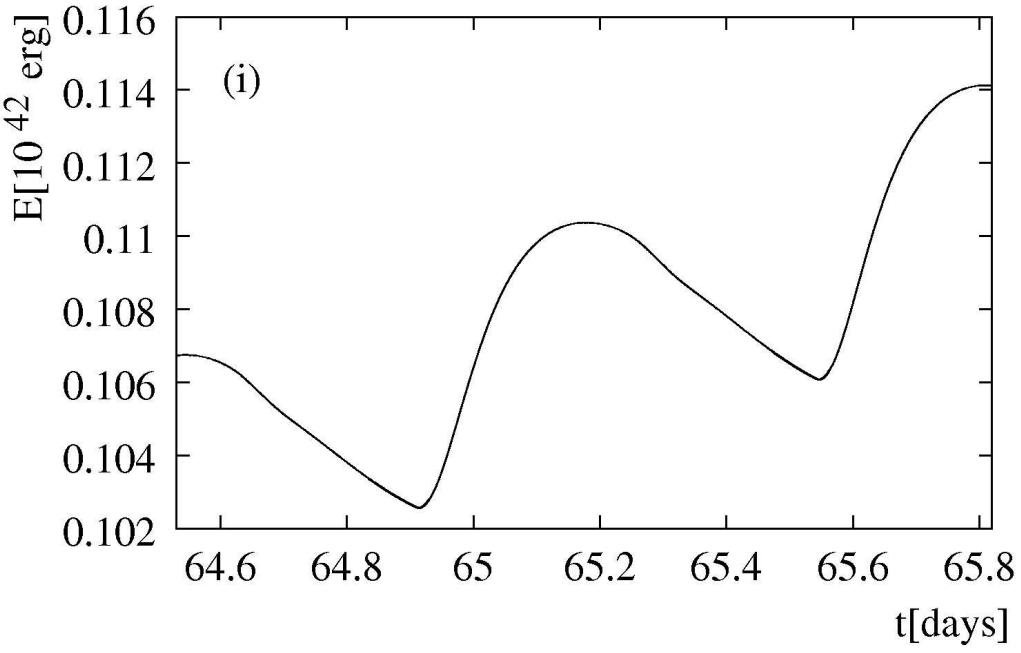

Figure 4. The time integral of the difference between top and bottom boundary of the envelope of the acoustic luminosity as a function of time for the same unstable stellar model as in Figure 1 (from Figure 1 of Grott et al. (2005)).

From Figures 2, 3 and 4 we deduce that the thermal and gravitational potential energies exceed the other terms by more than two orders of magnitude their sum being of the order of the kinetic energy and the time integral of the thermal luminosity which exceed the time integral of the acoustic luminosity by one order of magnitude. I.e., the terms in the energy balance 29 in general differ by up to four orders of magnitude. Therefore a meaningful determination of the kinetic energy (and thus also of the amplitude of the velocity) and the acoustic luminosity requires a relative accuracy of at least 10^{-5} which can never be achieved by grid refinement or increased time resolution in standard numerical schemes. A solution of the problem consists of adopting a fully conservative numerical scheme (see, e.g., Fraley (1968) and Grott et al. (2005)) which satisfies the energy balance intrinsically for each mass element. Necessary for full conservativity is that the difference operators have the same properties and satisfy the same relations as their differential counterparts. Some aspects of the explicit construction of a fully conservative scheme for the simulation of radial stellar pulsations will be discussed in section 2.3.

According to equation 29 the sum of all energy terms shown in Figures 2, 3 and 4 should vanish, if the energy balance is satisfied. In other words, this sum obtained from the results of a simulation corresponds to its error in the energy balance. It is given in Figure 5 as a function of time for the simulation of the unstable model considered above and found to be smaller by five orders of magnitude than the time integral of the acoustic luminosity being the smallest term in the energy balance 29. We conclude that all energies, in particular the kinetic energy and the time integral of the acoustic luminosity, are determined with sufficient accuracy to allow for meaningful statements concerning velocity amplitudes and acoustic energy fluxes of the final finite amplitude pulsations. Any simulation of stellar pulsations should be required to prove its quality by presenting the energy balance and its error. We emphasize that the extreme accuracy requirements can only be satisfied by fully conservative schemes.

Concerning pulsationally driven mass loss as a possible final result of a stellar instability the time integral of the acoustic luminosity (see Figure 4) is of particular interest. In each pulsation cycle phases of incoming and outgoing acoustic energy fluxes prevail, i.e., the time integral of the acoustic luminosity is not a monotone function. However, if the outgoing fluxes exceed the incoming fluxes, the average over one pulsation period of the time integral of the acoustic luminosity will increase with time. We deduce from Figure 4 that this holds for the final finite amplitude pulsations of the model discussed above. A consequence of the increase with time of the mean of the time integral of the acoustic luminosity is a mean acoustic luminosity driven by the pulsations, which can be derived from the simulations as the mean slope of the curve shown in Figure 4. Should this mean acoustic (mechanical) luminosity ultimately drive a stellar wind, its mass loss rate may be estimated by requiring the acoustic luminosity to be comparable with the kinetic energy per time lost in the wind.

2.3. Basic Properties of Fully Conservative Schemes

The derivation of the energy balance 28 for a mass element implies the multiplication of equation 25 (momentum conservation) with the velocity $v = \frac{\partial r}{\partial t}$ together with the following subsequent transformations of the time derivatives:

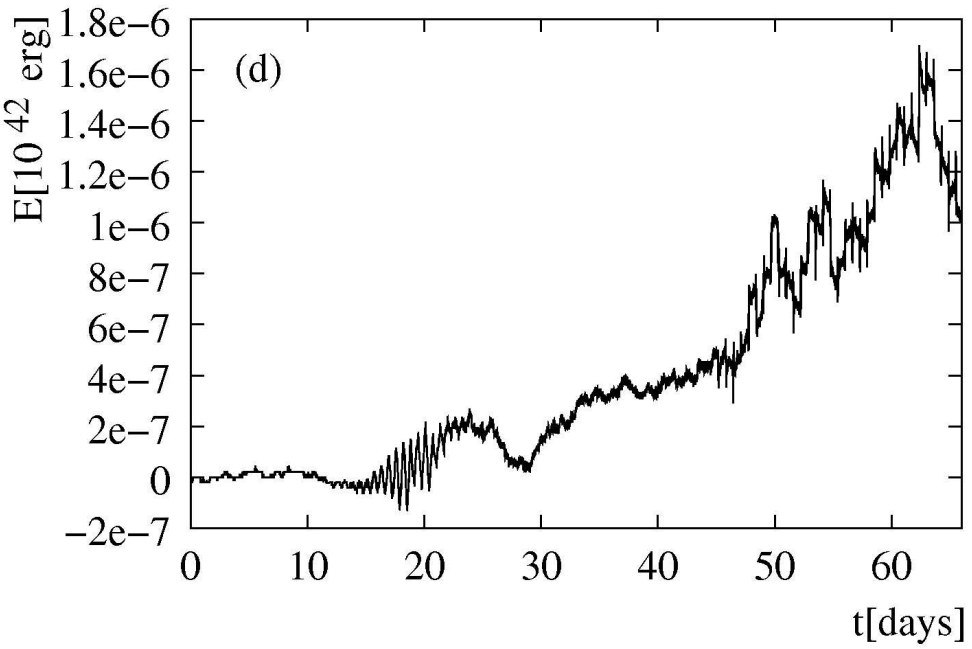

Figure 5. The sum of all energies (thermal, gravitational potential, kinetic, time integrated thermal luminosity, time integrated acoustic luminosity) presented in Figures 2, 3 and 4 as a function of time (from Figure 1 of Grott et al. (2005)). According to equation 29 it corresponds to the numerical error in the energy balance.

$$v \cdot \frac{\partial v}{\partial t} = \frac{\partial}{\partial t}\left(\frac{1}{2}v^2\right) \tag{31}$$

$$v \cdot \left(-\frac{GM_r}{r^2}\right) = \frac{\partial r}{\partial t} \cdot \left(-\frac{GM_r}{r^2}\right) = \frac{\partial}{\partial t}\left(\frac{GM_r}{r}\right) \tag{32}$$

Without the differential relations 31 and 32 the energy balance 28 would not hold. As a consequence, these relations must hold also for the difference analoga of the differential operators, if we require the energy balance to hold for the numerical solution of equations 22, 24, 25, 26 and 27. In other words, the numerical scheme has to be designed such that it satisfies equations 31 and 32 intrinsically.

For a numerical treatment the derivative with respect to time of a quantity Q may be represented by the difference scheme

$$\frac{\partial Q}{\partial t} \to \frac{\hat{Q} - Q}{\tau} \tag{33}$$

where $Q = Q(t)$ denotes the value of Q at time t and $\hat{Q} = Q(t+\tau)$ its value at time $t + \tau$. We introduce time averages $Q^{(\alpha)}$ by

$$Q^{(\alpha)} = \alpha\hat{Q} + (1-\alpha)Q \tag{34}$$

with $0 \leq \alpha \leq 1$. Thus we obtain for the difference analogon of equation 31

$$v^{(?)} \cdot \frac{\hat{v} - v}{\tau} \leftarrow v \cdot \frac{\partial v}{\partial t} = \frac{\partial}{\partial t}\left(\frac{1}{2}v^2\right) \to \frac{1}{2}\frac{\hat{v}^2 - v^2}{\tau} \tag{35}$$

If the relation 31 is required to hold also for the difference scheme we deduce $v^{(?)} = v^{(1/2)}$ from equation 35. As a consequence the difference analogon of equation 24 is given by

$$\frac{\hat{r} - r}{\tau} = v^{(1/2)} \tag{36}$$

Similarly we obtain for the difference analogon of equation 32

$$\frac{\hat{r} - r}{\tau}\left(-\frac{GM_r}{{r^{(?)}}^2}\right) \leftarrow \frac{\partial r}{\partial t} \cdot \left(-\frac{GM_r}{r^2}\right) = \frac{\partial}{\partial t}\left(\frac{GM_r}{r}\right) \to \frac{1}{\tau}\left(\frac{GM_r}{\hat{r}} - \frac{GM_r}{r}\right) \tag{37}$$

If the relation 32 is required to hold also for the difference scheme we deduce $\frac{1}{{r^{(?)}}^2} = \frac{1}{\hat{r}r}$ from equation 37.

Thus we have shown that the numerical representation of the velocity and the gravitational force cannot be chosen arbitrarily, if the energy balance is required to hold intrinsically for each mass element, i.e., if the numerical scheme has to be strictly conservative. Rather the time averages of the velocity and the gravitational force are determined by the condition of full conservativity:

$$v \to v^{(1/2)} \qquad , \qquad -\frac{GM_r}{r^2} \to -\frac{GM_r}{\hat{r}r} \tag{38}$$

An immediate consequence of the time averages 38 required by conservativity is that the numerical scheme is necessarily implicit with respect to time, i.e., at each time step a system of implicit algebraic equations has to be solved. Concerning the construction of strictly conservative numerical schemes for the simulation of nonlinear nonradial stellar pulsations we refer to Glatzel & Chernigovski (2016).

Acknowledgments. I would like to thank the organisers of the VIII LAPIS summer school for the perfect performance and the warm hospitality at La Plata.

References

Baker N., Kippenhahn R., 1965, *ApJ*, **142**, 868
Davey A., 1977, *Journal of Computational Physics*, **24**, 331
Dorfi E., Drury L., 1987, *Journal of Computational Physics*, **69**, 175
Dorfi E. A., Feuchtinger M. U., 1991, *A&A*, **249**, 417
Fraley G. S., 1968, *Ap&SS*, **2**, 96
Gautschy A., Glatzel W., 1990, *MNRAS*, **245**, 154
Glatzel W., Chernigovski S., 2016, *MNRAS*, **457**, 1190
Grott M., Chernigovski S., Glatzel W., 2005, *MNRAS*, **360**, 1532
Noh W., 1987, *Journal of Computational Physics*, **72**, 78
Scott M. R., 1973, *Journal of Computational Physics*, **12**, 334
Sloan D., 1977, *Journal of Computational Physics*, **24**, 320

Observational and Analysis Techniques

Pulsations Along Stellar Evolution
VIII LAPIS Summer School
AAA Workshop Series 12, 2021
M. Kraus & A.F. Torres, eds.

Analysis Techniques: the Lomb-Scargle Periodogram

D. D. Carpintero[1],[2]

[1]*Facultad de Ciencias Astronómicas y Geofísicas, Universidad Nacional de La Plata, Paseo del Bosque s/n 1900 La Plata, Argentina*
[2]*Instituto de Astrofísica de La Plata, UNLP-Conicet, Paseo del Bosque s/n 1900 La Plata, Argentina*

Abstract. Fourier's traditional signal analysis does not work when observations are not equispaced in time, as is usually the case in Astronomy. The Lomb Scargle periodogram is the favorite substitute. We will study the basics of this technique and some care that needs to be taken for its practical application and its interpretation.

Key words: asteroseismology — instabilities — stars: oscillations — stars: interiors — planet-star interactions

1. A Short Introduction

0. The structure of this class follows broadly that of the excellent article by VanderPlas (2018). Most examples are taken from that paper, though all the figures were rebuilt by the author.

1. There are many ways to get data in Astronomy. Let's list a few main ones:

Binned observations: this mode is used, for example, when recording the arrival of cosmic rays that produce Cherenkov radiation inside water-filled tanks, thus effectively binning the events into the volumes of the array of tanks.

Time-tag observations: data obtained, for example, when recording the arrival times of individual photons reflected from laser pulses which were sent to the Moon.

Time-to-spill observations: used, for example, when recording the time required for a fixed number of gamma rays to accumulate.

Point observations: this is the typical mode of optical astronomy, where stellar brightnesses are measured only at certain moments.

2. We will focus on point observations. To determine if there is any periodic signal in our observation, different techniques are available:

Fourier methods: they include the standard Fourier transform, the classical or Schuster periodogram, the Lomb-Scargle periodogram, various correlation functions, and wavelets.

Phase-folding methods: some trial periods are assumed, and the observations are folded in such a way that they fall in one cycle of those periods. If the period is correct, the resulting points will be almost aligned, except for observational errors. The string length method determines the best period by computing

the length of the path that joins neighboring points, and choosing the shortest. Analysis of variance is based on how the points get distributed in a histogram. The conditional entropy directly measures the disorder of the points.

Least-squares methods: among them, we will mention the Lomb-Scargle periodogram and the Supersmoother approach, which performs local least-squares fits instead of a global one.

Bayesian methods: they include phase binning, similar to the analysis of variance, and stochastic processes.

In the rest of the class, we will deal mainly with the Lomb-Scargle method, which is a favorite among astronomers. To do so, we first need to talk about the Fourier transform and the classical periodogram. You have probably noticed that the Lomb-Scargle periodogram also appears within the least-squares methods... we will come back to this unique feature later.

2. The Fourier Transform

3. Let's start with the Fourier transform. What are we doing when we do this transform? Let's suppose a space in which the three axes are not x, y and z, but $x^0 = 1$, $x^1 = x$ and x^2. A point in this space (Figure 1, left) will have, say, coordinates a_0, a_1 and a_2, so the point will be the second-degree polynomial $a_0x^0 + a_1x^1 + a_2x^2$. Any other point in this space represents another of these polynomials. The entire space is, therefore, the complete set of second-degree polynomials. We emphasize that this is possible because the different powers of x are linearly independent. For example, we cannot get x^2 by any linear combination of x^0 and x^1.

4. Now, suppose we add more orthogonal axes to our space. In such a case, the resulting space will represent higher-grade polynomials. If we keep adding axes until we have an infinite number of them, we will have an infinite sum of terms, what we know as Taylor's series. Any analytical function $f(x)$ developed as a polynomial gives us its Taylor series:

$$f(x) = a_0x^0 + a_1x^1 + a_2x^2 + \cdots + a_jx^j + \cdots = \sum_{n=0}^{\infty} a_nx^n. \tag{1}$$

The square of each coefficient a_i is the *power* with which the exponent i contributes to the function f. For example, a zero coefficient means that that exponent does not contribute to the function.

5. Now, let's suppose that the axes of our original 3D space are not powers of x but complex exponentials of the variable $-t$ (Figure 1, right): $\mathrm{e}^{-\mathrm{i}\,0\omega t} = 1$, $\mathrm{e}^{-\mathrm{i}\,\omega t}$, $\mathrm{e}^{-\mathrm{i}\,2\omega t}$, labeled by integer multiples of a given frequency ω: 0ω, 1ω, 2ω. We recall that these exponentials are again linearly independent. Let's call $a_{0\omega}$, $a_{1\omega}$ and $a_{2\omega}$ the coordinates of a point in this space. As before, this point defines a function. Changing the notation from $n\omega$ to ω_n, our function will be written like this:

$$f(t) = a_{\omega_0}\mathrm{e}^{-\mathrm{i}\,\omega_0 t} + a_{\omega_1}\mathrm{e}^{-\mathrm{i}\,\omega_1 t} + a_{\omega_2}\mathrm{e}^{-\mathrm{i}\,\omega_2 t} = \sum_{n=0}^{2} a_{\omega_n}\mathrm{e}^{-\mathrm{i}\,\omega_n t}. \tag{2}$$

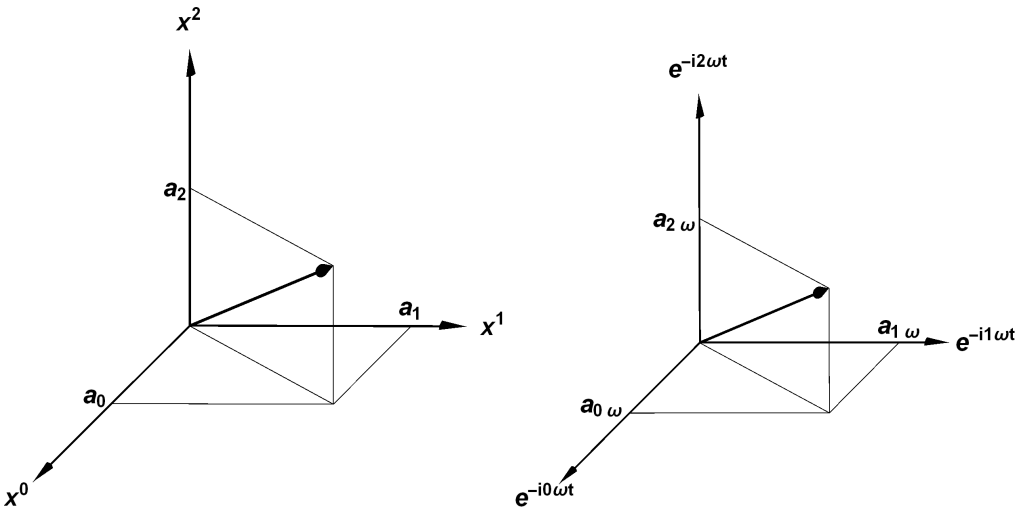

Figure 1. Left: the three-dimensional space of second-degree polynomials. Right: a new three-dimensional space for functions.

6. Let's suppose again that we add infinite orthogonal axes to our space, in this case adding also the negative multiples of the frequency ω. A point in this space will be a function composed of an infinite number of complex exponentials, each corresponding to an integer multiple of a given frequency, i.e. the Fourier series of a function f:

$$\begin{aligned} f(t) &= \cdots + a_{\omega_{-1}} \mathrm{e}^{-\mathrm{i}\omega_{-1}t} + a_{\omega_0} \mathrm{e}^{-\mathrm{i}\omega_0 t} + a_{\omega_1} \mathrm{e}^{-\mathrm{i}\omega_1 t} + \dots \\ &= \sum_{n=-\infty}^{\infty} a_{\omega_n} \mathrm{e}^{-\mathrm{i}\omega_n t} \\ &= \frac{1}{\sqrt{2\pi}} \sum_{n=-\infty}^{\infty} g_{\omega_n} \mathrm{e}^{-\mathrm{i}\omega_n t}, \end{aligned} \tag{3}$$

where in the last line we have redefined the coefficients $a \equiv g/\sqrt{2\pi}$ for future convenience. As before, the square of each coefficient $|g_{\omega_n}|^2$ is the power with which each frequency ω_n contributes to the function f. Note that the coefficients are now complex numbers, so the square means the square of their moduli.

7. We want to move now from discrete to continuous developments. To this end, we take all the real values of the frequency instead of an infinite countable number of them. In this way, the discrete subindexes of g become a continuous variable, the ω_n become the real variable ω, and the summation over ω_n becomes an integral over ω, so we obtain

$$f(t) = \frac{1}{\sqrt{2\pi}} \int_{-\infty}^{\infty} \mathrm{d}\omega \, g(\omega) \, \mathrm{e}^{-\mathrm{i}\omega t}, \tag{4}$$

which is called the *inverse Fourier transform* of the function g.

The amplitude $|g(\omega)|^2$, now a function of ω, is called the *power spectrum* of f. In other words, the function $g(\omega)$ contains all the information about how much power there is in each ω. This is very important: if we could compute g from a given f, we would know how much power a signal with frequency ω is contributing to f.

8. So let's see how to calculate g given a function f. Starting from Eq. (4), the first step is to multiply both members by a complex exponential with a frequency ω', a new variable. Then, we integrate over t, covering all possible times. The next step is to interchange the integrals of the second member; $g(\omega)$ can come out of the integral over t. The inner integral is then one of the definitions of the Dirac delta.

The Dirac delta is a distribution that has the following property, among others: if multiplied by another function and integrated, and if the interval of integration contains the zero of its argument, then the result is the other function evaluated at the point where the Dirac delta is zero. After doing this integral, the variable ω has gone, so we may eliminate the prime. Then we obtain

$$g(\omega) = \frac{1}{\sqrt{2\pi}} \int_{-\infty}^{\infty} \mathrm{d}t \, f(t) \, \mathrm{e}^{\,\mathrm{i}\,\omega t}, \tag{5}$$

that is, we have solved for our function g, which is the *Fourier transform* of the function f. Sometimes it is convenient to express the transform as an operation on f giving g as the result. In this case, the transform is seen as a functional, that is, as an operator on a function, and the notation is usually $g(\omega) = \mathcal{F}[f]$. An operator notation can be used for the inverse too: $f(t) = \mathcal{F}^{-1}[g]$.

9. Some interesting properties of the Fourier transform are:

Time scaling: $\mathcal{F}[f(at)] = \frac{1}{|a|}\, g\big(\frac{\omega}{a}\big)$.

Frequency scaling: $\mathcal{F}^{-1}[g(b\omega)] = \frac{1}{|b|}\, f\big(\frac{t}{b}\big)$.

Time shifting: $\mathcal{F}[f(t - t_0)] = g(\omega)\, \mathrm{e}^{\,\mathrm{i}\,\omega t_0}$.

Frequency shifting: $\mathcal{F}^{-1}[g(\omega - \omega_0)] = f(t)\, \mathrm{e}^{-\,\mathrm{i}\,\omega_0 t}$.

If $f(t) \in \mathbb{R} \implies g(-\omega) = g(\omega)^* \implies |g(-\omega)|^2 = |g(\omega)|^2$, i.e. the power spectrum is even. Physical data are always real, so their power spectrum is always even. If, in addition, $f(t)$ is even, then $g(\omega)$ is real and even too.

10. Recapitulating, the power spectrum is a positive real-valued function that quantifies the contribution of each frequency ω to the total signal. Let's see some examples (see Figure 2). All these examples are real even functions, so we may plot only the real parts of the Fourier transforms.

Suppose that we have a sinusoidal signal, with a period T and frequency ω. Its Fourier transform will be a pair of Dirac deltas, at frequencies ω and $-\omega$. That is, the only frequency contributing to our signal is ω.

Now, let our signal be a Gaussian, with dispersion σ. Its Fourier transform will be another Gaussian, but with a dispersion which is inversely proportional to the original one. This is a characteristic of the Fourier transform: the wider a feature in the original signal, the narrower the corresponding feature in the space of frequencies, and vice versa.

Now let our signal be a top hat function, that is, a constant signal only in a given time interval. On, off. The Fourier transform is a sinc function,

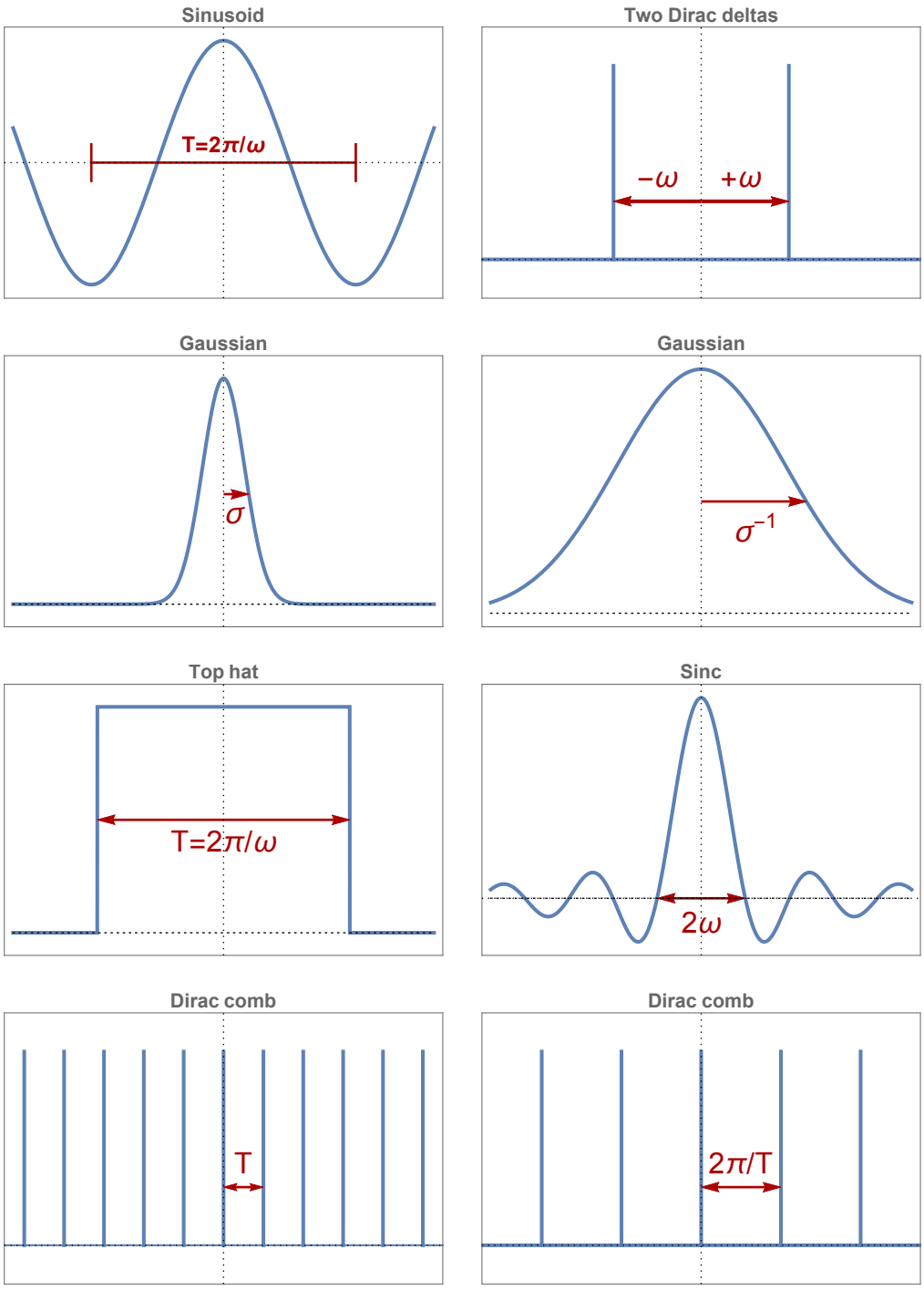

Figure 2. Left: different signals. Right: their Fourier transforms.

i.e. $\sin(\pi x)/(\pi x)$, with a width again inversely proportional to the width of the original signal.

If our signal is a Dirac comb, that is an infinite series of Dirac deltas evenly spaced in time representing a periodic instantaneous signal, then the Fourier transform is another Dirac comb, but with spacing in frequency inversely proportional to the time interval of the signal.

11. An important operation that we are going to use is convolution. The convolution $f * g$ between two functions f and g is defined as the integral over time of the product of the two functions, but with one of them delayed in time:

$$(f * g)(t) \equiv \int_{-\infty}^{\infty} \mathrm{d}t'\, f(t')\, g(t - t'). \tag{6}$$

This is equivalent to sliding one of the functions over the other and calculating the integral at each step.

There is a convolution theorem that establishes that the Fourier transform of a convolution is equivalent to the point-to-point product of the Fourier transforms of each function:

$$\mathcal{F}[f * g] = \mathcal{F}[f] \cdot \mathcal{F}[g]. \tag{7}$$

A corollary of this theorem is that the Fourier transform of a product of functions is equivalent to the convolution of the Fourier transforms of each function:

$$\mathcal{F}[f \cdot g] = \mathcal{F}[f] * \mathcal{F}[g]. \tag{8}$$

12. Now, when we observe a signal, we never observe the true signal. We are not talking about errors, but about the *observing window*. For example, if we observe the magnitude of a star, we are imposing both a top hat between our first and last observations and a discretization because we do not observe continuously. So, our observed signal will always be affected by a window function W. Then, when we compute the transform of an observed signal, a convolution with the transform of the window will always be present.

13. Let's see an example of this (Figure 3). Let's take a signal made up of four sines, with different amplitudes and frequencies. If we observe this signal continuously between two moments of time, that is, with a top-hat observing window, the resulting observed signal will be the point product of the two functions.

What happens in the frequency world? The transformed signal is, as expected, a set of peaks at the four frequencies that make up the signal. The transformed window will be, as we already know, a sinc function. We have to convolve both transforms to obtain the Fourier transform of the observed signal. As we can see in Figure 3, the form and width of the sinc function is replicated at each of the peaks of the original transform.

14. Let's see another example (Figure 4). Our original signal is now a simple Gaussian, but observed only in a set of moments uniformly spaced in time. Thus, our observed data is a series of Dirac deltas with amplitudes modulated by the Gaussian. The frequency content of the original signal will be a Gaussian, and that of the window will be a Dirac comb. When they are convolved they yield our Gaussian replicated on each of the peaks of the comb.

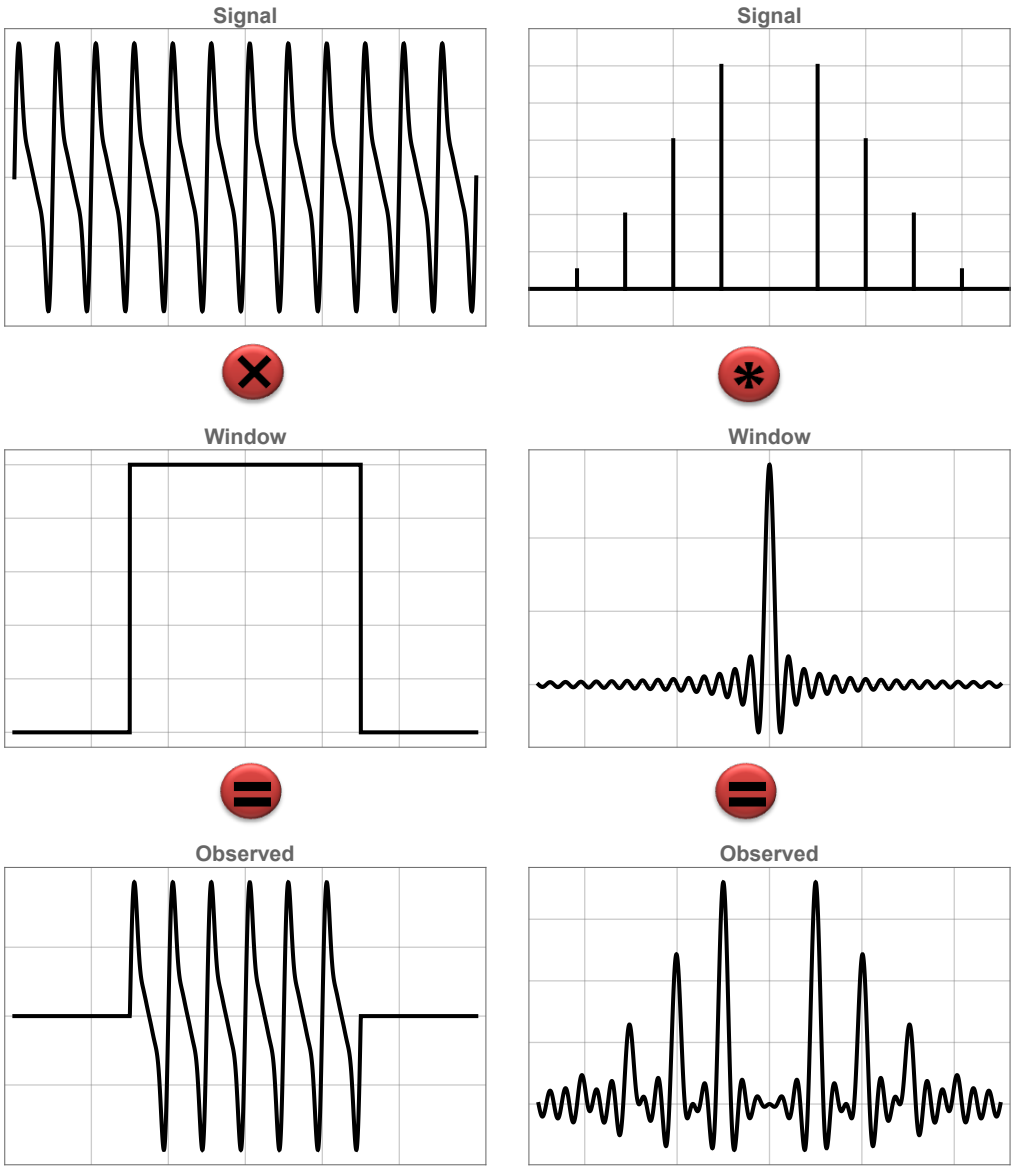

Figure 3. Left: a signal, a window and their point-to-point product. Right: their respective Fourier transforms.

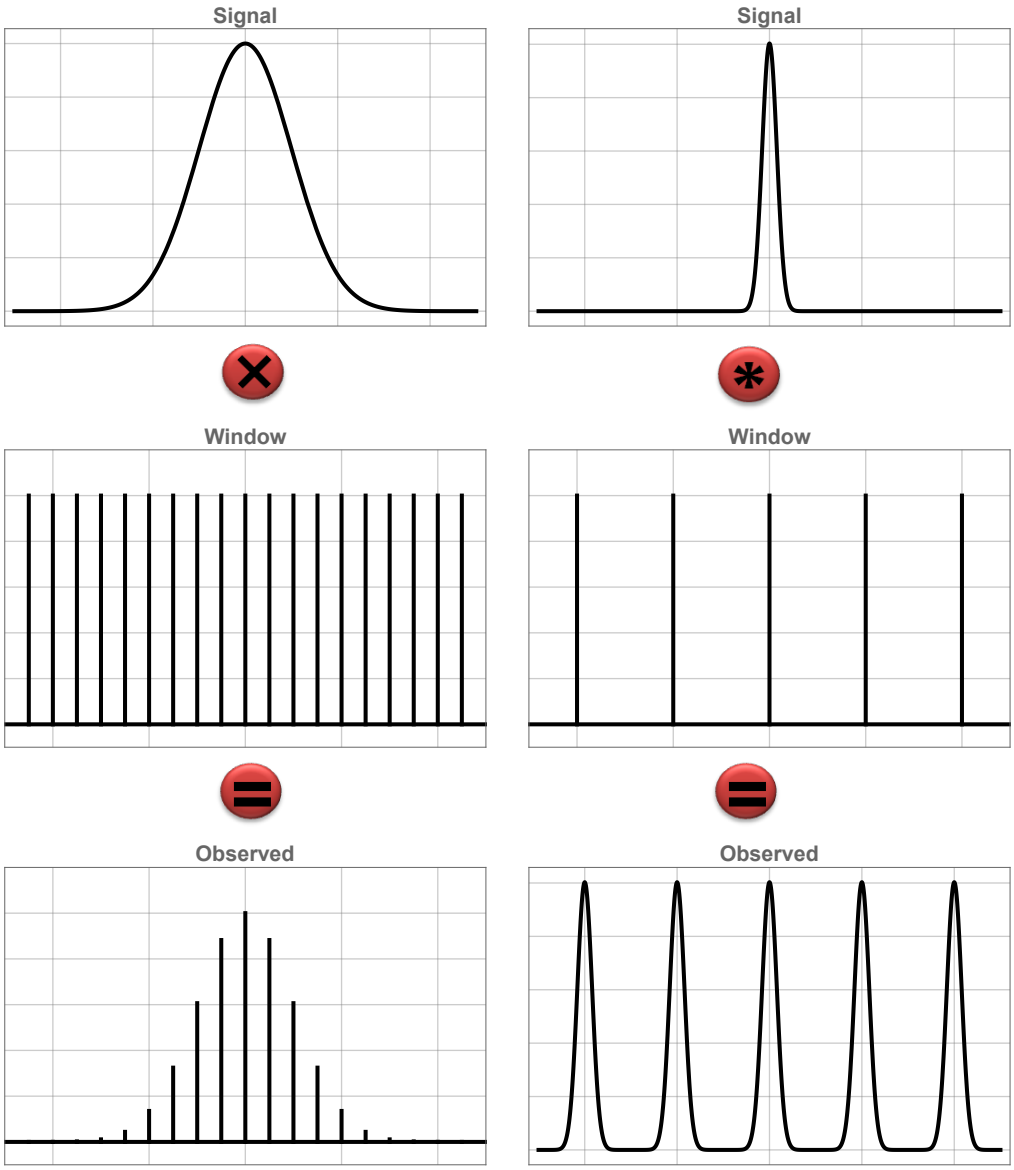

Figure 4. Left: another signal, another window and their point-to-point product. Right: their respective Fourier transforms.

15. The last example leads us to one of the problems of all this. Let's see. Let's take again the last Gaussian as the original signal. Now, we observe again the signal with a Dirac comb, but with a lower frequency than before (Figure 5). Therefore, we are observing now a few peaks. On the spectra side, we have our usual spectrum for the real signal, and a Dirac comb for the spectrum of the window, though with teeth closer to each other. Note in the resulting convolved spectrum how the Gaussians have no place to fit between the teeth of the comb. We can lose all hope of recovering the real spectrum.

16. This brings us to the *Nyquist limit*. Recapitulating: a function uniformly sampled in time can be fully recovered only if its Fourier transform can fit entirely between the teeth of the comb. Therefore, let's suppose we sample our signal at time intervals T. The sampling rate, let's call it ω_0, is then $2\pi/T$. To recover the signal, it should be made up only of frequencies in between $\pm\omega_0/2$ to fit between the teeth.

The traditional Nyquist theorem goes in the other direction: to fully represent the frequency content of a band-limited signal $\pm\omega_0$, we must sample the data with a rate of at least $2\omega_0$, called the Nyquist frequency.

17. Now, our last step towards the periodogram is to consider the discrete Fourier transform. Let's take an infinitely long and continuous signal $f(t)$, and let's sample it with a Dirac comb with spacing Δt. The observed signal will be the point-to-point product of both:

$$f_{\rm obs}(t) = f(t) \cdot \mathrm{III}_{\Delta t}(t), \tag{9}$$

where $\mathrm{III}_{\Delta t}$ symbolizes a Dirac comb with spacing Δt. Note that the signal is known only at the times $n\Delta t$, with n an integer. If we compute its Fourier transform, we obtain

$$\mathcal{F}[f_{\rm obs}](\omega) = \frac{1}{\sqrt{2\pi}} \sum_{n=-\infty}^{\infty} f_n \, \mathrm{e}^{\,\mathrm{i}\,\omega\, n\Delta t}, \tag{10}$$

where we have used $f_n \equiv f(n\Delta t)$ to simplify the notation.

However, in a real observation, we do not take an infinite number of samples, but a finite number of them. This is equivalent to applying a top-hat rectangular window of width $N\Delta t$ where $N+1$ is the total number of samples, so if we choose arbitrarily $t = 0$ at the first observation, the summation goes only from 0 to N:

$$\mathcal{F}[f_{\rm obs}](\omega) = \frac{1}{\sqrt{2\pi}} \sum_{n=0}^{N} f_n \, \mathrm{e}^{\,\mathrm{i}\,\omega\, n\Delta t}. \tag{11}$$

18. Note that, by construction, the last expression is the Fourier transform of the original signal sampled with a Dirac comb and convolved with a sinc function of width $4\pi/T = 4\pi/(N\Delta t)$ (because we have applied a top-hat window of width $N\Delta t$). Then the spectral Dirac comb will be smeared with this width. Now, according to the Nyquist theorem, two values of the spectrum at frequencies within $2\pi/(N\Delta t)$ will not be independent, but they will belong to more than

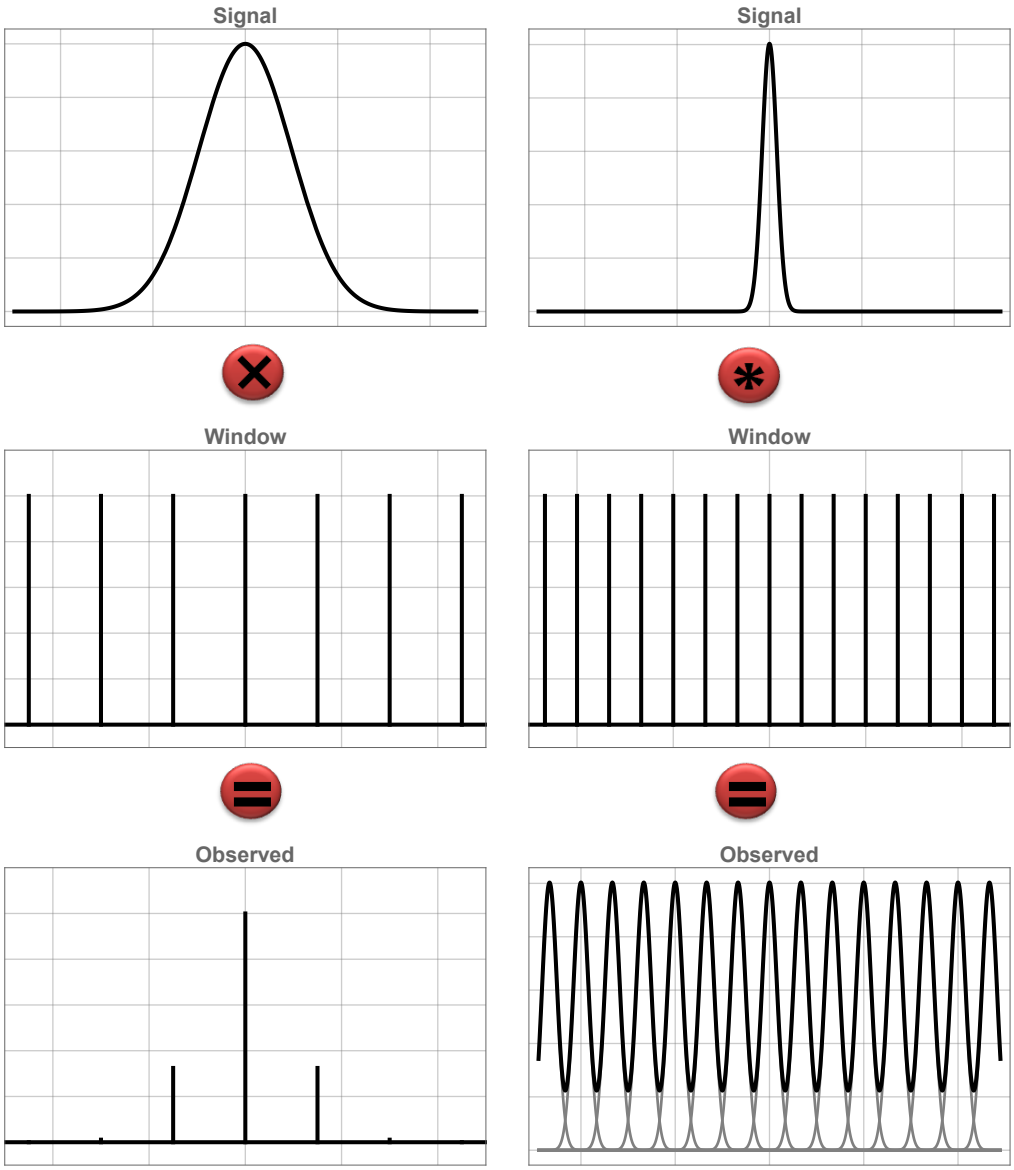

Figure 5. Left: same signal but another window, and their point-to-point product. Right: their respective Fourier transforms. The gray lines are the individual peaks generated by each tooth of the Dirac comb.

one peak. Then, to get the maximum information we should sample the spectrum at N evenly spaced frequencies with a separation

$$\Delta\omega = \frac{2\pi}{N\Delta t}. \tag{12}$$

If we call $k\Delta\omega$ the resulting frequencies, we get

$$\mathcal{F}[f_{\rm obs}](k\Delta\omega) = \frac{1}{\sqrt{2\pi}} \sum_{n=0}^{N} f_n \, \mathrm{e}^{\,\mathrm{i}\, k\Delta\omega\, n\Delta t}. \tag{13}$$

Defining for convenience

$$\hat{f}_k \equiv \sqrt{\frac{N}{2\pi}}\, \mathcal{F}[f_{\rm obs}](k\Delta\omega), \tag{14}$$

we finally get

$$\hat{f}_k = \frac{1}{\sqrt{N}} \sum_{n=0}^{N} f_n \, \mathrm{e}^{2\pi\,\mathrm{i}\, kn/N}, \tag{15}$$

which you will recognize as the discrete Fourier transform of the set f_n. Note that the spacing of the frequencies is optimal in terms of both the Nyquist sampling and the effect of the finite observing window.

3. The Periodogram

19. We are now in a position to study the periodogram. The classical periodogram was defined by Schuster (1898) as

$$P_{\rm S}(\omega) = \frac{1}{N} \left| \sum_{n=1}^{N} f_n \, \mathrm{e}^{\,\mathrm{i}\, \omega\, n\Delta t} \right|^2 . \tag{16}$$

If you look closely, you will find that it is the square of the modulus of the discrete Fourier transform of the set f_n, but evaluated at any real frequency.

What is the maximum frequency at which we should evaluate this function? Naturally, at the Nyquist frequency, since beyond that there is no new information. The spectrum begins to repeat itself, a feature called aliasing.

20. Now, we have to deal with a very important problem, always present in Astronomy: non-uniform sampling. In practice, we do not sample a signal at a periodic rate, but at a set of times t_n unevenly distributed:

$$W_{\{t_n\}}(t) = \sum_{n=1}^{N} \delta_{\rm D}(t - t_n), \tag{17}$$

where $\delta_{\rm D}$ is the Dirac delta. The observed signal is then a product of the true signal by this window, resulting in an uneven distribution of values of the function:

$$f_{\rm obs}(t) = f(t) \cdot W_{\{t_n\}}(t) = \sum_{n=1}^{N} f(t_n)\delta_{\rm D}(t - t_n), \tag{18}$$

and the Fourier transform of the observed set will be the convolution of the real signal with this irregular window:

$$\mathcal{F}[f_{\rm obs}] = \mathcal{F}[f] * \mathcal{F}[W_{\{t_n\}}]. \tag{19}$$

21. Let's see what happens. Let's take a Gaussian as a model of our signal. Figure 6 (left) shows the original signal, an irregular window, and their product which is the observed function. On the spectral side (Figure 6, right), see what happens with the spectrum of the window: it has lost all regularity. It is no longer a Dirac comb, but a completely irregular function. The convolution results in the ugly Fourier transform at the bottom. Note that the original Gaussian is almost lost.

We conclude that an irregular spacing of the observations leads to an irregular spacing of frequency peaks in the window transform, and that there is no exact aliasing of the true signal, so we cannot recover the true Fourier transform.

22. A question immediately arises: what is now the Nyquist frequency? The question is relevant because the uneven sampling has destroyed the symmetry on which the concept of Nyquist frequency rested. There are in the literature several attempts to define a substitute for the Nyquist frequency: the inverse of the mean of the sampling interval, their harmonic mean, their median, or even the minimum among them. It turns out that *none* of these approaches is correct. The practical pseudo-Nyquist frequency can be far larger than any of these.

23. Let's see an example. We analize 100 samples taken at random times between 0 and 1200 of the signal

$$f(t) = 10 + 7.5\sin(100t) + 13\,\%\text{ white noise.} \tag{20}$$

Note that the only frequency present in our signal is $\omega = 100$. Figure 7 (left) shows the resulting observed signal. Note that a frequency of 100 corresponds to a period of $2\pi/100$, something that is not (and cannot be) visible at all in the plot.

24. Figure 7 (right) shows the periodogram of this set, in an interval of frequencies that includes 100. Surprisingly, the periodogram recovers the true frequency even when the signal is invisible to the eye! But see also the proposed pseudo-Nyquist frequencies. With none of them we could have recovered the true result. Note that we have extended the periodogram beyond 100 because we knew that that was the target frequency. But in practice, this is precisely the unknown. How far do we have to extend the periodogram, that is, what is an effective pseudo-Nyquist frequency?

25. Eyer & Bartholdi (1999) have proved this theorem: the equivalent Nyquist frequency is π/p, where p is the largest factor such that each spacing Δt_i is exactly an integer multiple of this factor. In other words, p is such that we can put each observing time in a multiple of it. But a corollary is that if any pair of observation spacings has an irrational ratio, then the pseudo-Nyquist frequency is infinity! Fortunately, the observations always have a finite precision, so the limit frequency in practice can be computed as $\omega_{\rm Ny} = \pi 10^D$, where D is the number of decimal places of the observations.

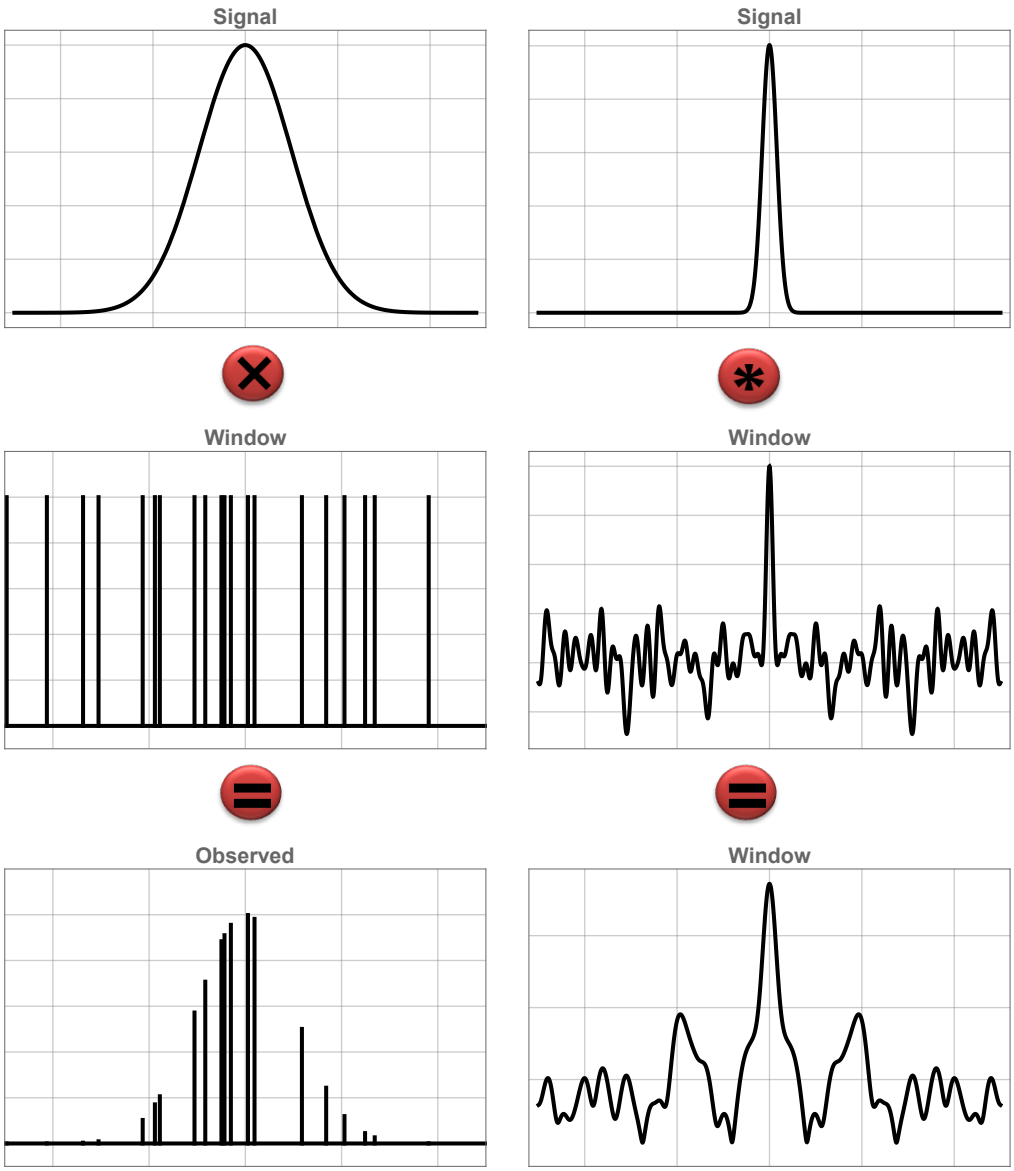

Figure 6. Left: a Gaussian signal, an irregular observing window, and their point-to-point product. Right: their respective Fourier transforms.

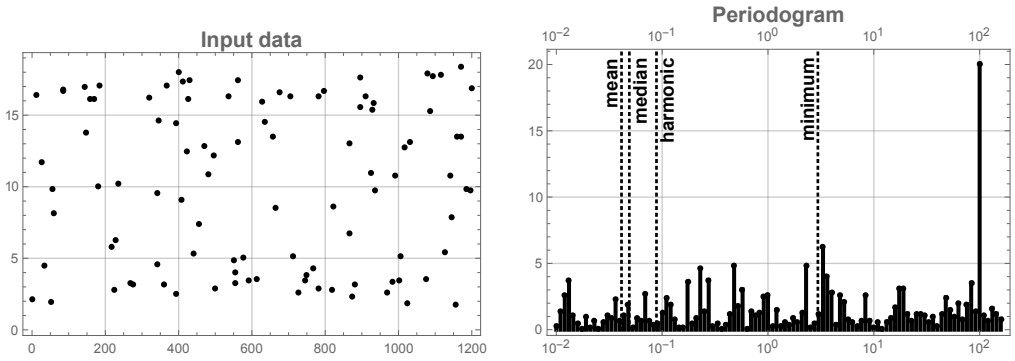

Figure 7. Left: an irregular sampling of a sinusoidal signal plus noise. Right: its periodogram, with some pseudo-Nyquist frequencies shown.

26. We finally got to the Lomb-Scargle periodogram. The classical periodogram can be rewritten

$$P_{\rm S}(\omega) = \frac{1}{N}\left[\left(\sum_{n=1}^{N} f_n\,\cos(\omega\,t_n)\right)^2 + \left(\sum_{n=1}^{N} f_n\,\sin(\omega\,t_n)\right)^2\right], \qquad (21)$$

where we have separated the exponentials in sines and cosines. This classical periodogram has nice statistical properties. For example, if the signal is pure Gaussian noise and it is uniformly sampled, then its values are χ^2 distributed. Therefore, when a signal is present it is easily detectable because the distribution of values of the periodogram will not be χ^2 distributed. The problem is: *when the sampling is irregular, this property is completely lost.*

27. Scargle (1982) was the one who solved this problem. He assumed a generalization of the periodogram,

$$P_{\rm L}(\omega) = \frac{\left(\sum_{n=1}^{N} f_n\,\cos(\omega\,[t_n-\tau])\right)^2}{2A^2} + \frac{\left(\sum_{n=1}^{N} f_n\,\sin(\omega\,[t_n-\tau])\right)^2}{2B^2}, \qquad (22)$$

with A, B and τ functions of ω. He proved that the three functions can be chosen so that a) the periodogram reduces to the classical one when the observations are equally-spaced in time; b) the periodogram's statistics are computable; and c) it is insensitive to time-shifts.

28. Here is the expression obtained by Scargle:

$$P_{\rm L}(\omega) = \frac{\left(\sum_{n=1}^{N} f_n\,\cos(\omega\,[t_n-\tau])\right)^2}{2\sum_{n=1}^{N}\cos^2(\omega\,[t_n-\tau])} + \frac{\left(\sum_{n=1}^{N} f_n\,\sin(\omega\,[t_n-\tau])\right)^2}{2\sum_{n=1}^{N}\sin^2(\omega\,[t_n-\tau])}, \qquad (23)$$

with

$$\tau(\omega) = \frac{1}{2\omega} \arctan \left(\frac{\sum_{n=1}^{N} \sin(2\omega t_n)}{\sum_{n=1}^{N} \cos(2\omega t_n)} \right). \tag{24}$$

Note that τ depends only on the times of observation.

29. As we have anticipated, the Lomb-Scargle periodogram has also a least-squares interpretation. Lomb (1976) showed that this periodogram is obtained if we fit a model to our data consisting of a sinusoid at each candidate ω:

$$y(t, \omega) = A_\omega \sin(\omega t - \varphi_\omega). \tag{25}$$

As usual in the least-squares method, we compute the merit figure χ^2 by summing up all the squares of the differences between the model and the observations:

$$\chi^2(\omega) = \sum_{n=1}^{N} \big(y_n - y(t_n, \omega)\big)^2. \tag{26}$$

If we call $\hat{\chi}^2$ the value obtained by minimizing Eq. (26) at each frequency with respect to the amplitude A_ω and the phase φ_ω, and $\hat{\chi}_0^2$ the dispersion of the observations, then the Lomb-Scargle periodogram can be written thus:

$$P_{\mathrm{L}}(\omega) = \frac{\hat{\chi}_0^2 - \hat{\chi}^2}{2}. \tag{27}$$

30. The least-squares interpretation of the Lomb-Scargle periodogram allows treating measurement errors easily. If each observation y_n carries an error σ_n, then the standard approach of the least-squares method is to add those errors in the denominators of the χ^2 statistic. Therefore, we do the same in our case:

$$\chi^2(\omega) = \sum_{n=1}^{N} \left(\frac{y_n - y(t_n, \omega)}{\sigma_n} \right)^2. \tag{28}$$

After some algebra, the resulting periodogram is the same as the standard Lomb-Scargle periodogram, but every sum of the expression adds a weight w_n computed as usual from the observational errors:

$$w_n = \frac{\sigma_n^{-2}}{\sum_{i=1}^{N} \sigma_i^{-2}}. \tag{29}$$

Thus for example,

$$\sum_{n=1}^{N} f_n \cos(\omega\,[t_n - \tau]) \quad \text{becomes} \quad \sum_{n=1}^{N} w_n f_n \cos(\omega\,[t_n - \tau]). \tag{30}$$

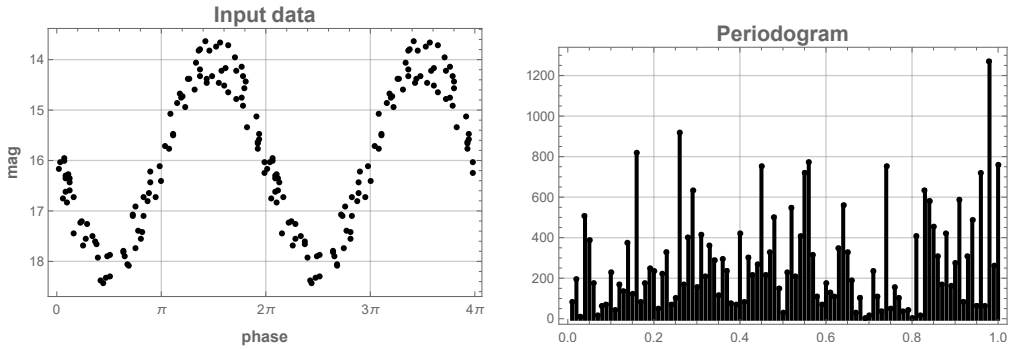

Figure 8. Left: random sampling of a sinusoidal signal plus noise, centered at a value of 16. Right: its periodogram.

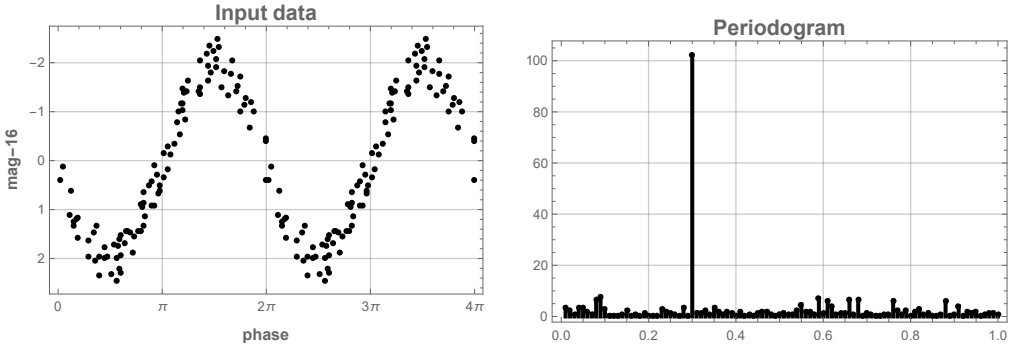

Figure 9. Left: the same random sampling, but now centered around 0. Right: its periodogram.

31. Another important issue relative to periodograms is that of the mean of the observations. Let's work with the signal

$$f(t) = 16 + 2\sin(\omega t) + \text{ white noise}, \tag{31}$$

with $\omega = 2\pi \cdot 0.3$. We generate 100 random observations between 0 and 100 in time, shown in Figure 8 (left) where we have folded all the observations modulo the period. The points were repeated in a second period to better visualize the results. Note that the data are centered around 16; this might be the result of observing the magnitude of some variable star.

The periodogram, in cycles per unit time, is shown in Figure 8, right. We look for a feature at a frequency 0.3, but there is nothing! In fact, there is not even a peak! What is happening here is that the periodogram is fooled by the mean value of the data.

32. Let's center the data around zero (Figure 9). Now it is! A clean, superb, lonely peak at a frequency of 0.3. The moral is: *always center the data before computing a periodogram.*

33. There is another problem to take care of. Let's suppose that we are measuring the magnitude of some variable star, with the same signal as before with

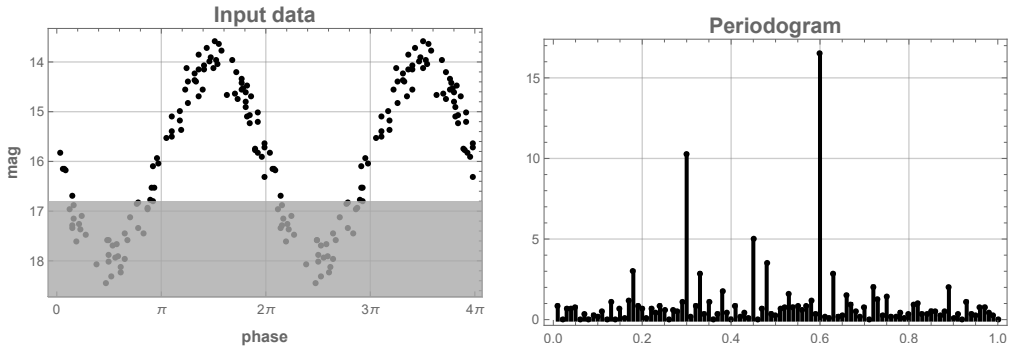

Figure 10. Left: data with an unreachable (gray) band. Right: its periodogram.

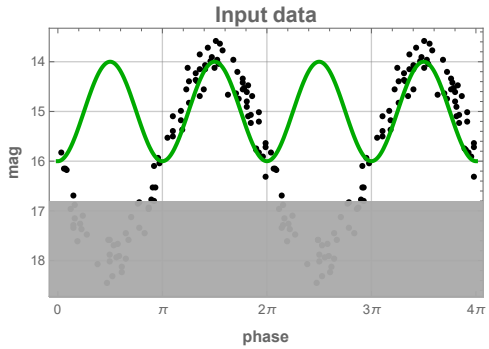

Figure 11. The signal that the periodogram sees (solid green curve).

frequency 0.3, but that our telescope has a limiting magnitude. Figure 10 (left) shows an example; the data is considered unreachable above magnitude 16.8.

Let's compute the periodogram (Figure 10, right). As we can see, it shows that 0.6 is the main frequency, a harmonic of the true one. What happens here is that the periodogram tries to adjust the frequency to the data it has, obtaining the signal shown in Figure 11.

34. The solution is to compute the periodogram with a so-called *floating mean*, also known as date-compensated discrete Fourier transform or generalized Lomb-Scargle periodogram. It consists of adding an offset to each frequency:

$$y(t, \omega) = y_0(\omega) + A_\omega \sin(\omega t - \varphi_\omega). \tag{32}$$

Then, this new problem has the offset $y_0(\omega)$ as a third parameter to be found, along with amplitude and phase. To simplify the notation, we define the following abbreviation:

$$[fc] \equiv \sum_{n=1}^{N} w_n f_n \cos(\omega [t_n - \tau]), \tag{33}$$

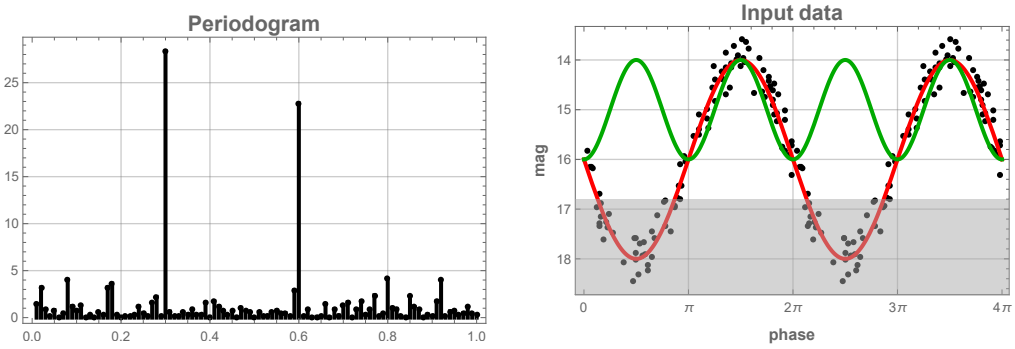

Figure 12. Left: floating mean periodogram. Right: the recovered signal (solid red curve).

and similar expressions for other cases. With this notation, the resulting periodogram with floating mean is

$$P_{\rm LS}(\omega) = \frac{1}{2}\left(\frac{([fc]-[f][c])^2}{[c^2]-[c]^2} + \frac{([fs]-[f][s])^2}{[s^2]-[s]^2}\right), \tag{34}$$

with

$$\tau(\omega) = \frac{1}{2\omega}\arctan\left(\frac{[2sc]-2[s][c]}{[c^2-s^2]-([c]^2-[s]^2)}\right). \tag{35}$$

35. Let's compute the periodogram of our limited-magnitude sample with a floating mean (Figure 12, left). Now it is. The correct frequency is recovered with high flying colors. The periodogram can see now the true frequency (Figure 12, right).

36. At last, the problem of uncertainty. We, as scientists, are supposed to give observational results with their error bars. For frequencies, we usually take the width of a line as a measure of its uncertainty. But since a periodogram is a set of values at discrete frequencies, we do not have proper lines. However, we can get a width of a line if we compute the values of the periodogram at many frequencies between those already computed, thus achieving a quasi-continuous curve by joining the values at each frequency.

37. We take as a benchmark

$$f(t) = \sin(\omega t) + \text{ white noise}, \tag{36}$$

with $\omega = 2\pi \cdot 1$, sampling it at N points randomly chosen between time 0 and 100. The periodogram, as said, is constructed with many more frequencies than needed, in such a way that joining its values a continuous-like line can be traced.

If we fix the signal-to-noise level at 10 and change the number N of samples, we obtain the three curves of Figure 13 (left). As we can see, the width of the peak, to first order, is invariant with respect to the number N. This is somewhat unexpected, because we may think that increasing the number of points would improve the precision. If we keep fixed the number of samples but change the

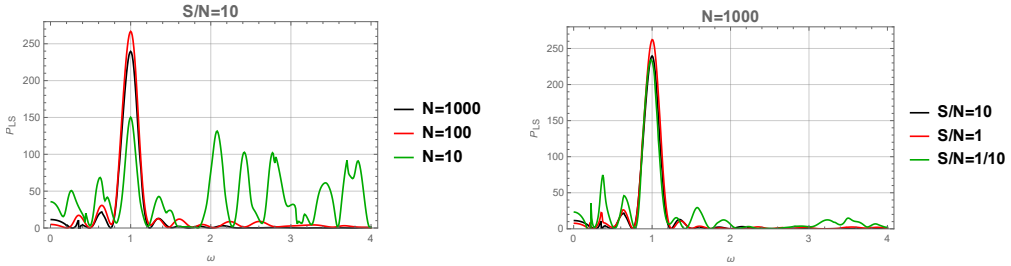

Figure 13. Left: the width of a line does not depend on the number of samples. Right: the width of a line does not depend on the signal-to-noise ratio.

signal-to-noise ratio from 10 to 1 to 1/10 (Figure 13, right), it happens the same as before. Noise is also not a measure of precision.

We conclude that the width of a line of the periodogram does not depend on either the number of observations or their signal-to-noise ratio. If it is frequencies, we cannot give the reader a number plus minus an error.

38. What we can give instead is the *false alarm probability* of a peak. The idea is to compare the height of a peak against the peaks of the background; in other words, to quantify the significance of a peak. The false alarm probability of a peak is the probability that a dataset which is pure noise would have a peak of magnitude equal to or greater than that of the peak in question.

Scargle (1982) proved that if the data is pure Gaussian noise, then the values of the periodogram follow a χ^2 distribution with 2 degrees of freedom, that is, a decreasing exponential. Let's call Z a value of the periodogram at an arbitrary frequency ω. Then the probability density function of Z is

$$p_Z(z) = \text{Prob}(z < Z < z + \text{d}z) = \exp(-z)dz. \tag{37}$$

Therefore, the cumulative probability is

$$F_Z(z) = \text{Prob}(Z < z) = \int_0^z p_Z(z')dz' = 1 - \exp(-z), \tag{38}$$

so the statistical significance of a given power at a preselected frequency is

$$\text{Prob}(Z > z) = 1 - F_Z(z) = \exp(-z). \tag{39}$$

In other words, it becomes exponentially unlikely that such a power Z or greater can be due to a chance noise fluctuation.

39. Now, let Z_m be the value of the maximum peak of the periodogram. We are now choosing a specific value of frequency among N values, not any frequency. Then, the probability of that power being less than z will be that of one frequency but to the power of N:

$$F_{Z_m}(z) = \text{Prob}(Z_m < z) = [1 - \exp(-z)]^N, \tag{40}$$

and the statistical significance of such a power will then be:

$$\mathrm{Prob}(Z_m > z) = 1 - F_{Z_m}(z) = 1 - [1 - \exp(-z)]^N. \quad (41)$$

40. Finally, we want a value of z such that a maximum with this value of z has a probability p of being obtained by chance. For this, we just need to solve for z in the above expression:

$$z = -\ln\left[1 - (1-p)^{1/N}\right]. \quad (42)$$

Different values of z for different probabilities p can then be plotted along with the periodogram to assess the significance of the lines. In practice, the presence of the window will make the powers at adjacent frequencies not independent, so we have to estimate how many independent frequencies there are in the spectrum, and replace the N of the exponent with this effective number. A good choice is that proposed by Press et al. (1992), p. 570.

Acknowledgments. I would like to thank the SOC and LOC for a beautiful, pleasant and enriching School.

References

Eyer L., Bartholdi P., 1999, *A&AS*, **135**, 1
Lomb N. R., 1976, *Ap&SS*, **39(2)**, 447
Press W. H., Teukolsky S. A., Vetterling W. T., Flannery B. P., 1992, *Numerical Recipes in Fortran 77: The Art of Scientific Computing*, Cambridge University Press, 2nd edition
Scargle J. D., 1982, *ApJ*, **263**, 835
Schuster A., 1898, *Terrestrial Magnetism (Journal of Geophysical Research)*, **3(1)**, 13
VanderPlas J. T., 2018, *ApJS*, **236(1)**, 16

Pulsations Along Stellar Evolution
VIII LAPIS Summer School
AAA Workshop Series 12, 2021
M. Kraus & A.F. Torres, eds.

Wavelets Analysis for Time Series

A. Christen[1]

[1] *Universidad de Valparaíso, Gran Bretaña 1111, 2340000 Valparaíso, Chile*

Abstract. Wavelet analysis has been widely used to analyze time series and has countless applications in astronomy. Because of its characteristics it is a method that is well suited to approximate functions, eliminate noise, detect points of change, discontinuities and periodicities. In this article an introduction to the wavelet theory and its use in time series is presented. Numerical simulations and some real examples are developed in the software R.

Key words: Methods: statistical — Methods: analytical — wavelets.

1. Introduction

Fourier transform is widely used in signal processing and analysis and for its inherent characteristics it has had satisfactory results in the study of signals that are periodic and regular enough, but the same is not true when their spectra vary over time (non-stationary signals). If the function $f(x)$ to be decomposed is a time series, and we think to analyze it, we have to take into account that the functions of the Fourier base are of infinite duration in time, but local in frequency. The Fourier Transform detects the presence of a certain frequency but does not provide information about the evolution in time of the spectral characteristics of the signal. Many temporal aspects of the signal, such as the beginning and end of a finite signal and the instant of appearance of a singularity in an instant of time, cannot be adequately analyzed by Fourier analysis. Even so, Fourier analysis is a cornerstone for the development of other mathematical and statistical theories including Wavelet analysis. In the following subsection we present the main concepts of Fourier analysis, which will be needed for the reading of the rest of the Chapter.

1.1. Some Concepts From Fourier Analysis

In this section we will review some concepts of Fourier analysis necessary for the following sections. Consider the space of all complex-valued functions f on R, such that f is absolutely integrable (ie: $\int_{-\infty}^{\infty} |f(x)|dx < \infty$) and denote it as $L^1(\mathrm{R})$ (Härdle et al. (1998)). For $f \in L^1(\mathrm{R})$, define the *Fourier Transform* of f by

$$\hat{f}(\xi) = \int_{-\infty}^{\infty} e^{-i\xi x} f(x)dx. \tag{1}$$

If $\hat{f}(\xi)$ is also absolutely integrable, define the *Inverse Fourier Transform* by

$$f(x) = \frac{1}{2\pi} \int_{-\infty}^{\infty} e^{i\xi x} \hat{f}(\xi) d\xi, \tag{2}$$

at almost every point x. By extension, the Fourier transform can be defined for any $f \in L^2(\mathrm{R})$ with $\int_{-\infty}^{\infty} |f(x)|^2 dx < \infty$.

Given a 2π-periodic function f on R, such that $f \in L^2(0, 2\pi)$ ($\int_0^{2\pi} |f(x)|^2 dx < \infty$), it can be represented by its Fourier series by

$$f(x) = \sum_k c_k e^{ikx}, \tag{3}$$

where $c_k = \frac{1}{2\pi} \int_0^{2\pi} f(t) e^{-ikx} dx$ is named the k-th Fourier coefficient. By periodicity, this holds for all $x \in \mathrm{R}$.

Therefore there exists the basis of functions, $\{e^{-ikx}\}_k$, in $L^2(\mathrm{R})$, for which we can write any function in $L^2(\mathrm{R})$ as an infinite linear combination of the members of this basis of functions. If we keep a finite number of terms on the right hand side of the equation (3), we will obtain an approximation of the function $f(x)$. Due to the characteristics of the Fourier series (the functions $\sin(x)$ and $\cos(x)$ in e^{-ikx} are non-zero over almost the entire domain), a large number of terms in the series are needed to get a good approximation of $f(x)$. In wavelet theory an alternative basis of functions is sought that has the property of being able to write any function in $L^2(\mathrm{R})$ as a series of the basis functions, but that they take values close to 0 outside a bounded interval, which allows a local adjustment in time and the use of few terms in the series to obtain a very good approximation of $f(x)$.

Let $\{a_k\}_{k \in \mathrm{Z}}$ denote an infinite sequence of real or complex-valued variables with the property that $\sum_{-\infty}^{\infty} |a_k|^2 < \infty$ what ensure that all the quantities we deal with are well defined. Then the complex function given by

$$A(r) = \sum_{k=-\infty}^{\infty} a_k e^{-i2\pi rk}, \tag{4}$$

is called the *Discrete Fourier Transform (DFT)* of $\{a_k\}_{k \in \mathrm{Z}}$, where $r \in \mathrm{R}$ is a variable known as *frequency* (see Percibal & Walden (2000)). For the interpretation of the formula in equation (4), $|r|$ is the number of cycles that the sinusoidal curves in the real and imaginary terms of the function $e^{-i2\pi rk} = cos(2\pi rk) - i\sin(2\pi rk)$ (i.e. $\cos(2\pi rk)$ and $-\sin(2\pi rk)$, respectively), go over when k sweeps from 0 to 1. Any negative frequency r will map to some positive frequency when a physical interpretation is required (see Percibal & Walden (2000), Exercise [2.1]).

As intuition, if $|A(r)|$ is large (small), then the sequences $\{a_k\}$ and $\{e^{-i2\pi rk}\}$ have a good agreement (bad agreement).

The sequence $\{a_k\}$ can be reconstructed or recovered from its DFT, $A(r)$, by

$$a_k = \int_{-\frac{1}{2}}^{\frac{1}{2}} A(r) e^{i2\pi rk} dr, \tag{5}$$

where $k \in \mathrm{Z}$. The larger the value of $|A(r)|$, the more important sinusoids of frequency r are in reconstructing $\{a_k\}$. If $\{a_k\}$ is a finite sequence for instance for $k = 1, \cdots, N$, it is extended to $k \in \mathrm{Z}$ by defining $a_k = 0$ for all $k \leq 0$ and $k > N$. In this case, $A(r) = \sum_{k=1}^{N} a_k e^{-i2\pi rk}$.

Filtering: In wavelets context it is often used the term "filter". Consider two infinite sequences of real or complex-valued variables, $\{a_k\}$ and $\{b_k\}$, satisfying $\sum_{k=-\infty}^{\infty} |a_k|^2 < \infty$, $\sum_{k=-\infty}^{\infty} |b_k|^2 < \infty$. The *convolution* of $\{a_k\}$ and $\{b_k\}$ is given by

$$(a * b)_k = \sum_{u=-\infty}^{\infty} a_u b_{k-u}. \tag{6}$$

This definition led us to the notion of filtering used in engineering. If we consider $\{a_k\}$ in equation (6) as a filter and $\{b_k\}$ as a sequence to be filtered, then their convolution, $\{(a*b)_k\}$, is the filtered version of $\{b_k\}$, filtered by the sequence $\{a_k\}$. There are 'low-pass' filters that preserve low frequency components and attenuate high frequency ones; and there are 'high-pass' filters that make the contrary. Finally there is a *cascade of filters*, involved in wavelet coefficients computation from data (see section 3), which is nothing more than the consecutive application of a set of filters to a sequence, one after the other.

1.2. Short Time Fourier Transform

An intermediate step between Fourier and Wavelet analysis was the use of the Short Time Fourier Transform (STFT) to detect local phenomena in time. It performs a time-dependent spectral analysis. The signal is divided into a sequence of time segments (depending on a window defined for this purpose) in which the signal can be considered as quasi-stationary and then the Fourier Transform is applied to each segment. Window functions are used to perform this procedure. To observe a signal over a finite period of time, we multiply it by a window function. The signal is divided into short fragments (short time intervals) delimited in time, by means of a window function. The segments sometimes overlap. Through the individual spectral analysis of each windowed segment, a sequence of measurements or spectra is obtained, what constitutes the time-varying spectrum. The four most common window types are the Rectangular window, the Hanning window, the Hamming window and the Blackman window.

Three kinds of examples where STFT has been applied are presented below: two curves with marked periodicities that change according to the time instant in Figure 1, two curves without periodicities in Figure 3 and one curve with variable periodicity in Figure 4.

Figure 1 shows the STFT of two sinusoidal curves, a curve with three different periods and amplitudes:

$$f_0(x) = \sin(0.2\pi x),\ f_1(x) = 1.5\sin(0.5\pi x),\ f_2(x) = 2\sin(0.8\pi x),$$

for the upper left panel, and

$$f_3(x) = \sin(0.6x),\ f_4(x) = 0.5\sin(0.5x),\ f_5(x) = 2\sin(0.1x),$$

for the lower left panel. In right panels of Figure 1 the computation of the corresponding STFT is shown. Time-slices of length 80 are extracted from the vector (in case of short vectors the window size is chosen so that 10 windows fit in the vector). The shift of one time-slice to the next one is given by 24 (for short vectors the increment is selected so that 30 increments fit in the vector). The values of these time-slices are smoothed by multiplying them with a Hanning window function. For these obtained windows, the Fast Fourier Transform[1] is computed. Then each window takes a segment of length 80 in time and is shifted by 24 which produces 414 calculations of the Fast Fourier transform. Therefore a matrix of 414 rows is produced where each row of the matrix contains the Fourier coefficients of one window which are plotted in a scale of 64 gray values, where white corresponds to the minimum value and black to the maximum. The right panel of the Figure 1 shows how the Fourier transform changes over time, which gives an indication of the change in periodicity over time. This is an advantage over the use of periodograms based on the Fourier transform in which the periods present are shown but without indicating their variability over time (see Figure 2 where the Lomb Scargle periodogram of the sine wave 1 is displayed). With wavelet analysis it will be possible to construct a time-sensitive measure, of the STFT type, where on the ordinate axis the exact time is shown.

In the Figure 3 two curves and their STFT are shown. On the left upper panel a Gaussian white noise is plotted. This curve is completely random with no periodicities, therefore no time with a specific value is highlighted in its STFT (right upper panel). On the left lower panel a sample of an Autoregressive Moving Average (ARMA) process with parameters $(2, 2)$ is shown. This is a linear model for time series analysis and together with Autoregressive Integrated Moving Average ARIMA and Continuous Autoregressive Moving Average CARMA models have been used to model light curves in astronomy (Cáceres (2019), Eyheramendy et al. (2018), Kelly et al. (2014)). The ARMA process is a stationary process with constant expectation and variance, so its representation contains no trend or periodicity. As a consequence, the STFT is less random than that of white Gaussian noise but with a time-varying Fourier transform. A curve with time-varying periodicity is plotted on the left panel of Figure 4. It can be seen that its STFT detects how the frequency decreases over time, although the exact time at which the changes occur or the exact trend of change is not visible due to the displacement of the windows used in the STFT calculation.

STFT allows that a certain location of a local phenomenon in a signal is detected. However, only the time interval in which the local phenomena occur will be known, since the location depends on the width of the window chosen. Moreover, the events will not be able to be differentiated or found if they are very close to each other, since it is not possible to distinguish different behaviors

[1]Fast Fourier Transform: Calculating the DFT is time consuming and requires on the order of N^2 floating point multiplications. As many of the multiplications are repeated by varying the indexes, an efficient algorithm is used, called Fast Fourier Transform (FFT) which consists of a collection of routines designed to reduce the amount of redundant calculations. Different implementations of the FFT have different features and advantages. One of the algorithms used is the "split-radix" algorithm which requires approximately $N \log_2(N)$ operations (Fischer-Cripps (2002)).

within the same window width. A mathematical tool to solve these problems is the Wavelet Transform.

In this Chapter, the theory of Wavelet analysis is described in Section 2 including multiresolution analysis. Section 3 describes the Cascade Algorithm and the discrete wavelet transform while Section 4 is devoted to continuous wavelet transform and its applications. Finally, in Section 5 we present our conclusions.

2. Theory of Wavelet Analysis

We can say that the theory of the analysis of the wavelets began with Mr. Joseph Fourier (1807), with his theory of frequency analysis, today often referred to as Fourier analysis. After 1807 and from the development of the Fourier convergent and orthogonal systems, the notion of frequency analysis led to scale analysis. The first mention of the wavelets appears in an appendix of the thesis of A. Haar (1909). The wavelet theory was developed mainly in the 80's by Meyer (1986), Daubechies (1988), Mallat (1989) and others.

Wavelets are used in a large number of applications, among them: astronomy, acoustics, nuclear engineering, sub-band code, signal and image processing, neurophysiology, bioinformatics, genetics, music, magnetic resonance imaging, classification of words in a text, optics, fractals, seismic turbulence prediction, radars, human vision, statistics (time series, correlations, stochastic processes, point processes, non-parametric regression, regression with census data) and mathematical applications such as: in pure frequency identification, eliminating signal noise, detecting discontinuities and cutting spots, detecting self-similarity (fractals), compression of data.

In this Chapter the use of wavelets focuses on their application to time series (i.e.: sequence of observations indexed on an ordered set of indices I which can be a discrete set of values such as integers or a subset of the real line, based on an independent variable $t \in I$). The variable t can be taken as time, depth, or distance along a line, among others. Examples of set of indexes are $I = (0, +\infty)$, that is, all $t > 0$ are possible indexes, and $I = \{0, 1, 2, \cdots, n\}$, where n can be any integer greater than 2.

The main points of the theory of wavelet analysis are developed to later analyze its use in applications through approximations, scalograms built from the wavelet transform, signal reconstruction, among others. The Wavelet Transform is efficient for the local analysis of locally changing and non-stationary signals and, like the Windowed Fourier Transform[2], assigns a time-scale representation to the signal. The time aspect of the signals is under consideration. The main difference with STFT is that the Transformed Wavelet has multiresolution analysis with variable windows. The analysis of higher range frequencies is done using narrow windows and the analysis of lower range frequencies is done using wide windows (Poularikas, 2010).

[2]Short Time Fourier Transform

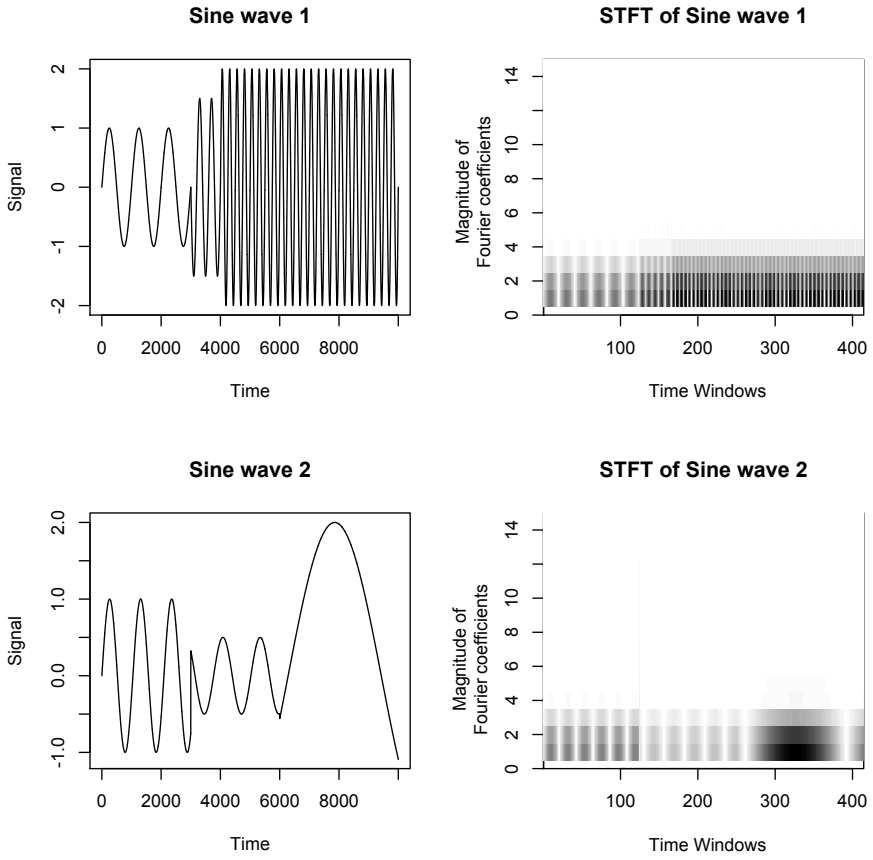

Figure 1. Examples of STFT. On the left panels, it can be seen two different sinusoidal curves and on the right panels their STFT. First, time segments of a fixed length are extracted from the data vector. This window is moved along the time axis by a fixed amount possibly smaller than the window size, which may produce an overlap between the time segments. The values of these time intervals are smoothed by multiplying them by a specified window function. For the windows thus obtained, the fast Fourier transform is calculated. For the data in the figure, segments of 80 time units were used. They were incremented by 24 units to obtain the next segment, which produced overlapping segments, yielding 414 windows. For each window 64 Fourier coefficients were calculated. The figure shows: on the x-axis the 414 windows and 64 cells on the vertical axis of each window which were colored with a gray scale according to the magnitude of the Fourier coefficients. In the figure only the cells with gray colors are observed, the rest are only white. The dark regions in the graph correspond to high values of the coefficients at the particular time/frequency location.

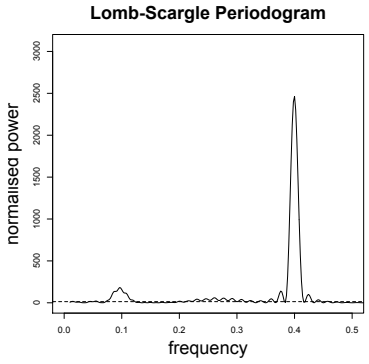

Figure 2. In the figure the Lomb Scargle periodogram of Sine wave 1 is shown. The frequencies of the curve 0.1 and 0.4 are clearly evidenced and more weakly the frequency 0.25.

Wavelets (small waves) are families of functions which, if they are translated and dilated, allow us to obtain an orthogonal base of functions in $L^2(\mathrm{R})$. A linear combination of the elements of this base of wavelet functions is used to represent a signal $f(t)$.

The classical Fourier analysis has been widely used in the problem of reconstructing a function f from dilations of a fixed sinusoidal function $x \mapsto e^{2\pi i x}$, when writing $f(x) = \int e^{2\pi i \xi x} \hat{f}(\xi) d\xi$. The Fourier transform, $\hat{f}(\xi)$, is considered the amount of sinusoidal oscillation $e^{2\pi i \xi x}$ present in the function f. Sinusoidal function bases are also used in Fourier series.

In the same way the wavelet basis of functions allows us to reconstruct the original signal through the inverse Wavelet Transform. There are several base wavelet functions, depending on the chosen family: Haar, Daubechies, Morlet, Symmlets, among others. Depending on the selected wavelet family, a different base function is used (first brick in the construction) and a certain base of functions is obtained which will allow the wavelet analysis to be performed. The main advantage of Wavelet analysis is that it is not only local in time, but also in frequency.

This feature allows using the continuous wavelet transform to detect an event in the data, either the period of a time series, a change point in the series, a discontinuity in a density function, and to know the moment (time) or abscissa at which it occurs. For example, knowing the time interval during which a detected period is present in the brightness measurements in a light curve, the moment when the flow of a river changes drastically, the day when an economic variable produces a change in its modeling.

Another feature of a wavelet functions basis is that any function in the function space L^2 can be decomposed as an infinite sum of functions in the wavelet basis, as with the Fourier series, but because of their great flexibility to approximate functions efficiently only a small number of summands are needed to produce very good approximations. The latter is because wavelet functions vanish outside a bounded interval and the basis of functions is formed by a count-

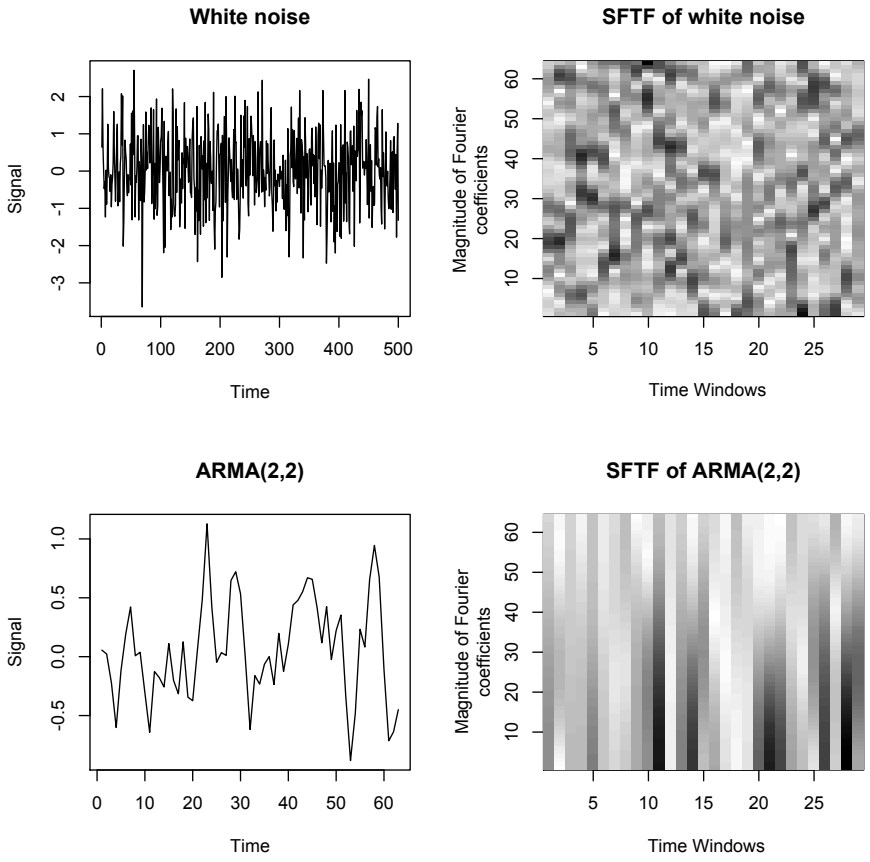

Figure 3. Examples of STFT: The upper panel shows a curve of 500 data points from a Gaussian white noise and its STFT. In the lower panel, the plots show the curve of a sample from an ARMA $(2, 2)$ process and its STFT. For the data in the upper right panel of the figure, segments of 50 time units were used. They were incremented by 16 units to obtain the next segment, which produced overlapping segments, yielding 29 windows. For each window 64 Fourier coefficients were calculated. The figure shows: on the x-axis the 29 windows and 64 cells on the vertical axis of each window which were colored with a gray scale according to the magnitude of the Fourier coefficients. The dark regions in the graph correspond to high values of the coefficients at the particular time/frequency location. In the lower right panel, segments of 6 time units with increments of 2 units were used, yielding 29 windows.

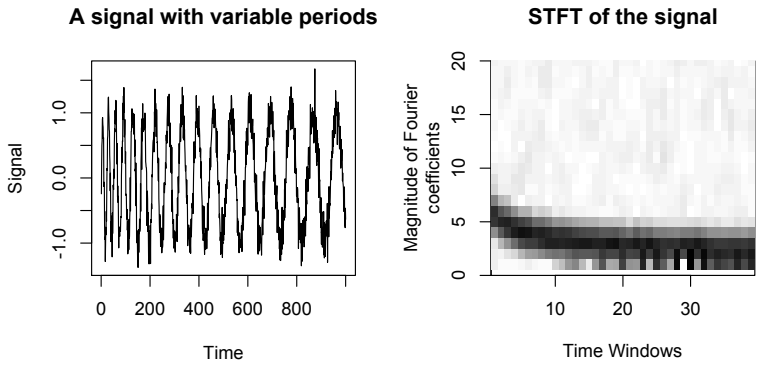

Figure 4. On the left panel, it can be seen a curve with periods varying over time and on the right panel its STFT, built from segments of 80 time units with increments of 24 units, yielding 39 windows on the x-axis. On the vertical axis of each window 64 cells were colored with a gray scale according to the magnitude of the Fourier coefficients. In this figure the dark regions, corresponding to a high magnitude of the Fourier coefficient, sweep across an interval as they move through time.

able number of dilations and contractions of a wavelet function called "parent", stretches and squashes of those functions and translations of all of them. This is equivalent to having bricks of various sizes and widths that can be placed under any house and that adding up all the volumes will give exactly the same volume of the house.

In the next section we will be introduced to multiresolution analysis, the main feature of wavelet analysis, which will allow us to define a basis of wavelet functions in $L^2(\mathrm{R})$ with which we can represent any function $f(x)$ in $L^2(\mathrm{R})$ through an infinite countable linear combination of the basis.

2.1. Multiresolution Analysis

Wavelets can be considered as a basis of functions generated by dilations and translations of a simple function which, in general, is not sinusoidal. They are connected to the notion of multiresolution analysis (MRA) in which the objects (signals, functions, data) can be examined using several levels of approach, as if zooming in and out. In both cases we can obtain relevant information about the object. As an example, suppose we are looking at a house, the observation can be made from a large distance from where only the basic shapes and structure can be distinguished (if it has a garage, the shape of the roof); or one can observe from a closer distance and various other characteristics of the house will appear (the door is made of hardwood, for example).

The basis function will be generated from a basic function that is usually called parent wavelet or scaling function, which in turn allows us to build another basic function that we will call mother wavelet or wavelet function. The repre-

sentation of a function $f(x)$ will be done through two summands: the sum of the dilations and translations of the father wavelet, $\varphi(x)$, will give us information about the general, coarse aspects (a kind of smoothing) of the $f(x)$ and the sum of the dilations and translations of the mother wavelet, $\psi(x)$, will give us information about the particular aspects and details (like a zoom) of the function. Each term in the second summand will add more clarity on the specific features.

In this section some basic concepts such as wavelet father, which provides smoothing, and wavelet mother, to describe the details, are defined to reach the multiresolution analysis definition. In the following it will be assumed that the function to be analyzed is a function of time t.
For $\varphi \in L^2(\mathrm{R})$, $k \in \mathrm{Z}$, $x \in \mathrm{R}$, we denote $\varphi_{0k}(x) = \varphi(x-k)$ the family of translations of φ and we denote

$$\varphi_{jk}(x) = 2^{\frac{j}{2}}\varphi(2^j x - k), j, k \in \mathrm{Z},$$

the family of translations and dilations of φ with the indexes k and j respectively. The functional sub-spaces $\{V_j\}_{j\in\mathrm{Z}}$, $V_j \subseteq L^2(\mathrm{R})$ are defined by:

- for $j = 0$:

$$V_0 = \left\{ g \in L^2(\mathrm{R}) : g(x) = \sum_k c_k \varphi(x-k),\ \sum_k |c_k|^2 < +\infty \right\}$$

  that is, V_0 is the subspace spanned by the translations of $\varphi(x)$ by k, $\varphi(x-k)$.

- and for $j \in \mathrm{Z}$:

$$V_j = \left\{ h(x) = g(2^j x) : g \in V_0 \right\}.$$

  Then $h(x) \in V_{j_1}$ if $h(x) = \sum_k c_k \varphi(2^{j_1}x - k)$ for $\{c_k\}$ such that $\sum_k |c_k|^2 < +\infty$, or, V_{j_1} is the subspace spanned by the functions $\{\varphi(2^{j_1}x - k)\}_{k\in\mathrm{Z}}$.

Therefore φ generates the sequence of subspaces $\{V_j\}$. The sequence $\{V_j\}$ is called *multiresolution analysis* if

1. $\{\varphi_{0k}\}$ is an ortonormal system in $L^2(\mathrm{R})$,
2. the subspaces are nested, that is,

$$V_j \subset V_{j+1}, j \in \mathrm{Z}, \tag{7}$$

3. every function in $L^2(\mathrm{R})$ can be obtained as a limit of a sequence of functions in $\bigcup_{j\geq 0} V_j$, that is, every function $f \in L^2(\mathrm{R})$ can be written as a series of elements in $\bigcup_{j\geq 0} V_j$.

In this case, φ is called *Wavelet father*. Another sequence $\{W_j\}_{j\in\mathrm{N}_0}$ is considered such that W_j is the orthogonal complement of $V_j \subseteq V_{j+1}$, $W_j =$

$V_{j+1} \ominus V_j$, then $\bigcup_{j\geq 0} V_j = V_0 \cup (V_1 \ominus V_0) \cup (V_2 \ominus V_1) \cdots \cup (V_{j+1} \ominus V_j) \cdots$. Then $\bigcup_{j\geq 0} V_j = V_0 \oplus \overset{\infty}{\underset{j=0}{\oplus}} (V_{j+1} \ominus V_j)$ is a direct sum of sub-spaces that completes $L^2(\mathrm{R})$ leading to

$$L^2(\mathrm{R}) = V_0 \oplus \overset{\infty}{\underset{j=0}{\oplus}} W_j,$$

therefore any function $f(x)$ in $L^2(\mathrm{R})$ can be written as a linear combination of functions in V_0 and $\{W_j\}$. For each $j \in \mathrm{N}_0$, let ψ be a function such that its translations and dilations, $\{\psi_{jk} = 2^{j/2}\psi(2^j x - k), k \in \mathrm{Z}\}$, are an orthogonal basis of W_j. Then, for instance, the translations $\{\psi_{0k}(x) = \psi(x-k)\}_k$ is an orthogonal system of W_0, this system is orthogonal to V_0 and $V_1 = V_0 \oplus W_0$ is the subspace spanned by the system $\{\{\varphi_{0m}\}_m, \{\psi_{0k}\}_k\}$, where $\varphi_{0m}(x) = \varphi(x-m)$ for all m.

As a consequence, each function $f(x)$ can be represented as a convergent series given by

$$f(x) = \sum_{k\in\mathrm{Z}} \alpha_k \varphi_{0k}(x) + \sum_{j=0}^{\infty} \sum_{k\in\mathrm{Z}} \beta_{jk} \psi_{jk}(x), \tag{8}$$

where

$$\alpha_k = \int f(x)\varphi_{0k}(x)dx, \quad \beta_{jk} = \int f(x)\psi_{jk}(x)dx. \tag{9}$$

According to the function $f(x)$ sometimes it is necessary to start with a subspace V_{j_0} with $j_0 > 0$, in that case, the first function in the sum, $\varphi_{0k}(x)$, is replaced by $\varphi_{j_0 k}(x)$ and the index j starts at $j_0 > 0$ in the right term of equation (8).

The representation of $f(x)$ as an expansion of translations and dilations of functions φ and ψ is called *wavelet expansion* and ψ the *Wavelet mother*.

Each W_j in the sequence of sub-spaces $\{W_j\}$ represents a *resolution level* of the multiresolution analysis. There are several levels j of resolution, what gives rise to its name.

The resolution level means a zoom level that is performed on the function, so each one will allow you to see details at different scopes. Thus the function is decomposed into an initial smoothing, given by the parent wavelet in the first term of the right-hand side of eq. (8) and different levels of details that are added according to the value of the level j in the second term of the right side. The greater the value of j, the greater the level of resolution and the finest details will be visible, which will be represented by the j-th term.

An example of wavelet system is the Haar system. The wavelet father and wavelet mother are given by

$$\varphi(x) = I_{(0,1]}(x), \quad \psi(x) = -I_{\left[0,\frac{1}{2}\right]}(x) + I_{\left(\frac{1}{2},1\right]}(x), \tag{10}$$

respectively, where

$$I_A(x) = \begin{cases} 1 & if\ x \in A \\ 0 & if\ x \notin A \end{cases}$$

and the interval $(a, b]$ is the set of real numbers between a and b, including b but not a. The basis of functions for the Haar wavelet system are:

$$\varphi_{0k}(x) = \{I_{(0,1]}(x-k)\}_{k\in \mathrm{Z}},$$

$$\psi_{jk}(x) = 2^{j/2}\left(I_{\left(\frac{1}{2},1\right]}\left(2^j x-k\right) - I_{\left[0,\frac{1}{2}\right]}(2^j x-k)\right),$$

for wavelet father and mother respectively, where $j, k \in \mathrm{Z}$, $j \geq 0$. We can observe that $\{\varphi_{0k}(x)\}_{k\in \mathrm{Z}}$ is an orthonormal basis (ONB, i.e.: a basis of orthogonal and normalized vectors) in

$$V_0 = \{h(x) \in L^2(\mathrm{R}) : h(x) \text{ is constant on } (k, k+1], k \in \mathrm{Z}\},$$

$\{\varphi_{jk}(x) = 2^{j/2}\varphi(2^j x-k)\}_{k\in \mathrm{Z}}$ is an ONB in

$$V_j = \{h(x) \in L^2(\mathrm{R}) : h(x) = g(2^j x), g(x) \in V_0\},$$

$V_j \subseteq V_{j+1}$ and $V_j = V_{j-1} \oplus W_{j-1}$, where W_j is spanned by $\{\psi_{jk}(x)\}_{k\in \mathrm{Z}}$. Finally, $L^2(\mathrm{R}) = V_0 \oplus W_0 \oplus W_1 \oplus \cdots W_j \oplus \cdots$.

By way of illustration,

1. $\{\varphi_{0k}(x)\}$ is an ONB of V_0.

2. $V_1 = \{h(x) \in L^2(\mathrm{R}) : h(x) = g(2x), g(x) \in V_0\} = \{h(x) \in L^2(\mathrm{R}) : h(x) \text{ is constant on } (\frac{k}{2}, \frac{k+1}{2}], k \in \mathrm{Z}\}$ and it is spanned by the ONB $\{\varphi_{0k}(x), \psi_{0k}(x) = I_{\left[0,\frac{1}{2}\right]}(x-k) - I_{\left(\frac{1}{2},1\right]}(x-k)\}$.

3. The functions $\varphi_{1k}(x) = 2^{1/2}\varphi(2x-k)$ for $k \in \mathrm{Z}$ span V_1 and can be written in terms of $\{\varphi_{0k}(x)\}$ and $\{\psi_{0k}(x)\}$, since $V_1 = V_0 \oplus W_0$. For instance:

$$\varphi_{10}(x) = \sqrt{2}I_{\left(0,\frac{1}{2}\right]}(x) = \frac{\sqrt{2}}{2}(I_{(0,1]}(x) - I_{\left[0,\frac{1}{2}\right]}(x) + I_{\left(\frac{1}{2},1\right]}(x)) = \frac{1}{\sqrt{2}}(\varphi_{00} - \psi_{00}),$$

$$\varphi_{11}(x) = \sqrt{2}I_{(0,1]}(2x-1) = \frac{1}{\sqrt{2}}(\varphi_{00} + \psi_{00}).$$

A suitable property of the Haar wavelets is that they are cancelled out of a limited interval. Unfortunately, Haar wavelets are not continuously differentiable which limits their applications (see Figure 5). There are wavelet families with compact support (vanish out of an interval) and wavelet families defined over the whole line. Among the former wavelet families are Daubechies, Coiflets, Symmlets. Some examples of the last ones are the Battle-Lemarié and Morlet wavelets.

Father and mother wavelets can be defined from some of the properties of their Fourier transforms (see Härdle et al. (1998)).

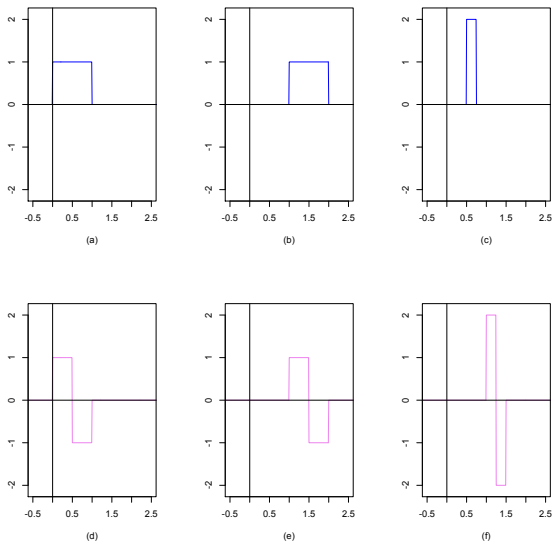

Figure 5. Some representations of Haar wavelet. On the top panel it is shown Haar father wavelet for (a) $j = 0$, $k = 0$, (b) $j = 0$, $k = 1$, (c) $j = 1$, $k = 1/2$. On the bottom panel it is shown Haar mother wavelet for (d) $j = 0$, $k = 0$, (e) $j = 0$, $k = 1$, (c) $j = 1$, $k = 1$.

2.2. Obtaining a Wavelet Expansion

In this section the conditions about functions φ and ψ that guarantee the existence of a wavelet system are formulated. That is to say, what characteristics should have so that φ_{0k} is an orthogonal and normalized system, the V_j are nested, the span of $\bigcup_j V_j$ is equal to $L^2(\mathrm{R})$, ψ_{jk} is an orthogonal and normalized system of W_j, etc. This section follows closely Härdle et al. (1998).

Properties on $\hat{\varphi}$, the Fourier transform of φ, are sought that guarantee the validity of the necessary and sufficient conditions for the wavelet expansion:

1. $\{\varphi_{0k}, k \in \mathrm{Z}\}$ is an orthonormal system (ONS)
2. $V_j \subset V_{j+1}, j \in \mathrm{Z}$
3. $\bigcup_{j\geq 0} V_j$ is dense in $L^2(\mathrm{R})$ (i.e.: the linear combinations of functions in $\bigcup_{j\geq 0} V_j$ span all the functional space $L^2(\mathrm{R})$).
4. $\{\psi(x-k), k \in \mathrm{Z}\}$ is an ONB in W_0.

In what follows functions φ, that satisfy that there is a constant $M > 0$ such that $\sum_{k\in\mathrm{Z}} |\varphi(x-k)| < M$ for $x \in \mathrm{R} - A$, will be considered, where A is a null measurement set.

The following results that allow characterizing the father wavelet and the mother wavelet from properties of their Fourier transform can be demonstrated (see Härdle et al. (1998)).

(a) Set $\varphi \in L^2(\mathrm{R})$. The system $\{\varphi_{0k}, k \in \mathrm{Z}\} = \{\varphi(x-k), k \in \mathrm{Z}\}$ is an ONS if and only if,

$$\sum_{k \in \mathrm{Z}} |\hat{\varphi}(\xi + 2\pi k)|^2 = 1, \tag{11}$$

almost everywhere (a.e.), where $\hat{\varphi}$ is the Fourier transform of the function φ.

(b) The sub-spaces $\{V_j, j \in \mathrm{Z}\}$, spanned by translations and dilations of φ, are nested $V_j \subset V_{j+1}, j \in \mathrm{Z}$, if and only if, there exists a 2π - periodic function $m_0 \in L^2(0, 2\pi)$ such that

$$\hat{\varphi}(\xi) = m_0\left(\frac{\xi}{2}\right)\hat{\varphi}\left(\frac{\xi}{2}\right), \ a.e. \tag{12}$$

Moreover, $|m_0(\xi)|^2 + |m_0(\xi+\pi)|^2 = 1$ a.e.

(c) If φ satisfies items (a) and (b) above then $\bigcup_{j \geq 0} V_j$ is dense in $L^2(\mathrm{R})$.

(d) If φ is a father wavelet that generates a MRA in $L^2(\mathrm{R})$, $m_0(\xi)$ is a solution of equation (12) then

$$\hat{\psi}(\xi) = m_1\left(\frac{\xi}{2}\right)\hat{\varphi}\left(\frac{\xi}{2}\right) \tag{13}$$

is the Fourier transform of a mother wavelet ψ, where $m_1(\xi) = \overline{m_0(\xi+\pi)}e^{-i\xi}$ and the bar represents the complex conjugate.

In summary, to construct a father wavelet φ for a MRA, sufficient conditions on its Fourier transform $\hat{\varphi}$ should satisfy the following restrictions:

$$\sum_{k \in \mathrm{Z}} |\hat{\varphi}(\xi + 2\pi k)|^2 = 1, \ a.e.,$$

$$\hat{\varphi}(\xi) = m_0\left(\frac{\xi}{2}\right)\hat{\varphi}\left(\frac{\xi}{2}\right),$$

where $m_0 \in L^2(0, 2\pi)$ is a periodic function of period 2π such that

$$\begin{cases} |m_0(\xi)|^2 + |m_0(\xi+\pi)|^2 = 1, \\ m_0(0) = 1, \end{cases} \tag{14}$$

where the last restriction in equation (14) is deduced of eq. (12) after adding the condition $|\hat{\varphi}(0)| = |\int \varphi(t)dt| = 1$ for the father wavelet.

Since $V_0 \subset V_1$, then $\varphi \in V_1$ and it can be written as a linear combination of the system $\{\sqrt{2}\varphi(2x-k)\}$, an ONB of the subspace V_1. Therefore, there is a sequence $\{h_k\}$ such that

$$\varphi(x) = \sqrt{2}\sum_{k\in \mathrm{Z}} h_k \varphi(2x-k), \quad h_k = \sqrt{2}\int \varphi(x)\varphi(2x-k)dx, \tag{15}$$

with $\sum_{k\in \mathrm{Z}} |h_k|^2 < \infty$ and the constraints

1. $\sum_k \overline{h_k} h_{k+2l} = \delta_{0l}$
2. $\frac{1}{\sqrt{2}}\sum_k h_k = 1.$

where $\delta_{0l} = 0$ if $l \neq 0$ and $\delta_{0l} = 1$ if $l = 0$. By the same argument the mother wavelet satisfies

$$\psi(x) = \sqrt{2}\sum_k \lambda_k \varphi(2x-k), \tag{16}$$

where $\lambda_k = (-1)^{k+1}\overline{h_{1-k}}$.

Taking Fourier transform to both sides of left equation in (15) we obtain $\hat{\varphi} = \frac{1}{\sqrt{2}}\sum_k h_k e^{-i\xi k}\frac{\hat{\varphi}}{2}$ and by eq. (12) we have that

$$m_0(\xi) = \frac{1}{\sqrt{2}}\sum_k h_k e^{-i\xi k}. \tag{17}$$

If the wavelets considered are compactly supported (i.e.: they vanish outside a bounded interval), the sums in eqs. (15), (16) and (17) have a non-zero number of terms. These relations allow us to determine the coefficients in eq. (9) of a function in its wavelet representation in eq. (8) through a linear transformation given by the product of a matrix by a vector.

Compactly supported wavelets

Some of the wavelet families with compact support are the Daubechies, Coiflets and Symmlets. We briefly describe each of them.
Ingrid Daubechies, to whom we owe the original construction of Wavelets with compact support (Daubechies (1988)), proposed to take $m_0(\xi)$ such that

$$|m_0(\xi)|^2 = c_N \int_\xi^\pi \sin^{2N-1}(x)dx, \tag{18}$$

where the constant c_N is chosen to produce $m_0(0) = 1$. For such functions $m_0(\xi)$ the coefficients $\{h_k\}$ are tabulated (see Daubechies (1988) or Härdle et al. (1998)). Wavelets constructed from the function $m_0(\xi)$ satisfying eq. (18) are called *Daubechies Wavelets* and they are denoted $D2N$ or $Db2N$.

For $N = 1$, we have $D2$ where $c_N = \frac{1}{2}$ and

$$|m_0(\xi)|^2 = \frac{1}{2}\int_{\xi}^{\pi} \sin(x)dx = \frac{1 + cos(\xi)}{2}.$$

Choosing $m_0(\xi) = \frac{1+e^{-i\xi}}{2}$ we obtain

$$\hat{\varphi}(\xi) = \lim_{n\to\infty} \prod_{j=1}^{n} \frac{1}{2}(1 + e^{-\frac{i\xi}{2^j}}) = \frac{1 - e^{-i\xi}}{i\xi},$$

hence Daubechies father wavelet $D2$ matches with Haar father wavelet, $\varphi(x) = I\{x \in (0, 1]\}$.

The supports of Daubechies father wavelet and mother wavelet are included in the intervals $[0, 2N - 1]$ and $[-N + 1, N]$, respectively. Besides, Daubechies mother wavelet has null m-moment (i.e.: $\int x^m \psi(x)\, dx = 0$) for $m = 0, ..., N - 1$.

Beylkin et al. (1991) proposed a new class of wavelets with essentially the same good properties of the Daubechies wavelets and, in addition, the father wavelet has some zero moments. If the father wavelet has certain null moments the wavelet coefficients could be approximated by evaluations of the function $f(t)$ at discrete points:

$$\alpha_{jk} = 2^{-j/2} f\left(\frac{k}{2^j}\right) + r_{jk},$$

with r_{jk} small enough. This can be a useful property in applications.

This class of wavelets was called *Coiflets Wavelets* and is denoted CK. To build the Coiflets wavelets, Beylkin et al. (1991) consider $m_0(\xi)$ of the form

$$m_0(\xi) = \left(\frac{1 + e^{-i\xi}}{2}\right)^{2K} P_1(\xi),$$

where

$$P_1(\xi) = \sum_{k=0}^{K-1} C_{K-1+k}^{k} \left(\sin^2\left(\frac{\xi}{2}\right)\right)^k + \left(\sin^2\left(\frac{\xi}{2}\right)\right)^K F(\xi),$$

and $F(\xi)$ is a trigonometric polynomial chosen such that $|m_0(\xi)|^2 + |m_0(\xi + \pi)|^2 = 1$. The supports of Coiflets father wavelet and mother wavelet are included in the intervals $[-2K, 4K - 1]$ and $[-4K + 1, 2K]$, respectively.

According to Daubechies (1992) the only symmetric wavelet with compact support is the Haar system (father wavelet). The family of *Symmlet Wavelets* is made up of wavelets for which $m_0(\xi)$ is chosen to be close to symmetry. They are denoted by SN, where N is the order of the wavelet. Symmlet mother wavelet has null m-moment (i.e.: $\int x^m \psi(x)\, dx = 0$) for $m = 0, ..., N - 1$. The support of the father wavelet and mother wavelet are the intervals given by $[0, 2N - 1]$ and $[-N + 1, N]$, respectively.

3. Cascade Algorithm

Some recursive formulas are presented that will allow the calculation of the wavelet coefficients sequentially (see Härdle et al. (1998)). The procedure is called **Cascade algorithm** (or pyramidal). It was proposed by Mallat (1989).

This method (Härdle et al. (1998)) is used only with wavelet bases that vanish outside a finite interval and built from the function $m_0(\xi) = \frac{1}{\sqrt{2}} \sum_k h_k e^{-ik\xi}$ (see eq. (17)) where h_k are coefficients of real values with only a finite number of non-zero values. This assumption is satisfied by the families of Daubechies, Coiflets and Symmlets wavelets, among others.

Given a function $f(t)$, the coefficients $\alpha_{jk} =< f, \varphi_{jk} >$, $\beta_{jk} =< f, \psi_{jk} >$ satisfy for $j, k \in \mathrm{Z}$ the relationships:

$$\alpha_{jk} = \sum_k h_{l-2k} \alpha_{j+1,l}, \tag{19}$$

$$\beta_{jk} = \sum_k \lambda_{l-2k} \alpha_{j+1,l} \tag{20}$$

where $\lambda_k = (-1)^{k+1} h_{1-k}$ and $\{h_k\}$ are the coefficients of $m_0(\xi)$.

Indeed, by multiresolution analysis,

$$\begin{aligned}
\beta_{jk} &= 2^{\frac{j}{2}} \int f(x)\psi(2^j x - k)dx \\
&= 2^{\frac{j+1}{2}} \sum_s \lambda_s \int f(x)\varphi(2(2^j x - k) - s)dx \\
&= 2^{\frac{j+1}{2}} \sum_s \lambda_s \int f(x)\varphi(2^{j+1} x - 2k - s)dx \\
&= \sum_s \lambda_s \alpha_{j+1,s+2k} = \sum_l \lambda_{l-2k} \alpha_{j+1,l}.
\end{aligned}$$

The relation (19) is obtained in a similar way. The cascade algorithm is defined by both equations (19) and (20).

Only a finite number of coefficients α_{jk} are non-zero in each level j. Therefore if the vector of coefficients, $y = \{\alpha_{j_1 l}\}$ is known for a certain level j_1, it is possible to recursively rebuild the coefficients α_{jk}, β_{jk} for levels $j \leq j_1$, with the use of the recursive equations (19) and (20).

If the procedure stops at level j_0, the vector of resulting wavelets coefficients $w = (\{\alpha_{j_0 k}\}, \{\beta_{j_0 k}\}, ..., \{\beta_{j_1 - 1,k}\})^t$ can be computed by

$$w = \mathcal{W} y, \tag{21}$$

where $\mathcal{W}$ is a matrix.

It is possible to invert the cascade algorithm to obtain the values of the coefficients y, starting from w by the recursive scheme:

$$\alpha_{j+1,s} = \sum_k h_{s-2k}\alpha_{j,k} + \sum_k \lambda_{s-2k}\beta_{j,k}, \tag{22}$$

allowing j to vary from j_0 to $j_1 - 1$.

3.1. Discrete Wavelet Transform

Given the initial values $\{\alpha(K,k), k = 0, ..., 2^K - 1\}$ the *Discrete Wavelet Transform* (DWT) recursively calculates the coefficients $\alpha(j,k)$ and $\beta(j,k)$ for $0 \leq k \leq 2^j - 1$ and $0 \leq j \leq K - 1$, in the following manner:

$$\alpha(j,k) = \sum_l h_l \, \alpha(j+1, (l+2k) \; mod \; 2^{j+1}), \tag{23}$$

$$\beta(j,k) = \sum_l \lambda_l \, \alpha(j+1, (l+2k) \; mod \; 2^{j+1}). \tag{24}$$

where $(l+2k) \; mod \; 2^{j+1}$ denotes[3] the remainder of dividing $(l+2k)$ by 2^{j+1}. Therefore the DWT is just a composition of linear orthogonal transformations presented by the recursions (23) and (24). These recursions can be extended to $k \in$ Z and these extensions are periodic, in the sense that $\alpha(j,k) = \alpha(j, k + 2^j)$, $\beta(j,k) = \beta(j, k + 2^j)$ for all $k \in$ Z.

The Discrete Inverse Wavelet Transform is defined in a similar way but with the data periodically extended. It starts with the vectors:

$$\{\alpha(j_0,k), k = 0, ..., 2^{j_0} - 1\}, \; \{\beta(j_0,k), k = 0, ..., 2^{j_0} - 1\}$$

and its periodic extensions are denoted by $\{\widetilde{\alpha}(j_0,k), k \in Z\}$, $\{\widetilde{\beta}(j_0,k), k \in Z\}$.

Then the vectors $\{\alpha(j,s), s = 0, ..., 2^j - 1\}$ are computed until level $j = K - 1$, following the recursive equations:

$$\widetilde{\alpha}(j+1,s) = \sum_k h_{s-2k} \, \widetilde{\alpha}(j,k) + \sum_k \lambda_{s-2k} \, \widetilde{\beta}(j,k), s \in Z, \tag{25}$$

$$\alpha(j+1,s) = \widetilde{\alpha}(j+1,s), s = 0, ..., 2^{j+1} - 1. \tag{26}$$

4. Continuous Wavelet Transform

The continuous wavelet transform is a wavelet transform where the dilation and translation parameters, named a and b in this case, vary continuously over R with $a \neq 0$ (Daubechies (1992)). Given the wavelet $\psi \in L^2(\mathrm{R})$ such that $\int \psi(t)dt = 0$ and a function $f \in L^2(\mathrm{R})$, the *Continuous Wavelet Transform (CWT)*, Tf, of $f(t)$, with $a \neq 0$ and $b \in$ R is defined by

[3]The remainder of dividing x by y is usually expressed as $x \, mod \, y$.

$$(Tf)(a,b) = |a|^{-1/2} \int dt f(t) \bar{\psi} \left(\frac{t-b}{a} \right). \tag{27}$$

The expression (27) computes the inner product in $L^2(\mathrm{R})$ of the function f against the family of functions, $\{\psi^{a,b}\}$, indexed by the parameters a, b, defined by

$$\psi^{a,b}(s) = |a|^{-1/2} \psi(\frac{s-b}{a}) \tag{28}$$

where $a \neq 0$ and $b \in \mathrm{R}$. The inner product is defined by $< f, g >= \int dt \bar{f}(t) g(t)$, where $\bar{f}(t)$ is the complex conjugate of $f(t)$.

When a changes and b remains fixed, $\psi^{a,b}(s) = |a|^{-1/2} \psi(\frac{s}{a})$ covers different frequency ranges. Changing the parameter b allows moving the location in time (x-axis or time-axis), every $\psi^{a,b}(s)$ is located around of $s = b$.

If $\psi \in L^2$ and that satisfies the following condition of admissibility

$$0 < C_\psi = 2\pi \int_{-\infty}^{\infty} d\xi |\xi|^{-1} |\widehat{\psi}(\xi)|^2 < \infty, \tag{29}$$

where $\widehat{\psi}$ is the Fourier transform of ψ (see eq. (1)), then the function f can be reconstructed from its CWT using the equation:

$$f = C_\psi^{-1} \int_{-\infty}^{\infty} \int_{-\infty}^{\infty} \frac{da \cdot db}{a^2} < f, \psi^{a,b} > \psi^{a,b}, \tag{30}$$

where $\psi^{a,b}(s) = |a|^{-1/2} \psi(\frac{s-b}{a})$, and $<,>$ denotes the inner product in L^2. The constraint (29) is satisfied if $\psi \in L^1(\mathrm{R})$ (i.e.: $\int |f(t)| dt < \infty$) and $\int \psi(x) dx = 0$ since under this assumption $\widehat{\psi}$ is continuous, then to get $C_\psi < \infty$ is sufficient that $\widehat{\psi}(0) = 0$, or equivalently, $\int \psi(x) dx = 0$.

As an example consider the Haar mother wavelet $\psi(x)$ given in equation (10). For $a > 0$ we have

$$\psi^{a,b}(x) = \frac{1}{\sqrt{|a|}} \left(-I_{\left[b, b+\frac{a}{2}\right]}(x) + I_{\left(b+\frac{a}{2}, b+a\right]}(x) \right),$$

and the CWT

$$(Tf)(a,b) = \frac{1}{\sqrt{|a|}} \left(\int_{b+\frac{a}{2}}^{b+a} f(t) dt - \int_{b}^{b+\frac{a}{2}} f(t) dt \right).$$

For $a < 0$ the CWT is developed in a similar way. In the context of CWTs, some of the most frequently used wavelet families are real and complex Morlet wavelet, real and complex Mexican hat wavelet, real and complex Shannon wavelet, among others.

The *Morlet Wavelet* or Gabor wavelet (Daubechies (1992)), is a continuous wavelet depending on parameter σ. Its Fourier transform, $\hat{\psi}$, is a displaced Gaussian, tuned somewhat so that $\hat{\psi}(0) = 0$,

$$\hat{\psi}(\xi) = \pi^{-\frac{1}{4}} \left(e^{-(\xi-\xi_0)^2/2} - e^{-(\xi^2+\xi_0^2)/2} \right), \tag{31}$$

$$\psi(t) = \pi^{-\frac{1}{4}} \left(e^{-i\xi_0 t} - e^{-\xi_0^2/2} \right) e^{-\frac{t^2}{2}}, \tag{32}$$

where ξ_0 is often chosen as $\pi \left(\frac{2}{\ln(2)} \right)^{1/2} \simeq 5.336$ or $\xi_0 = 5$ for simplicity. The Morlet wavelet for $\xi_0 = 5$ is shown in Figure 6. This wavelet can be found in its complex version or in a real-valued version.

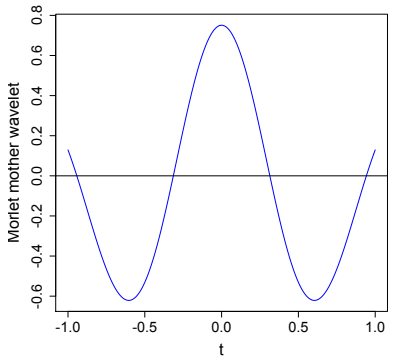

Figure 6. Morlet mother wavelet for $\xi = 5$ is shown in blue colour.

The Mexican hat wavelet or the Ricker wavelet is the second derivative of the Gaussian $e^{-x^2/2}$ and is defined by

$$\psi(x) = \frac{2}{\sqrt{3}} \pi^{-1/4} (1 - x^2) e^{-x^2/2}$$

after normalization to get $||\psi||_2 = 1$ (L^2(R)-norm) and $\psi(0) > 0$. Its plot is reminiscent of a cross section of a Mexican hat. The complex Mexican hat wavelet is formulated in terms of its Fourier transform given by $\hat{\psi}(\xi) = 2\sqrt{\frac{2}{3}} \pi^{-1/4} \xi^2 e^{-\frac{1}{2}\xi^2} I_{(0,+\infty)}(\xi)$.

The Fourier transform of the Shannon wavelet (Mallat (1998)) is the following:

$$\hat{\psi}(\xi) = \begin{cases} e^{-\frac{i\xi}{2}} & \text{if } \xi \in [-2\pi, -\pi] \cup [\pi, 2\pi] \\ 0 & \text{otherwise} \end{cases}$$

and the continuous wavelet is $\psi(x) = \frac{\sin(2\pi(t-1/2))}{2\pi(t-1/2)} - \frac{\sin(\pi(t-1/2))}{\pi(t-1/2)}$. This wavelet has infinite continuous derivatives with decay as $\frac{1}{t}$ at infinity due to the discontinuities of $\hat{\psi}(\xi)$ at $\xi = \pm\pi$ and $\xi = \pm 2\pi$.

4.1. Scalogram

The scalogram, a graph of the absolute value of the CWT, $|Tf|$, as a function of time, is used for different types of analysis. Color levels (high values of $|Tf|$ are in red) or gray levels are used (high values of $|Tf|$ are in black, zero in white) and a^{-1} is plotted on the ordered (y-axis). Some applications of the scalogram include

period detection in time series, change point detection, function discontinuity detection, signals recovering, among others. In all cases, the wavelet transform can detect the location in time of the event found.

The CWTs of 4 time series examples are shown below. They were done with the package Wavecomp in R [4] that uses Morlet wavelet family. In the scalogram, a range of colors appears related to the p-value obtained from a hypothesis test that is carried out via simulations:

H_0: There is no joint periodicity.

When H_0 is rejected, it indicates a great possibility that the periodicity is present in the data set. Given a level of significance, for example 0.01 or 0.05, the null hypothesis will be rejected if the p-value is smaller than the level of significance chosen. The scalogram shows the CWT values for each time and period in a range of colors from blue to red and a black contour line where the maximum values of the CWT are found for each instant of time. This black line, like the red regions, is found at the times and periods of highest wavelet power levels, where H_0 is rejected.

The first example is a sinusoidal data set with a period P=50. In Figure 7 you can see, from left to right, the original signal, the scalogram (with the period on the y-axis) and the reconstruction of the signal from the CWT. In this example 'Time' and 'Index' on the x-axis correspond to the step of time of the curve. In the middle panel, you can see that the CWT detects the period of 50 of the signal.

In Figure 8 the second example is showed: a signal with a variable period between $P = 20$ and $P = 100$. In this figure, from left to right, the original signal, the scalogram (with the period on the y-axis and the time step on the x-axis) and the reconstruction of the signal from the CWT can be seen. In the center panel of the figure, it is shown how the scalogram detects the variable period of the signal, its tendency and the reconstruction of the signal on the left panel is quite accurate. We can compare the performance of the scalogram with the STFT showed on the right panel of Figure 4.

In Figure 9, a signal with two periods: $P = 30$ and $P = 80$, both along all the range, is shown. In the figure, from left to right, the original signal, the scalogram (with the period on the y-axis and the time step called 'Index' on the x-axis) can be observed. On the right panel, it is easy to see two zones in red with a black line across indicating the two periods present in the signal.

Figure 10 shows a signal with two periods: $P = 30$ and $P = 80$, in separate intervals of time. On the right panel, it is simple to see two intervals of time with two different periods for the signal. The CWT can detect the instant of time when the change of period occurs.

In the four examples presented, some of the potentialities of the CWT can be observed: it can detect one or more periods present in the curve and indicate the time interval in which the detected period influences the behavior of the time series as well as it can detect the points of change where the change between

[4] https://cran.r-project.org/web/packages/WaveletComp/WaveletComp.pdf

periods occurs. All of these are regarding an evenly sampled time series. Because of this, for 55 Cyg light curve (from TESS mission) a partition of the data is made and they are analyzed separately obtaining the scalograms in Figure 12. Although each partition still has irregularly sampled data, the time differences between the measurements are quite similar allowing the use of the Wavecomp package which is for equidistant time series.
Figure 12 shows two significant periods (solid black lines). A first period p_1 that starts with a value $2 \leq p_1 \leq 4$, grows in time and stands at $p <\approx 4$ at the end of the time interval (right panel); and a local in time period $p = 2$ that appears during the middle time of the first part of the data (middle panel) and decreases to a value just below 2 during the second part (right panel).

The graph is seen divided into two regions, one with brighter colours and the other with fainter colours. It corresponds to the cone of influence, described in Lenoir & Crucifix (2018), the wavelet analysis extends a little at the edges of the time series, due to the wavelet support (values where the wavelet is not null) then a part goes beyond after the last point of the time series, or before the first point of the time series. Due to this, one half cone is removed from the left end and another from the right end, from the area under analysis, producing the region with fainter colors. This situation is present in each of the plots but is more evident in this figure.

For data with time differences between more irregular measurements it is recommended to look for other alternatives. Some of them are listed below. Developments have been made by interpolating the data to obtain equispaced data (see for instance Thiebaut & Roques (2005)) or in other cases the continuous wavelet transform has been used on the raw data (Lenoir & Crucifix (2018)). Foster (1996) proposed the use of the weighted wavelet Z transform to face this problem. In his work the author proposed an adaptation of wavelet analysis for irregularly spaced data called Weighted Wavelet Z transform (WWZ-transform). It consists of analyzing the data through projections of the Morlet mother wavelet, which add up with some specific weighting. Foster (1996) showed the efficiency of the method in some signals although its limitation consists in detecting periods and amplitudes when the gap in data is larger than the period to be detected. WWZ transform proved good performance discerning in frequency and time, period and amplitude of long-period stars in presence of unevenly data.

According to Lenoir & Crucifix (2018), interpolation procedures can significantly affect the results especially when hypothesis testing is used. The authors proposed a method to analyzed unevenly time series by means of the scalogram of wavelet analysis without interpolation of the data. The authors proposed to use projections of the continuous Morlet mother wavelet, without weighting, and implemented his methodology in the WEAVEPAL software (developed on Python 2, Lenoir & Crucifix (2017)). The method seems efficient as long as the length of the intervals without observations is little variable. It is also observed as a limitation the inability to detect periods when the gap is larger than the period to be detected.

Tarnopolski et al. (2020) argue that irregular data makes it difficult to calculate certain magnitudes and introduces spurious peaks in the power spectral

density. To solve this problem the authors propose to interpolate the data to make them regular using a method based on the ARMA time series model called MIARMA.

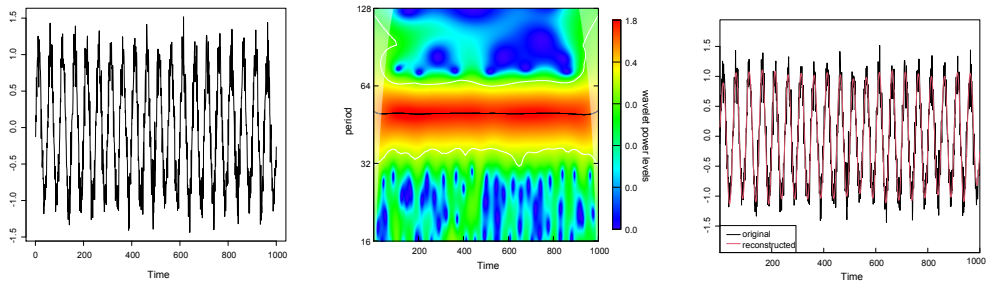

Figure 7. The original sinusoidal signal with period 50, the scalogram and the reconstruction from the CWT are shown from left to right panels.

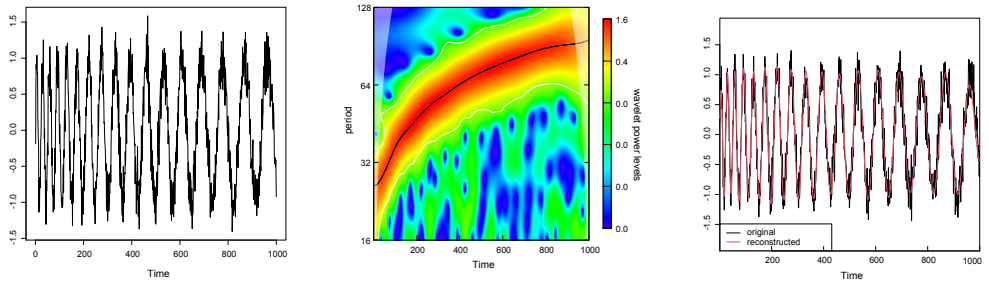

Figure 8. The original sinusoidal signal with a variable period from 20 to 100, the scalogram and the reconstruction from the CWT are shown from left to right panels. Center panel shows how the scalogram manages to capture the variable period.

5. Conclusions

In this paper we presented a brief summary of the theory of wavelet analysis, multiresolution analysis, and the continuous wavelet transform along with some applications in periodic time series to detect periods or points of change through simulations and real data. The R software was used for the implementation of numerical simulations and the wavelet analysis.

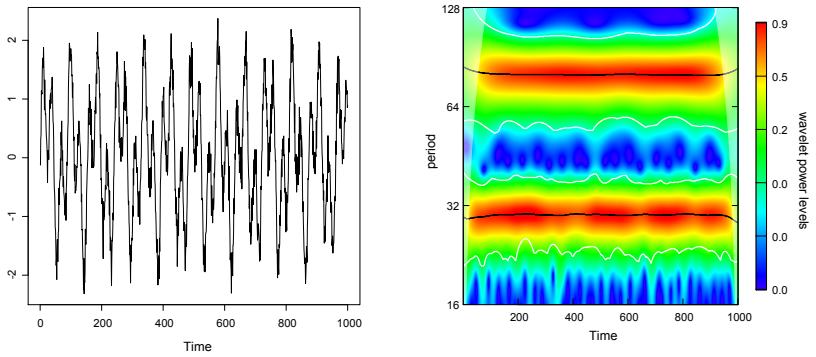

Figure 9. The original sinusoidal signal with two periods $(30, 80)$ along the curve is shown on the left panel. The corresponding scalogram with the evidence of the two periods along all the range of the signal is shown on the right panel.

6. R Codes

Some of the R codes used in this Chapter are presented in this section. Note that the '+' sign is used in some commands to indicate that they continue on the next line. When running them in R you must select all the lines corresponding to the command, deleting the '+'. For example, for the command:

```
plot(t,haar3, type='l', ylim=c(-2.1,2.1),xlim=c(-0.5,2.5),
+                 col='blue')
```

put in R without '+' and select all the sentences in order to run it:

```
plot(t,haar3, type='l', ylim=c(-2.1,2.1),xlim=c(-0.5,2.5), col='blue')
```

6.1. STFT

Figure 1:

```
install.packages('e1071')
library(e1071)

t1<-seq(0,100,0.01)
length(t1)
x1<-sin((0.2*pi)*t1[1:3000])
x2<-1.5*sin(0.5*pi*t1[3001:4000])
x3<-2*sin((0.8*pi)*t1[4001:10001])
x<-c(x1,x2,x3)
z1<-sin((3/5)*t1[1:3000])
z2<-0.5*sin(0.5*t1[3001:6000])
z3<-2*sin((1/10)*t1[6001:10001])
obj<-c(z1,z2,z3)
```

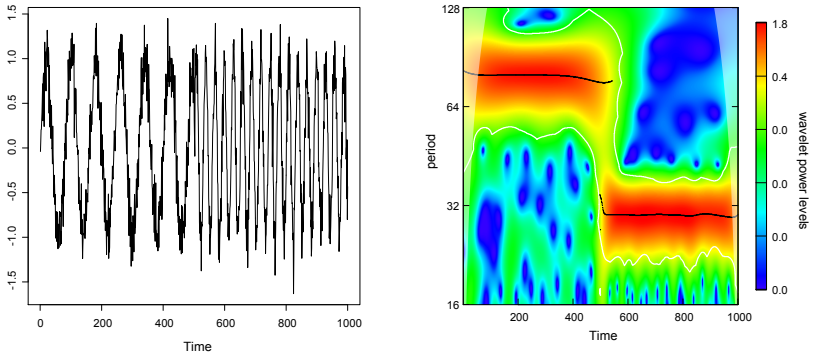

Figure 10. The original sinusoidal signal with two periods, $P = 80$ for the first part of the curve and $P = 30$ for the final part is shown on the left panel. The corresponding scalogram with the evidence of the two detected periods and the time interval involving each one is shown on the right panel.

```
par(mfrow=c(2,2))
plot(x, type='l', main='Sine wave 1', xlab='Time', ylab='Signal')
y<-e1071::stft(x)
plot(y, xlab='', ylab='', main='STFT of Sine wave 1', ylim=c(0,15))
plot(obj, main='Sine wave 2', xlab='Time', ylab='Signal',type='lines')
z<-e1071::stft(obj)
plot(z, xlab='', ylab='', main='STFT of Sine wave 2', ylim=c(0,15))
```

Figure 2:

```
install.packages('lomb') #Lomb Scargle periodogram
library(lomb)
lsp(x, times=t1,ofac=5, xlim=c(0,0.5))
```

Figure 3:

```
install.packages('e1071')
library(e1071)

x<-rnorm(500)
y<-e1071::stft(x)
obj<-arima.sim(n = 63, list(ar = c(0.8897, -0.4858), ma = c(-0.2279, 0.2488)),
+                  sd = sqrt(0.1796))
```

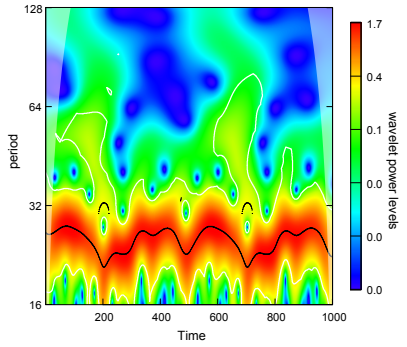

Figure 11. The scalogram of the same sinusoidal curve of Figure 7 with period 50 where 50% of data was removed. In presence of irregular sampled data the scalogram underestimates the period.

```
z<-e1071::stft(obj)


plot(x, type='l', main='White noise', xlab='Time', ylab='Signal')
plot(y, xlab='', ylab='', main='STFT of white noise')
plot(obj, main='ARMA(2,2)', xlab='Time', ylab='Signal')
plot(z, xlab='', ylab='', main='STFT of ARMA(2,2)')
```

Figure 4:

```
install.packages('WaveletComp')
library(WaveletComp)

w = periodic.series(start.period = 20, end.period = 100, length = 1000)
w = w + 0.2*rnorm(1000)
wy<-e1071::stft(w)

par(mfrow=c(1,2))
plot(w, type='l', main='A signal with variable periods', xlab='Time', ylab='Signal')
plot(wy, xlab='', ylab='', main='STFT of the signal', ylim=c(0,20))
```

6.2. Haar Wavelet

Figure 5:

```
t<-seq(-2,3,0.01)
length(t)
```

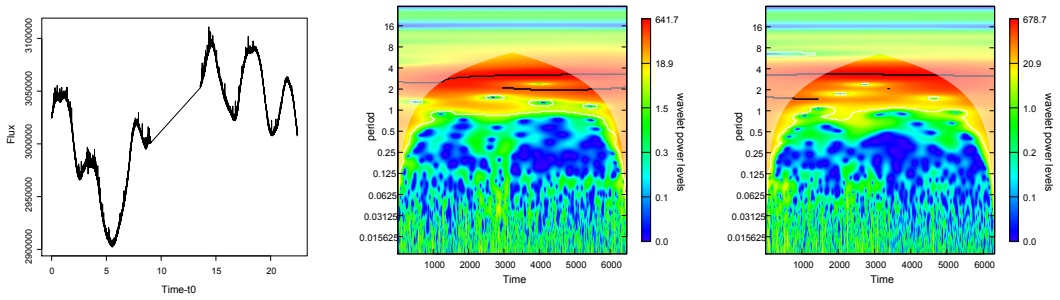

Figure 12. The original light curve of 55 Cyg is shown on the left panel. After splitting the signal in two parts the two corresponding scalograms are shown on the right panels.

```
par(mfrow=c(2,3))
title('Wavelet Haar')
#Plot 1: Wavelet Haar father: j=0 k=0. -----------------ORIGINAL
haar1<-c(rep(0,200), rep(1,100), rep(0,201))
plot(t,haar1, type='l', ylim=c(-2.1,2.1),xlim=c(-0.5,2.5), col='blue',
+              ylab='', xlab='(a)')
abline(v=0)
abline(h=0)

#Plot 2: Wavelet Haar father: j=0 k=1
haar2<-c(rep(0,300), rep(1,100), rep(0,101))
plot(t,haar2, type='l', ylim=c(-2.1,2.1),xlim=c(-0.5,2.5), col='blue',
+              ylab='', xlab='(b)')
abline(v=0)
abline(h=0)

#Plot 3: Wavelet Haar father: j=1 k=1/2
haar3<-c(rep(0,250), rep(2,25), rep(0,226))
plot(t,haar3, type='l', ylim=c(-2.1,2.1),xlim=c(-0.5,2.5), col='blue',
+               ylab='', xlab='(c)')
abline(v=0)
abline(h=0)

#Plot 4: Wavelet Haar mather: j=0 k=0.  ---------------ORIGINAL
haar4<-c(rep(0,200), rep(1,50), rep(-1,50),rep(0,201))
plot(t,haar4, type='l', ylim=c(-2.1,2.1),xlim=c(-0.5,2.5), col='violet',
+              ylab='', xlab='(d)')
abline(v=0)
abline(h=0)

#Plot 5: Wavelet Haar mather: j=0 k=1
haar5<-c(rep(0,300), rep(1,50), rep(-1,50),rep(0,101))
```

```
plot(t,haar5, type='l', ylim=c(-2.1,2.1),xlim=c(-0.5,2.5), col='violet',
+             ylab='', xlab='(e)')
abline(v=0)
abline(h=0)

#Plot 6: Wavelet Haar mather: j=1 k=1
haar6<-c(rep(0,300), rep(2,25), rep(-2,25),rep(0,151))
plot(t,haar6, type='l', ylim=c(-2.1,2.1),xlim=c(-0.5,2.5), col='violet',
+              ylab='', xlab='(f)')
abline(v=0)
abline(h=0)
```

6.3. CWT and Scalogram

This section is based on Roesch & Schmidbauer (2018).

Figure 7: A series with a constant period, period equal 50

```
install.packages('WaveletComp')
library(WaveletComp)

set.seed(1)
x1 = periodic.series(start.period = 50, length = 1000)
x1 = x1 + 0.2*rnorm(1000)  # add some noise
plot(x1, type='l', xlab='Time')
date=1:1000

my.data <- data.frame(date=date, x = x1)
my.w <- analyze.wavelet(my.data, "x",
loess.span = 0,
dt = 1, dj = 1/250,
lowerPeriod = 16,
upperPeriod = 128,
make.pval = TRUE, n.sim = 10)
#scalogram
wt.image(my.w, color.key = "quantile", n.levels = 250,
legend.params = list(lab = "wavelet power levels", mar = 4.7))
#red zones with black lines corresponds to more significant periods


#recover the significant periods and the average period
ta<-my.w$Period[which(my.w$Ridge==1,arr.ind = TRUE)[,1]]
mean(ta)

#reconstruct the signal using wavelets
reconstruct(my.w, plot.waves = FALSE, lwd = c(1,2),
legend.coords = "bottomleft", ylim = c(-1.8, 1.8))
```

Figure 8: A series with a variable period.

```
install.packages('WaveletComp')
library(WaveletComp)

x = periodic.series(start.period = 20, end.period = 100, length = 1000)
x = x + 0.2*rnorm(1000)
plot(x1, type='l', xlab='Time')

my.data <- data.frame(x = x)
my.w <- analyze.wavelet(my.data, "x",
loess.span = 0,
dt = 1, dj = 1/250,
lowerPeriod = 16,
upperPeriod = 128,
make.pval = TRUE, n.sim = 10)
wt.image(my.w, n.levels = 250,
legend.params = list(lab = "wavelet power levels"))
#The variable period is observed in the scalogram

#reconstruction
my.rec <- reconstruct(my.w)
```

Figure 9: A series with two periods.

```
install.packages('WaveletComp')
library(WaveletComp)

set.seed(1)
x1 <- periodic.series(start.period = 80, length = 1000)
x2 <- periodic.series(start.period = 30, length = 1000)
x <- x1 + x2 + 0.2*rnorm(1000)
plot(x, type='l', xlab='Time')


my.data <- data.frame(x = x)
my.w <- analyze.wavelet(my.data, "x",
loess.span = 0,
dt = 1, dj = 1/250,
lowerPeriod = 16,
upperPeriod = 128,
make.pval = TRUE, n.sim = 10)
wt.image(my.w, n.levels = 250,
legend.params = list(lab = "wavelet power levels") )

#reconstruction
reconstruct(my.w, plot.waves = TRUE, lwd = c(1,2),
legend.coords = "bottomleft")
```

Figure 10: A series with two periods in different times.

```
install.packages('WaveletComp')
library(WaveletComp)

set.seed(1)
x1 <- periodic.series(start.period = 80, length = 1000)
x2 <- periodic.series(start.period = 30, length = 1000)
x <- c(x1 , x2) + 0.2*rnorm(1000)
plot(x, type='l', xlab='Time')


my.data <- data.frame(x = x)
my.w <- analyze.wavelet(my.data, "x",
loess.span = 0,
dt = 1, dj = 1/250,
lowerPeriod = 16,
upperPeriod = 128,
make.pval = TRUE, n.sim = 10)
wt.image(my.w, n.levels = 250,
legend.params = list(lab = "wavelet power levels") )
```

Figure 11: An unevenly sampled data.

```
install.packages('WaveletComp')
library(WaveletComp)

set.seed(1)
x1 = periodic.series(start.period = 50, length = 1000)
x1 = x1 + 0.2*rnorm(1000)  # add some noise
date=1:1000


#Deleting some data to produce gaps
obs <- sample(seq(x1), 0.5*length(x1)) # 50% gaps
x11 <- x1[sort(obs)]
date1 <- date[sort(obs)]

par(mfrow=c(1,2))
plot(x1 ~ date, pch=".", cex=2)
plot(x11 ~ date1, pch=".", cex=2)

par(mfrow=c(1,1))

my.data11 <- data.frame(date=date1, x = x11)   #with unevenly data
my.w11 <- analyze.wavelet(my.data11, "x",
loess.span = 0,
```

```
dt = 1, dj = 1/250,
lowerPeriod = 16,
upperPeriod = 128,
make.pval = TRUE, n.sim = 10)

wt.image(my.w11, color.key = "quantile", n.levels = 250,
legend.params = list(lab = "wavelet power levels", mar = 4.7))
#In presence of unevenly data wavecomp subestime the period.

reconstruct(my.w11, plot.waves = FALSE, lwd = c(1,2),
legend.coords = "bottomleft", ylim = c(-1.8, 1.8))
#Be carefull, Wavecomp analyze the serie sticking the gaps
```

7. Notation

Some notation used in the article is the following:

R is the set of real numbers,

Z is the set of integer numbers,

$\oplus$ direct sum of two or more linear sub-spaces, that is, a new subspace spanned for generators of each sub-space in the direct sum where each is orthogonal to any other.

$\ominus$ of a subspace included in another subspace, if $B \subset A$, then $A \ominus B$ is the orthogonal complement of B within A,

$||.||_2$ 2-norm of functions, $||.||_2 = \int_{-\infty}^{\infty} |f(t)|^2 dt$,

$L^2(\mathrm{R})$ Hilbert space of real functions with finite 2-norm.

Acknowledgments. This project has received funding from the European Union's Framework Programme for Research and Innovation Horizon 2020 (2014-2020) under the Marie Skłodowska-Curie Grant Agreement No. 823734.

References

Beylkin G., R. C., V. R., 1991, *Comm. Pure and Appl. Math.*, **44**, 141
Cáceres G. A. e. a., 2019, *Astron. J.*, 158(57)
Daubechies I., 1988, *Comm. Pure and Appl. Math.*, **41**, 909
Daubechies I., 1992, *Ten Lectures on Wavelets*, Society for Industrial and Applied Mathematics
Eyheramendy S., Elorrieta F., Palma W., 2018, *MNRAS*, **481(4)**, 4311
Fischer-Cripps A., 2002, *"Newnes Interfacing Companion", A. Fischer-Cripps (ed.)*, Newnes, Oxford
Foster G., 1996, *AJ*, **112**, 1709
Härdle W., Kerkyacharian G., Picard D., Tsybakov A., 1998, *Wavelets, approximation, and statistical applications*, Springer-Verlag, New York

Kelly B. C., C. B. A., M. S., A. S., P. U., 2014, *ApJ*, **788(1)**, 33
Lenoir G., Crucifix M., 2017, *EGU General Assembly Conference Abstracts*, EGU General Assembly Conference Abstracts, p. 15162
Lenoir G., Crucifix M., 2018, *Nonlin. Processes Geophys.*, **25**, 175
Mallat S., 1989, *IEEE Transactions on Pattern Analysis and Machine Intelligence*, **11**, 674
Mallat S., 1998, *A Wavelet tour of signal processing*, Academic Press, Elsevier, United States, 1998
Meyer Y., 1986, *Lectures given at the University of Torino, Italy*, pp 1–42
Percibal D. B., Walden A. T., 2000, *Wavelet Methods for Time Series Analysis*, Cambridge University Press
Poularikas A., 2010, *The Transforms and Applications Handbook. 3rd Edition*, Taylor and Francis Group, LLC
Roesch A., Schmidbauer H., 2018, *WaveletComp: Computational Wavelet Analysis*, R package version 1.1
Tarnopolski M., Åżywucka N., Marchenko V., Pascual-Granado J., 2020, *The Astrophysical Journal Supplement Series*, **250(1)**, 1
Thiebaut C., Roques S., 2005, *EURASIP Journal on Applied Signal Processing*, **2005**, 852587

Pulsations Along Stellar Evolution
VIII LAPIS Summer School
AAA Workshop Series 12, 2021
M. Kraus & A.F. Torres, eds.

Observing Techniques and Missions

M. Kraus[1]

[1]*Astronomical Institute, Czech Academy of Sciences, Fričova 298, 251 65 Ondřejov, Czech Republic*

Abstract. Stellar pulsations can cause variability in the brightness of the star as well as in the shape and radial velocity of photospheric lines. To determine the periods and modes of pulsations, two different but complementary observational techniques are in use: photometric light curves to measure the brightness variations, and spectroscopic time series to analyze the time-dependent motions at the stellar surface. In the first part of this Chapter, both observing techniques and their sources of errors and limitations are presented. In the second part, an overview of the various space and ground-based missions for both photometry and spectroscopy is given. Considering all the currently available and newly planned instruments, the future for research in variable and pulsating stars is bright.

Key words: asteroseismology — stars: oscillations — stars: atmospheres

1. Introduction

Pulsations modify the observable properties of stars. The motion of the surface elements cause variations in both the velocity and the stellar flux. Changes in flux are primarily due to temperature variations[1] and can be traced by photometric monitoring. The velocity variations are detectable in spectroscopic time series.

Most stars pulsate in more than one mode and observations provide only the combined effect of all modes simultaneously. A simple example is shown in Figure 1, in which two sine-curve modes with different period, amplitude and phase superimpose to the total observable signal shown in the right panel. The combined signal can be either a photometric light curve or a radial velocity curve. The aim of any data analysis is to deconvolve the observed signal into the contributions of each individual mode thereby determining their properties, i.e., frequency, amplitude, and mode identification. These are the fundamental sets of data in asteroseismology.

To disentangle the various contributing modes, suitable frequency analysis techniques are needed, which are described in other Chapters of this book. Here, the focus is on another aspect: The quality of the data used for the analysis. Because both photometry and spectroscopy require different instrumentation and

[1]Unless the star undergoes large-amplitude radial pulsations. In this case, photometric observations are also sensitive to the changes in stellar radius.

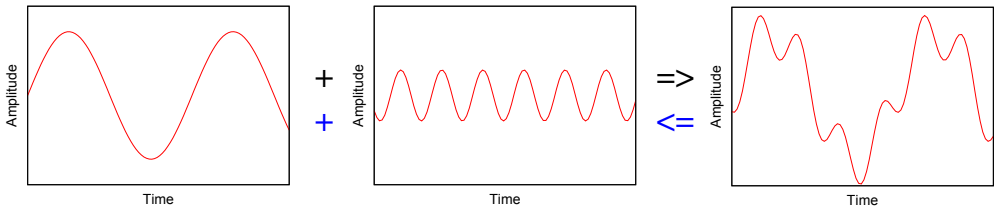

Figure 1. Example of two periods (left and middle panels) with different frequencies, amplitudes, and phases that superimpose (black path) to the total, observable signal (right panel). To extract information about pulsations, the observed signal needs to be deconvolved into the individual contributions (blue path).

observing conditions, these two observing modes are described separately. But before coming to the details, a few general terms need to be introduced and discussed as well, which are relevant for both photometry and spectroscopy[2].

Precision The most relevant parameter in asteroseismology is precision. As we will see later (Section 4), asteroseismology and the search for and characterization of exoplanets post the same demands on instrumentation. Consequently, space missions as well as high-duty-cycle ground-based projects dedicated to one of them, also delivers data for the other scientific branch. And the need for extremely high precision is the ultimate driver for instrumental development to satisfy these requirements.

During the past $\sim$ 50 years the precision in astronomical photometry has increased from ~ 0.01 mag to a few μmag. Equally, the precision in radial velocity determination has increased from $\sim 1\,\mathrm{km\,s^{-1}}$ to 10s of $\mathrm{cm\,s^{-1}}$. In both, an improvement by four orders of magnitude has been achieved. Each observer should make every effort to minimize errors and to improve the precision because only the best data will deliver meaningful results. As a matter of fact, the higher the precision in both photometry and spectroscopy the larger are the sets of identified frequencies.

Duty Cycle Besides precision, the duty-cycle of observations is of great importance. Generally speaking, the duty-cycle is a measure for the fraction of the observing time spent on the variability of the target. Ideally, one would wish for a duty cycle of 100%, because every gap in the observations can lead to confusion in frequency determination. Therefore, space missions are best suited for following the variability of objects. But these have enormous costs. For ground-based observations, the duty-cycle is usually much smaller, typically less than 50% for single site observations for a short time span under good weather conditions.

Time The principal data of asteroseismology are time series, either in photometry (light curve) or in spectroscopy (radial velocity curve). Time series

[2]Parts of this Chapter are based on and follow the excellent textbook of Aerts et al. (2010).

allow us to derive asteroseismic frequencies. For reliable results, the time of the observations must be known to high precision.

In asteroseismology normally the Coordinated Universal Time (UTC) which depends on the Earth's rotation is used as reference system[3]. But the UTC is not a uniform timescale because the length of the day has an annual variation of about a millisecond. Moreover, long term drifts appear as well due to the tidal interaction between the Moon and the Earth. Therefore, a sort of "leap seconds" are introduced to keep UTC in phase with the atomic time. For the most precise studies, however, a constant, "ephemeris time" scale without leap seconds is needed.

Depending on the desired precision, the effects of the Earth's motion about the Sun, or about the solar system barycenter are removed and times are converted to Julian Dates. The term "Julian Date (JD)" was introduced by Joseph Justus Scaliger in 1583 at the time of the Gregorian Calendar reform, who set the starting point to noon Universal Time (UT), 1 January 4713 BCE (before current era). Because of this historically chosen zero point, JD is nowadays a huge number, and astronomers often opt to use the "Modified Julian Date (MJD)", which is defined as JD-2400000.5, which reduces the number and also eliminates the half-day offset. Another convention is the "Heliocentric Julian Date (HJD)", which provides the observation time corrected to the solar center by accounting for the disturbances introduced by the orbit of Jupiter. For many purposes in astronomy and asteroseismology based on single site data this is a sufficiently precise timescale.

Better precision is achieved when the observation time is corrected to the barycenter of the solar system ("Barycentric Julian Date (BJD)"), whereas the ultimate precision is obtained when the leap seconds are subtracted. This is called the "Barycentric Julian Ephemeris Date (BJED)". BJD or BJED should be used for long-term (years) data sets as well as for data collected from multiple sites.

Every astronomer has to make sure that the time base(s) are correct, especially when merging data sets from different sources and sites. An easy time trap when being careless with the use of the time base can lead to the detection of a planet in the signal which is, however, not related to any new discovery, but just due to the Earth's orbit.

2. Photometry

The most widely used tool to study stellar variability is by measuring precisely the changes in stellar intensity. This is done by means of photometry.

The quality of detectors has drastically changed over the past centuries. Observations started with the human eye which can provide visual observations with an accuracy of about 0.05–0.10 mag. Such kind of data are sufficient for the study of large amplitude pulsators, e.g Mira variables.

---

[3]The reader interested in the complexity of the precise time is referred to the website of the U.S. Naval Observatory: https://www.usno.navy.mil/USNO/time

A considerable improvement in precision was achieved with photographic plates. This technology started in the 19$^{\rm th}$ century and dominated the measurement of stellar brightness until the CCD era started in the 1990s and revolutionized astronomical observations. While photographic plates are still occasionally in use, CCDs are nowadays ubiquitously established and will be the predominant method of measuring stellar intensity and its variations in the 21$^{\rm st}$ century.

While ground-based photometry has reached precisions of 10s of μmag, space photometric missions are capable of μmag precision. Considering that the mean magnitude of a star may be known only with an accuracy of a few millimag, the variations in stellar brightness, and hence the amplitudes of the pulsations, can be determined to precisions 1000 times better.

2.1. Sources of Error in Photometry

A number of effects exist that can cause errors to the photometric measurements. Some are due to the limitations of the technical equipment, others are because of restrictions set by the observing conditions.

Photon Statistics The process of photon detection has a normal distribution. Consequently, if we denote with N the number of detected photons, the statistical error is given by $\sqrt{N}$, and the signal-to-noise ratio goes as $S/N = N/\sqrt{N} = \sqrt{N}$. In principle, the noise level can be reduced by improving the signal, i.e., by increasing the integration time. However, very long integrations for a highly reduced error due to photon statistics is not useful in case the signal that is supposed to be detected has short periods. And many pulsating stars, such as pulsating white dwarfs, roAP stars, solar-like oscillators, or sdB stars have rather short variability timescales but are faint objects. For those targets, a large telescope can help in increasing the signal, but it is still limited by photon statistics.

Atmospheric Sources of Errors – Extinction Variations In the absence of clouds, the extinction of the Earth's atmosphere is a further factor influencing and disturbing photometric observations. It measures the amount of starlight that is removed along the line of sight as a function of the airmass. By definition, Earth's atmosphere has an airmass (X) of unit 1 for observations towards the zenith, and increases towards the horizon, because of the longer light path through the atmosphere. If one approximates the atmosphere with a plane-parallel slab model, the airmass for the observation of an object under the zenith distance angle z would simply be $X = \sec(z)$. To account for the curvature of the Earth's atmosphere, a polynomial approximation has been derived and is generally in use (Hardie, 1964),

$$X = \sec(z) - 0.0018167(\sec(z)-1) - 0.002875(\sec(z)-1)^2 - 0.0008083(\sec(z)-1)^3.$$

This relation is precise for zenith angles up to $z = 85°$, which is much closer to the horizon than the angle under which observations are usually carried out. In many cases it is even sufficient to use just the first two terms of this equation. The reduction of the observable starlight due to the airmass is thus just a function of the zenith angle.

However, in reality the sky transparency is always variable in time and in both zenith angle and azimuth. The reason is, that the atmospheric conditions depend not only on the airmass, but also on other parameters, such as temperature and humidity, and on the levels of dust and aerosols in the atmosphere. The timescales of these variations in sky transparency are on the order of 15 min and longer. These transparency variations thus cause an atmospheric noise that depends on frequency and that has higher amplitudes at lower frequencies. It is referred to as "pink" noise. To account for this variable atmospheric extinction, in particular in photometric observations of stars with pulsation periods (much) longer than about 15 min, it is required to observe also non-variable standard stars for comparison.

A cloudless night with no highly variable dust or aerosols in the atmosphere is usually called "photometric".

Atmospheric Sources of Errors – Scintillation With the term scintillation one refers to the variable refraction in the atmosphere, which makes the stars "twinkle" when observed with the naked eye. The Earth's atmosphere consists of many gas cells. Each of them has a radius of 10s of cm, and the gas within each cell has slightly different values of pressure, temperature and humidity thus causing a slight variation in refraction from cell to cell. The light path from the top of the atmosphere down to the telescope hence passes through many cells, and at each of them it changes slightly its direction. Moreover, the positions of these cells are not fixed but depend on and travel with the wind conditions, so that the total amount of light that reaches the detector is variable. In this way, scintillation causes a "white" noise in the signal, i.e. a noise with no frequency dependence. It is thus the dominant source of error in a photometric night for periods shorter than the 15 min limit set by the atmospheric extinction.

The noise caused by scintillation follows also (as photon statistics) a normal distribution, because the light simultaneously passes through many independent cells, and its level drops with the square root of the number of gas cells along the light path. As the number of scintillation cells increases with increasing telescope aperture, the amount of noise decreases. Big telescopes are therefore better suited for observations of pulsating stars with scintillation as the limiting noise source.

Instrumental Sources of Noise The technical equipment used for photometric observations has also sources of errors. Some are periodic, others random.

Every CCD has pixel-to-pixel sensitivity variations. For the high-quality CCDs that are nowadays in use these variations can still be on the order of 1%, which is too high to be ignorable. Other sources of CCD noise are dark currents, bias, and read-out noise. They can be accounted for by collecting additional calibration images along with the science frames.

- *Bias images.* These have zero second exposures. They are taken to remove any internal bias structure across the chip such as the amount of counts accumulated during the reading out of the CCD.
- *Flat-field images.* Flats contain the information about the pixel-to-pixel variation. They are obtained by illumination of the entire CCD with a constant light source.

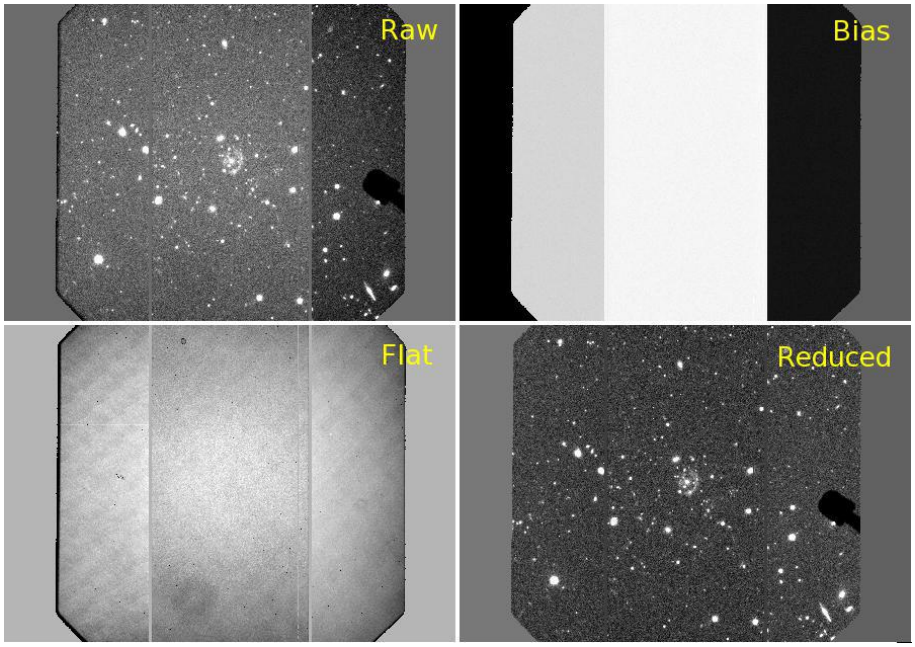

Figure 2. Example set of photometric observations. The raw image needs to be corrected for bias and flat frames to achieve a reduced image suitable for reliable intensity measurements.

- *Dark images.* Darks are long exposure images taken with the shutter closed. These are only necessary in case of a considerable dark current in the CCD. Most modern CCDs have no significant dark current so that dark images are usually not required anymore.

Examples of the calibration images (bias and flat) and their impact on the science frames are shown in Figure 2 for demonstration purpose. For a comprehensive description of CCDs and data reduction the interested reader is referred to the Handbook of CCD Astronomy by Howell (2006).

For the most precise photometry, it is essential to keep a stellar image fixed at the sub-pixel scale to avoid that stars are moving over the CCD, but no telescope can track to that precision. Therefore, autoguiding is needed. The use of autoguiding also eliminates another instrumental effect which might cause an artificial periodic signal. This is the periodic error in the right ascension drive in the telescope which, in the absence of autoguiding, injects a signal into photometric time series with the frequency of the telescope drive. Typical drive periods are 2 or 4 siderial minutes. They can cause confusion with stellar periods for stars pulsating in that frequency range such as roAP stars, solar-like oscillators, sdBV stars, or pulsating white dwarfs. To identify and eliminate such periodic instrumental signals it is necessary to have a standard star observed, ideally in the same field of view as the target.

2.2. Filters

Photometric observations provide information about the stellar brightness in a certain wavelength range, defined by the used filter. Many different filter systems exist, and the interested reader might inspect the work of Bessell (2005) for an overview of the various broad and narrow band systems as well as of the observational complications with standard photometry. The three most commonly used systems are Johnson $UBVRI$, Strömgren $uvby$, and the Sloan Digital Sky Survey (SDSS) $u'g'r'i'z'$ filters (Fukugita et al., 1996).

Every filter has its defined wavelength coverage, transmission curve, and sensitivity curve. Therefore, the use of identical filters is important when combining data from different facilities, or when organizing multi-site campaigns, because the amplitudes and phases of stellar pulsations are wavelength dependent. Changes in stellar brightness caused by oscillations are predominantly due to temperature variations, which manifest themselves particularly in the blue spectral range. Consequently, the monochromatic amplitudes of the pulsations due to temperature variations are highest in the blue as well.

One might interpret photometry through filters as sort of spectroscopy, just at very low resolution. But we need high-resolution spectroscopy to extract additional and viable complementary information about the pulsation properties of stars.

3. Spectroscopy

Spectroscopic observations provide an important tool, not only for asteroseismology, but for all fields of astronomy and astrophysics. With respect to stellar astronomy they are used for spectral classification, for the derivation of stellar parameters such as effective temperature and gravity, as well as for the determination of the atmospheric chemical abundances. Spectroscopic data are also vital to derive the mass-loss rates of stars, and to characterize circumstellar environments. Moreover, whenever spectroscopic time series are at hand, they can provide information on stellar multiplicity or the presence of a planet, or they can be used to analyze and classify stellar variability either due to surface spots, magnetic fields, or pulsation activity.

High-resolution spectroscopic data, suitable for asteroseismology, can to date only be acquired with ground-based facilities. Different types of spectrographs exist, ranging from linear single order to echelle systems, but they all usually consist of a collimator, a prism or grating for dispersion, and a CCD camera. While every instrument needs its own reduction procedure, for which often an instrument pipeline exists, the basic steps are the same for most spectrographs.

As for photometry (Section 2), calibration images need to be taken along with the target frames. These are again bias, flats, and eventually dark frames. However, in contrast to photometry, also calibration lamp spectra need to be secured. An example of how the required observational sets look like in both single order and echelle spectroscopy is shown in Figure 3 and 4, respectively, and detailed descriptions of spectroscopic observations and data reduction can be found in Massey & Hanson (2013).

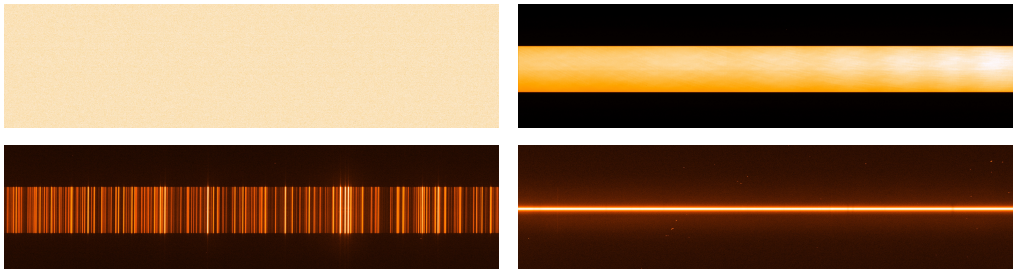

Figure 3. Example set of spectroscopic single-order observations. These are: bias (top left), flat (top right), and comparison lamp spectrum (bottom left) which are needed along with the stellar spectrum (bottom right) for correction and calibration.

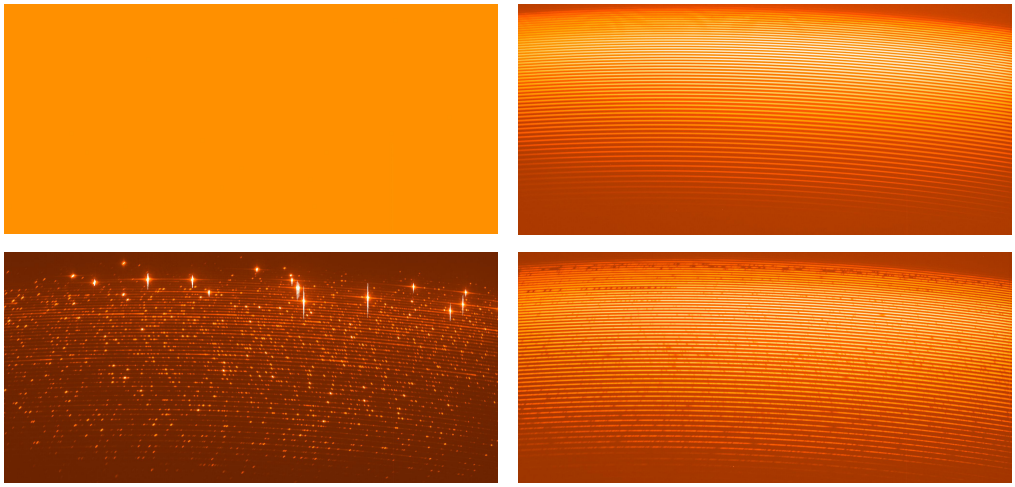

Figure 4. Example set of spectroscopic observations taken with an echelle spectrograph. Shown are the same set of observations as for single-order spectroscopy: bias, flat, calibration lamp and stellar spectrum with the different spectral orders projected parallel to each other on the CCD. Note that in the shown calibration lamp spectrum several intense lines are saturated causing bright artifacts.

In brief, the raw images need to be corrected for dark current (if available), then the bias needs to be subtracted and the images have to be divided by the master flat, which is created from a number of flats taken throughout the observing night (depending on stability of the spectrograph). Then the stellar spectrum has to be extracted whereby the sky background is subtracted. For echelle data, each spectral order needs to be identified and extracted separately thereby correcting for the so-called blaze function. Afterwards, the spectrum needs to be wavelength calibrated by using the comparison lamp spectrum. Fi-

nally, the wavelength calibrated spectrum needs to be shifted to the solar system barycentric reference frame.

Any changes in pressure, temperature or humidity within the environment in which the instrument is located lead to small shifts in wavelength. Modern spectrographs are therefore placed in a room with stable conditions. Nevertheless, observations taken during a night can still display some wavelength drifts on a timescale of hours. These drifts cause a low-frequency noise in the amplitude spectrum of the radial velocity variations, in analogy to the low-frequency noise in photometry due to extinction variations.

For exoplanet studies a precision in radial velocity measurements down the level of $\mathrm{m\,s^{-1}}$ or better is required. In this case, it is advised to implement an iodine cell into the light path. The iodine imprints its rich I_2 molecular line spectrum onto the stellar spectrum for very accurate wavelength calibration. The downside of using an iodine cell is that it requires detailed modeling of the molecular lines and their deconvolution from the stellar spectrum. Even worse, it reduces the S/N of the spectrum, because the iodine reduces the incoming starlight by about a factor of two. Therefore, this method of wavelength calibration is usually not used for asteroseismology.

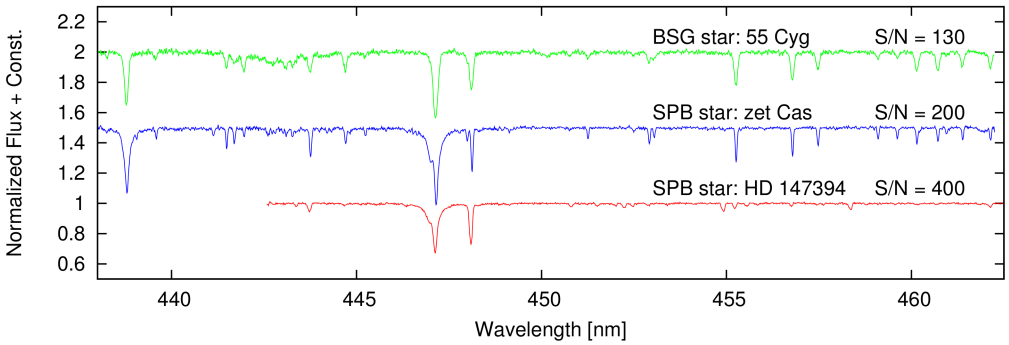

Figure 5. Examples of final, normalized spectral pieces of the pulsating B supergiant (BSG) 55 Cyg (top) and two slowly pulsating B (SPB) stars (middle and bottom). The upper two stars are of early B-type, the bottom star is a late-type B star. Data have been taken with the single order spectrograph at the Perek 2-m telescope at Ondřejov Observatory providing a resolution of $R \sim 18\,000$ around 450 nm.

An example of final, normalized spectral pieces of three pulsating stars is shown in Figure 5. The upper two stars are of early B-type, whereas the bottom spectrum is from a late B-type star. Noticeably, the spectral appearance changes with effective temperature and luminosity class of the star. Therefore, the choice of suitable lines for the analysis depends on the spectral type of the star. But also on the stellar rotation, which can lead to significant broadening and, hence, to blending of adjacent lines. When analyzing time series, one should make sure to focus on deep, unblended lines, ideally of metals.

A further important parameter is the S/N value of the spectra. The higher S/N, the more accurately the line profile parameters can be measured. However,

to achieve a high S/N in high-resolution data for faint and short-period pulsators is a further challenge and not always achievable, requiring compromises.

3.1. Line Profile Variations

The profile of a spectral line contains a variety of information about the physical conditions within the line-forming region. While emission lines provide insight into the parameters of stellar winds and circumstellar matter, stellar absorption lines carry (besides temperature, gravity and stellar rotation) the information about the dynamical conditions within the atmosphere, that is at the surface of the star. Any change in the atmospheric kinematics, e.g., due to non-radial pulsations, causes temporal variations in the shape and center of gravity of line profiles. Nice examples of computed line-profile variations of stars pulsating in various non-radial modes can be seen, e.g., on John Telting's webpage[4].

To identify pulsations in spectroscopic time series, the profile variability can be visualized by various means as shown in Figure 6 for the example of β Cep. Overplotting the normalized profiles of a time series of an individual photospheric line (second panel) often shows already whether the profiles are constant and symmetric or not. In the shown example, the profiles vary in three ways: they change their shape and their intensity, and they move in wavelength, so that they seem to swing from one side to the other. When plotting the intensity variation of the lines in a gray-scale plot as a function of time (third panel), a sine-curve like variability pattern appears. Alternatively, one might compute the mean of all observed lines (top panel) which can then be subtracted from each individual line profile to obtain the residuals (fourth panel). These residuals can also be represented in a gray-scale plot as a function of time (bottom panel) to highlight the positive and negative deviations from the mean profile. The use of such gray-scale images has been invented by Gies & Kullavanijaya (1988). These plots guide the eye and in such way facilitate the identification of any features or patterns traveling across the profile.

However, not every periodically varying profile is automatically an indication of stellar oscillations. Other effects can cause variability as well. For instance, a companion (either star or planet) leads to periodic variability. But in this case, only a change in radial velocity is seen. Companions do not alter the shape of the absorption lines. A different scenario leading to line profile variability is due to spots caused by temperature or abundance patterns on the stellar surface. These spots are usually not (or at least not on short timescales) changing their sizes and distributions over the surface, so that the observable profile variability is due to (and follows) stellar rotation, and hence just a single frequency (and its (sub)harmonics) is detected. In contrast to these scenarios, stellar pulsations are typically multi-periodic and create highly complex variations in both radial velocity and profile shapes. Consequently, the analysis of spectroscopic time series of variable stars provides an important diagnostics for distinguishing pulsating stars from other objects with variabilities. Furthermore, it is an essential tool for a proper characterization of the pulsation behavior of oscillating stars.

[4]http://staff.not.iac.es/~jht/science/

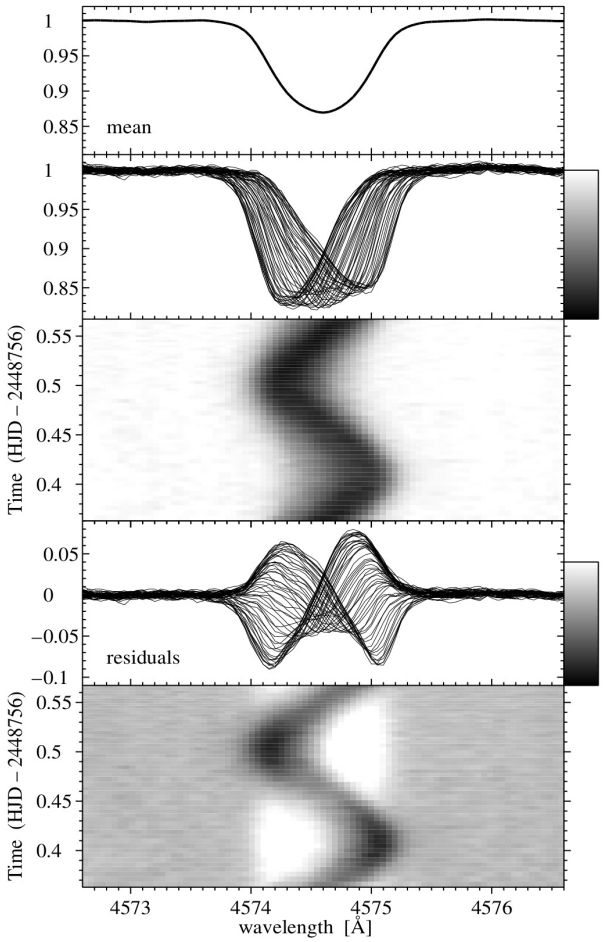

Figure 6. Representations of line-profile variability for the example of the SiIIIλ 4574 line in the pulsating star β Cep. From top to bottom: mean line profile of 620 observations – a subset of 54 normalized spectra – gray-scale image of intensity variations – 54 residual spectra (having the mean spectrum subtracted) – gray-scale representation of residuals. Figure is taken from Telting et al. (1997).

3.2. Specific Requirements for Spectroscopy

Before concluding this section on spectroscopy, the specific requirements for the data sets should be emphasized. Most important for the detection of the rather small deviations in shape and radial velocity from an unperturbed, symmetric line profile is the high quality of the data with respect to both resolution and S/N level.

The resolving power, R, at a given wavelength λ (for example, the laboratory wavelength of the investigated spectral line) is defined as $R = \lambda/\Delta\lambda$. The resolution should be at least 30 000. Certainly better are spectra with $R > 50\,000$.

The same principle holds also for the signal-to-noise ratio: the higher the better. However, the higher the resolution and the fainter the object, the longer is the integration time to achieve adequately high S/N values. Therefore, in reality one has to find the best suitable combination for the object that is supposed to be studied. As sort of a guideline, one should opt to sample the observed line profile in wavelength with about 50 points and to achieve a S/N value greater than 200.

But there are more constraints than just resolution and noise level. To unveil the signature of oscillations, there should be at least ten measurements distributed over each pulsation cycle. This can be achieved by observing over many cycles for a long time base, which also guarantees that at least some of the cycles are densely covered for a decent frequency spectrum, in particular for stars with multi-periodic oscillations and complicated beating patterns. For the data to be considered sufficiently time-resolved they are required to cover at least two points per cycle for all harmonics needed to reproduce the shape of the variability pattern which is usually the radial velocity curve.

Furthermore, the data also need to have a good temporal resolution. This means, that the integration time should not exceed about 1–2% of the pulsation period. Only in this case, the measurements can be considered as instantaneous. Otherwise, the signal appears to be smeared out, an effect which then needs to be simulated and corrected for.

Considering all these requirements, one should make sure to carefully adjust the observational setup and strategy according to the specific needs for the target under investigation and the research goal that one wishes to achieve.

Having introduced all the targeted demands for the observational data, we now turn to the various missions dedicated to (or useful for) the acquisition of data for different types of variable stars.

4. Space Missions

4.1. Observations of Variable Stars - How It All Started

The HIgh Precision PARallax COllecting Satellite (**HIPPARCOS**[5]) of the European Space Agency (ESA) was one of the most important and pioneering large surveys of variable stars. During its 3.5 years of operation from 1989 to 1993, the parallaxes of about 120 000 bright stars in the solar neighborhood were measured with unprecedented precision of 2 mas, and their proper motions with an accuracy of 2 mas/year. This accuracy has been achieved from about 100 individual observations per star that have been randomly distributed over the mission lifetime. The observations of HIPPARCOS have been performed with a broad-band white-light filter covering the wavelength range $400 - 800\,\mathrm{nm}$.

The satellite has been equipped with an auxiliary star mapper (the Tycho experiment) that pinpointed many more stars. Its accuracy was lower, but still good enough to determine the parallax and proper motion of a million fainter stars with an accuracy of 30 mas (per year). The total number of measured objects has been compiled in the Tycho 2 Catalogue, which has been completed

[5]https://www.cosmos.esa.int/web/hipparcos/home

in 2000. It lists the total of 2 539 913 stars, and includes 99% of all stars down to magnitude 11.

Besides the position and proper motion measurements, the major achievement of the HIPPARCOS mission was the discovery of a few thousand new periodically variable stars that have been reported in the *Catalogue of Periodic Variables* and another few thousand variables without a clear dominant periodicity, listed in the *Catalogue of Unsolved Variables*. Numerous new variables have been discovered with periods of the order of days. Such stars are difficult to find from ground. The results from the HIPPARCOS mission particularly impacted the studies of slowly pulsating B (SPB) stars, for which HIPPARCOS increased the number by a factor of ten (Waelkens et al., 1998), and it doubled the number of γ Dor stars (Handler, 1999). Moreover, HIPPARCOS also discovered 343 new eclipsing binaries and thus doubled their number (Söderhjelm, 2000).

The new catalogs of variable stars triggered extensive follow-up long-term ground-based photometric and spectroscopic campaigns. The brightest stars of each class were monitored to study their pulsational behavior and to derive the general properties of the objects.

4.2. Follow-up Surveys of Variable Stars

It took ten years after the end of the HIPPARCOS mission before the next satellite, dedicated to the observations of variable stars, was sent to space. An overview of all relevant space missions and their (actual or planned) duration periods is depicted in Figure 7.

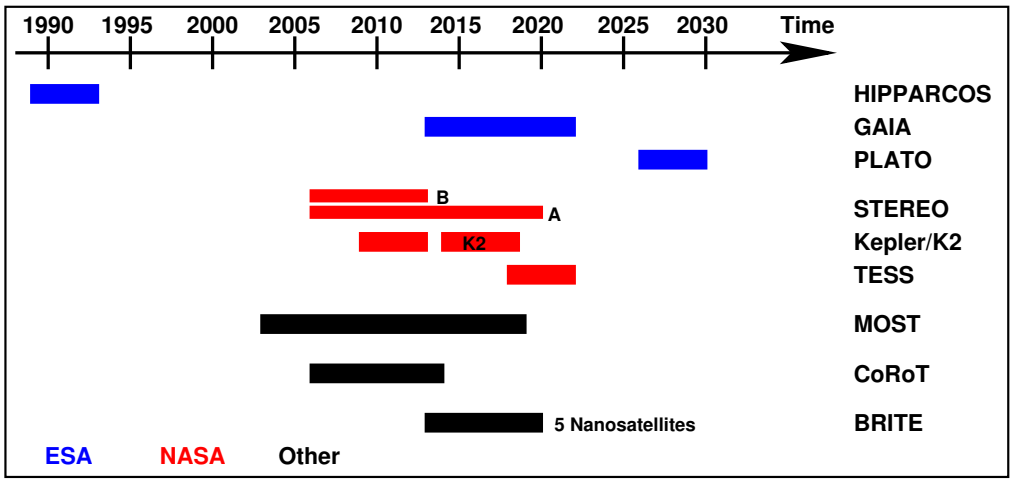

Figure 7. Space missions suitable for variable star research, even if their prime objective was sometimes quite different.

MOST The Canadians were the next to launch a satellite called Microvariability & Oscillations of Stars (MOST[6]). It was Canada's first space telescope,

[6]http://most.astro.ubc.ca//index.html

and the first spacecraft dedicated purely to the study of asteroseismology of a variety of pulsating objects.

MOST consisted of a visible-light dual-CCD camera, fed by a 15-cm aperture Maksutov telescope. One CCD observed the science target, while the other was used for star-tracking with a pointing accuracy better than $1''$. With its broad-band (300 nm) filter centered at 525 nm, MOST performed ultra-high-precision photometry measuring brightness variations down to the mmag level.

With its suitcase size (65 cm $\times$ 65 cm $\times$ 30 cm) and a weight of just 54 kg, this microsatellite was given the nickname "Humble Space Telescope". It was launched in June 2003 and was intended to be a one-year mission to observe a total of ten bright ($V = 0.4 - 6.0$ mag) stars for a period up to 60 days. However, MOST succeeded to survive for more than 15 years and was in operation until March 2019. During this period it delivered precise data for more than 5000 objects.

CoRoT The next mission, initiated and led by the French Space Agency (CNES) in conjunction with ESA and other international partners, was entitled Convection, Rotation and planetary Transits (CoRoT[7]). It was designed to investigate stellar pulsations and to search for exoplanets.

The telescope was equipped with a 27 cm diameter lens and a wide-field camera observing in visible light and with a field of view of 7 square degrees. The camera had 4 CCD detectors with 2000×2000 pixels. For its asteroseismic goals the satellite operated in two modes: long runs of 150 days (central program) devoted to a small number of ($\sim$ 50) selected main-sequence targets brighter than magnitude 9, and short runs of 20 days (exploratory program) inserted in between two long runs dedicated to a variety of stars across the whole HR diagram from spectral type B to K. For the exoplanet hunting, the targets were red dwarfs (F to M) with magnitudes between 12 and 15.5.

The satellite was launched on 27 December 2006 and it terminated its operation in June 2014. During this 7.5-year mission, CoRoT discovered several hundred exoplanet candidates and collected light curves for about 160 000 variable stars.

Kepler Space Telescope Another satellite, dedicated primarily to the search for Earth-size planets, was NASA's Kepler Mission[8]. Kepler was a 0.95-m aperture Schmidt telescope equipped with a photometer that operated at 430–890 nm and continually monitored the brightness of approximately 150 000 main sequence stars in a fixed field of view of 105 square degrees ($\sim$ 12 degree diameter). The focal plane consisted of an array of 42 CCDs pointing to one field, read-out every 3 seconds for stars brighter than $R \sim 16$ mag and integrated over 30 min. For uninterrupted observations, the field of view had to be out of the ecliptic plane, and to maximize the number of stars in the field, it pointed towards a region in the constellations Cygnus and Lyra.

The satellite was launched in March 2009, and the mission's lifetime was initially planned to 3.5 years. This lifetime has been extended, because the data

[7]https://corot.cnes.fr/en/COROT/index.htm

[8]https://www.nasa.gov/mission_pages/kepler/overview/index.html

had higher than expected noise which required longer integration (hence longer duration) for a successful completion of the planned mission. In 2012, one of the spacecraft's four reaction wheels used for pointing the spacecraft stopped turning, and in May 2013 the second wheel failed. This was the end of the main mission.

A new concept for the satellite has been developed, which allowed a restart of observations relying only on the remaining two reaction wheels. This so-called "Second Light" of Kepler was dubbed the K2 mission and was in operation from 2014 until the spacecraft ran out of fuel in 2018. To cope with the satellite's limitations, the new observing mode was a series of sequential fields distributed around the ecliptic plane with a length of 80 days each.

In total, Kepler observed 530 506 stars and discovered 2 662 exoplanets over its lifetime. Despite its major goal of exoplanet research, Kepler observed many more stars as a side product, and in fact, the number of publications based on Kepler and K2 data in other fields of astrophysics became even higher than the one dealing with exoplanets, showing that other scientific branches can greatly benefit from missions that are not directly related to their fields.

STEREO How stellar astrophysics can benefit from missions other than their own is impressively demonstrated by another NASA mission called Solar TErrestrial RElations Observatory (STEREO[9]). This mission consists of two nearly identical satellites orbiting the sun at 1 AU distance equipped with white light coronagraphs. The prime goal of that mission was to provide the first-ever stereoscopic measurements to study the sun and space weather, and to construct a 3D structure of the sun and of coronal mass ejections. Nevertheless, the satellites imaged also stars in the vicinity of the sun. These are monitored each year for a period of about 20 days and the images can be used to extract light-curves of the objects.

The mission was launched in October 2006. While the STEREO B satellite died in 2014, STEREO A still continues to deliver data which can also be used for asteroseismic studies of variable stars.

BRITE A mission dedicated solely to the monitoring of objects with V-band magnitudes brighter than 6 is provided by the constellation of nanosatellites, each of them being a BRIght Target Explorer (BRITE[10]). The first two have been provided by Austria (BRITE-AUSTRIA and UniBRITE) and were launched on February 25, 2013. These have been followed by two Polish BRITEs, BRITE-Lem launched on November 21, 2013, and BRITE-Heweliusz, launched on August 19, 2014. Finally the Canadians launched two more BRITES (BRITE-Toronto and BRITE-Montreal) together on June 19, 2014. Unfortunately, BRITE-Montreal is not operating, so that the final constellation consists of just 5 nanosatellites.

To achieve their goal of investigating the stellar structure and evolution of the brightest stars in the sky, the camera exposure times range from 1 to 5 seconds, collected about 3-4 times per minute and for 15-35 minutes per orbit. The observing run for each field is limited to about 180 days. The satellites are

[9]https://www.nasa.gov/mission_pages/stereo/main/index.html

[10]https://brite-constellation.at/

equipped with an instrument sensitive either in a red bandpass (550 – 700 nm; UniBRITE, BRITE-Toronto, and BRITE-Heweliusz) or in a blue one (390 – 460 nm; BRITE-Austria and BRITE-Lem). The field of view of both the red and the blue version of the camera is about 24 degrees in diameter allowing for the observation of about 15 bright targets per field at the time.

Gaia ESA's next big mission was Gaia[11]. As a follow-up of the HIPPARCOS mission, Gaia has the ultimate goal to measure the positions, distances and space motions of about one billion stars. On board are two identical telescopes that point in different directions with a separation angle of 106.5 degrees. Three instruments collect the light coming from the two telescopes and merged into a common path. The astrometric instrument measures the stellar positions on the sky. By the end of the mission, the global astrometry will be measured for all one billion stars down to $G \sim 20$ mag down to micro-arcsecond precision. The two photometers, one operating in the blue (330 – 680 nm) and one in the red (640 – 1050 nm), collect low-resolution spectra and provide color information of the stars that will allow to derive stellar parameters such as temperature, mass and chemical composition. The radial velocity spectrometer measures the stars' radial velocity at medium resolution ($R \sim 11\,500$) based on absorption lines in the red part (845 – 872 nm) of the spectrum.

Gaia is observing since July 2014. It is expected that throughout the mission, many thousands of extra-solar planets will be discovered (from both their astrometric wobble and from photometric transits) and that their detailed orbits and masses will be determined. During its 5-year mission, a sky-averaged number of 70 photometric measurements is expected from the astrometric field and from the blue and red photometers. Moreover, variability on short (seconds) to long (of order 5 years) time scales can be detected.

TESS A further mission, primarily devoted to the discovery of transiting exoplanets, is NASA's Transiting Exoplanet Survey Satellite (TESS[12]). The satellite is equipped with four identical, highly optimized, red-sensitive (600 – 1000 nm bandpass) wide-field cameras, each with a 24 deg by 24 deg field of view so that together they can monitor a 24 deg by 90 deg strip of the sky. Each strip is observed for a total of 27 days so that almost the full sky is mapped within a period of 2 years. The first year of its operation TESS scanned the southern sky, and in the second year the northern one. The CCDs read out continuously at 2-second intervals, and the data are stacked to the length of the chosen cadence. During the 2-year run, a selected number of 200 000 brightest stars were observed with 2-minute cadence and provided with postage stamp sizes (usually 10×10 pixels), whereas full-frame images had a cadence of 30 minutes. All data become public four months after observations, providing an unprecedented pool of high-quality light curves for all types of variable stars.

TESS is in operation since 2018 July 25 and finished its 2-year prime monitoring mission on 2020 July 5. Right after, the TESS extended mission started, which will last for another 27 months, beginning again with the southern sky

[11] https://www.cosmos.esa.int/web/gaia/home

[12] https://tess.mit.edu/

and focusing on those targets that fell into gaps between sectors during the first monitoring period. During the extended mission, about 20 000 objects will be monitored per sector at 2-minute cadence as during the prime mission. However, a sample of up to 1000 targets per sector will be read out with a 20 s cadence, whereas the full-frame image cadence has been reduced from 30 to 10 min to broaden the range of scientific investigations.

PLATO Finally, it is worth mentioning that ESA is currently preparing a new mission called PLAnetary Transits and Oscillations of stars (PLATO[13]). The launch of this satellite is scheduled for 2026 with an intended 4 years of operation.

The prime goal of that mission is again to find and study a large number of extrasolar planetary systems. The emphasis is hereby on determining the properties of terrestrial planets in the habitable zone around solar-like stars and to investigate seismic activity for a precise characterization of the planet host stars. To achieve these goals, PLATO will perform high precision, long (months to years), uninterrupted photometric monitoring in the visible band of a very large sample of stars brighter than $V \sim 11$ mag.

In addition, many other objects will be observed, which fall outside PLATO's core science but are of high value for other branches in Astronomy dealing with stellar variability. These other aspects of astrophysics (e.g., binary and multiple stars, pulsating stars, magnetic stars, transient phenomena, stars with mass loss, etc. just to mention a few) are lumped together into what is called the PLATO Complementary Science (PLATO-CS[14]). The PLATO-CS will rely on the calibrated light curves provided by the PLATO mission. These light curves will be assembled in a variability catalog and will be offered to the scientific community for exploitation.

5. Ground-Based Photometric Surveys and Databases

For accessing photometric light curves and data from long-term monitoring one has not solely to rely on space missions, but can use products from their ground-based counterparts. Several large surveys have been carried out, not always with the prime goal to study stellar pulsations and not always performed by professional astronomers, but providing high-quality data that can be used for asteroseismological purposes. This section gives an overview of the diverse ground-based surveys and databases.

5.1. Missions Dedicated to Variable Stars

AAVSO The American Association of Variable Star Observers (AAVSO) is the world largest association of variable star observers. It was founded in 1911 to coordinate the variable star observations of mostly amateurs astronomers, and to foster collaboration between amateurs and professionals in the field of variable star research.

---

[13]https://sci.esa.int/web/plato

[14]https://fys.kuleuven.be/ster/research-projects/plato-cs

AAVSO's International Database[15] contains over 34 million variable star observations going back over one hundred years. It is the largest and most comprehensive digital variable star database in the world. To date, over 1 000 000 new variable star brightness measurements are added to the database every year by observers from all over the world. The database contains a diversity of photometric measurements in different bands, and the AAVSO webpage provides a light curve generator allowing the user to see and download the available data for a given object.

ASAS The All Sky Automated Survey (ASAS[16]) is a low-cost automated survey with the prime goal to detect any kind of photometric variability. ASAS consists of two observing stations, one at the Las Campanas Observatory in Chile (since 1997) and another one at Haleakala, Maui (since 2006). Both telescopes are equipped with two wide-field instruments that enable them to simultaneously observe in the V and I bands. The telescopes constantly monitor the whole available sky, meaning that they provide photometric data for about 10^7 stars which have magnitudes brighter than 14. The observations are converted to standard V and I magnitudes. They are collected in a variety of catalogs and can be accessed from the ASAS webpage.

5.2. Surveys Related to MACHOs

As for the space telescopes, there were also several ground-based missions not specifically targeted at variable stars, but providing data of variable stars as side-products. One of them was the search of MAssive Compact Halo Objects (MACHOs). These objects, which were considered to be mainly brown dwarfs and planets, have been proposed to constitute a significant fraction of the dark matter in the halo of the Milky Way. If they were detected, they could help explain parts of the missing dark matter in the Universe. To search for MACHOs, several large surveys were initiated in the early nineties. The idea was to discover these dark compact massive objects via microlensing events, in which the MACHOs would serve as gravitational lens passing in between us and a background light source, such as the stars of the Magellanic Clouds or of the Galactic Bulge. As such lensing events are extremely rare, long-time monitoring of a huge number of light sources with high precision photometry is required. Such monitoring naturally provides data for millions of stars as side-products and led to the discovery of many thousands of variable stars in the Magellanic Clouds and in the Galactic Bulge (e.g., Sarro et al., 2009). Based on these surveys, significant progress on the properties of large-amplitude oscillators, such as Cepheids, RR Lyrae stars, and red-giant and supergiant pulsators could be achieved. Here we list only the most important surveys related to the search for MACHOs.

MACHO The MACHO Project[17] started in 1992. It has been carried out by a two channel system that employs eight CCDs, mounted on the 50 inch

[15]https://www.aavso.org/aavso-international-database-aid

[16]http://www.astrouw.edu.pl/asas/?page=main

[17]http://wwwmacho.anu.edu.au/

telescope at Mt. Stromlo for simultaneous imaging in two passbands, in the red (630 - 760 nm) and blue (450 - 630 nm) bands.

EROS In 1990 started the Expérience pour la Recherche d'Objets Sombres (EROS[18]) survey which consisted of two phases, EROS-I and EROS-II. This survey has been carried out based on a 40 cm telescope with a CCD camera, operated at the La Silla Observatory in Chile, and 1 meter Schmidt ESO telescope, with photographic plates, alternately with a blue and a red filter. In 1995, a 1.5-m telescope recuperated from French observatories replaced the 40 cm telescope. This was the start of the EROS-II era which ended in 2003. EROS monitored in total 90 million stars located in the Galactic Center and in the Magellanic Clouds.

OGLE The Optical Gravitational Lensing Experiment (OGLE[19]) started in 1992 with the first phase (OGLE-I) during which the 1-m Swope telescope at the Las Campanas Observatory in Chile has been utilized. The telescope was replaced in 1996 by the 1.3-m Warsaw Telescope, with which the second phase (OGLE-II) started in 1997. In 2001 OGLE-III started when a new CCD mosaic camera was installed covering a $35' \times 35'$ field of view. Finally a 32 chip mosaic camera with a total field of view of 1.4 square degrees has been installed in 2010, initiating the so far last phase, OGLE-IV, which is still ongoing. While during the phases OGLE-II and OGLE-III standard $UBVRI$ filters have been available, these have been replaced by standard VI interferometric filters.

5.3. Survey Related to Transiting Exoplanets

KELT The Kilodegree Extremely Little Telescope (KELT[20]) mission was a survey aimed at searching for transiting exoplanets around bright stars. The mission consisted of two fully robotic telescopes, one on each hemisphere. KELT-North is located at Winer Observatory in Arizona and went into operation in 2005. KELT-South followed in 2009. It is located at the Sutherland observing station of the South African Astronomical Observatory. Each telescope has a field of view of 26×26 degrees and observed multiple fields with between 50 000 and 200 000 stars per field. Their main focus was on stars with apparent visual magnitudes of $V = 8 - 11$ mag.

The KELT light curve data archive is publicly available via the NASA Exoplanet Archive (NEA[21]). It contains about 1.1 million light curves. The KELT transit search was concluded in March 2020. During its observing run, 26 planets have been discovered.

5.4. Future Ground-based Photometric Mission

To my knowledge, there is so far one large mission in preparation:

---

[18] http://eros.in2p3.fr/

[19] http://ogle.astrouw.edu.pl/

[20] https://keltsurvey.org/

[21] https://exoplanetarchive.ipac.caltech.edu/

LSST The Large Synoptic Survey Telescope (LSST[22], renamed into Rubin Observatory) is currently under construction on Cerro Pachón in Chile. It has a three mirror system and the world largest CCD. The 3.2 gigapixels camera will operate from the UV to the near-infrared in the spectral bands labeled u, g, r, i, z, & y. With its almost 10 square degrees field of view (corresponding to 40 times the size of the full moon), the LSST will survey the night sky for a period of 10 years. Each night, more than 800 panoramic wide-field images with 30 second exposures will be taken with this 8.4-m telescope, resulting in a recording of the entire visible sky twice per week, and a total of about 1000 visits for each object during the planned duration of the survey. The total data volume generated each night will be on the order of 20 Terabytes. Image data products will be made available daily, and data products resulting from coherent processing will be made available via yearly releases.

The scientific goal of this survey is to detect changes in brightness and position of objects as big as far-distant galaxy clusters and as small as near-by asteroids. The start of full science operations and the beginning of the survey is foreseen for the end of 2022.

5.5. Ground-based Spectroscopic Monitoring Facilities

The situation with observing missions dedicated to spectroscopic monitoring is much worse than the photometric possibilities. While many, especially national spectroscopic facilities exist and are used by individual research teams, there is to my knowledge only one coordinated network.

SONG This very promising project was launched in 2006 by the Stellar Observations Network Group (SONG[23]). Its ultimate goal is to construct a global network of six to eight small robotic telescopes distributed over the world to collect uninterrupted time series from ground for solar-type stars, and to search for and characterize planets.

Currently, only one 1-m telescope, located at the Teide Observatory in Tenerife, is in operation. It is equipped with a high-resolution echelle spectrograph with a resolution from 35 000 to 112 000 and a wavelength coverage of 440 – 690 nm. A second 0.7-m telescope is in its testing phase and will be located at the Delingha Observatory in China, and a further node is under development for Southern Queensland, Australia.

6. Conclusions

In this Chapter, the observational techniques for obtaining high-quality data in both photometry and spectroscopy and their adequacy, limitations, and benefits for investigating pulsating stars have been presented. To study all aspects of stellar pulsations concurrently, it would be most ideal to simultaneously monitor stars photometrically (preferentially from space to have continuous light curves) and spectroscopically (which is currently possible only from ground) utilizing

[22]https://www.lsst.org/lsst/

[23]https://phys.au.dk/song/

multiple, identical facilities distributed all over the world to minimize the losses due to day-time and bad weather, ideally with high cadence, excellent temporal resolution, high signal-to-noise and high spectral resolution. Obviously, this is wishful thinking and in reality the situation looks different from that.

For space photometry, many objects are very bright, meaning that the signal is polluted by read-out noise, or stars are saturated on the chip, if they are observed at all. Therefore, preference is often given to less bright objects.

For spectroscopy, many of the photometrically easily followed objects are too faint to monitor them with high cadence in high spectral resolution and high S/N. For this task, large 6-10 m-telescopes would be required, but monitoring campaigns at the big observatories have no or only little chance for getting time at their telescopes because of their low output but high costs. Therefore, such monitoring is usually performed with smaller, 1-2 m class telescopes. The advantage of these telescopes is that there is much lower pressure, but for the price of being limited to bright(er) or long-period objects, for which the needed coverage and data quality can be achieved.

These limitations mean that for each target a compromise needs to be made and for the observational setup a strategy has to be selected such that the specific science goal will be achieved. Nevertheless, despite these hindrances the field of asteroseismology has been steadily growing in the past decades. And considering all the currently available and newly planned instruments and missions for photometry and spectroscopy, I am confident that the future for research in variable and pulsating stars is bright.

Acknowledgments. I wish to thank the SOC and LOC for their fantastic job in organizing and implementing this interesting and pleasant Summer School. Most of the data and images shown have been collected with the Perek 2-m telescope at Ondřejov Observatory. The Astronomical Institute, Czech Academy of Sciences, is supported by the project RVO:67985815. This project has received funding from the Czech Science Foundation (GA ČR 20-00150S) and from the European Union's Framework Programme for Research and Innovation Horizon 2020 (2014-2020) under the Marie Skłodowska-Curie Grant Agreement No. 823734.

References

Aerts C., Christensen-Dalsgaard J., Kurtz D. W., 2010, *Asteroseismology*
Bessell M. S., 2005, *ARA&A*, **43(1)**, 293
Fukugita M., Ichikawa T., Gunn J. E., Doi M., Shimasaku K., Schneider D. P., 1996, *AJ*, **111**, 1748
Gies D. R., Kullavanijaya A., 1988, *ApJ*, **326**, 813
Handler G., 1999, *MNRAS*, **309(2)**, L19
Hardie R. H., 1964, *Photoelectric Reductions*, p. 178
Howell S. B., 2006, *Handbook of CCD Astronomy*, Vol. 5
Massey P., Hanson M. M., 2013, *Astronomical Spectroscopy*, p. 35
Sarro L. M., Debosscher J., López M., Aerts C., 2009, *A&A*, **494(2)**, 739
Söderhjelm S., 2000, *Astronomische Nachrichten*, **321(3)**, 165
Telting J. H., Aerts C., Mathias P., 1997, *A&A*, **322**, 493
Waelkens C., Aerts C., Kestens E., Grenon M., Eyer L., 1998, *A&A*, **330**, 215

Diverse Pulsating Stars

Pulsations Along Stellar Evolution
VIII LAPIS Summer School
AAA Workshop Series 12, 2021
M. Kraus & A.F. Torres, eds.

Pulsating Hot Subdwarf Stars

Alejandra D. Romero[1]

[1]*Physics Institute, Universidade Federal do Rio Grande do Sul, Av. Bento Gonçalves 9500, Porto Alegre, RS-91501-970, Brazil*

Abstract. Hot subdwarf stars are core helium–burning objects, located at the hot end of the horizontal branch, and therefore, they are also known as Extreme Horizontal Branch stars. We can divide them into two large groups, of spectral types B and O, depending on their effective temperature. Each spectroscopic class has subgroups showing luminosity variations due to pulsations, opening the possibility to study these compact objects through Asteroseismology. In this notes I will briefly review the main characteristics of hot subdwarfs B and O stars and the different pulsating subgroups.

Key words: asteroseismology — instabilities — stars: oscillations — stars: interiors

1. Introduction

Hot subdwarfs stars are evolved compact stars with temperatures between $\sim 20\,000 - 70\,000$ K and surface gravities ranging from 5.6 to ~ 6.1. They are evolved low mass stars, $M_* < 0.5 M_\odot$, that consist in helium burning cores and a thin hydrogen atmosphere which is unable to support hydrogen shell–burning (Heber et al., 1984; Heber, 1986). They are found in the Galactic field population, classified as type O and B (sdO, sdB), depending on the temperature, and in globular clusters as Extreme Horizontal Branch (EHB) stars.

The progenitors of hot subdwarfs are main sequence stars with initial masses $< 2.0\ M_\odot$, that have undergone a core helium flash and made their way to the Horizontal Branch (HB), with a thin hydrogen envelope ($M_{\rm env} \lesssim 0.01 M_\odot$). As a result of this low hydrogen mass, after core helium exhaustion, the stars move directly to the white dwarf stage.

Around half of hot subdwarf stars are found in binary systems with short periods, from hours to days, with mostly white dwarf companions (Maxted et al., 2001; Napiwotzki et al., 2004; Copperwheat et al., 2011). Since the sdB stars have evolved from red giants, much larger than current orbital separation of a few radii, the progenitor system must have undergone a common envelope (CE) phase.

Subdwarf B and O occupy neighboring regions in the HR diagram. However, they are quite different, both with respect to their chemical compositions and evolutionary status (Heber, 2016). The atmospheres of sdBs are mostly helium poor, their helium abundances might be as low as 1/1000 solar or less. sdO stars,

on the odder hand, show a variety of helium abundances, ranging from 1/100 solar to pure helium atmospheres (He-sdO).

A subgroup of both sdB and sdO stars show luminosity variability due to pulsations. In the case of sdBV there are three classes including the $p-$mode pulsators EC 14026 stars, the $g-$mode pulsators PG 1716 and the hybrid sdBV, showing both $p-$ and $g-$modes. The hotter counterpart, the variable sdO stars show short $p-$mode pulsations. The main characteristics of the classes of pulsating hot subdwarf stars will be addressed in this work.

2. Evolution Towards the Horizontal Branch

The stars in the lower main sequence start their evolution with initial high densities (10^3 g/cm^3 for $\sim 1M_\odot$) and low temperatures, as compared to more massive stars. Thus, at the end of the central hydrogen–burning stage the remaining helium core is close to degeneracy. With the increase in the helium core mass due to the hydrogen burning shell, it soon reaches electron degeneracy conditions, and a new source of pressure is now balancing the gravitational collapse. This structure, of a degenerate core and a non–degenerate envelope is in hydrostatic equilibrium. The hydrogen burning–shell is active and its energy is used to expand the envelope in a giant configuration, thus the star enters the Red Giant Branch (RGB). The effective temperature decreases until it reaches the Hayashi line[1] and then the star starts to increase its luminosity.

The contraction of the core releases gravitational energy that heats up the region where the hydrogen burning–shell is located, also increasing its productivity ($\epsilon_{CNO} \sim T^{20}$). Thus the envelope expands even further, increasing the luminosity.

As the hydrogen–burning shell moves towards the surface of the star, it produces helium increasing the mass of the core. Since the temperature of the core is proportional to its mass ($T \sim M_c/R_c$), it also increases. Thus, when the mass of the core is $\sim 0.45M_\odot$, independently of the total mass of the star, the core reaches a temperature of $\sim 10^8$ K, necessary to start the nuclear reaction of helium. However, since the pressure of the core is dominated by the degenerate electrons, an increase in the temperature due to the release of nuclear reactions does not lead to an expansion of the core. Thus, the expansion work is zero and all the released energy is transformed into internal energy, increasing the temperature even more, leading to an unstable release of energy. The large amount of energy is released fast as compared to evolution timescales, in an event called the helium–flash (He–flash). The energy produced in the core by the He–flash can reach luminosity of $10^{10}L_\odot$ comparable to the luminosity of our Galaxy. Finally, the temperature will increase until $T > T_{\rm Fermi}$ and the pressure depends on the temperature again. The core expands and cools, and the stable nuclear burning stage begins, i.e. the Horizontal Branch.

[1]The Hayashi line marks the lowest effective temperature than can be reached by a stable configuration. The line itself corresponds to a fully convective star.

3. The Formation of Extreme Horizontal Branch Stars

Hot subdwarf stars are located at the hot end of the Horizontal Branch, characterized by a hydrogen envelope too thin to support nuclear shell–burning. The main issue to understand the formation of EHB stars is the large amount of mass that needs to be lost prior to or at the beginning of core helium burning. Two main formation channels have been proposed, being close binary evolution or the hot flasher scenario. Binary evolution through mass transfer and common envelope ejection must be important for sdB stars due to the high percentage of close binaries with periods of less than ten days. In addition, merger of two helium white dwarfs is another vital option to explain the origin of single hot subdwarfs. Enhanced mass loss during the RGB can decrease the hydrogen content of the envelope, delaying the core helium flash (the so-called *hot flasher scenario*), during which surface hydrogen is burnt after mixing into deeper layers (Heber, 2016). More detail on the possible formation channels are given below.

3.1. Hot Flasher Scenario

Stars corresponding to the low main sequence, where hydrogen burning is mainly due to the $p-p$ cycle, begin the central helium burning stage with the He–flash at the tip of the RGB. However, if sufficient mass loss occurs during the RGB, the star will experience the He–flash at higher effective temperatures (Castellani & Castellani, 1993). The remnants of these "hot flashers" (Brown et al., 2001) are found to be close to the helium main sequence. The outcome of a hot flasher depends on the evolutionary phase during which it occurs (Cassisi et al., 2003), as shown in Figure 1. Panel (a) shows the evolution where the mass loss was slightly enhanced. In this case, the He–flash occurs near the tip of the RGB and the star settles near the blue horizontal branch. If the He–flash occurs early after departure from the RGB (*Early hot flasher*) at high luminosities and effective temperatures, the further evolution results in a standard H/He envelope hot subdwarf star (see panel b in Figure 1). The *Late hot flasher* scenario occurs when the He–flash happens after the star enters the white dwarf cooling sequence. If the He–flash occurs at high $T_{\rm eff}$, there is shallow mixing, resulting in a hot subdwarf star with an atmosphere enriched in helium and nitrogen due to convective dilution of the envelope (see panel c in Figure 1). If the He–flash occurs at a lower luminosity in the white dwarf cooling sequence (see panel d in Figure 1), the hydrogen–rich envelope is mixed and burned in the convective zone generated by the flash itself leading to strong enrichment of helium, carbon and nitrogen in the atmosphere (Heber, 2009, 2016; Battich et al., 2018). Thus, when in the evolution the He–flash occurs, it not only determines the effective temperature of the star on the EHB but also its envelope chemical composition.

3.2. Close Binary Evolution

The large fraction of sdB stars in close binaries suggests that they are formed by binary interaction. There are three main formation channels: Roche–lobe overflow (RLOF) evolution, common envelope (CE) evolution (Paczynski, 1976), and the merger of two he–core white dwarfs (Webbink, 1984; Han et al., 2002, 2003).

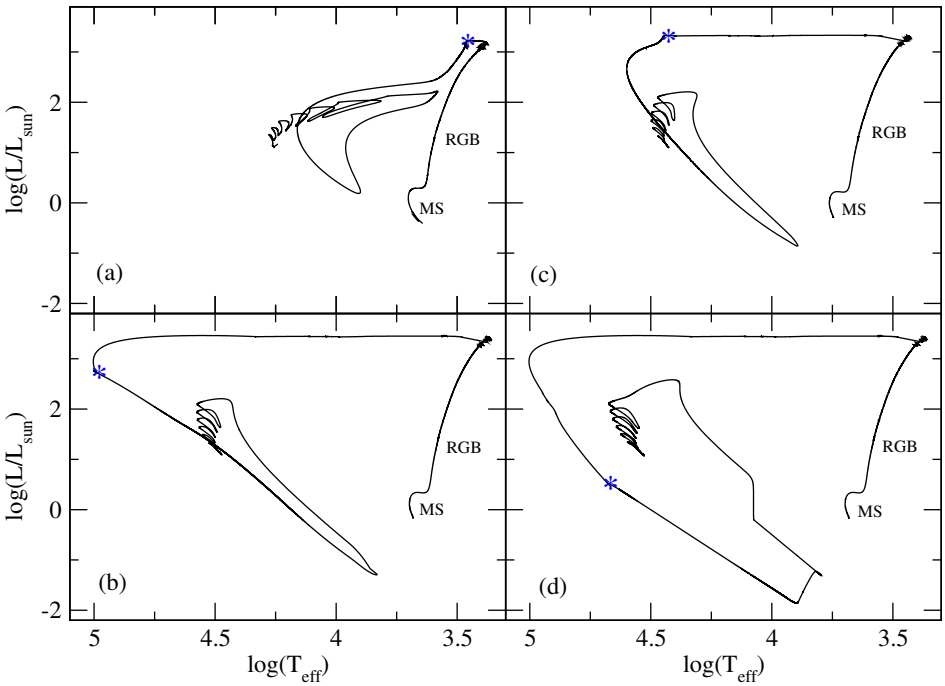

Figure 1. Evolution of a solar metallicity star from the main sequence to the zero–age horizontal branch for different mass loss rates on the RGB. The peak of the He–flash is indicated with a blue asterisk. (a) The He–flash occurs soon after the tip of the RGB. (b) *Early hot flasher*: the He–flash occurs at high luminosities and effective temperatures. (c) *Late hot flasher*: The He–flash occurs soon after entering the white dwarf cooling curve, causing a shallow mixing episode. (d) *Late hot flasher*: The He–core occurs during the white dwarf cooling sequence causing a deep mixing episode. Credit: The evolutionary sequences from panels b, c and d were provided by Tiara Battich (private communication), Battich et al. (2018).

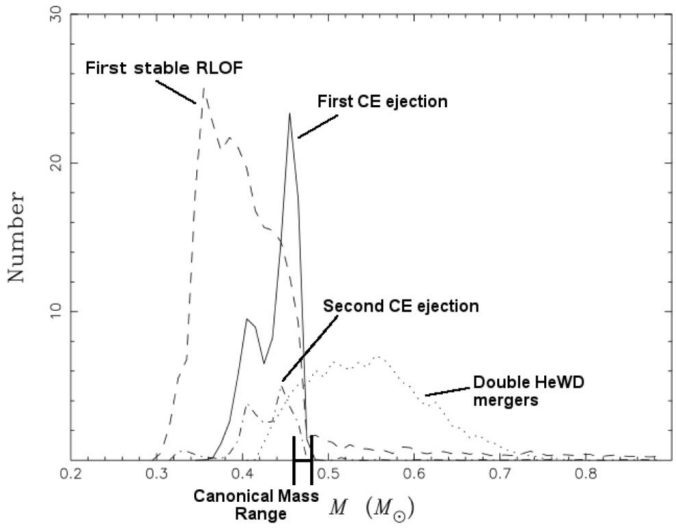

Figure 2. Contribution of the different close binary formation channels to the population of hot subdwarf stars. Credit: Adapted by Ingrid Pelisoli from Han et al. (2003).

In the RLOF formation channel, the mass transfer is dynamically stable and the companion star accretes all the matter. The red giant loses almost all its hydrogen–rich envelope during this stage and becomes a sdB star in a long period binary with a main sequence component. The orbital periods are in the range of 700–1300 days (Chen et al., 2013).

In the CE formation channel, the sdB progenitor fills its Roche lobe near the tip of the RGB. If the mass transfer rate is too high, the companion will not be able to accrete all the material, forming a common envelope. Due to friction with the gas the system will lose orbital energy and the orbit will shrink. The orbital energy is transferred to the common envelope until it is enough to eject it. The remaining core of the red giant will become the sdB star. Because the CE phase is short as compared to the evolutionary timescale of the single stars, the companion will remain almost unchanged. If the companion is a main sequence star the resulting close binary is a sdB+MS with a period between 0.1 and 10 days (Heber, 2016). Even with the current advances in modeling, the physics behind common envelope and accretion is not well understood. Recent works as Davis et al. (2010) and Toonen & Nelemans (2013) are aimed at explaining the formation of white dwarf binaries, while Clausen et al. (2012) is focused on sdB binaries (Heber, 2016).

The most popular formation channel for single hot subdwarfs is the merger of two helium core white dwarf stars (Webbink, 1984). The merger scenario can be slow, fast or a combination of both (Zhang & Jeffery, 2012). In the slow merger scenario the largest star, i.e. the less massive white dwarf, fills its Roche lobe and all the mass is transferred to the companion. The material will form a disk in a few minutes and it will remain cold. The accretion is slow and can last for a few million year, with the angular momentum being dissipated towards

the disk circumference. On the other hand, in the fast merger scenario, no disk is formed and the material falls directly onto the surface of the more massive, smaller companion. A combination of both scenarios is also possible, where one part of the disrupted donor star forms a corona (30%-50% of its mass), and the rest forms a cold disk (Zhang & Jeffery, 2012; Lorén-Aguilar et al., 2009).

Each channel contributes to the population of hot subdwarfs in different amounts and mass range. Han et al. (2003) carried out a detailed binary population synthesis study considering CE and RLOF formation channels. In particular, they predicted that the distribution of masses for sdB stars is wider than is commonly assumed, with stellar masses ranging from 0.3 to $\sim 0.8 M_{\odot}$, as shown in Figure 2. The canonical mass range, indicated in the figure, corresponds to the contribution from the hot flasher scenario. This result is in very good agreement with the distribution of the current population of hot subdwarf stars shown by Schneider (2019)[2], where the mass range can be as low as $0.2 M_{\odot}$ and larger than $0.7 M_{\odot}$ in a few cases. There is a large contribution of objects near $\sim 0.4 M_{\odot}$, that also have contributions from the hot flasher scenario, and a tail at lower masses that can only be formed through binary interaction.

4. Chemical Structure and the Characteristic Frequencies

Hot subdwarf stars are part of the Extreme Horizontal Branch stage, where helium in the core is being transformed into carbon and oxygen due to nuclear reactions. At first, nuclear energy is being produced through the 3α process, where three nuclei of helium, or α particles, are combined to form a carbon nucleus. Once the abundance of carbon in the convective core is high enough, $\sim 50\%$, the reaction $^{12}\mathrm{C}(\alpha,\gamma)\mathrm{O}^{16}$ starts to be dominant, since it is more likely to combine two particles than three. Thus, the carbon abundance reaches a maximum and then decreases, along with the helium abundance. As a result, the star leaves the horizontal branch with a carbon/oxygen core, usually with $\mathrm{C/O} < 1$.

The chemical profile of a hot sdB model with stellar mass $0.474 M_{\odot}$, and $T_{\rm eff} = 26\,214$ K is shown in Figure 3. In this figure only the more abundant elements are depicted. As expected, the central regions are a mixture of carbon, oxygen and helium. Carbon is still dominant but eventually its abundance will decrease and oxygen will become the dominant element. The helium rich region on top of the core is the remnant from hydrogen burning during the main sequence, since the He–burning core is always smaller than the H-burning regions. Finally, no diffusion was considered in the computations, thus the envelope is a mixture of helium and hydrogen.

Each chemical transition in the inner structure, will lead to a distinctive signature in the characteristic frequencies for pulsation. In Figure 4 we show the propagation diagram for an sdB model with stellar mass $0.473 M_{\odot}$, $T_{\rm eff} = 28\,700$K and $\log g = 5.53$. The full line corresponds to the run of the Brunt-Väisaälä frequency (N^2), while the dashed curve is the run of the Lamb frequency (L_ℓ) for $\ell = 2$. The gray shaded region corresponds to the evanescence region.

[2] https://zenodo.org/record/3428841#.XcWlWJLYpE4

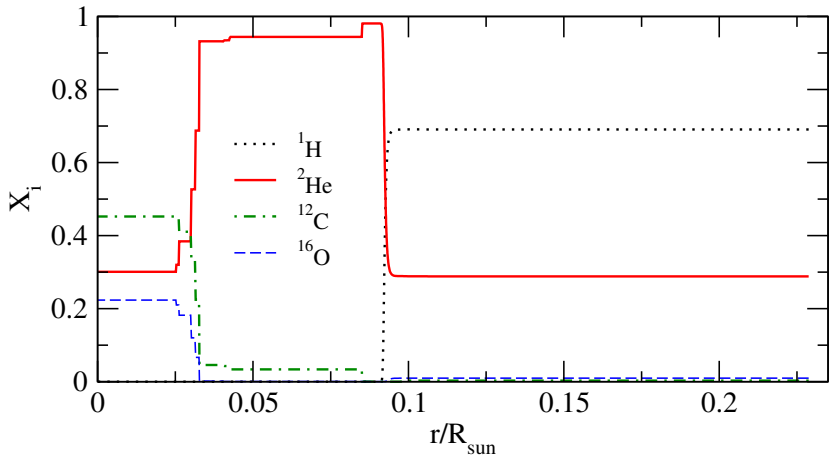

Figure 3. Chemical abundance as a function of radius for a sdB model of $0.474 M_{\odot}$, and $T_{\rm eff} = 26\,214$ K. Only the most abundant elements are depicted.

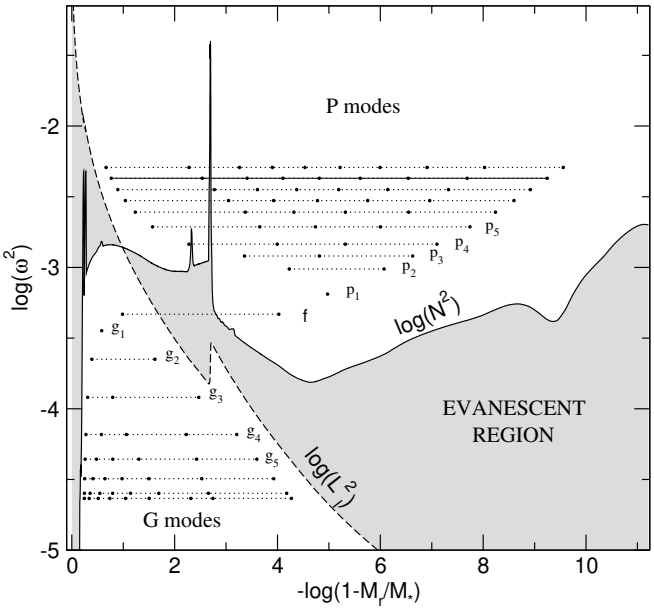

Figure 4. Propagation diagram for a sdB model with $0.473 M_{\odot}$, and $T_{\rm eff} = 28\,700$ K, for $\ell = 2$ modes. The Brunt-Väisälä (full line) and Lamb (dashed line) frequencies are also depicted, separating the propagation and evanescent regions. The horizontal lines show the square values of the eigenfrequencies and the circles mark the position of the nodes in the radial eigenfunction.

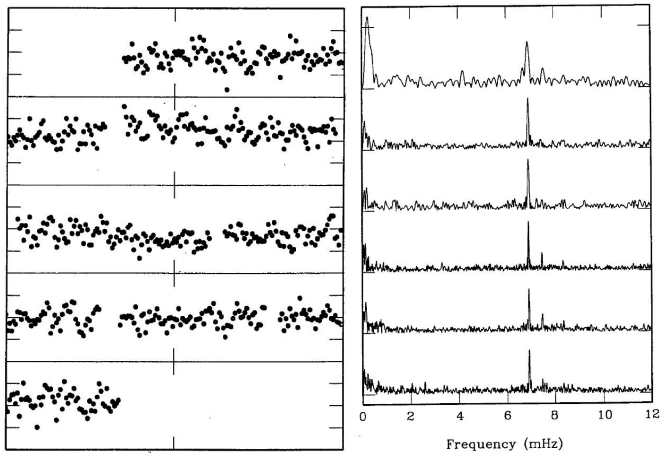

Figure 5. Light curve (left) and Fourier Transform (right) EC 14026-2647 for the original data from Kilkenny et al. (1997). The ordinate in the light curve are separated by 0.05 mag and the abscissae by 0.01 d, so that the data read continuously from left to right and top to bottom, from fractional Julian date 0.307 to 0.387. For the FT the ordinate carets are separated by 0.015 mag. Credit: Kilkenny et al. (1997).

Propagation is possible if the frequency of the mode is higher or lower than N^2 and L_ℓ. Modes in the region of high frequency correspond to pressure modes while gravity modes are found in the low frequency regions (Unno et al., 1979). As can be seen from Figure 4, pressure modes propagate in regions closer to the surface while gravity modes will show larger amplitudes in the inner regions of the star. This effect is better depicted by the horizontal lines showing the square values of the eigenfrequencies and the circles marking the position of the nodes in the radial eigenfunction (y_1). Thus, p–modes will bring information on the outer layers while g–modes will bring information on the central regions.

5. Pulsating Subdwarf B Stars

The first pulsating sdB was discovered by Kilkenny et al. (1997) with the South African Observatory, EC 14026-2647, showing short period variability with a main period around ~ 144 s. Therefore, this class of variable sdB is known as EC 14026. The light curve and Fourier Transform are presented in Figure 5. Independently and almost at the same time, Charpinet et al. (1996) predicted the existence of pulsation instability for pressure modes in sdB stars, due to the classical κ-mechanism associated to the $Z-$peak in the opacity. Figure 6 shows the run of the Rosseland opacity compared to the time derivative of the work function dW/dr for the fundamental mode with $\ell = 2$ (Charpinet et al., 1996). The peak in dW/dr is directly related to the peak in the opacity due to heavy elements marked as "Z-bump". Charpinet et al. (1996) first found that instability was only present for high metallicity models with $Z > 0.04$, but in a later work (Charpinet et al., 1997) they found that the enhancement in

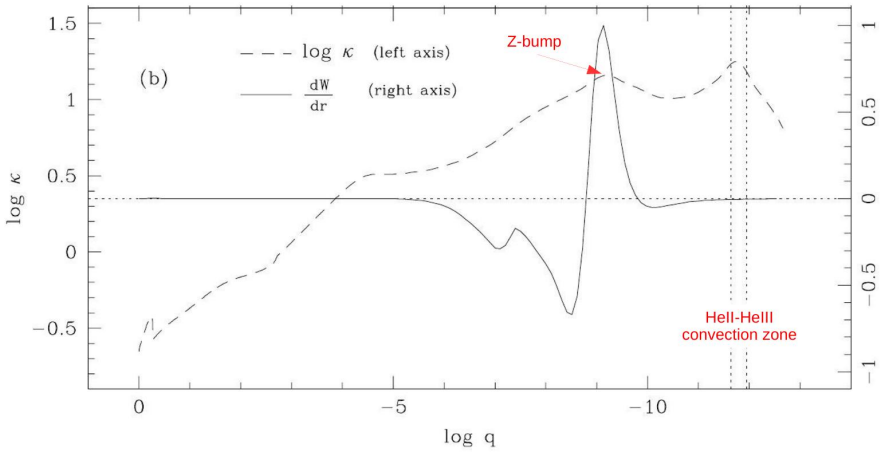

Figure 6. Run of the Rosseland opacity (dashed line) and the integrand of the work integral for the fundamental mode with $\ell = 2$ (solid line). Driving regions ($dW/dr > 0$) are clearly associated with the opacity bump, caused by heavy element ionization (Z-bump). The HeII-HeIII convection zone is indicated with vertical dotted lines. Credit: Charpinet et al. (1996), © AAS. Reproduced with permission.

the Fe–peak elements in the driving region was enough to drive pulsations. The local overabundance of heavy elements is possible due to the equilibrium between radiative levitation and gravitational settling processes.

EC 14026, also called V361 Hya stars, pulsate in pressure modes with short periods between 80 s and 580 s, with amplitudes of $0.3 - 64$ mmag. They are found mainly among the hotter sdBs, with effective temperatures between 28 000 and 35 000 K, and $\log g \sim 5.8$. The position of the current sample of EC 14026 stars in the $\log g - T_{\rm eff}$ plane is depicted in Figure 7 (blue circles) in the low $\log g$ part of the diagram, along with all classes of pulsating hot subdwarfs, that will be discussed below. The data was extracted from Table 1 of Holdsworth et al. (2017). The sdB instability strip is not pure, and around 10% of the objects in the temperature range where EC 14026 stars are found, show pulsations (Østensen et al., 2010).

The second class of variable sdB stars was discovered by Green et al. (2003). These stars are known as V1093 Her, or PG 1716 after the prototype PG 1716+426. PG 1716 stars are long period pulsators with periods between 1400 and 43 500 s, and amplitudes of $0.4 - 4.1$ mmag. As can be seen from Figure 7 (red triangle–up), they are cooler than the p-mode pulsators EC 14026, with effective temperatures between 23 000 and 30 000 K, and $\log g \sim 5.4$. Fontaine et al. (2003) showed that g-mode pulsations are excited in PG 1716 stars by the same κ-mechanism proposed by Charpinet et al. (1996, 1997), if the observed g-modes are high radial order and high harmonic degree ($\ell \geq 3$) modes. Around %75 of the objects inside the PG 1716 instability strip show brightness variations.

Three years later, Schuh et al. (2006) reported the first pulsating sdB, HS 0702+6043, that showed both short and long periods, and thus it was called a

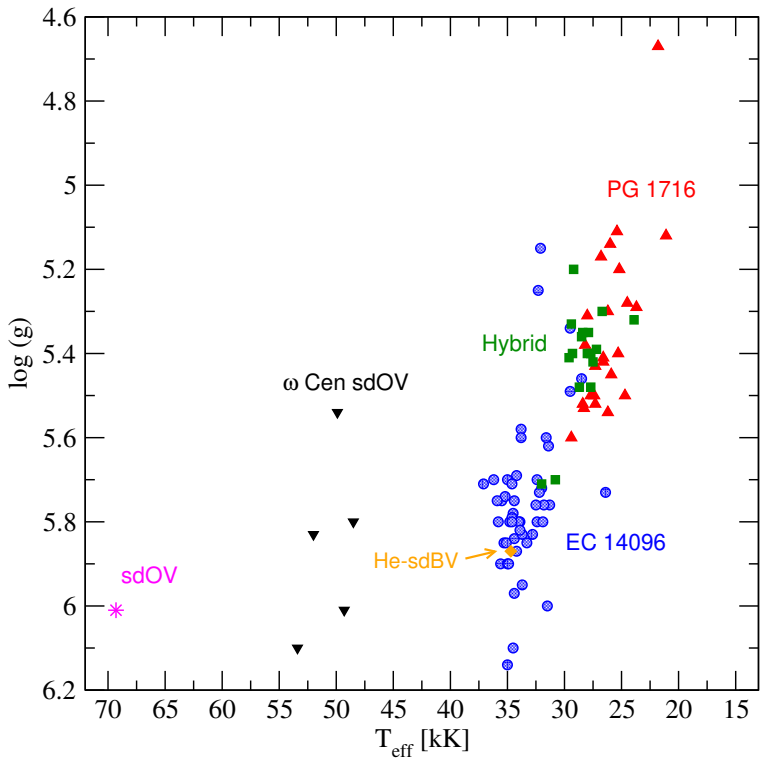

Figure 7. The distribution of the variable hot subdwarf stars in the $\log g - T_{\rm eff}$ plane. Each class is indicated with different symbols and colors. The sub-classes of sdBV stars EC 14026 (blue circles), PG 1716 (red up triangle) and the Hybrid (green squares) are depicted in the low temperature part of the plane. The only He-sdBV is also included (orange diamond). SdO variables are located in the hot part of the diagram, the only sdOV detected in the field of the Galaxy (magenta star) and those discovered in the globular cluster ω Cen (black down triangle). The values of $\log g$ and effective temperatures where taken from Table 1 of Holdsworth et al. (2017).

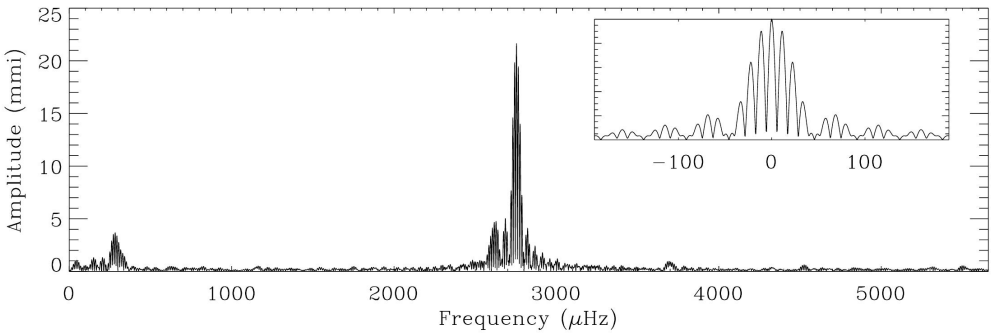

Figure 8. Fourier transform for the discovery of the hybrid sdB star HS 0702+6043. The plot shows the Fourier Transform of the full light curve, with the window function for the two–night data set displayed in the inset panel in the upper right corner (frequency in μHz as in the main plot, the amplitude scaling is arbitrary). Credit: Schuh et al. (2006). Copyright A&A. Reproduced with permission © ESO.

hybrid sdBV star. HS 0702+6043 was previously identified as a EC 14026 star with two short periods of 363 s and 383 s, but further observations revealed a low–amplitude ($\sim$ 4 mmag), long–period of 3538 s, identified by Schuh et al. (2006) as a g-mode pulsation. The Fourier Transform from Schuh et al. (2006) is shown in Figure 8. Hybrid sdBV stars show effective temperatures $\sim$ 28 000 K, between long and short period sdBVs, as it is shown in Figure 7, where hybrid sdBVs are depicted with green squares. Since $p-$modes propagate in the outer regions of the star, whereas $g-$modes do in the deep interior, the whole internal structure of the star can be sampled in the case of hybrid sdB stars (Heber, 2016).

The only pulsating He–sdBV is also depicted in Figure 7 (orange diamond). He–sdB stars are a very small group of subdwarf stars that show varying degrees of helium enrichment in the envelope, but have effective temperatures similar to hydrogen rich sdB stars (Ahmad & Jeffery, 2003). Variability of the He-sdBV, LV IV–14° 116, was reported by Ahmad & Jeffery (2003), with the detection of two long periods of 1953 s and 2870 s, characteristic of g–mode pulsations.

The period range for each class of pulsating sdB stars is shown in Figure 9, where the period range for all sdB stars from Figure 7 are depicted in the Period–log g plane. EC 14026 $p-$mode pulsators show periods in the range of 60–600 s, while PG 1716 $g-$mode pulsators show long periods in the range of 1400–44000 s. Hybrids are in between, with periods in the range of 118–28500 s.

6. Pulsating Subdwarf O Stars

Subdwarf O stars are intrinsically hotter than sdB stars. In addition, they show a range of helium abundance in the atmosphere, from a hundredth of solar content to pure helium. As an example, Figure 10 shows the normalized spectra of the sdO J16007+0748 (Woudt et al., 2006). The He II lines are clearly present in

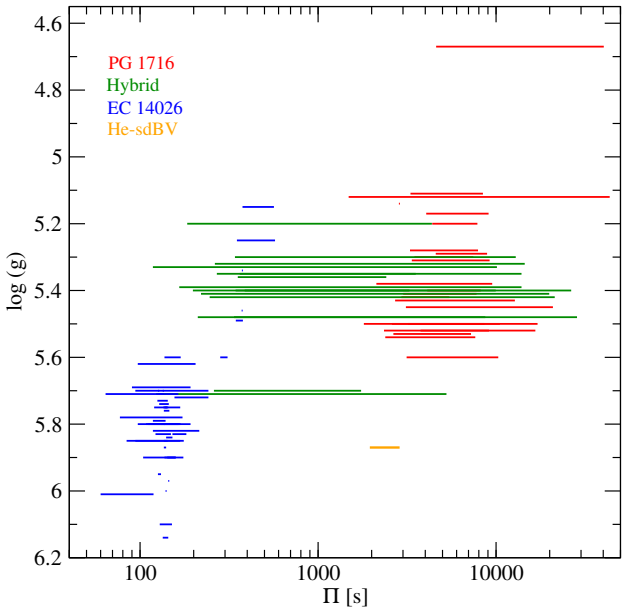

Figure 9. Period-log g diagram for the pulsating sdB stars presented in Figure 7. The colors represent the same as the previous figure. The data was taken from Table 1 of Holdsworth et al. (2017).

absorption, along with the Balmer series lines from $H\beta$ to $H\epsilon$. Given the small binary fraction of sdO stars, merger of two helium white dwarfs or hot flasher evolution are the most likely formation channels.

J16007+0748 is the first and only pulsating sdO in the Galactic field. Woudt et al. (2006) reported the detection of short period variability with a main period of 119.33 s, being identified with p–mode pulsations. The position of the sdOV is depicted in Figure 7 with a magenta star, being the hottest object of the sample.

Latter, Randall et al. (2010, 2011) reported the detection of four sdOV stars in the globular cluster ω Cen. The objects showed periods in the range between 84 s and 119 s, in agreement with the sdOV found by Woudt et al. (2006). Currently, there are five sdOV stars from ω Cen, depicted with black down–triangles in Figure 7. Contrary to the sdOV star found in the field, the objects belonging to the globular cluster, show hydrogen dominated atmospheres, and are also cooler. This could be related to the lower metallicity of the cluster as compared to the disk population. The excitation mechanism seems to be $\kappa-$mechanism, similar to sdBV stars (Randall et al., 2016).

7. Concluding Remarks

In this work I briefly described the main characteristics of the pulsating hot subdwarf stars. I recommend the excellent reviews of Heber (2009) and Heber (2016) and references therein, for more details.

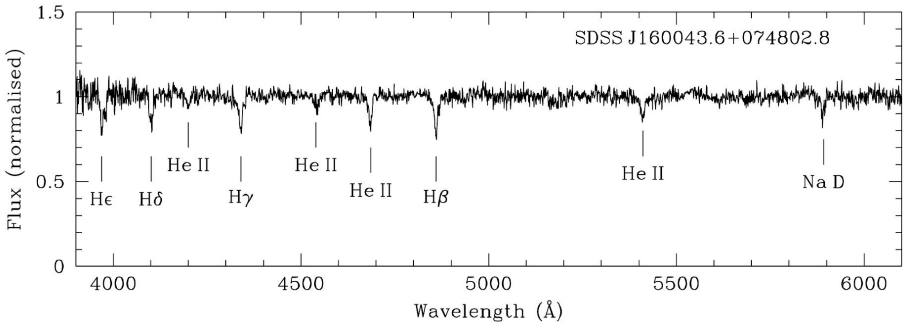

Figure 10. Combined SALT spectrogram of J16007+0748 (only sdOV star) obtained with a total exposure time of 1800 s. The absorption lines are marked and labelled. Credit: Woudt et al. (2006).

There are currently, $\sim$ 100 sdB variables and six sdO variables reported (Holdsworth et al., 2017), including those found with *Kepler* satellite observations. New space and ground-based surveys are expected to increase this sample. In particular the *TESS* (*Transit Exoplanet Survey Satellite*) is a great tool to find bright variables, as hot subdwarf stars, with around 40 confirmed objects.

It is important to notice that, in order to study hot subdwarf stars using asteroseismology, physically sound representative models should be available, in order to compare the observed periods with theoretical pulsation spectrum. In particular, by studying the inner structure of hot subdwarf stars we could shed some light on the formation channels of these compact blue objects.

Acknowledgments. We would like to thank Larissa Antunes Amaral, Maja Vučković and Murat Uzundag for their help in preparing the presentation.

References

Ahmad A., Jeffery C. S., 2003, *A&A*, **402**, 335
Battich T., Miller Bertolami M. M., Córsico A. H., Althaus L. G., 2018, *A&A*, **614**, A136
Brown T. M., Sweigart A. V., Lanz T., Land sman W. B., Hubeny I., 2001, *ApJ*, **562(1)**, 368
Cassisi S., Schlattl H., Salaris M., Weiss A., 2003, *ApJL*, **582(1)**, L43
Castellani M., Castellani V., 1993, *ApJ*, **407**, 649
Charpinet S., Fontaine G., Brassard P., Chayer P., Rogers F. J., Iglesias C. A., Dorman B., 1997, *ApJL*, **483(2)**, L123
Charpinet S., Fontaine G., Brassard P., Dorman B., 1996, *ApJL*, **471**, L103
Chen X., Han Z., Deca J., Podsiadlowski P., 2013, *MNRAS*, **434(1)**, 186
Clausen D., Wade R. A., Kopparapu R. K., O'Shaughnessy R., 2012, *ApJ*, **746(2)**, 186
Copperwheat C. M., Morales-Rueda L., Marsh T. R., Maxted P. F. L., Heber U., 2011, *MNRAS*, **415(2)**, 1381
Davis P. J., Kolb U., Willems B., 2010, *MNRAS*, **403(1)**, 179

Fontaine G., Brassard P., Charpinet S., Green E. M., Chayer P., Billères M., Rand all S. K., 2003, *ApJ*, **597(1)**, 518
Green E. M., Fontaine G., Reed M. D., Callerame K., Seitenzahl I. R., White B. A., Hyde E. A., Østensen R., Cordes O., Brassard P., Falter S., Jeffery E. J., Dreizler S., Schuh S. L., Giovanni M., Edelmann H., Rigby J., Bronowska A., 2003, *ApJL*, **583(1)**, L31
Han Z., Podsiadlowski P., Maxted P. F. L., Marsh T. R., 2003, *MNRAS*, **341(2)**, 669
Han Z., Podsiadlowski P., Maxted P. F. L., Marsh T. R., Ivanova N., 2002, *MNRAS*, **336(2)**, 449
Heber U., 1986, *A&A*, **155**, 33
Heber U., 2009, *ARA&A*, **47(1)**, 211
Heber U., 2016, *PASP*, **128(966)**, 082001
Heber U., Hunger K., Jonas G., Kudritzki R. P., 1984, *A&A*, **130**, 119
Holdsworth D. L., Østensen R. H., Smalley B., Telting J. H., 2017, *MNRAS*, **466(4)**, 5020
Kilkenny D., Koen C., O'Donoghue D., Stobie R. S., 1997, *MNRAS*, **285(3)**, 640
Lorén-Aguilar P., Isern J., García-Berro E., 2009, *A&A*, **500(3)**, 1193
Maxted P. F. L., Heber U., Marsh T. R., North R. C., 2001, *MNRAS*, **326(4)**, 1391
Napiwotzki R., Karl C. A., Lisker T., Heber U., Christlieb N., Reimers D., Nelemans G., Homeier D., 2004, *Ap&SS*, **291(3)**, 321
Østensen R. H., Oreiro R., Solheim J. E., Heber U., Silvotti R., González-Pérez J. M., Ulla A., Pérez Hernández F., Rodríguez-López C., Telting J. H., 2010, *A&A*, **513**, A6
Paczynski B., 1976, P. Eggleton, S. Mitton, and J. Whelan (eds.), *Structure and Evolution of Close Binary Systems*, Vol. 73 of *IAU Symposium*, p. 75
Randall S. K., Calamida A., Bono G., 2010, *Ap&SS*, **329(1-2)**, 55
Randall S. K., Calamida A., Fontaine G., Bono G., Brassard P., 2011, *ApJL*, **737(2)**, L27
Randall S. K., Calamida A., Fontaine G., Monelli M., Bono G., Alonso M. L., Van Grootel V., Brassard P., Chayer P., Catelan M., Littlefair S., Dhillon V. S., Marsh T. R., 2016, *A&A*, **589**, A1
Schuh S., Huber J., Dreizler S., Heber U., O'Toole S. J., Green E. M., Fontaine G., 2006, *A&A*, **445(3)**, L31
Toonen S., Nelemans G., 2013, *A&A*, **557**, A87
Unno W., Osaki Y., Ando H., Shibahashi H., 1979, *Astronomy Quarterly*, **3**, 197
Webbink R. F., 1984, *ApJ*, **277**, 355
Woudt P. A., Kilkenny D., Zietsman E., Warner B., Loaring N. S., Copley C., Kniazev A., Väisänen P., Still M., Stobie R. S., Burgh E. B., Nordsieck K. H., Percival J. W., O'Donoghue D., Buckley D. A. H., 2006, *MNRAS*, **371(3)**, 1497
Zhang X., Jeffery C. S., 2012, *MNRAS*, **419(1)**, 452

Pulsations Along Stellar Evolution
VIII LAPIS Summer School
AAA Workshop Series 12, 2021
M. Kraus & A.F. Torres, eds.

Pulsating White Dwarf Stars

Alejandra D. Romero[1]

[1]*Physics Institute, Universidade Federal do Rio Grande do Sul, Av. Bento Gonçalves 9500, Porto Alegre, RS-91501-970, Brazil*

Abstract.

White dwarf stars are the endpoint of the evolution of more than 95% of all stars in the Milky Way. They are compact objects, where the gravity is balanced by the pressure of a degenerate electron gas. Along the cooling curve, there are several instability strips where white dwarfs show photometric variability due to pulsations, opening the possibility to study these compact objects through asteroseismology. In this notes I will briefly review the main characteristics of white dwarf stars and the different pulsating subgroups.
Key words: asteroseismology — instabilities — stars: oscillations — stars: interiors — planet-star interactions

1. Introduction

White dwarf stars are the endpoint in the evolution of all stars with initial masses below $8 - 12 M_{\odot}$ (Siess, 2010; Woosley & Heger, 2015; Doherty et al., 2015; Lauffer et al., 2018). This comprises more than 95% of all stars in the Milky Way. Thus, they can be considered as fossils and they convey important information on the structure, evolution and chemical enrichment of our Galaxy and its components. They are compact objects with radius similar to the radius of the Earth and surface gravities of $\log g \sim 8$. They can also be found in a wide range in luminosity $L/L_{\odot} \sim 10^{-4.7} - 10^{3}$, and effective temperatures from $\sim 200\,000$ K to 4000 K. White dwarf stars are degenerate objects, where the inner pressure is dominated by a degenerate electron gas (it does not depend on temperature), while the thermal structure is dominated by the non–degenerate ions. In the Hertzprung-Russell (HR) diagram white dwarfs are found below the main sequence, being mostly of types O, B and A.

Pulsating white dwarf stars can also be found along the cooling curve. They show $g-$mode non–radial pulsations with periods from minutes to a few hours and variation amplitudes of millimag. White dwarf asteroseismology fully exploits the comparison between the observed pulsation periods in white dwarfs and the periods computed for appropriate theoretical models. It allows us to infer details of the origin, internal structure and evolution of white dwarfs (Fontaine & Brassard, 2008; Winget & Kepler, 2008; Althaus et al., 2010). In particular, constraints on the stellar mass, the thickness of the helium and hydrogen layers, the core chemical composition, weak magnetic fields and slow rotation rates can be inferred from the period patterns of pulsating white dwarfs.

There are currently several families of pulsating white dwarfs and related objects, that can be found in specific ranges of effective temperature along the cooling curve. At high effective temperatures we found the GW Vir stars, followed by He–rich atmosphere V777 Her, C-rich atmosphere DQV and the cool H–rich atmosphere ZZ Cetis. For low stellar masses, below $\sim 0.3 M_{\odot}$, we find the Extremely Low Mass (ELM) white dwarfs and their progenitors the pre-ELMs. The main characteristics of the classes of pulsating white dwarf stars will be addressed in this work.

2. Spectroscopic Classification of White Dwarfs

From a spectroscopic point of view, the population of white dwarfs can be divided into two groups: DAs, with hydrogen–rich atmospheres, and non–DAs, with hydrogen–deficient atmospheres. DA white dwarfs can be identified from the Balmer line series in their spectrum, as shown in the top panel of Figure 1. This group is the most abundant and corresponds to $\sim 85\%$ of all known white dwarfs (Kepler et al., 2016, 2019). The non–DA white dwarfs can be classified by the dominant element in their spectra and effective temperature: a DO class with strong lines of He II and effective temperatures of $\sim 45\,000 - 200\,000$ K; a DB class with strong He I lines and $T_{\rm eff} \sim 11\,000 - 30\,000$ K; and for effective temperatures below $T_{\rm eff} \sim 11\,000$ K, DC, DQ and DZ classes with a continuum spectrum, traces of carbon and metals in their spectra, respectively. Among the non–DA white dwarfs, DB stars are the most abundant. The spectrum for DB stars is characterized by He I lines, as shown in the bottom panel of Figure 1.

White dwarf stars show a mass distribution that is a combination of the initial mass function and the timescale of evolution –that depends on the mass. Both DA and DB distributions show a peak at $\sim 0.55 M_{\odot}$ (Ourique et al., 2019). However, DA white dwarfs show a wider mass range, extending to low mass, below $0.45 M_{\odot}$ and high mass, higher than $\sim 0.7 M_{\odot}$. At the low mass end, a contribution from close binary evolution is necessary, while for high stellar masses, mergers should be the main formation channel (Cheng et al., 2019).

3. The Formation of White Dwarf Stars

White dwarfs are the endpoint of all stars with initial masses below $8 - 12 M_{\odot}$ that evolved as single stars. Isolated stars or stars in non–interacting binary systems, will evolve as single stars. Binary evolution can also produce white dwarf stars. In particular, low mass white dwarf stars are produced from close binary interaction while white dwarf stars with stellar masses $> 0.8 M_{\odot}$ are thought to be produced mainly by merger episodes.

Hydrogen atmosphere white dwarfs (DA) with stellar masses around $\sim 0.55 M_{\odot}$ are expected to have evolved from single stars. Figure 2 shows the evolution from the main sequences to the white dwarf cooling curve for stars with initial masses between 0.92 $M_{\odot}$ and 3 $M_{\odot}$. The evolution starts in the main sequence, where hydrogen is burnt in helium via the $p-p$–chain or CNO–cycle (see for instance Kippenhahn et al., 2012, for details). Once the hydrogen in the core is exhausted, they move to the first giant stage: the Red Giant Branch (RGB). The hydrogen burning is now in a shell around the helium core, and its energy

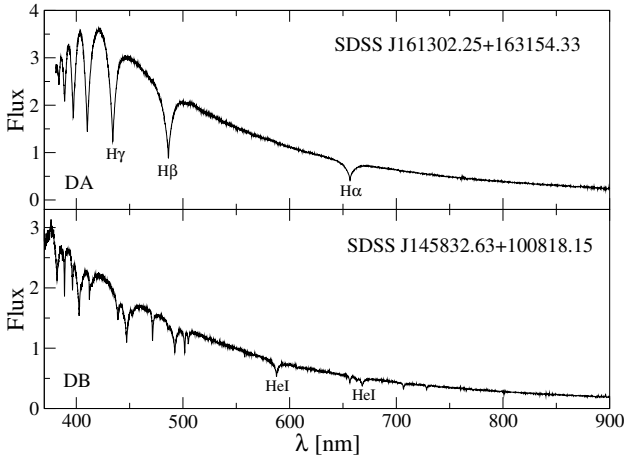

Figure 1. Spectra for two white dwarf stars from the Sloan Digital Sky Survey (SDSS). Top: DA white dwarf with $T_{\rm eff} \sim 14\,660$ K. Bottom: DB white dwarf with $T_{\rm eff} \sim 19\,420$ K.

is used to expand the outer layers. The inner helium core contracts releasing gravitational energy which in turn increases its temperature. Once the helium burning temperature is reached, a second central nuclear burning stage begins. If the hydrogen envelope is massive enough, the star has two energy sources, the central helium burning and the hydrogen burning–shell. After the exhaustion of helium, the star goes through a second giant stage: the Asymptotic Giant Branch (AGB). The AGB ends after the Thermal Pulses strip most of its envelope (TP-AGB in Figure 2) and the star evolves to higher effective temperatures at a nearly constant luminosity. Finally, after reaching the maximum $T_{\rm eff}$ the star enters the white dwarf cooling sequence.

White dwarf stars with hydrogen–deficient atmospheres are believed to be formed from a *Very Late Thermal Pulse* scenario, where the last thermal pulse occurs at high effective temperatures, burning all remaining hydrogen (Althaus et al., 2005, 2009). Close binary evolution or mergers are less likely to form hydrogen–deficient white dwarfs since most donor stars will have hydrogen–rich envelopes.

For white dwarfs with stellar masses below $\sim 0.45 M_{\odot}$, depending on initial metallicity, the helium core will not reach the temperature for nuclear reactions and the star will become a helium–core white dwarf. In addition, for stellar masses $< 0.3 M_{\odot}$ binary evolution is the only possible formation channel, since a single star will take more than the age of the Universe to reach the white dwarf stage (Pelisoli & Vos, 2019). The HR diagram of the evolution of ELM progenitor of $0.28 M_{\odot}$ is shown in Figure 3. The progenitor star, transfers most of its mass due to a Roche lobe overflow (RLO) during its giant stage, leaving the RGB before the ignition of nuclear reactions in the helium core. The loops in the HR diagram are caused by residual hydrogen shell–burning, that reduces the hydrogen content in the envelope (see Istrate et al., 2014a, 2016, for details).

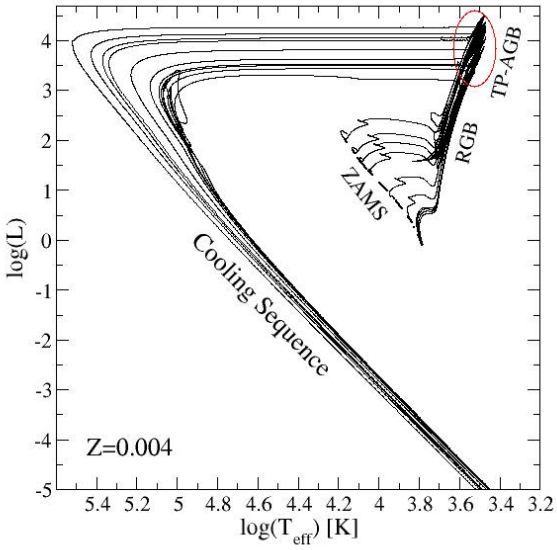

Figure 2. HR diagram for evolutionary sequences for $Z = 0.004$ and initial masses in the range $0.92 - 3.0 M_{\odot}$ and white dwarf masses in the range $0.503 - 0.817 M_{\odot}$ (Romero et al., 2015). The dashed line represents the location of the beginning of the main sequence.

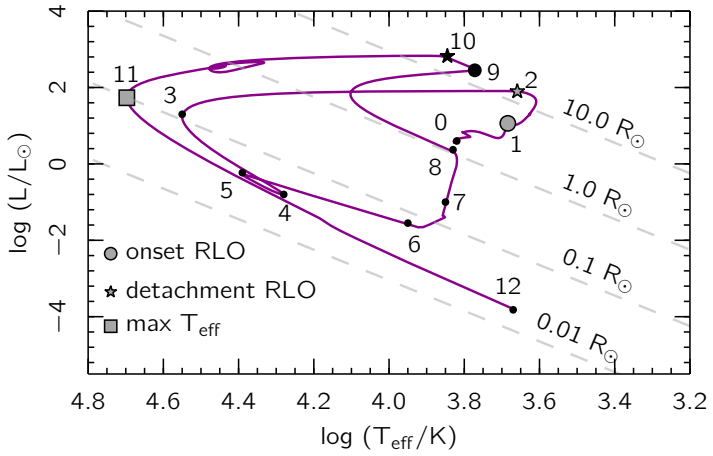

Figure 3. HR diagram showing the evolution of a $0.28 M_{\odot}$ white dwarf, with helium core. The progenitor star, with initial mass $1.4 M_{\odot}$ and $Z = 0.02$, is in a binary system with a neutron star of 1.2 $M_{\odot}$ and initial orbital period of 50 days. Credit: Courtesy of Alina Istrate (private communication).

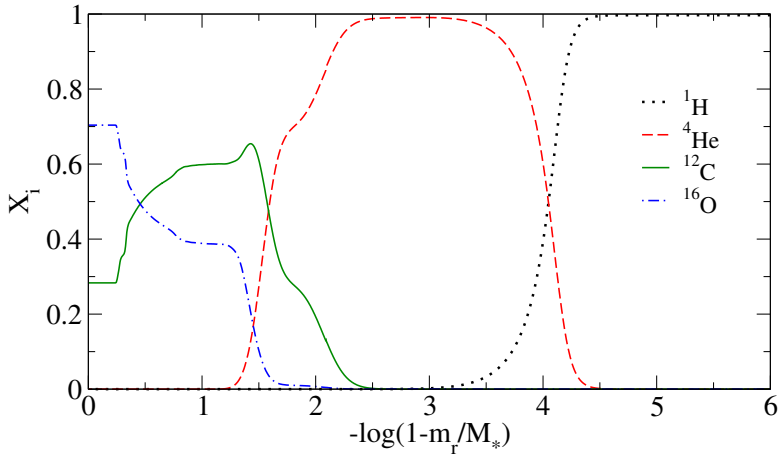

Figure 4. The internal chemical profiles of DA white dwarf model with $M_* = 0.593 M_\odot$ and $T_{\rm eff} \sim 11\,500$ K. Only the main nuclear species are depicted. The core is composed by a mixture of carbon and oxygen.

4. Chemical Structure and Characteristic Frequencies

Depending on the stellar mass, we can also classify the white dwarf stars by their central composition. Most progenitors will go through the hydrogen and helium central burning stages, resulting in a C/O core white dwarf. The chemical profile for a $0.593 M_\odot$ DA white dwarf is shown in Figure 4, where we show the abundances by mass as a function of the outer mass. We consider only the most abundant elements, in this case, hydrogen, helium, carbon and oxygen. The central regions (left side) correspond to the C/O core, formed mainly during the central helium burning stages. On top of the core, there is a helium buffer, with $\sim 10^{-2} M_*$. Finally, a hydrogen rich atmosphere is formed due to diffusion. Due to the characteristic high $\log g$ of white dwarf stars, chemical diffusion and gravitational settling will play a main role in determining the chemical structure of the star. Diffusion processes are responsible for the chemical stratification, where lighter elements are lifted to the envelope and heavier elements sink down.

For stellar masses below $0.30 - 0.45 M_\odot$ the progenitor star does not experience central helium burning and it is left with a helium core, surrounded by a thick hydrogen envelope ($M_{\rm H} > 10^{-3} M_*$), as shown in Figure 5, for a $0.198 M_\odot$ star. As mentioned in section 3, white dwarf stars with stellar masses below $0.3 M_\odot$ can only be formed by close binary evolution. These objects can be classified as low–mass or extremely low–mass white dwarfs, the limit between both is not well defined in the literature. In this work I will consider white dwarfs with masses below $0.3 M_\odot$ as ELMs to be consistent with the pulsating subclass.

For stellar masses higher than $\sim 1 M_\odot$, carbon can still be ignited in degenerate conditions, giving rise to a O/Ne/Mg white dwarf star. An example of the chemical profile for a white dwarf of $1.22 M_\odot$ is shown in Figure 6. The shaded region indicates the part of the core that is crystallized. The relative amount of each element in the central regions depends on the total mass and

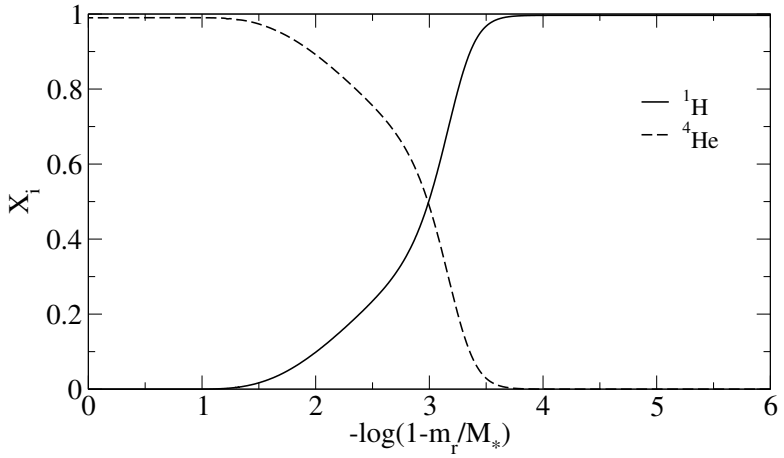

Figure 5. Same as Figure 4 but for a model with $M_* = 0.198 M_\odot$ and $T_{\rm eff} \sim 8985$ K. The core is composed only by helium.

whether carbon burning reaches the center of the star, among other things (see for example Denissenkov et al., 2013; Lauffer et al., 2018).

In case of the non–DA white dwarfs, hydrogen is depleted in the outer regions of the star, leaving a He/C/O envelope for high effective temperatures, and a helium–rich envelope, for lower effective temperatures. This can be seen from Figure 7, where we show a chemical profile for a non–DA white dwarf star of $0.515 M_\odot$ at three different temperatures during the cooling sequence. The top panel corresponds to a model at $T_{\rm eff} = 81\,752$ K, that can be considered a DO white dwarf star. The central composition is similar to that of a DA white dwarf of the same mass, but the outer layers are composed by a mixture of helium, carbon and oxygen (Althaus et al., 2009). As the star cools down, diffusion processes begin to model the chemical profile (see middle and bottom panel from Figure 7). The oxygen and carbon sink down, leaving a helium–rich envelope, characteristic of DB stars. In addition, a "double-layer" structure forms in the helium rich region (Althaus et al., 2009).

White dwarf stars show luminosity variations due to gravity modes. Since, these are compact objects, pressure modes will have periods shorter than ~ 10 s. Due to the core degeneracy, the Brunt Väisälä frequency decreases at the center, "trapping" the pressure modes in the most inner regions. In addition, the propagation region for gravity modes extends to the surface of the model. Thus the propagation regions for $p-$ and $g-$modes are inverted in comparison with other types of pulsators. This can be seen from Figure 8, where the Brunt Väisälä (N^2) and Lamb (L_ℓ) frequencies for $\ell = 1$ and 2 are depicted. The propagation regions for $p-$ and $g-$modes are also indicated.

5. Pulsating White Dwarfs

In this section, I will present the main characteristics of the most populous classes, being GW Vir, V777 Her, ZZ Cetis, pre-ELMV and ELMV. For a com-

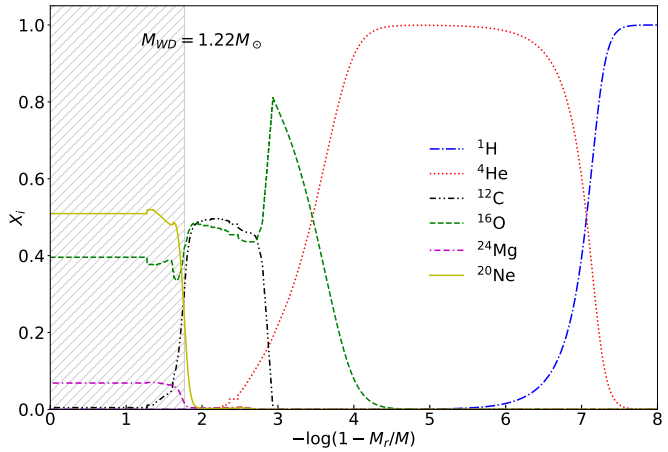

Figure 6. Same as Figure 4 but for a model with stellar mass of $1.22 M_\odot$ and $T_{\rm eff} = 10\,000$ K. The central composition is a mixture of oxygen, magnesium and neon. Courtesy of Gabriel Lauffer Ramos (private communication).

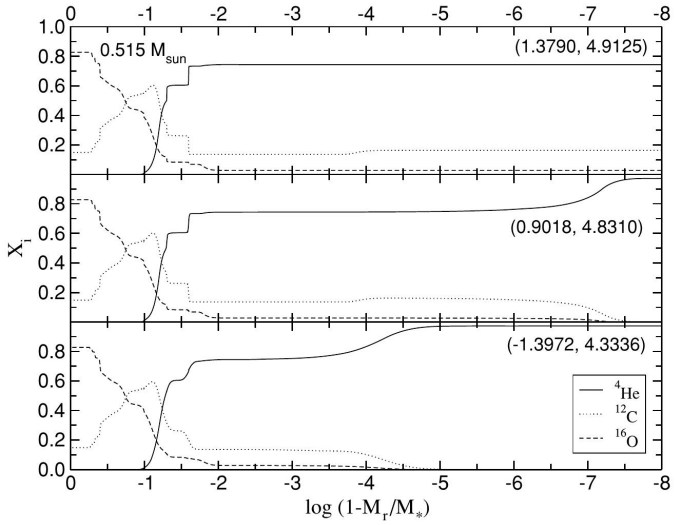

Figure 7. Internal abundance distribution of the main chemical elements as a function of the outer mass fraction ($\log(1 - M_r/M_*)$) for a hydrogen–deficient $0.515 M_\odot$ sequence at three stages on its cooling branch, as specified by the luminosity and effective temperature values ($\log(L/L_\odot)$), $\log T_{\rm eff}$) in each panel. The upper panel represents the chemical profile for a DO white dwarf star, while the middle and lower panels are characteristic of DB white dwarfs. Credit: Althaus et al. (2009), © AAS. Reproduced with permission.

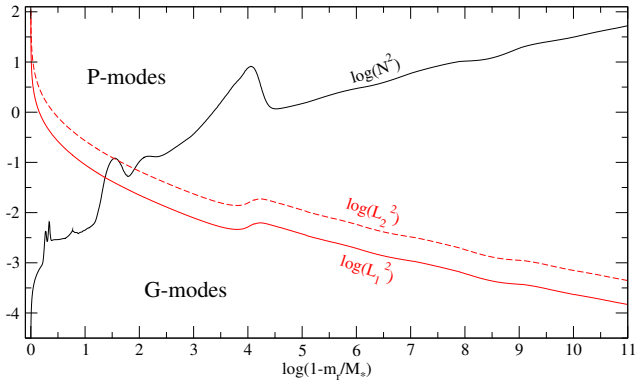

Figure 8. Characteristic frequencies for a DA white dwarf model of $T_{\rm eff} = 11\,500$ K and $0.593 M_{\odot}$ a s function of $\log(1 - m_r/M_*)$. The Brunt-Väisälä frequency (black line) and Lamb frequency (red line) for $\ell = 1$ (full line) and $\ell = 2$ (dashed line) are plotted in a logarithmic scale. The propagation regions for pressure and gravity modes are indicated as $P-$ and $G-$modes, respectively.

plete overview on pulsating white dwarfs I recommend the reader the reviews from Winget & Kepler (2008); Fontaine & Brassard (2008); Córsico et al. (2019).

The excitation mechanism acting on pulsating white dwarf stars is the $\kappa-$mechanism related to the opacity bump due to partial ionization of a given element, being carbon and oxygen (K II–shell electrons) for GW Vir (DO) stars, helium for V777 Her (DB) stars and pre-ELMVs, hydrogen for ZZ Ceti (DA) stars and ELMVs and iron peak elements for BLAPs. Since each element begins to be ionized at different effective temperatures, this will lead to instability strips at different positions in the $T_{\rm eff} - \log g$ plane. Figure 9 shows the location of all known classes of pulsating white dwarfs as associated objects. Each class is depicted with a different color, while the symbol indicates which element is responsible for the excitation due to the $\kappa-$mechanism. Also included, are theoretical evolutionary tracks for different stellar masses in the cooling curve.

5.1. ZZ Ceti Stars

The first pulsating white dwarf star was reported by Arlo Landolt in 1946, and it was the DA white dwarf HL Tau 76, showing a dominant period at 12.5 min (Landolt, 1968). Since then, 253 objects are part of the DA white dwarf variable class, known as ZZ Cetis (black circles in Figure 9).

The excitation mechanism enabling pulsations in ZZ Ceti stars corresponds to the $\kappa-$mechanism due to the opacity bump caused by partial ionization of hydrogen at the base of the hydrogen–rich envelope. At effective temperatures characteristic of ZZ Ceti stars, diffusion already shaped their chemical structure, leaving a hydrogen pure envelope. Because of this, it is believed that the instability strip for ZZ Cetis is pure, meaning that all DA white dwarfs in it should present photometric variability due to pulsations.

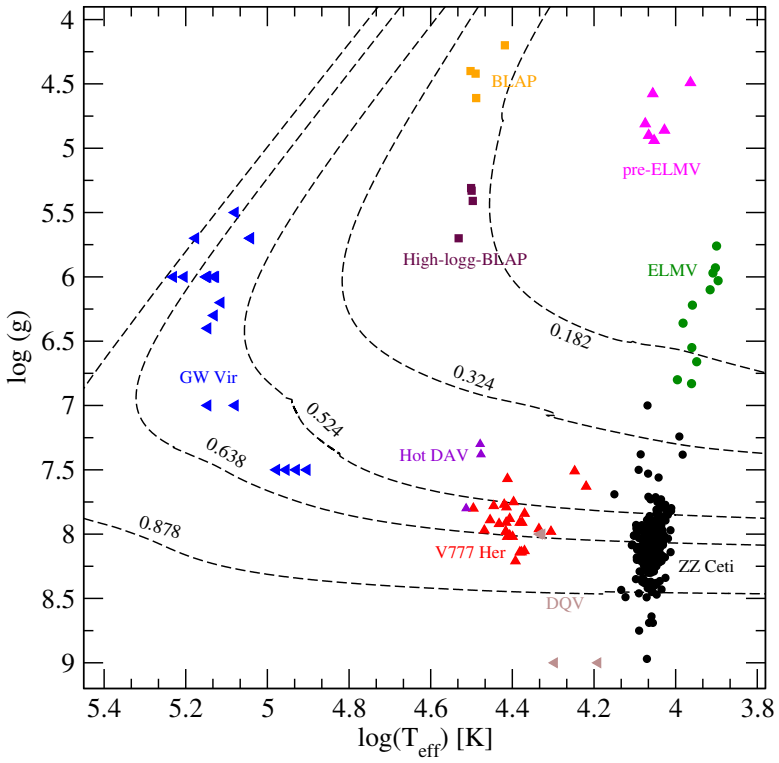

Figure 9. The classes of pulsating WDs. The data was extracted from Fontaine & Brassard (2008); Bognar & Sodor (2016); Pietrukowicz et al. (2017); Córsico et al. (2019); Romero et al. (2019a); Kupfer et al. (2019). Some theoretical sequences are included for stellar masses of 0.878, 0.638 and 0.524 $M_{\odot}$ from Romero et al. (2015) and for 0.324 and 0.182 $M_{\odot}$ from Istrate et al. (2016). The different symbols indicate the element related to the excitation mechanism: hydrogen (circles), helium (triangle–up), carbon and/or oxygen (triangle–left) and iron peak elements (squares).

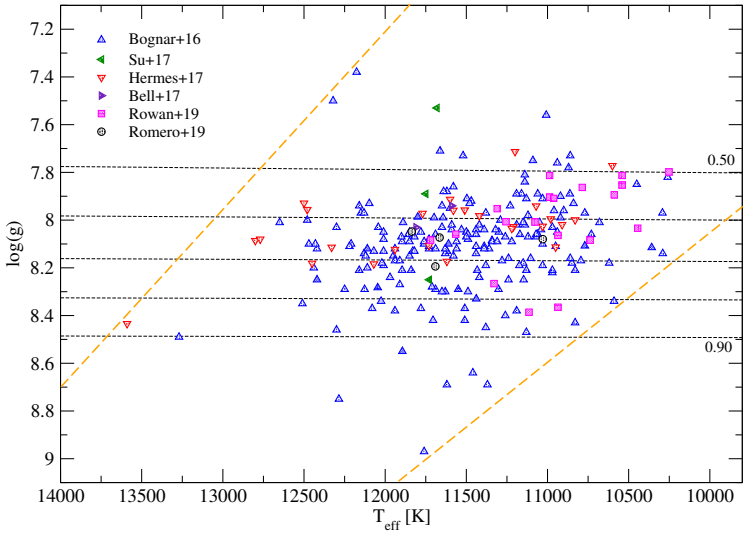

Figure 10. Distribution of ZZ Ceti stars on the $T_{\rm eff} - \log g$ plane. Coloured symbols correspond to the ZZ Ceti stars known to date, extracted from Bognar & Sodor (2016) (blue triangle-up), Su et al. (2017) (green triangle-left), Hermes et al. (2017a) (red triangle-down), Bell et al. (2017) (violet triangle-right), Rowan et al. (2019) (magenta square) and Romero et al. (2019a) (black circle). We include evolutionary tracks (dashed lines) with stellar masses of 0.5, 0.6, 0.7, 0.8 and $0.9 M_{\odot}$ from top to bottom (Romero et al., 2019b). For visualization purposes we include the observed blue and red edges (no uncertainties are considered).

ZZ Ceti stars are the most populous class of pulsating white dwarfs (Romero et al., 2019a), with periods in the range $70 - 2000$ s and variation amplitudes of 0.01–0.3 mag. The instability strip for ZZ Cetis extends ~ 2500 K in effective temperature, from $\sim 13\,000$ K to $\sim 10\,400$ K, depending on stellar mass (Kepler & Romero, 2017; Hermes et al., 2017a). All ZZ Cetis known to date are depicted in Figure 10 in the $T_{\rm eff} - \log g$ plane. As can be seen from this, the instability strip is intrinsically hotter for higher stellar masses.

The ZZ Cetis can be classified into three groups, depending on the effective temperature (Clemens, 1993; Mukadam et al., 2006). The hot ZZ Cetis, which define the blue edge of the instability strip, exhibit a few modes with short periods (< 350 s) and small amplitudes (1.5–20 mma). The pulse shape is sinusoidal or sawtooth-shaped and is stable for decades. On the opposite side of the instability strip, there are the cool DAV stars, showing several long periods (up to 2000 s), with large amplitudes (40–110 mma), and non-sinusoidal light curves that change dramatically from season to season due to mode interference. Mukadam et al. (2006) suggested introducing a third class, the intermediate ZZ Cetis, with mixed characteristics from hot and cool ZZ Cetis.

Asteroseismological studies including large samples of ZZ Ceti stars, $\sim 40 - 100$ objects, found that the thickness of the hydrogen envelope is not the same

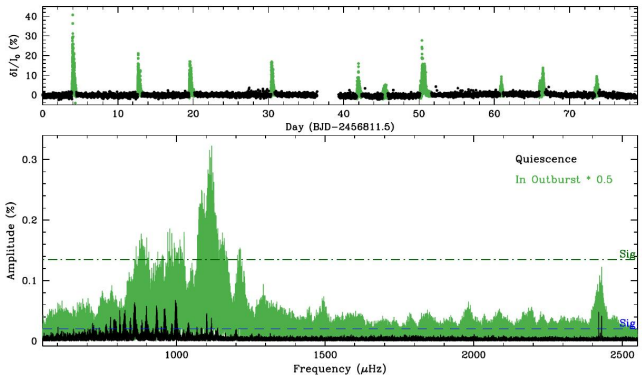

Figure 11. Light curve (top panel) and Fourier Transform (low panel) for the outburst ZZ Ceti star PG 1149+057. The 10 outburst events are marked in green while the data in quiescence is marked as black points. Pulsations persist during outbursts but have higher amplitudes and shorter periods than in quiescence. Credit: Hermes et al. (2015). © AAS. Reproduced with permission.

for all stars, but it shows a distribution in mass, from $\sim 10^{-4} M_*$ to $10^{-10} M_*$ (Castanheira & Kepler, 2008, 2009; Romero et al., 2013, 2019a). Thin hydrogen envelopes, with $M_{\rm H} < 10^{-8}$, have been confirmed from mass–radius observations of white dwarfs in binaries (Romero et al., 2019b), and it is also consistent with spectral evolution due to mixing processes in the outer layers (Cunningham et al., 2020; Ourique et al., 2020).

At the red edge of the ZZ Ceti instability strip, some objects show outburst events (Bell et al., 2015). These stars show a rich period spectrum combined with bursts repeating every few days, with peaks of up to 45% above the quiescent level and involving very energetic events ($\sim 10^{33} - 10^{34}$ erg). Figure 11 shows the light curve and Fourier Transform for the second outbursting ZZ Ceti, reported by Hermes et al. (2015). The outburst episodes are coupled with the $g-$mode pulsations, due to highly non–linear effects (Luan & Goldreich, 2018).

5.2. GW Vir Stars

GW Vir stars are hot pulsating white dwarfs with hydrogen–deficient atmospheres composed by a mixture of helium ($\sim 30 - 80\%$), carbon ($\sim 15 - 60\%$) and oxygen ($\sim 2 - 20\%$) (Werner & Herwig, 2006), as shown in the top panel of Figure 7. Luminosity variations are due to $g-$mode pulsations with low harmonic degree ($\ell \leq 2$) and high radial order $k \geq 18$), showing periods in the range of 300–6000 s and variation amplitudes of 0.01–0.15 mag.

The prototype of the class PG 119–035 was discovered to be variable by McGraw et al. (1979), and it is the pulsating star with more detected periods after the Sun, with 198 periods (Costa et al., 2008; Hermes et al., 2017b). Currently, there are 20 GW Vir stars, depicted as blue triangle–left symbols in Figure 9. The instability strip of GW Vir stars extends from $\sim 180\,000$ K to $\sim 75\,400$ K in effective temperature and from 5.5 to 7.7 in surface gravity (Fontaine &

Brassard, 2008; Córsico et al., 2019). GW Vir stars are sometimes divided into two subclases. The objects with $\log g = 5.5 - 7.0$ are still surrounded by the Planetary Nebula, that formed from the mass loss episodes during the thermal pulses, and are called Planetary Nebula Nuclei Variable (PNNV). The objects with surface gravity $\log g = 7.0 - 7.3$ have already lost the planetary nebula and are also known as DOV stars.

The excitation mechanism is the κ–mechanism caused by the cyclic ionization of the K–shell electrons of carbon and oxygen, as originally proposed by Starrfield et al. (1983). Latter computations using modern opacity values demonstrated that the presence of non–variables inside the GW Vir instability strip can be explained by an excessively large abundance of helium (Quirion et al., 2004). Thus, the GW Vir instability strip is intrinsically impure.

5.3. V777 Her Stars

By direct analysis with ZZ Ceti stars, Winget et al. (1982b) predicted that DB white dwarf stars should show photometric variability due to $g-$mode pulsations. The excitation mechanism is the $\kappa-$mechanism due to partial ionization of helium. Soon after, the first pulsating DB white dwarf star GD 358 was found by Winget et al. (1982a). GD 358 shows a complicated non–stable period spectrum as can be seen from Figure 12, where light curves from 1996 to 2006 are shown (Provencal et al., 2009). The star shows 27 periods, corresponding to 10 independent modes, between 250 s and 1000 s. The general frequency locations of the identified modes are consistent throughout the years, but the high–k multiplets exhibit significant variability in structure, amplitude and frequency (Provencal et al., 2009). These changes in the amplitude spectrum with timescales of a few years are thought to be consequences of strong non–linear coupling, due to the interaction between the pulsations and the convective layer.

The instability strip of V777 Her stars extends from $\sim 32\,000$ K to $\sim 22\,400$ K in effective temperature and from 7.5 to 8.3 in surface gravity, with periods between 120 s and 1100 s, and amplitudes of 0.05 to 0.3 mag (Fontaine & Brassard, 2008; Córsico et al., 2019). There are ~ 50 pulsating DB white dwarfs known to date, 27 of them depicted with triangle–up symbol in Figure 9.

The V777 Her instability strip is currently non–pure. However, this fact is related to the determination of the effective temperature and $\log g$ obtained from fitting of the spectra with model atmospheres. Small and undetected amounts of hydrogen in the helium–rich envelope can lead to spectroscopic effective temperatures considerably lower than those obtained with pure helium model atmospheres. Thus, the purity of the V777 Her instability strip is still an open subject in the field.

5.4. ELMV and Pre–ELMV

Extremelly low mass white dwarfs are helium core stars with stellar masses below $0.3 M_{\odot}$ (Pelisoli & Voss 2019), formed necessarily by close binary evolution, that correspond to the low mass wing of the mass distribution of white dwarf stars (Kepler et al., 2016, 2019). A typical chemical profile of an ELM white dwarf is shown in Figure 5.

Contrary to the case of other pulsating white dwarf classes, in pulsating ELMs $g-$modes should be core modes, while the propagation region for $p-$modes

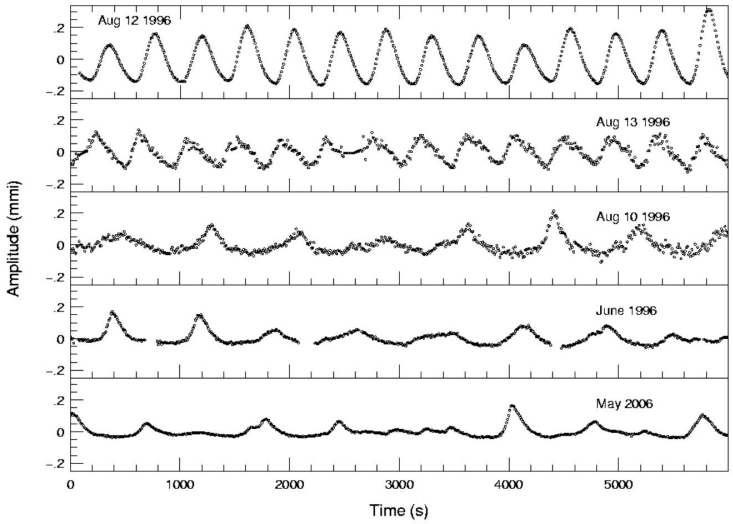

Figure 12. Light curve of GD358 from 1996 to 2006. Credit: Provencal et al. (2009). © AAS. Reproduced with permission.

extends to the surface. This is shown in Figure 13, where the characteristic frequencies are depicted for a model with $0.198M_{\odot}$ and $T_{\rm eff} \sim 8950$ K. This is due to the low degeneracy degree in the center regions.

Pulsational instabilities in ELMs were predicted by Steinfadt et al. (2010), based on scaling of the thermal timescale at the basis of the outer convective zone with surface gravity. Two years later, the first pulsating ELM, J184037.78+642312.3, was reported by Hermes et al. (2012), with periods between 2000 s and 4900 s, much longer than the ones observed in ZZ Ceti stars. This can be expected since its stellar mass is $\sim 0.17M_{\odot}$. These long periods were identified with $g-$mode pulsations. Binarity was also confirmed, with a detection of a degenerate companion of $\sim 0.8M_{\odot}$ and an orbital period of 4.6 h. Hermes et al. (2013) reported the detection of two variable ELMs (ELMV) with one of them, J111215.82+1117450.0, showing a period of 134 s apart from long periods in the range of 1792–2855 s. This short period is consistent with $p-$mode pulsations for the stellar masses of ELM white dwarfs.

The instability strip for ELMV white dwarfs extends in the effective temperature range of $7800-10\,000$ K and from 6.0 to 6.8 in $\log g$. To date 11 objects are known as variable ELMs, depicted with green circles in Figure 9. All but one object show long periods from 1100 s to 6300 s, while the short periods detected for J111215.82+1117450.0 are 134.275 s and 107.56 s (Hermes et al., 2013). Variation amplitudes range from 0.002 to 0.044 mag. The instability strip of ELMV stars can be considered as the natural extension of the ZZ Ceti instability strip to low stellar masses, since the excitation mechanism is the same for both, i.e., the $\kappa-$mechanism due to the opacity bump caused by partial ionization of hydrogen at the base of the hydrogen–rich envelope.

Pre-ELM stars are identified as the evolutionary progenitors of ELM white dwarfs. They are found at high luminosity, low $\log g$ compared to the ELMs,

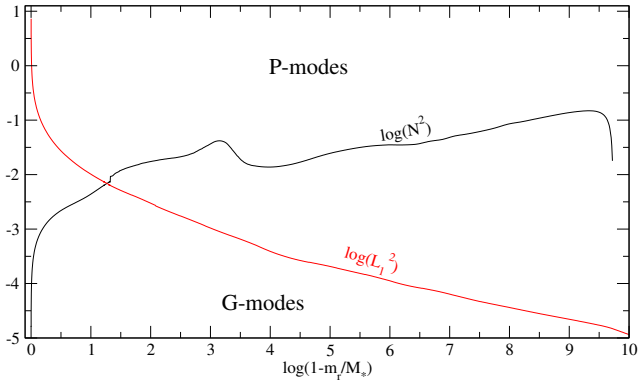

Figure 13. Characteristic frequencies for a DA white dwarf model with $M_* = 0.198 M_\odot$ and $T_{\rm eff} = 8950$ K. The Brunt-Väisälä frequency (black line) and Lamb frequency (red line) for $\ell = 1$ are plotted in a logarithmic scale. The propagation regions for pressure and gravity modes are indicated as $P-$ and $G-$modes, respectively.

during the loop in the HR diagram caused by residual hydrogen–burning (see Figure 3, Istrate et al., 2014b). The surface composition is a mixture of hydrogen and helium (Gianninas et al., 2016), suggesting that chemical diffusion is being inhibited (Córsico & Althaus, 2016; Istrate et al., 2016).

The first variable pre–ELM was reported by Maxted et al. (2013), WASP J024743.37-251549.2, showing periods in the range 380–420 s. The star is a low mass object (0.186 $M_\odot$) in an eclipsing binary with an orbital period of 16 h with a 1.356 $M_\odot$ companion. To date, there are 10 known objects (magenta triangle–up in Figure 9) with periods in the range of 300 to 5000 s and amplitudes of 0.001–0.05 mag. The instability strip for pre–ELMs extends from 800 K to 13 000 K in effective temperature and from 4.0 to 5.0 in surface gravity. Pulsations in pre–ELM stars are identified with high frequency $p-$modes and intermediate frequency mixed $p-g$ modes. Due to the peculiar shape of the Brunt-Väisälä frequency in the inner regions, mixed modes show properties of $p-$modes in the outer parts and of $g-$modes in the inner parts of the star (Córsico & Althaus, 2016).

Jeffery & Saio (2013) found that modes in pre–ELM models are excited by the $\kappa-$mechanism combined with convection, operating mainly in the second helium ionization zone ($He^+ \rightarrow He^{++}$), provided that the driving region is depleted in hydrogen.

6. Blue Large Amplitude Pulsators

The Blue Large Amplitude Pulsators (BLAPs) were discovered by Pietrukowicz et al. (2017), as a result of a long time photometric study of the OGLE. These objects show regular brightness variations with periods in the range 20 – 40 min and amplitudes of 0.2 – 0.4 mag. The light curves have a characteristic sawtooth shape, similar to the shape of classical Cepheids and RR Lyrae-type stars that

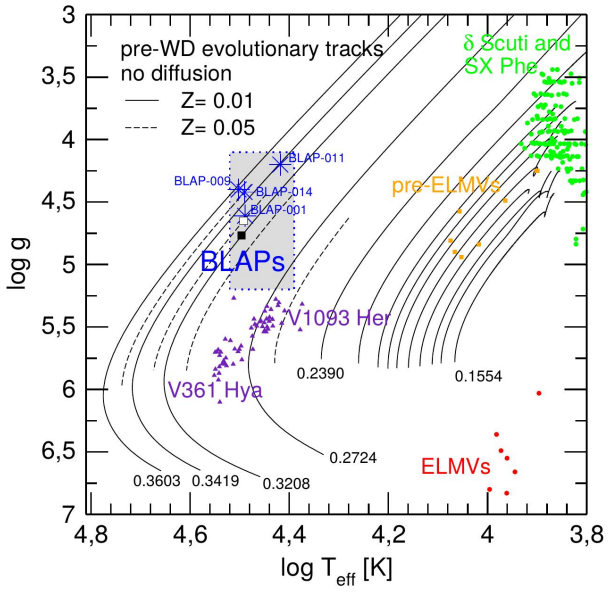

Figure 14. The location of the BLAPs on the $\log T_{\rm eff} - \log g$ diagram (shaded rectangle area, blue star), along with other classes of pulsating stars: ELMVs (red dots), pre–ELMVs (orange dots), pulsating sdBs (violet triangles) and δ Sct/SX Phe stars (green dots). Solid (dashed) black lines correspond to low-mass He-core pre–WD evolutionary tracks with $Z = 0.01$ ($Z = 0.05$). Credit: Romero et al. (2018).

pulsate in the fundamental radial mode. The BLAP stars are blue hot objects with effective temperatures of $\sim 30\,000$ K, and $\log g \sim 4.2 - 4.6$ similar to main sequence and pre–ELM stars. In addition, their effective temperature is similar to that of hot subdwarf stars. This is shown in Figure 14 where the position of the BLAPs in the $T_{\rm eff} - \log g$ plane is depicted, compared to variable hot subdwarfs and main sequences pulsators. Pietrukowicz et al. (2017) proposed that BLAPS, are either shell–burning, helium core, low mass stars or core helium burning pre–sdOB stars. Exploring the first possibility, Romero et al. (2018) proposed that BLAPs are hot pulsating pre–ELM WD stars with masses of $\sim 0.30 - 0.40 M_{\odot}$. They found that pulsations can be excited by the $\kappa-$mechanism due to the iron peak elements, as it is the case for pulsating hot subdwarf stars, for fundamental and low radial order $g-$modes. Romero et al. (2018) found pulsation instability only in models where the total initial metallicity was increased to five times the solar metallicity. However, they proposed that only an enhancement of the iron peak elements in the driving region would be enough for pulsations to be excited. This was proved later by Byrne & Jeffery (2018).

Recently, a new class of pulsating stars was reported by Kupfer et al. (2019). They show similar effective temperatures as BLAPs but higher $\log g$ values, and thus are called high–logg–BLAPs (purple squares in Figure 9). They are monoperiodic, showing large pulsation amplitudes of $> 5\%$, with periods in the range

200–475 s, consistent with radial oscillations. To test the evolutionary origin of these objects, Kupfer et al. (2019) computed models for low–mass helium–core pre–white dwarfs and low mass core helium–burning stars, and found that the pulsation periods show better agreement with the pre–white dwarf models. This suggests that the high–logg–BLAPS and the BLAPS are both helium core pre-ELM white dwarfs with stellar masses of $\sim 0.25 - 0.35 M_{\odot}$.

7. Final Remarks

This work was intended to give a brief review on pulsating white dwarf stars for those who whant to start learning about these very interesting objects. I recommend the reviews of Winget & Kepler (2008); Fontaine & Brassard (2008) and Córsico et al. (2019) and references therein, for more details.

The number of white dwarf in general, and of pulsating white dwarfs in particular, keeps growing due to large spectroscopic surveys and space and ground-based observations. In particular, the *Kepler* satellite allowed us to discover new phenomena associated with stellar pulsations and to increase our knowledge on variable white dwarf stars. Further detection will allow us to study the interiors of white dwarfs through asteroseismology, and with that to uncover the evolution of our Galaxy.

Acknowledgments. I would like to thank Alina Istrate, Ben Thomas Pepper, Gabriel Lauffer Ramos, Ingrid Pelisoli and S. O. Kepler.

References

Althaus L. G., Córsico A. H., Isern J., García-Berro E., 2010, *A&A Rev.*, **18(4)**, 471

Althaus L. G., Panei J. A., Miller Bertolami M. M., García-Berro E., Córsico A. H., Romero A. D., Kepler S. O., Rohrmann R. D., 2009, *ApJ*, **704(2)**, 1605

Althaus L. G., Serenelli A. M., Panei J. A., Córsico A. H., García-Berro E., Scóccola C. G., 2005, *A&A*, **435(2)**, 631

Bell K. J., Hermes J. J., Bischoff-Kim A., Moorhead S., Montgomery M. H., Østensen R., Castanheira B. G., Winget D. E., 2015, *ApJ*, **809(1)**, 14

Bell K. J., Hermes J. J., Montgomery M. H., Winget D. E., Gentile Fusillo N. P., Raddi R., Gänsicke B. T., 2017, *The First Six Outbursting Cool DA White Dwarf Pulsators*, Vol. 509 of *Astronomical Society of the Pacific Conference Series*, p. 303

Bognar Z., Sodor A., 2016, *Information Bulletin on Variable Stars*, **6184**, 1

Byrne C. M., Jeffery C. S., 2018, *MNRAS*, **481(3)**, 3810

Castanheira B. G., Kepler S. O., 2008, *MNRAS*, **385(1)**, 430

Castanheira B. G., Kepler S. O., 2009, *MNRAS*, **396(3)**, 1709

Cheng S., Cummings J. D., Ménard B., Toonen S., 2019, *arXiv e-prints*, p. arXiv:1910.09558

Clemens J. C., 1993, *Baltic Astronomy*, **2**, 407

Córsico A. H., Althaus L. G., 2016, *A&A*, **585**, A1

Córsico A. H., Althaus L. G., Miller Bertolami M. M., Kepler S. O., 2019, *A&A Rev.*, **27(1)**, 7

Costa J. E. S., Kepler S. O., Winget D. E., O'Brien M. S., Kawaler S. D., Costa A. F. M., Giovannini O., Kanaan A., Mukadam A. S., Mullally F., Nitta A., Provençal J. L., Shipman H., Wood M. A., Ahrens T. J., Grauer A., Kilic M., Bradley P. A., Sekiguchi K., Crowe R., Jiang X. J., Sullivan D., Sullivan T., Rosen R., Clemens J. C., Janulis R., O'Donoghue D., Ogloza W., Baran A., Silvotti R., Marinoni S., Vauclair G., Dolez N., Chevreton M., Dreizler S., Schuh S., Deetjen J., Nagel T., Solheim J. E., Gonzalez Perez J. M., Ulla A., Barstow M., Burleigh M., Good S., Metcalfe T. S., Kim S. L., Lee H., Sergeev A., Akan M. C., Çakırlı Ö., Paparo M., Viraghalmy G., Ashoka B. N., Handler G., Hürkal Ö., Johannessen F., Kleinman S. J., Kalytis R., Krzesinski J., Klumpe E., Larrison J., Lawrence T., Meištas E., Martinez P., Nather R. E., Fu J. N., Pakštienė E., Rosen R., Romero-Colmenero E., Riddle R., Seetha S., Silvestri N. M., Vučković M., Warner B., Zola S., Althaus L. G., Córsico A. H., Montgomery M. H., 2008, *A&A*, **477(2)**, 627

Cunningham T., Tremblay P.-E., Gentile Fusillo N. P., Hollands M., Cukanovaite E., 2020, *MNRAS*, **492(3)**, 3540

Denissenkov P. A., Herwig F., Truran J. W., Paxton B., 2013, *ApJ*, **772(1)**, 37

Doherty C. L., Gil-Pons P., Siess L., Lattanzio J. C., Lau H. H. B., 2015, *MNRAS*, **446(3)**, 2599

Fontaine G., Brassard P., 2008, *PASP*, **120(872)**, 1043

Gianninas A., Curd B., Fontaine G., Brown W. R., Kilic M., 2016, *ApJL*, **822(2)**, L27

Hermes J. J., Gänsicke B. T., Kawaler S. D., Greiss S., Tremblay P. E., Gentile Fusillo N. P., Raddi R., Fanale S. M., Bell K. J., Dennihy E., Fuchs J. T., Dunlap B. H., Clemens J. C., Montgomery M. H., Winget D. E., Chote P., Marsh T. R., Redfield S., 2017a, *ApJS*

Hermes J. J., Kawaler S. D., Bischoff-Kim A., Provencal J. L., Dunlap B. H., Clemens J. C., 2017b, *ApJ*, **835(2)**, 277

Hermes J. J., Montgomery M. H., Bell K. J., Chote P., Gänsicke B. T., Kawaler S. D., Clemens J. C., Dunlap B. H., Winget D. E., Armstrong D. J., 2015, *ApJL*, **810(1)**, L5

Hermes J. J., Montgomery M. H., Winget D. E., Brown W. R., Gianninas A., Kilic M., Kenyon S. J., Bell K. J., Harrold S. T., 2013, *ApJ*, **765(2)**, 102

Hermes J. J., Montgomery M. H., Winget D. E., Brown W. R., Kilic M., Kenyon S. J., 2012, *ApJL*, **750(2)**, L28

Istrate A. G., Marchant P., Tauris T. M., Langer N., Stancliffe R. J., Grassitelli L., 2016, *A&A*, **595**, A35

Istrate A. G., Tauris T. M., Langer N., 2014a, *A&A*, **571**, A45

Istrate A. G., Tauris T. M., Langer N., Antoniadis J., 2014b, *A&A*, **571**, L3

Jeffery C. S., Saio H., 2013, *MNRAS*, **435(1)**, 885

Kepler S. O., Pelisoli I., Koester D., Ourique G., Romero A. D., Reindl N., Kleinman S. J., Eisenstein D. J., Valois A. D. M., Amaral L. A., 2016, *MNRAS*, **455(4)**, 3413

Kepler S. O., Pelisoli I., Koester D., Reindl N., Geier S., Romero A. D., Ourique G., Oliveira C. d. P., Amaral L. A., 2019, *MNRAS*, **486(2)**, 2169

Kepler S. O., Romero A. D., 2017, *European Physical Journal Web of Con-*

ferences, Vol. 152 of *European Physical Journal Web of Conferences*, p. 01011

Kippenhahn R., Weigert A., Weiss A., 2012, *Stellar Structure and Evolution*

Kupfer T., Bauer E. B., Burdge K. B., Bellm E. C., Bildsten L., Fuller J., Hermes J., Kulkarni S. R., Prince T. A., van Roestel J., Dekany R., Duev D. A., Feeney M., Giomi M., Graham M. J., Kaye S., Laher R. R., Masci F. J., Porter M., Riddle R., Shupe D. L., Smith R. M., Soumagnac M. T., Szkody P., Ward C., 2019, *ApJL*, **878(2)**, L35

Landolt A. U., 1968, *ApJ*, **153**, 151

Lauffer G. R., Romero A. D., Kepler S. O., 2018, *MNRAS*, **480(2)**, 1547

Luan J., Goldreich P., 2018, *ApJ*, **863(1)**, 82

Maxted P. F. L., Serenelli A. M., Miglio A., Marsh T. R., Heber U., Dhillon V. S., Littlefair S., Copperwheat C., Smalley B., Breedt E., Schaffenroth V., 2013, *Nature*, **498(7455)**, 463

McGraw J. T., Starrfield S. G., Liebert J., Green R., 1979, H. M. van Horn, V. Weidemann, and M. P. Savedoff (eds.), *IAU Colloq. 53: White Dwarfs and Variable Degenerate Stars*, p. 377

Mukadam A. S., Montgomery M. H., Winget D. E., Kepler S. O., Clemens J. C., 2006, *ApJ*, **640(2)**, 956

Ourique G., Kepler S. O., Romero A. D., Klippel T. S., Koester D., 2020, *MNRAS*, **492(4)**, 5003

Ourique G., Romero A. D., Kepler S. O., Koester D., Amaral L. A., 2019, *MNRAS*, **482(1)**, 649

Pelisoli I., Vos J., 2019, *MNRAS*, **488(2)**, 2892

Pietrukowicz P., Dziembowski W. A., Latour M., Angeloni R., Poleski R., di Mille F., Soszyński I., Udalski A., Szymański M. K., Wyrzykowski Ł., Kozłowski S., Skowron J., Skowron D., Mróz P., Pawlak M., Ulaczyk K., 2017, *Nature Astronomy*, **1**, 0166

Provencal J. L., Montgomery M. H., Kanaan A., Shipman H. L., Childers D., Baran A., Kepler S. O., Reed M., Zhou A., Eggen J., Watson T. K., Winget D. E., Thompson S. E., Riaz B., Nitta A., Kleinman S. J., Crowe R., Slivkoff J., Sherard P., Purves N., Binder P., Knight R., Kim S. L., Chen W.-P., Yang M., Lin H. C., Lin C. C., Chen C. W., Jiang X. J., Sergeev A. V., Mkrtichian D., Andreev M., Janulis R., Siwak M., Zola S., Koziel D., Stachowski G., Paparo M., Bognar Z., Handler G., Lorenz D., Steininger B., Beck P., Nagel T., Kusterer D., Hoffman A., Reiff E., Kowalski R., Vauclair G., Charpinet S., Chevreton M., Solheim J. E., Pakstiene E., Fraga L., Dalessio J., 2009, *ApJ*, **693(1)**, 564

Quirion P. O., Fontaine G., Brassard P., 2004, *ApJ*, **610(1)**, 436

Romero A. D., Amaral L. A., Klippel T., Sanmartim D., Fraga L., Ourique G., Pelisoli I., Lauffer G. R., Kepler S. O., Koester D., 2019a, *MNRAS*

Romero A. D., Campos F., Kepler S. O., 2015, *MNRAS*, **450(4)**, 3708

Romero A. D., Córsico A. H., Althaus L. G., Pelisoli I., Kepler S. O., 2018, *MNRAS*, **477(1)**, L30

Romero A. D., Kepler S. O., Córsico A. H., Althaus L. G., Fraga L., 2013, *ApJ*, **779(1)**, 58

Romero A. D., Kepler S. O., Joyce S. R. G., Lauffer G. R., Córsico A. H., 2019b, *MNRAS*

Rowan D. M., Tucker M. A., Shappee B. J., Hermes J. J., 2019, *MNRAS*,

486(4), 4574
Siess L., 2010, *A&A*, **512**, A10
Starrfield S. G., Cox A. N., Hodson S. W., Pesnell W. D., 1983, *ApJL*, **268**, L27
Steinfadt J. D. R., Bildsten L., Arras P., 2010, *ApJ*, **718(1)**, 441
Su J., Fu J., Lin G., Chen F., Khokhuntod P., Li C., 2017, *ApJ*, **847(1)**, 34
Werner K., Herwig F., 2006, *PASP*, **118(840)**, 183
Winget D. E., Kepler S. O., 2008, *ARA&A*, **46**, 157
Winget D. E., Robinson E. L., Nather R. D., Fontaine G., 1982a, *ApJL*, **262**, L11
Winget D. E., van Horn H. M., Tassoul M., Fontaine G., Hansen C. J., Carroll B. W., 1982b, *ApJL*, **252**, L65
Woosley S. E., Heger A., 2015, *ApJ*, **810(1)**, 34

Pulsations Along Stellar Evolution
VIII LAPIS Summer School
AAA Workshop Series 12, 2021
M. Kraus & A.F. Torres, eds.

Pulsating A-F Stars

J. P. Sánchez Arias[1,2]

[1]*Instituto de Astrofísica de La Plata. CONICET-UNLP, Argentina*
[2]*Astronomical Institute, Czech Academy of Sciences, Fričova 298, 251 65 Ondřejov, Czech Republic*

Abstract.
This Chapter provides a brief description of the different classes of pulsating A-F stars emphasising hybrids δ Sct-γ Dor stars. A modelling technique for hybrid δ Sct-γ Dor stars is presented along with the typical features that these stars "print" on their light curves and frequency spectra. Finally, we present a very different family of pulsating stars overlapping the region where pulsating A-F stars usually lie, the precursors of the so-called extremely low mass white dwarf stars. These stars have very similar atmospheric characteristics and their oscillation periods partially overlap making them difficult to discern. We discuss tools based on their seismic oscillation properties to distinguish them.

Key words: asteroseismology — stars: oscillations — stars: interiors

1. The Zoo of Pulsating A-F Stars

There are many families of pulsating stars grouped in different regions of the Hertzsprung-Russel (H-R) diagram. Figure 1 shows schematically some of these families in a seismic H-R diagram. Pulsating A-F stars lie approximately at the lower part of the classical instability strip and its intersection with the Main Sequence (MS) toward temperatures between 6700 and 8500 K. This interesting region of the seismic H-R diagram, harbours a large variety of families and subfamilies of pulsating stars with different physical and pulsational characteristics at different evolutionary stages (pre-MS, MS and post-MS).

Among these families, the best known are: solar-like stars with solar-like oscillations, the rapid oscillators Ap stars, SX Phoenicis stars, λ Boo stars, γ Dor, δ Sct and hybrids δ Sct-γ Dor stars. We will begin this section with a brief description of each of these families.

1.1. Solar-Like Stars With Solar-Like Oscillations

The internal structure of these stars is similar to the Sun, they have a radiative core with a large convective envelope. In general, stellar pulsations can be classified according to their driving mechanism in self-excited oscillations and stochastic oscillations. Self-excited oscillations arise from a perturbation of the energy flux resulting in a heat-engine mechanism. If the variation is in the opacity, we have the κ-mechanism; if the variation cames from the temperature rising

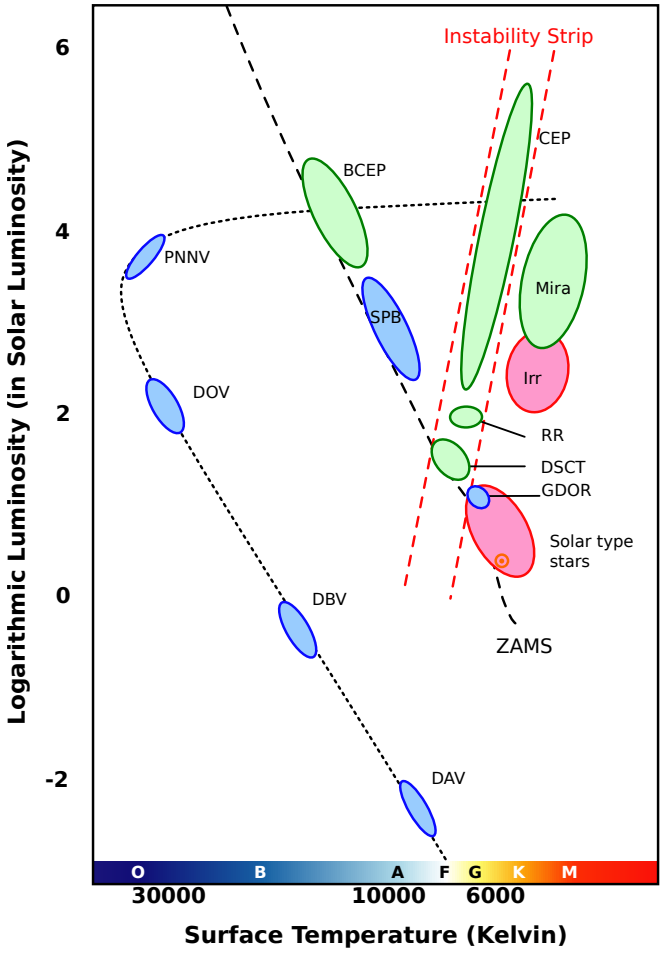

Figure 1. Seismic H-R diagram showing different families of pulsating stars. The classical instability strip is indicated in red lines, the beginning of the MS in black dashed line and the cooling track in black dotted line.

from nuclear reactions, then the operating mechanism is the ϵ-mechanism. On the other hand, stochastic oscillations are excited and damped usually by turbulent convection. Solar-like oscillations are driven stochastically and are expected to be present in all stars with outer convective zones.

1.2. Rapidly Oscillating Ap Stars

Rapidly Oscillating Ap (RoAp) stars belong to Population I. They have a particular chemical surface composition caused by atomic diffusion (specifically due to the effect of gravitational settling and radiative levitation). One of their main characteristics is their strong magnetic field. In addition, they usually present spots and stratification (Aerts et al., 2010). Their oscillation periods are between ~ 4.7 and 21 min and they correspond to high radial order, low degree pressure modes (or p-modes).

1.3. SX Phoenicis Stars

These stars belong to Population II and are characterised by low metallicities between 0.002 and 0.0002. SX Phoenicis (SX Phe) stars have masses in the range 0.9 to 1.15 $M_{\odot}$ and oscillations very similar to those of δ Sct stars. They are thought to be blue straggler stars, i.e. MS stars in a open or globular cluster that are more luminous and bluer than stars at the MS turnoff point for the cluster. One possible explanation for this behaviour lies in mass transfer between two stars born in a binary star system. The more massive star will evolve first and as it expands, will overflow its Roche lobe. Then mass will quickly transfer from the initially more massive companion on to the less massive one and this would explain why there would be MS stars more massive than other stars in the cluster which have already evolved off the MS.

1.4. λ Boo Stars

This family of pulsating A-F stars, consists of Population I stars with a superficial chemical impoverishment possibly due to the accretion of metal deficient gas in the circumstellar environment. Recent studies indicate that not all λ Boo stars are young and are found at a variety of MS ages (Murphy et al., 2020). Their oscillations are similar to δ Sct stars.

1.5. δ Sct Stars

One of the most representative group of pulsating A-F stars are δ Sct stars. They can be found on the MS and pre-MS with masses usually between 1.5 and 2.5 $M_{\odot}$. They oscillate in non-radial p-modes of low to intermediate radial order, and also show radial modes, with periods usually between 0.008 and 0.42 days which allow to probe the external layers of the star. These oscillations are driven mainly by the κ-mechanism operating in the partial ionisation He layer and the turbulent pressure acting in the H ionisation zone (Antoci et al., 2014). Their internal structure is characterised by a convective core surrounded by a radiative layer with a thin outer convective layer. In the Sun, this layer encompasses approximately 30% of the Sun, while in δ Sct stars this layer encompasses $\sim 1\%$.

1.6. γ Dor Stars

Another important group among pulsating A-F stars is formed by γ Dor stars. These stars are found in pre-MS, MS and post-MS. In general, they are less massive than δ Sct stars, with masses between 1.5 and 1.8 $M_{\odot}$ and effective temperatures between 6700 K and 7500 K. They pulsate in high radial order gravity-modes (or g-modes) with periods around 8 hrs and 3 d driven by the convective blocking mechanism. In γ Dor stars, the convective envelope is thought to be deeply enough to reach the layer where the κ-mechanism usually operates, i.e. the ionisation He II layer. The heat flux is then conducted by convection and the κ-mechanism is suppressed. The presence of g-modes in these stars allows us to probe the near-to-core layers.

1.7. Hybrid δ Sct-γ Dor Stars

These stars pulsate in many radial and non-radial p- and g-modes which makes them excellent targets for asteroseismology. The simultaneous presence of p- and g- modes allows to explore their external layers as well as the near-to-core layers, respectively. A typical light curve of this kind of stars often shows two separate ranges of frequencies: one corresponding to high frequencies characteristic of δ Sct (p-modes) and the other one at low frequencies usually characteristic of γ Dor (g-modes) (see Section 2.1). They usually lie in the overlapping instability region of δ Sct and γ Dor stars. However, the advance of space missions opened new interrogations due to the interesting results of such observations. For instance, several new hybrid δ Sct-γ Dor stars were found thanks to these missions and some of them lie outside their predicted instability strip. Moreover, the same is true for δ Sct and γ Dor stars. These observations showed that hybrid δ Sct-γ Dor stars are more common than expected and also made us wonder about the intrinsic characteristics of δ Sct, γ Dor, and hybrid stars, along with the driving mechanisms operating in these stars. It is believed that both mechanisms operate in hybrid stars: the κ-mechanism and the convective blocking mechanism, but up to date these have not been further analyzed.

2. Asteroseismology of Hybrid δ Sct- γ Dor Stars

As we mentioned before, asteroseismology is a magnificent tool which allows us to obtain valuable information about the interior variable stars and the physical processes that take place inside them. The main aims of asteroseismic modelling of stars are to get high precision in astrophysical parameters such as the mass (M), the radius (R) and the age; and to improve input physics of the stars by means of a comparison between theory and observations. The input physics of the target object is first adjusted to derive a stellar model and theoretical predictions for oscillations. Then, these predictions are compared to the observed properties of identified oscillation modes through photometric, spectroscopic and/or astrometric observations.

Next, we will see the features commonly found in the light curves of hybrid δ Sct-γ Dor stars and we will review the main steps for a particular kind of modelling of these stars.

2.1. Light Curves and Frequency Analysis of Hybrid δ Sct-γ Dor Stars

In this section, we will introduce the main features usually present in the frequency spectra of hybrid δ Sct-γ Dor stars as well as some corrections that usually have to be made in the light curves, specially for those provided by the COnvection ROtation et Transits planétaires (CoRoT) CNES/ESA space mission (Auvergne et al., 2009) before we can perform the frequency analysis. This space mission was launched in 2006 and offers five observing runs with durations of 59, 28, 157, 148 and 20 days with different integration time: 1, 32 and 512 s.

One of the phenomena that usually affect light curves and should be inspected before performing the frequency analysis is the impact of cosmic rays. These impacts lead to individual outlier measurements that should be removed before the frequency analysis. Another phenomenon we have to take into account for CoRoT light curves is that they usually have a slope which translates into frequencies below 0.25 c/d (Chapellier & Mathias, 2013). These frequecies must not be taken into account during the frequency analysis. Finally, it is important to remove the rotational frequency of the satellite ($f_{orb} = 13.97213\, c/d$) and its harmonics ($n * f_{orb}$), in order to employ only pulsational frequencies during the modelling.

Let us consider as example the star CoRoT ID 102358531 observed during the third CoRoT long run, LRa03, which targeted the Anti-Galactic center. According to the EXODAT database (Deleuil et al., 2009) this star has $\alpha =$ 6h12m29.58s, $\delta = +4°58'54.2244''$, it has an A0V spectral type and 2MASS photometry $J = 13.363$, $H = 13.191$ and $K = 13.085$. In Figure 2 we show the resulting light curve of CoRoT ID 102358531. This light curve clearly shows a hybrid nature for this star, since it displays both low and high frequency components corresponding to the γ Dor and δ Sct domains, respectively.

After cleaning the light curve we are in conditions to derive the frequency spectrum yielded by the Fourier transform in order to obtain the individual frequencies. As expected, the resulting frequencies from light curves of hybrid δ Sct-γ Dor stars, are usually grouped within two different domains: one corresponding to low frequencies typically related to γ Dor stars, and another domain at higher frequencies typically associated with δ Sct stars. In Figure 3 we show these two groups in the frequencies spectrum of CoRoT 102358531.

Once we obtained the individual frequencies, the search of pattern begins with the aim to identify each frequency and to perform later an asteroseismic modelling. There are different kinds of patterns to look for during the frequency analysis of hybrid stars. We will mention here the mean period spacing of g-modes and rotational splittings.

As we mentioned before, hybrid δ Sct-γ Dor stars oscillate in high order g-modes. According to the asymptotic theory (Tassoul, 1980) the difference between the periods of two consecutive radial order modes with the same harmonic degree (ℓ) tends to be constant for higher radial order modes. Therefore, if we find consecutive equidistant periods in the γ Dor range, these will probably correspond to an asymptotic ($n >> \ell$) series of g-modes with the same ℓ and high radial order. These series will allow us to derive later the mean period spacing of g-modes (if the series has n periods, Π_i, equally separated, then the mean period spacing is $(\Pi_n - \Pi_1)/(n-1)$). This quantity is extremely useful for the

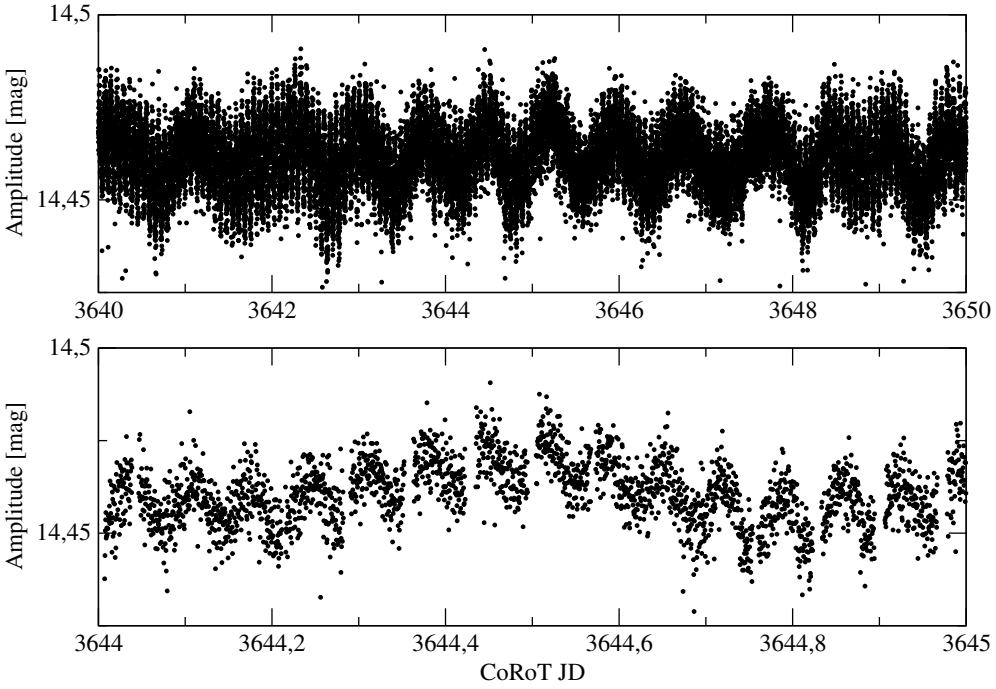

Figure 2. Light curve of the star CoRoT 102358531 with different timescales, a subset over 10 d at the top and a zoom into one day subset at the bottom.

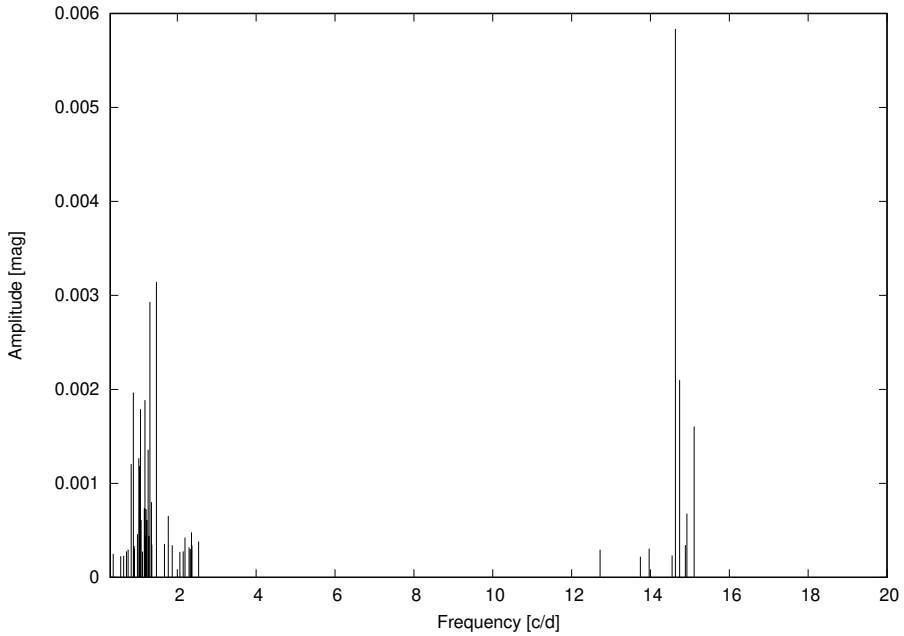

Figure 3. The resulting frequencies and their corresponding amplitudes in CoRoT 102358531. Two different domains are distinguished for this hybrid δ Sct- γ Dor star.

study of hybrid δ Sct-γ Dor stars since it can be employed as an indicator of the evolutionary stages of these stars.

The asymptotic period spacing for g-modes can be written in terms of the Brunt-Väisälä frequency (N):

$$\Delta\Pi_l^a = \frac{2\pi^2}{\sqrt{l(l+1)}} \left[\int_a^b \frac{N}{r} dr\right]^{-1} \tag{1}$$

where a and b are the inner and outer boundaries of the propagation zone of g-modes, respectively. As stars evolve on the MS and consume the H in the core, the Brunt-Väisälä (B-V) frequency, which governs the behaviour of g-modes, is affected by the change of the convective core. For masses greater than $\sim 1.5 M_\odot$, the core shrinks as the star evolves and its edge moves inward. In the case of hybrid stars, the propagation region of g-modes belongs to the inner region of the star and the lower boundary of this region begins immediately after the edge of the convective core. Therefore, during the evolution, the integral increases since it expands toward inner regions resulting in a decreasing asymptotic period spacing of g-modes and therefore a decreasing mean period spacing. This allows us to employ the mean period spacing, usually detected in hybrid stars, to place restrictions for the modelling of these stars.

Another extremely useful patterns that should be investigated during the frequency analysis of these objects are rotational splittings. Pulsating A-F stars are intermediate to fast rotators. In rotating stars, modes can be separated into several components forming multiplets. Considering rigid rotation and the first order perturbation theory, the components of the rotational multiplets are given by:

$$\nu_{nlm} = \nu_{nl} + m(1 - C_{nl})\frac{\Omega}{2\pi} \tag{2}$$

where ν_{ln} is the central mode of the multiplet, C_{nl} is the Ledoux constant and $\Omega/2\pi$ is the rotational frequency of the star. The Ledoux constant tends to zero for p-modes with an increase in the radial order and tends to $1/(\ell(\ell+1))$ for g-modes. For instance, if we find in the δ Sct regime, the next frequencies series: $\nu_{nl} - f$, ν_{nl}, $\nu_{nl} + f$ they might correspond to a triplet ($\ell = 1$) and we would be able to derive the rotational velocity.

This information along with any other information we can obtain through other methods such as spectroscopy and astrometry should be employed in the theoretical modelling of stars. Next subsection will be devoted to the modelling of hybrid δ Sct-γ Dor stars.

2.2. Modelling Hybrid δ Sct-γ Dor Stars

There are different ways to perform a modelling of a star. In this subsection we will describe a classical grid-based modelling applied to hybrid δ Sct-γ Dor stars based on statistic searches. This procedure is fully described in Sánchez Arias et al. (2017) along with its application to 5 hybrid stars.

The first step in the modelling of stellar interiors is to select a suitable code to create the models. There are several codes to compute stellar structure and pulsational models. Among the best known codes to develop stellar interior

structure models we can mention MESA (Paxton et al., 2011), CESAM2k (Morel & Lebreton, 2008) and LPCODE (Althaus et al., 2005). The first two mentioned codes allow the development of stellar interior models for a wide range of masses at different evolutionary stages including also different physical phenomena such as rotation, different theories of convection and diffusion of chemical elements, among others. On the other hand, LPCODE was fully developed at La Plata Observatory and is also widely employed to simulate the evolution of low-mass stars, mainly, at different stages. This code is coupled to an oscillation code named LP-PUL(Córsico et al., 2006) which allows computing adiabatic oscillation and those which take into account the excitation mechanism, i.e. non-adiabatic oscillations. Apart from LP-PUL, we can mention ADIPLS (Christensen-Dalsgaard, 2008) and GYRE (Townsend & Teitler, 2013) among the best-known oscillation codes. Both codes allow the calculation of adiabatic oscillations and the latter also calculate non-adiabatic oscillations.

Once we have selected a suitable code, we must set the input physics for the target object in order to obtain representative models. The main ingredients to be set are the nuclear reaction network, the opacity tables, the equation of state, a theory for the mixing of elements, a theory for stellar rotation if any, to decide which and how extra mixing process are going to be included, which kind of oscillations we want to study, etc. The input physics should be carefully selected, since the output model strongly depends on it, obviously. We encourage the reader to look for the details of the input physics in Sanchez Arias et al. (2017) and we will focus here in the steps of a particular modelling technique applied to the hybrid δSct-γ Dor stars.

The procedure we will describe next is a grid-based modelling consisting of a statistic search of the model which best fits the observations in a previously constructed grid of representative models of hybrid δ Sct-γ Dor stars. After having carefully selected the input physics in the code, the next step is to construct a grid of representative models. In Figure 4 we can see the location of a sample of δ Sct (open circles), γ Dor (grey squares), and hybrid δ Sct-γ Dor (red star symbols) stars taken from Grigahcène et al. (2010) in an H-R diagram. The grid should fully cover the region where hybrid δ Sct-γ Dor stars usually lie in the H-R diagram in order to employ it for different targets. Precisely, with the aim to encompass these objects with our models, we varied different parameters in our grid such as the mass ($1.2 \leq M_\star/M_\odot \leq 2.2$), the metallicity ($0.01 \leq Z \leq 0.02$), the overshooting[1] parameter ($0 \leq f \leq 0.03$) at different evolutionary stages from the Zero Age Main Sequence (ZAMS) to the Terminal Age Main Sequence (TAMS).

For each evolutionary sequence, we recorded the stellar structure model every 10 K approximately and we computed for them the adiabatic oscillations, specifically we calculated radial modes as well as non radial p- and g-modes with harmonic degree of 1, 2 and 3 with periods between 1200 s and 300000 s encompassing widely the usual periods of the modes found in these stars. Some of the evolutionary sequences of this grid are shown in Figure 4. Those corresponding

[1]Overshooting is the mixing of chemical elements beyond the formal convective boundary set by the Schwarzschild criterion. This phenomenon extends the evolutionary tracks during the evolution on the MS since extra mixing adds more H to the core to be burnt.

to a metallicity of 0.01 with an overshooting parameter of 0.03 are depicted in cyan; while those in black correspond to a metallicity of 0.015 and no overshooting, for different masses indicated with black numbers. It can be seen that the models of the grid encompass the occupied region by these observed stars.

Once we have a grid of representative models for the kind of object we want to study, we are able to perform a search for the model that best reproduces the observations of a given target star. The usually procedure in this grid-based modelling is to calculate a "quality function" for each model. This quality function compares observationally derived quantities with those calculated from the models. This function should reflect the nature of the objects we want to model, which in this case are hybrid δ Sct-γ Dor stars. For instance, hybrid stars oscillate in high order g-modes (as γ Dor stars) and low- to intermediate-order p-modes (as δ Sct stars). As we mentioned before (Section 2.1) it is possible to recognise high order g-mode features during the frequency analysis and employ that pattern as a constraint in the search of the best model. Therefore, including this pattern (or the mean period spacing) in the quality function of hybrid δ Sct-γ Dor stars, along with the information of the individual frequency p- and g-modes, boost this search efficiency.

As an example of the modelling of hybrid stars, we show the application of this procedure for HD 49343 as it was performed in Sánchez Arias et al. (2017). This star was previously studied in Brunsden et al. (2015). We used the information about the individual periods in the γ Dor range ([28800-288000]s), as well as in the δ Sct range ([1080-28800]s) and the observed mean period spacing of g-modes ($\overline{\Delta\Pi} = 2030.4s$) to create the "quality function".

First we calculated the mean period spacing of g-modes for each model. In Figure 5 we show the mean period spacing of g-modes calculated in the range of the observed g-mode periods, for those models of the grid with $Z = 0.01$ and $f = 0.01$ as an example. Each curve corresponds to certain mass and models in the ZAMS have higher mean period spacings (see Section 2.1). As already mentioned, the mean period spacing of g-modes decreases with the evolution. Therefore, this quantity can be used as an indicator of the evolutionary stage of hybrid δ Sct-γ Dor stars. After calculating this quantity, we selected for each $M_\star$, Z and f, the model which best reproduces the mean period spacing of g-modes derived from observations, i.e. those models closer to the straight line in Figure 5.

Next, for the models selected in the previous step we performed a period-to-period fit of p-modes as well as of g-modes, including this information in the quality function. The resulting quality function is:

$$F = \sum_{j=1}^{N} \frac{[\overline{\Delta\Pi_n} - \overline{\Delta\Pi}]_j^2}{(\sigma^2_{\overline{\Delta\Pi}})_j} + \chi_j^p + \chi_j^g, \tag{3}$$

where $\overline{\Delta\Pi_n}$ is the calculated mean period spacing that best reproduces the observed one ($\overline{\Delta\Pi}$) for a certain Z, $M_\star$ and f, $\sigma_{\overline{\Delta\Pi}}$ is the error corresponding to the observed mean period spacing, χ_j^p is the sum of the difference between the periods of p-modes calculated for each model and the period observed in the δ Sct range divided by the error corresponding to the observed frequency; and χ_j^g is the same for individual g-modes. This quality function has its own peculiar-

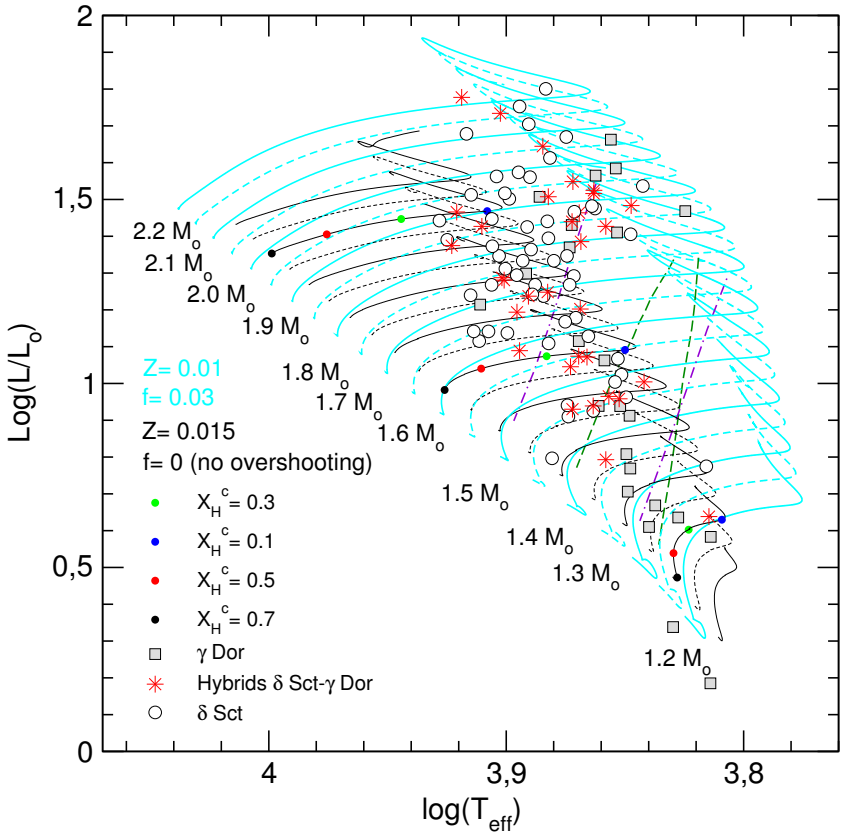

Figure 4. HR diagram showing evolutionary tracks for stellar models with different masses ($1.2M_{\odot} \leq M_{*} \leq 2.2M_{\odot}$), $Z = 0.015$ and without overshooting ($f = 0$) in black, and $Z = 0.01$ and $f = 0.03$ in light blue, from ZAMS to TAMS. The value of the stellar mass ($M_{\star}$) is indicated for a subset of tracks (those displayed in solid lines). Black, red, green, and blue dots correspond to the location of stellar models with $M_{\star}/M_{\odot} = 1.3, 1.7$ and 2.1 having a central H abundance of $X_H^c = 0.7, 0.5, 0.3, 0.1$, respectively. A sample of δ Sct (open circles), γ Dor (grey squares), and hybrid δ Sct-γ Dor (red star symbols) stars taken from Grigahcène et al. (2010) are included for illustrative purposes. Also, the boundaries of the δ Sct (violet dot-dashed lines) and γ Dor (green dashed lines) theoretical instability strips from Dupret et al. (2005) are plotted. Extracted from Sánchez Arias et al. (2017).

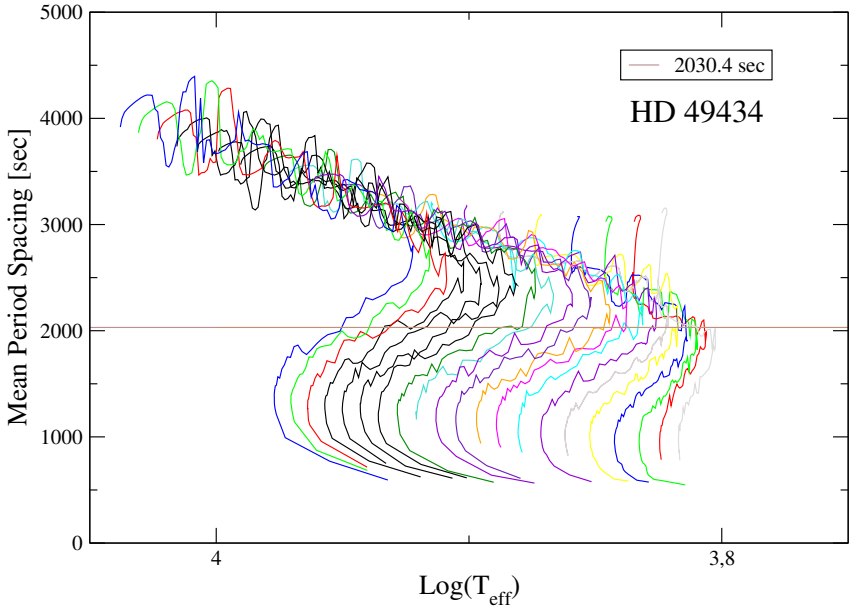

Figure 5. Mean period spacing vs. effective temperature for grid models calculated with $Z = 0.01$ and $f = 0.01$. The straight line represents the observed mean period spacing for g-modes calculated from observations of HD 49434. Extracted from Sánchez Arias et al. (2017).

ities depending on the observed star. For instance, if the harmonic degree was determined for a certain mode, this quality function can be properly adjusted in order to reflect this information, as it has been performed in Sánchez Arias et al. (2017) for every considered star.

Finally, we search for the model with the minimum quality function, which will be the model that best reproduces the observed frequency spectrum of the star.

As it has been mentioned, this is only one way to perform an asteroseismic modelling based on a grid of models. There are several ways to search for a representative model, for instance you can perform a similar search including more information in the quality function such as spectroscopic data.

As a result of the modelling, we obtain valuable information about our object. For example, in the case of HD 49434, we derived the next astrophysical parameters: $M_* = 1.75 M_\odot$, $Z = 0.01$, $f = 0.01$, $T_{eff} = 7399K$, $\log g = 3.85$, $R_{star} = 2.57 R_\odot$, $Age = 1169.08 \times 10^6 yr$, $L_* = 19.39 L_\odot$ and $\overline{\Delta\Pi} = 2045.42s$.

3. Comparing the Asteroseismic Properties of Pulsating Pre-extremely Low Mass White Dwarf and δ Scuti Stars.

There are several problems that can be addressed with asteroseismology. The problem we will focus on in this section concerns the distinction between two very different families of pulsating stars, which have similar atmospherics parameters (T_{eff} and $\log g$).

Thanks to the advance of space missions, new kinds of families started to be discovered. The family of variable stars we are interested in, are the precursors of the so-called the extremely low mass white dwarf stars or pre-ELMV. Extremely low mass white dwarf (ELM) stars (or low mass He-core white dwarfs) are the result of a strong mass transfer event at the red giant stage of low mass star evolution in close binary system. Their masses are below 0.3 solar masses and they oscillate in p- and g-modes driven by the κ-mechanism operating in the second He ionisation zone with periods between 380 and 3500 s approximately. The precursors of these white dwarf stars lie before the cooling sequence of ELM white dwarfs, in the region where pulsating A-F stars usually are (see Figure 6). This is one of the reasons that makes them difficult to distinguish from some pulsating A-F stars, specially δ Sct stars, as we will see next. The correct distinction between these types of pulsating stars will help to discover new members for pre-ELMV white dwarfs and to understand the formation channels for this new family of pulsating white dwarf stars.

In Sánchez Arias et al. (2018) we provided asteroseismic tools in order to distinguish between these two different families, the δ Sct stars and pre-ELMV white dwarf stars. Here we will present a brief resume on such tools aimed to highlight the power of asteroseismology.

Figure 6 shows the position in the HR diagram of δ Sct stars in white circles from Uytterhoeven et al. (2011), Bradley et al. (2015) and Bowman et al. (2016). SX Phe stars are those from Balona & Nemec (2012) depicted in magenta circles. With blue diamonds we show the position of the known pre-ELMVs (Maxted et al., 2013, 2014; Gianninas et al., 2016), while the ELMVs are depicted with light green triangles (Hermes et al., 2012, 2013a,b; Kilic et al., 2015; Bell

et al., 2017). It is also displayed the position of the pulsating object J0757+1448 reported for the first time in Sánchez Arias et al. (2018) with a cyan diamond and the cyan squares indicate the position of two stars reported by Corti et al. (2016), J1730+0706 and J1458+0707. These three stars lie in our region of interest where pre-ELMV stars can be confused with δ Sct star. The nature of these objects was discussed in the previously mentioned paper. We have also included theoretical evolutionary tracks for low mass He-core WD from Althaus et al. (2013) (dotted black lines) and Serenelli et al. (2001) (dashed black lines). Black numbers correspond to the values of the stellar mass of low mass He-core WD evolutionary tracks. In the same figure we illustrate MS evolutionary tracks (with red lines), for different values of metallicity (Z), mass ($M_\star$) and overshooting parameter (f) from Sánchez Arias et al. (2017). Besides, we included the location of the theoretical blue edge and the empirical red edge of the δ Sct instability strip from Pamyatnykh (1999), and also the blue edge of the pre-ELMV instability strip (Córsico et al., 2016).

From this figure, we can see that the theoretical evolutionary sequences of pre-ELMV stars partially overlap with those corresponding to MS stars and the region where pre-ELMVs can lie partially overlaps with the region occupied by the δ Sct stars. Besides, we note that both instability strips overlap for $3 \leq \log g \leq 4.4$. In summary, pre-ELMV and δ Sct stars have very similar atmospheric parameters T_{eff} and $\log g$, their evolutionary sequences partially overlap as well as their instability strips. In addition, both families show an overlapping range of pulsating periods (see Figure 7). Therefore, some pre-ELMV stars might be polluting the region where δ Sct usually lie. With the aim to provide tools to discover more interesting pre-ELMV stars, and distinguish them from δ Sct stars, we analysed and compared theoretical models of their structure and oscillations. The selected models are represented in orange triangles in Figure 6.

Although both kinds of families have the previously mentioned similarities, pre-ELMV and δ Sct stars are at very different stages of their evolution and their internal structure is different. For instance, δ Sct stars have radii between 1.5 and 3.5 $R_\odot$ while pre-ELMV stars with the same $\log g$ have $\sim 0.6\,R_\odot$ and the density for δ Sct stars are much lower than for pre-ELMV white dwarf stars. This fact is of course reflected in their pulsational behaviour, therefore employing only asteroseismology should allow us to distinguish between these kind of stars despite their similar atmospheric parameters.

In order to do this, in Sánchez Arias et al. (2018) we selected, as we mentioned, two sets of models of each type of family in different regions of the H-R diagram in which these families can be incorrectly classified, and we measured the period differences at different ranges of mode periods for each type of stars. Specifically we found that the mean period difference of p-modes of consecutive radial orders for δ Sct model is at least four times larger than the mean period spacing (or the mean period difference of g-modes of consecutive radial order) for the pre-ELMV white dwarf model in the period range $[2000-4600]$ s. Therefore, if we detect two periods and we calculate their differences, assuming they have consecutive radial order, we can say whether the star belongs to the pre-ELMV family or to the δ Sct star family according to the obtained value. However, mode

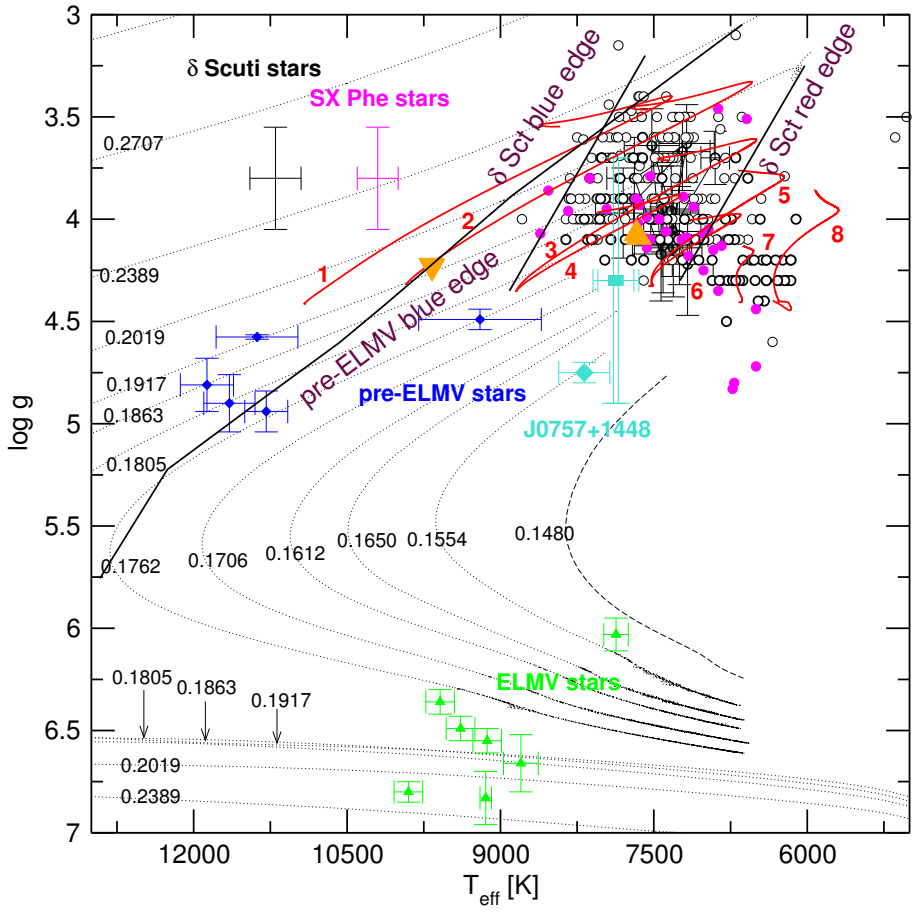

Figure 6. $T_{eff} - \log g$ diagram showing the location of ELMV stars (light green triangles), pre-ELMV stars (blue diamonds) and δ Sct stars (white circles) including SX Phe stars (magenta circles). The atmospheric parameters are extracted from different papers detailed in the main text. The error bars for the δ Sct and the SX Phe stars are depicted in black and magenta respectively. Also, we included the theoretical evolutionary tracks of low mass He-core WDs (black dotted and dashed lines) from Althaus et al. (2013) and Serenelli et al. (2001), and MS evolutionary tracks (red lines) from Sánchez Arias et al. (2017). Black numbers correspond to different values of the stellar mass of low mass He-core WDs, whereas red numbers are associated to the value of the mass, metallicity and overshooting parameter of MS stars. It is also shown the location of the theoretical blue edge and the empirical red edge of δ Sct instability strip from Pamyatnykh (1999), and also the blue edge of the pre-ELMV instability strip (Córsico et al., 2016). Orange triangles show the position of the template models. The cyan squares indicate the position of J1730+0706 and J1458+0707, and the cyan diamond represents the position of J0757+1448. Figure extracted from Sánchez Arias et al. (2018).

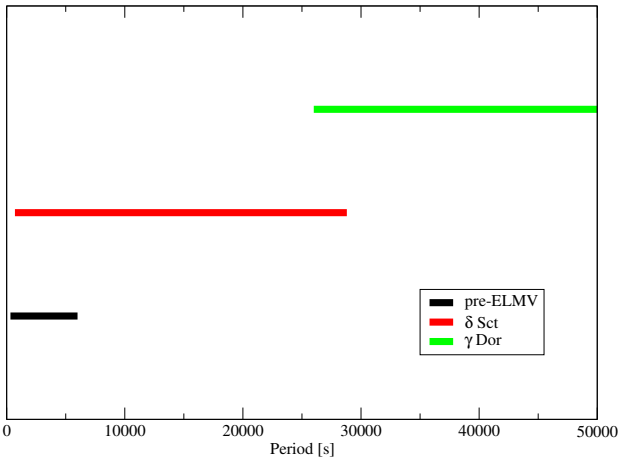

Figure 7. Scheme showing the usually ranges of the observed modes periods for pre-ELMV in black, δ Sct in red and γ Dor stars in green. The γ Dor range extends up to $\sim$260000 s.

identification is not an easy task and in general we cannot verify the hypothesis of consecutive radial order for the observed periods.

Therefore, we can employ another tool which does not depend on mode classification: the rate of period change. As stars evolve their structure changes, therefore their frequencies will also change since they depend on the stellar structure. On the MS the periods change slowly as the stars burn H in their core, while in the stages prior to the cooling sequence of white dwarf stars, they spend just a few years crossing the HR diagram very quickly. Therefore the rate of period change of δ Sct stars and pulsating pre-ELM white dwarf stars should be very different. This is exactly what we found in our models. The predicted rate of period change in δ Sct stars is $\frac{dP}{dt} \approx 5.45 \times 10^{-5}$ s/yr, and for pre-ELMV WD stars is $\frac{dP}{dt} \approx -1.42 \times 10^{-3}$ s/yr. Therefore, this difference allows us to distinguish between these two kinds of families without mode identification and is based only on the oscillation properties of these stars.

4. Summary

In this Chapter we briefly characterised pulsating A-F stars. The differences present between each family belonging to this interesting group allow us to investigate different physical phenomena such as the differential rotation, magnetic field, conservation of angular transport and excitation mechanisms in low mass stars at the pre-MS, MS and post-MS phases.

We focused on hybrid δ Sct-γ Dor stars since the simultaneous presence of p- and g- modes allows us to probe their internal layers as well as their external regions turning them into excellent targets for asteroseismology. We have introduced the main characteristics in the light curves of these objects, along with some of the most useful features in the frequency spectra we should recognise to

perform a modelling of the star. Furthermore, we briefly described one method to perform a grid-based modelling of hybrids δ Sct-γ Dor.

Finally we introduced a very different family of pulsating stars, pre-ELMV white dwarf stars, which lie very close to pulsating A-F stars and might be polluting the region where δ Sct stars usually lie. We showed how asteroseismology can be employed to distinguish them and we presented two different asteroseismic tools to achieve this goal in order to discover new interesting pulsating pre-ELM white dwarf stars.

Acknowledgments. I am very grateful to the organisers for letting me participate as a lecturer in this school and for their work organising an excellent LAPIS School 2019. I would like to thank CONICET for the postdoctoral Fellowship during which this proceeding was partially written. This project has received funding from the European Union's Framework Programme for Research and Innovation Horizon 2020 (2014-2020) under the Marie Skłodowska-Curie Grant Agreement No. 823734.

References

Aerts C., Christensen-Dalsgaard J., Kurtz D. W., 2010, *Asteroseismology*

Althaus L. G., Miller Bertolami M. M., Córsico A. H., 2013, *A&A*, **557**, A19

Althaus L. G., Serenelli A. M., Panei J. A., Córsico A. H., García-Berro E., Scóccola C. G., 2005, *A&A*, **435**, 631

Antoci V., Cunha M., Houdek G., Kjeldsen H., Trampedach R., Handler G., Lüftinger T., Arentoft T., Murphy S., 2014, *ApJ*, **796(2)**, 118

Auvergne M., Bodin P., Boisnard L., Buey J.-T., Chaintreuil S., Epstein G., Jouret M., Lam-Trong T., Levacher P., Magnan A., Perez R., Plasson P., Plesseria J., Peter G., Steller M., Tiphène D., Baglin A., Agogué P., Appourchaux T., Barbet D., Beaufort T., Bellenger R., Berlin R., Bernardi P., Blouin D., Boumier P., Bonneau F., Briet R., Butler B., Cautain R., Chiavassa F., Costes V., Cuvilho J., Cunha-Parro V., de Oliveira Fialho F., Decaudin M., Defise J.-M., Djalal S., Docclo A., Drummond R., Dupuis O., Exil G., Fauré C., Gaboriaud A., Gamet P., Gavalda P., Grolleau E., Gueguen L., Guivarc'h V., Guterman P., Hasiba J., Huntzinger G., Hustaix H., Imbert C., Jeanville G., Johlander B., Jorda L., Journoud P., Karioty F., Kerjean L., Lafond L., Lapeyrere V., Landiech P., Larqué T., Laudet P., Le Merrer J., Leporati L., Leruyet B., Levieuge B., Llebaria A., Martin L., Mazy E., Mesnager J.-M., Michel J.-P., Moalic J.-P., Monjoin W., Naudet D., Neukirchner S., Nguyen-Kim K., Ollivier M., Orcesi J.-L., Ottacher H., Oulali A., Parisot J., Perruchot S., Piacentino A., Pinheiro da Silva L., Platzer J., Pontet B., Pradines A., Quentin C., Rohbeck U., Rolland G., Rollenhagen F., Romagnan R., Russ N., Samadi R., Schmidt R., Schwartz N., Sebbag I., Smit H., Sunter W., Tello M., Toulouse P., Ulmer B., Vandermarcq O., Vergnault E., Wallner R., Waultier G., Zanatta P., 2009, *A&A*, **506**, 411

Balona L. A., Nemec J. M., 2012, *MNRAS*, **426**, 2413

Bell K. J., Gianninas A., Hermes J. J., Winget D. E., Kilic M., Montgomery M. H., Castanheira B. G., Vanderbosch Z., Winget K. I., Brown W. R., 2017, *ApJ*, **835(2)**, 180

Bowman D. M., Kurtz D. W., Breger M., Murphy S. J., Holdsworth D. L., 2016, *MNRAS*, **460**, 1970
Bradley P. A., Guzik J. A., Miles L. F., Uytterhoeven K., Jackiewicz J., Kinemuchi K., 2015, *AJ*, **149**, 68
Brunsden E., Pollard K. R., Cottrell P. L., Uytterhoeven K., Wright D. J., De Cat P., 2015, *MNRAS*, **447**, 2970
Chapellier E., Mathias P., 2013, *A&A*, **556**, A87
Christensen-Dalsgaard J., 2008, *Ap&SS*, **316(1-4)**, 113
Córsico A. H., Althaus L. G., Miller Bertolami M. M., 2006, *A&A*, **458**, 259
Córsico A. H., Althaus L. G., Serenelli A. M., Kepler S. O., Jeffery C. S., Corti M. A., 2016, *A&A*, **588**, A74
Corti M. A., Kanaan A., Córsico A. H., Kepler S. O., Althaus L. G., Koester D., Sánchez Arias J. P., 2016, *A&A*, **587**, L5
Deleuil M., Meunier J. C., Moutou C., Surace C., Deeg H. J., Barbieri M., Debosscher J., Almenara J. M., Agneray F., Granet Y., Guterman P., Hodgkin S., 2009, *AJ*, **138(2)**, 649
Dupret M. A., Grigahcène A., Garrido R., Gabriel M., Scuflaire R., 2005, *A&A*, **435(3)**, 927
Gianninas A., Curd B., Fontaine G., Brown W. R., Kilic M., 2016, *ApJL*, **822**, L27
Grigahcène A., Antoci V., Balona L., Catanzaro G., Daszyńska-Daszkiewicz J., Guzik J. A., Handler G., Houdek G., Kurtz D. W., Marconi M., Monteiro M. J. P. F. G., Moya A., Ripepi V., Suárez J. C., Uytterhoeven K., Borucki W. J., Brown T. M., Christensen-Dalsgaard J., Gilliland R. L., Jenkins J. M., Kjeldsen H., Koch D., Bernabei S., Bradley P., Breger M., Di Criscienzo M., Dupret M. A., García R. A., García Hernández A., Jackiewicz J., Kaiser A., Lehmann H., Martín-Ruiz S., Mathias P., Molenda-Żakowicz J., Nemec J. M., Nuspl J., Paparó M., Roth M., Szabó R., Suran M. D., Ventura R., 2010, *ApJL*, **713(2)**, L192
Hermes J. J., Montgomery M. H., Gianninas A., Winget D. E., Brown W. R., Harrold S. T., Bell K. J., Kenyon S. J., Kilic M., Castanheira B. G., 2013a, *MNRAS*, **436**, 3573
Hermes J. J., Montgomery M. H., Winget D. E., Brown W. R., Gianninas A., Kilic M., Kenyon S. J., Bell K. J., Harrold S. T., 2013b, *ApJ*, **765**, 102
Hermes J. J., Montgomery M. H., Winget D. E., Brown W. R., Kilic M., Kenyon S. J., 2012, *ApJL*, **750**, L28
Kilic M., Hermes J. J., Gianninas A., Brown W. R., 2015, *MNRAS*, **446**, L26
Maxted P. F. L., Serenelli A. M., Marsh T. R., Catalán S., Mahtani D. P., Dhillon V. S., 2014, *MNRAS*, **444**, 208
Maxted P. F. L., Serenelli A. M., Miglio A., Marsh T. R., Heber U., Dhillon V. S., Littlefair S., Copperwheat C., Smalley B., Breedt E., Schaffenroth V., 2013, *Nature*, **498**, 463
Morel P., Lebreton Y., 2008, *Ap&SS*, **316**, 61
Murphy S. J., Gray R. O., Corbally C. J., Kuehn C., Bedding T. R., Killam J., 2020, *MNRAS*
Pamyatnykh A. A., 1999, *AcA*, **49**, 119
Paxton B., Bildsten L., Dotter A., Herwig F., Lesaffre P., Timmes F., 2011, *ApJS*, **192(1)**, 3
Sánchez Arias J. P., Córsico A. H., Althaus L. G., 2017, *A&A*, **597**, A29

Sánchez Arias J. P., Romero A. D., Córsico A. H., Pelisoli I., Antoci V., Kepler S. O., Althaus L. G., Corti M. A., 2018, *A&A*, **616**, A80

Serenelli A. M., Althaus L. G., Rohrmann R. D., Benvenuto O. G., 2001, *MNRAS*, **325**, 607

Tassoul M., 1980, *ApJS*, **43**, 469

Townsend R. H. D., Teitler S. A., 2013, *MNRAS*, **435**, 3406

Uytterhoeven K., Moya A., Grigahcène A., Guzik J. A., Gutiérrez-Soto J., Smalley B., Handler G., Balona L. A., Niemczura E., Fox Machado L., Benatti S., Chapellier E., Tkachenko A., Szabó R., Suárez J. C., Ripepi V., Pascual J., Mathias P., Martín-Ruíz S., Lehmann H., Jackiewicz J., Hekker S., Gruberbauer M., García R. A., Dumusque X., Díaz-Fraile D., Bradley P., Antoci V., Roth M., Leroy B., Murphy S. J., De Cat P., Cuypers J., Kjeldsen H., Christensen-Dalsgaard J., Breger M., Pigulski A., Kiss L. L., Still M., Thompson S. E., van Cleve J., 2011, *A&A*, **534**, A125

Pulsations Along Stellar Evolution
VIII LAPIS Summer School
AAA Workshop Series 12, 2021
M. Kraus & A.F. Torres, eds.

Pulsations in Evolved Massive Stars

M. Kraus[1]

[1]*Astronomical Institute, Czech Academy of Sciences, Fričova 298, 251 65 Ondřejov, Czech Republic*

Abstract. The post-main sequence evolution of massive stars still bears many unknowns. In particular, the physical processes involved in triggering enhanced mass-loss or eruptions are yet to be established. In this Chapter, the post-main sequence evolution of massive stars, and the various phases which are well-known for their mass ejections, are briefly touched upon. Amongst those transition phases, two classes of objects are discussed in more detail: the B-type supergiants and the Yellow Hypergiants. Their ability to perform pulsations is presented based on observational and theoretical evidences. Moreover, the possibility of a pulsation–mass-loss relation in these two classes of objects is delineated.

Key words: asteroseismology — instabilities — stars: oscillations — stars: winds, outflows

1. Introduction to Massive Stars

Massive stars are stars that are born with initial masses $>8\,\mathrm{M}_\odot$. They are few in numbers, but their significance lies in their powerful winds with which they enrich their environments throughout their entire life in both momentum and chemically processed material. With their enormous energy transfer, in particular during their explosion as powerful supernovae, massive stars may trigger the formation of next generations of stars and planets. Consequently, they play a crucial role in the dynamical and chemical evolution of their host galaxies. It is therefore surprising that stellar evolution theory is still most uncertain for massive stars, despite their importance.

1.1. Evolution of Massive Stars - Theoretical Aspects

From a theoretical point of view, the various phases in the life of a massive star are clearly defined, namely in terms of the individual nuclear burning stages. On the main-sequence, the star burns hydrogen in its core into helium. As soon as the hydrogen core is exhausted, the star turns off the main-sequence and performs pure hydrogen shell-burning in a layer around the core, whereas the core itself contracts and heats until helium burning sets in. This sequence of core and shell burning into heavier and heavier elements continues until the core consists only of the iron ashes. In this final pre-supernova stage, the iron core is surrounded by multiple shell-burning layers, of which the hydrogen-burning layer is closest to the stellar surface, underneath the outermost, non-burning stellar hydrogen envelope.

From stellar evolution theory, all these individual burning phases can be unambiguously determined and chronologically ordered. However, these phases refer purely to the properties inherent to the stellar interior. They are not directly accessible by observations. Moreover, stars can rotate and undergo strong mass-loss, influencing and altering significantly the internal structure and surface appearance of massive stars.

Stellar Winds An excellent introduction into the subject of stellar winds is provided by the textbook of Lamers & Cassinelli (1999). Here, only some general aspects are briefly outlined.

Multiply ionized elements can have excited states with extremely short lifetimes. If such a state is excited due to the absorption of a photon, the de-excitation happens quasi instantaneously. Lines of such transitions are called resonance lines. Based on their energies, these resonance lines typically arise within the ultraviolet spectral range.

Ions of various elements in the upper atmosphere of a hot, massive star can produce resonance lines. These ions continuously absorb photons from the underlying photosphere into their resonance states. The re-emission occurs into the solid angle 4π, resulting in a net momentum transfer from the photospheric photons to the ions in predominantly radial direction. Consequently, the ions experience a constant radial "push" and as such an acceleration beyond the sonic point. Collisions between these accelerated ions and other elements and free electrons in their vicinity drag these particles along, leading to a global removal of matter from the stellar surface known as mass-loss via line-driven winds. Depending on the physical properties of the star, the mass-loss during some evolutionary phases can be so high, that the outer layers of the star are completely peeled off. If this happens, deeper layers, which are enriched in heavier elements due to shell-burning processes, show up on the stellar surface, and the star appears "stripped".

Stellar Rotation Rotation in the interior of stars can lead to mixing and hence transportation of chemically processed material from deeper layers to the stellar surface. But rotation has also another effect: it can deform the shape of the star. With increasing rotation speed stars loose their spherical shape and instead appear flattened. The best known rotating body that displays a deviation from spherical symmetry is the Earth with its equatorial radius exceeding the polar one by about 21 km, corresponding to a flattening of 0.00335.

The parameter $\omega = v_{\rm rot,eq}/v_{\rm crit}$ defines the ratio between the equatorial rotation velocity, $v_{\rm rot,eq}$, and the critical velocity, $v_{\rm crit}$. The latter is given by $v_{\rm crit} = \sqrt{GM_{\rm eff}/R_{\rm eq}}$, where G is the gravitational constant, $M_{\rm eff}$ is the effective stellar mass, i.e. the stellar mass reduced by the effects of radiation pressure due to electron scattering, and $R_{\rm eq}$ is the stellar radius at the equator. Critical rotation is reached if $\omega = 1$, meaning that the centrifugal force balances the gravitational force. In this case, $R_{\rm eq} = 1.5R_{\rm pole}$, where $R_{\rm pole}$ is the radius at the pole, and a maximum flattening of $(R_{\rm eq} - R_{\rm pole})/R_{\rm pole} = 0.5$ is reached.

The deformation of the stellar shape has a further consequence. The compression of the polar regions results in a heating of the poles, whereas the expansion of the equatorial regions leads to a cooling. This effect is also known as gravitational darkening. The gradient in surface temperature from the pole

to the equator leads also to a latitude dependence of the mass flux. As long as no change in the ionization state of the wind material occurs from the polar to the equatorial region, rotating stars tend to have higher mass flux over the poles and less mass flux along equatorial regions (see Figure 2 in Kraus, 2006). The situation may be different in rapidly rotating stars, in which the ionization state of the gas in the wind can change at a certain latitude due to the drastic drop in surface temperature. For such stars higher mass flux may be expected in equatorial regions due to the increased number of ions suitable for line-driving. This effect is known as the rotation induced bi-stability mechanism (Pelupessy et al., 2000). Moreover, the star may switch from the classical fast solution (Castor et al., 1975) to the so-called slow solution (Curé, 2004) leading also to increased mass-loss in equatorial regions.

The real rotation speed of a star is difficult to guess, because usually the inclination of the rotation axis is not known. Therefore, observations typically deliver only $v_{\rm rot,eq} \sin i$, i.e. the rotation velocity projected to the line-of-sight, which is a *lower limit* to the real rotation velocity. Estimates of projected rotation velocities for massive single-star non-supergiant samples, performed in the Tarantula (30 Dor) nebula of the Large Magellanic Cloud, revealed a velocity distribution with a strong peak at low values ($\sim 80\,{\rm km\,s^{-1}}$) and a high-velocity tail (up to $600\,{\rm km\,s^{-1}}$) for O-type stars ($16 - 60\,{\rm M_\odot}$, Ramírez-Agudelo et al., 2013), whereas B-type stars ($8 - 16\,{\rm M_\odot}$, Dufton et al., 2013) can show a bi-modal distribution with a significant fraction of stars having projected rotation velocities $< 100\,{\rm km\,s^{-1}}$ and another peak spreading from 200 to $250\,{\rm km\,s^{-1}}$. Also for these type of stars a high-velocity tail (up to $\sim 500\,{\rm km\,s^{-1}}$) is observed, meaning that a small fraction of O and B-type stars are born with intrinsic rotation speeds corresponding to a significant fraction of their critical velocities.

A deeper discussion of the effects of rotation on the physics and evolution of massive stars is provided by the excellent textbook of Maeder (2009).

Evolutionary Tracks To predict the properties of massive stars along their entire life path, various research groups have developed their own computer codes (see Martins & Palacios, 2013, for an overview). All these codes are pure one-dimensional and utilize a variety of input physics that is implemented in different ways. Computation of evolutionary tracks of massive stars is performed from the point of ignition of hydrogen in the stellar cores, defined as the zero-age main-sequence (ZAMS), up to pre-supernova stages. But comparison of the model predictions for the evolutionary track of a massive star with initially identical properties clearly shows a huge diversity and strong disagreement, especially after the star turns off from the main sequence. This was impressively demonstrated by the analysis of Martins & Palacios (2013) (see, e.g., their Figure 4).

Moreover, both effects, rotation and mass-loss, significantly influence and alter the evolution of massive stars as previously discussed. Rotation drives the internal mixing and influences mass-loss rates already on the main-sequence. Consequently, stars with initially identical masses on the ZAMS but diverse rotation velocities will end up with different properties when they reach the end of their main-sequence evolution (Meynet & Maeder, 2000).

Given the uncertainties in stellar models and in the (usually poorly constraint) initial physical properties such as rotation, it is tricky to assign a star a

proper initial mass and evolutionary state from a pure comparison of its position in the Hertzsprung-Russell (HR) diagram with evolutionary model predictions.

1.2. Observed Spectroscopic Phases

From the observational point of view, massive stars in their post-main sequence evolution are classified based on their spectroscopic appearance. In general, one distinguishes two types of objects: supergiants and hypergiants.

Supergiants are stars of luminosity class I with subclasses Ia, Iab, and Ib. In the HR diagram they spread from the hottest to the coolest stars and are classified according to their effective temperature into blue supergiants (spectral types O and B), yellow supergiants (A, F, G), and red supergiants (K, M).

Objects in the category hypergiants spread also over a certain temperature range in the HR diagram. Known hypergiants have spectral types ranging from late-O to G. Hypergiants are often assigned a luminosity class 0 or Ia^+, indicating that these stars have luminosities close to the Eddington limit[1].

In addition to these purely temperature and luminosity-class based categories, evolved massive stars are also found in some evolutionary transition phases, typically associated with strong mass-loss and eruptions. These classes are briefly introduced.

Wolf-Rayet Stars Stars with a Wolf-Rayet (WR) classification are of spectral-type O and comprise the hottest ($30\,000 - 200\,000\,\mathrm{K}$) sample of evolved massive stars. WR stars have strong stellar winds with high mass-loss rates ($10^{-5} - 10^{-4} M_\odot \mathrm{yr}^{-1}$) and wind velocities ranging from $\sim 1000\,\mathrm{km\,s^{-1}}$ up to $5500\,\mathrm{km\,s^{-1}}$. These intense winds peel off the outer shells of the star, uncovering successively the products from the various burning phases. The characteristic emission lines of WR stars are formed in the extended and dense high-velocity wind region enveloping the very hot stellar photosphere. According to the spectral appearance one distinguishes nitrogen-rich and carbon-rich WR stars as type WN (strong nitrogen lines) and WC (with carbon lines), or WO (with strong oxygen and carbon lines). WN and WC stars are further subdivided into early (E) and late (L) types: WNE (early WN, spreading from WN1 to WN5), respectively WCE (WC1 to WC5), and WNL (late WN, spreading from WN6 to WN11), respectively WCL (WC6 to WC9).

WR stars are descendants of massive main-sequence stars (with initial masses $> 25\,\mathrm{M}_\odot$) and most likely progenitors of core-collapse supernovae. More details on WR stars[2] and their physical properties can be found in Crowther (2007).

B[e] Supergiants A special class of blue supergiants comprise the B[e] supergiants. These are mostly supergiants of spectral type B (including a few objects of spectral types late-O and early-A) that are surrounded by dense circumstellar environments, typically in the form of a dusty disk and a massive, ionized polar wind. The central stars have luminosities in the range $10^4 < L/L_\odot < 10^6$.

---

[1]This is the maximum luminosity a star reaches when the outwards acting radiation force balances the inwards acting gravitational force.

[2]For a list with all Galactic WR stars see http://pacrowther.staff.shef.ac.uk/WRcat/

The circumstellar matter gives rise to numerous emission (e) lines, including emission from forbidden transitions (marked by square brackets), leading to the designation B[e]. Their massive disks are factories for various molecular species whose emission features allow to deduce the structure and kinematics of these disks (e.g., Kraus et al., 2015b; Maravelias et al., 2018), which might be highly dynamical and variable (Oksala et al., 2012; Torres et al., 2018) or long-lived enough to provide an environment suitable for the formation of even minor bodies or planets (Kraus et al., 2016).

B[e] supergiants are rare. They constitute just a few percent of all B-type supergiants. To date, a total of 33 objects has been identified and confirmed within the Milky Way and close-by galaxies, whereas another 25 objects have the status of B[e] supergiant candidates (Kraus, 2019).

Luminous Blue Variables Luminous Blue Variables (LBVs) are hot and luminous ($\log L/L_{\odot} > 5.4$) evolved massive stars that display characteristic variability in the form of either giant eruptions (such as the proto-type η Car) or excursions to the cool A-F-type supergiant region within the HR diagram in the form of an S Dor cycle named after the first object, S Dor in the Large Magellanic Cloud, showing this behavior. These excursions to the red are sometimes also termed 'outburst', but are not real outbursts connected with mass ejections but rather with an inflation of their envelopes at more or less constant luminosity.

S Dor cycles are a characteristic feature of LBVs based on which they can be distinguished from other types of hot luminous objects. They can last from years to decades. Without having displayed at least one full S Dor cycle or a major eruption, stars with otherwise similar properties to those of bona-fide LBVs, are only assigned the status of LBV candidates. A list of currently confirmed and candidate LBVs in Local Group galaxies is provided in Weis & Bomans (2020).

During the quiescent state of such an S Dor cycle, the stars appear like normal OB supergiants, sometimes displaying a WR-type (e.g., Maryeva et al., 2019) or a B[e] supergiant spectrum with intense emission lines. But from the latter they can be separated based on specific optical and infrared characteristics defined in Kraus (2019). Quiescent LBVs cluster along a diagonal region in the HR diagram called the LBV or S Dor instability strip (see Figure 1). When they reach maximum brightness in the S Dor cycle, they all appear at about the same cool temperature.

Due to the high mass-loss of LBVs and their (at least for some objects) giant eruptions, many LBVs are surrounded by nebulae of gas and dust with sizes of a few parsecs. While the morphology of the nebulae can be diverse, the majority displays bipolar structures (Weis, 2011).

It was long assumed that LBVs are a transitional phase in single star evolution. However, the detection of LBVs as progenitors of core-collapse supernovae is not in line with a transitional phase. Instead, it has been suggested that (at least some) LBVs might be the products of binary evolution (Smith, 2017).

Open Issues In summary, the evolution and final fate of massive stars depend severely on the initial conditions (mass, rotation speed, metallicity, magnetic fields, companion) and the amount of mass lost within each phase of their life.

Typically, stars within a certain category populate the same region within the HR diagram. However, diverse groups of stars may overlap, because they

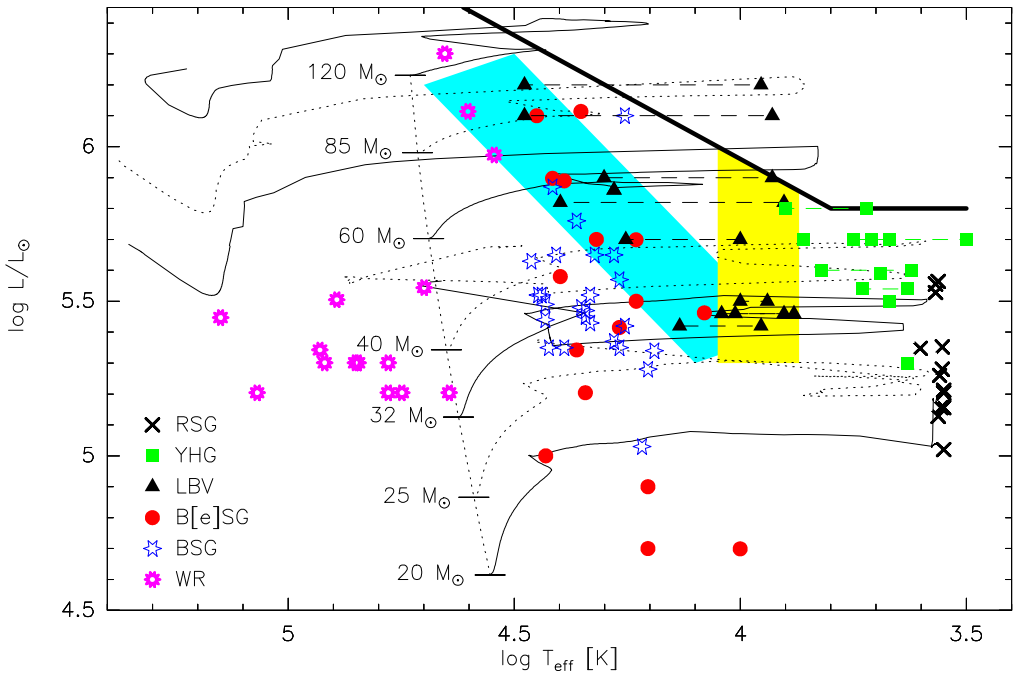

Figure 1. HR diagram for massive stars. Shown are evolutionary tracks of non-rotating stars from Ekström et al. (2012) for the indicated initial stellar masses on the ZAMS. Also included are representatives of the diverse groups of evolved massive stars. Dashes connecting symbols indicate the two temperature states, i.e., outburst and S Dor cycle for YHGs and LBVs, respectively. The thick solid kinked line represents the Humphreys-Davidson limit, the light-blue area marks the LBV/S Dor instability strip, and the yellow region highlights the Yellow Void.

have the same effective temperature and luminosity, but are in different evolutionary states (Figure 1). This can happen, because a certain combination of stellar parameters may occur more than once during the (red-ward, blue-ward, blue-loop) evolution of a massive star. Disentangling these populations is not always straight-forward. Consequently, some of the most relevant unsolved issues in massive star research comprise:

- What is their evolutionary state and connection to each other?
- Which physical mechanism causes enhanced mass-loss and outbursts?
- How much mass is lost and on which timescales?
- What is the structure and evolution of the ejected material?

Here, focus is given to the second item, and in the following observational and theoretical considerations of stellar pulsations in some types of evolved massive stars are discussed.

1.3. Pulsations in Evolved Massive Stars

Pulsations are nowadays ubiquitously found in stars all over the HR diagram. But currently, we cannot infer from observations whether massive stars in transition phases such as the LBVs, WRs and B[e]SGs are pulsating[3], because their dense winds usually hide their surfaces, and photometric variability is most likely affected by temporal changes in the wind and circumstellar matter rather than being purely due to pulsation activity. For the remaining of this Chapter, the attention is given to two groups of evolved massive stars: B supergiants and yellow hypergiants, and the possible role of pulsations as physical mechanism to trigger mass-loss and eruptions in these objects.

2. B Supergiants

Stars in the B supergiant (BSG) evolutionary state are the descendants of OB main-sequence stars. They have surface temperatures in the range $T_{\rm eff} = 10\,000-30\,000\,{\rm K}$ and luminosities of $L = 10^4 - 10^6\,L_\odot$. BSGs drive winds with mass-loss rates of $\dot{M} = 10^{-7} - 10^{-5}\,M_\odot{\rm yr}^{-1}$ and terminal velocities of $v_\infty = 200 - 3500\,{\rm km\,s}^{-1}$. These stars have been assumed to be well-behaved H-shell burning stars on their red-ward evolution, until the first BSG star exploded as supernova (SN1987A, West et al., 1987). While stars just off the main-sequence will not explode as supernova, this finding of a blue supergiant progenitor of SN1987A means that the group of BSGs consists of at least two coexisting populations: BSGs just beyond the main-sequence and BSGs in a post-red or post-yellow supergiant phase. A possible third population might comprise stars on a blue loop.

2.1. Characteristics of BSGs

BSGs can be characterized by three distinct properties, which are briefly outlined.

Light Curve Variability In principle, all OBA supergiants are variable in their visual light with amplitudes (A) and periods (P) of these microvariations in the range $A = 0.01\ldots0.1\,{\rm mag}$ and $P = 5\ldots100\,{\rm d}$, respectively. The variabilities have been reported to obey an amplitude-luminosity relation, meaning that the brightest stars display the largest amplitudes (Maeder & Rufener, 1972). The light variations follow no clear periodicities, instead they appear to be semi-regular. They are most pronounced in the sub-group of BA-type supergiants with luminosity class Ia. These extreme luminous stars are also often referred to as α Cygni variables (Sterken, 1977), named after the prototype of such stars α Cyg (Deneb). Detailed analyses of light curves of BSGs, e.g. from HIPPARCOS, resulted in the discovery of hundreds of new variable stars, of which 29 objects have been classified by Waelkens et al. (1998) as new α Cygni variables exhibiting clear periodic variations with amplitudes between 1 and a few tens of millimagnitude with periods ranging from a few hours to a few weeks.

[3]There is one exception: The B[e]SG star LHA 120-S 73 in the Large Magellanic Cloud has been suggested to pulsate based on detected line-profile variability of its photospheric He I line (Kraus et al., 2016).

Line-Profile Variability BSGs and their sub-class, the α Cyg variables, display variability in their line-profiles with Hα being the most prominent one. Due to the winds of the BSGs, their Hα lines display typically a P Cygni-type profile, which can vary significantly in strength and shape (see, e.g., Rosendhal, 1973; Kaufer et al., 1996). But also pure photospheric lines seem to display complex variability patterns indicating cyclic variations in radial velocities. This might indicate the possible simultaneous excitation of pulsation modes with periods typical for non-radial oscillations and radial overtones (Kaufer et al., 1997).

"Macro-turbulent" Line Broadening The most puzzling characteristic of BSGs is their huge amount of broadening in excess to stellar rotation. Simón-Díaz & Herrero (2007) analyzed photospheric line profiles of OB stars to derive the stellar rotation velocities projected to the line of sight ($v_{\rm rot} \sin i$) using the Fourier transform method. This mathematical approach is a very valuable tracer for stellar rotation velocities, because the Fourier transform of the rotation profile possesses zero points, which are correlated with $v_{\rm rot} \sin i$. Computing the Fourier transform of observed photospheric lines thus allows to directly read off the rotation velocity of the star projected to the line of sight. For more details on the stellar rotation profile and its Fourier transform, the interested reader is pointed to Chapter 18 in the textbook of Gray (2005).

The sample of Simón-Díaz & Herrero (2007) contained also OB supergiants, for which the authors recognized an extra, non-negligible broadening component. This component has more or less a Gaussian profile shape so that it has been dubbed as "macro-turbulence" without knowing a priori its physical origin. In fact, the velocities of this "macro-turbulence" needed to reproduce the observed widths of photospheric lines of BSGs turned out to exceed by far the value of the sound speed in the atmosphere of BSGs[4], meaning that this "macro-turbulence" has highly supersonic values (see Figure 1 in Simón-Díaz et al., 2010). If this velocity was due to real turbulences, shocks would form, creating X-ray emission which is not observed. Therefore, the extra broadening cannot be due to turbulence but must have another physical nature. And a possible explanation might be given by the superposition of many pulsations.

2.2. Discovery of Pulsations in BSGs

The previously mentioned characteristics of BSGs (light-curve and line-profile variability along with macro-turbulent line broadening) are a strong indication for a highly dynamical atmosphere and might point towards the presence of oscillations in these luminous objects. However, it was not expected that BSGs pulsate because of their radiative helium core, which immediately damps all modes propagating towards the core. Therefore, it was a big surprise when Saio et al. (2006) reported on the discovery of multiple oscillations in the BSG star HD 163899. These authors had analyzed a 37 day long continuous, high precision photometric light curve collected with the Canadian satellite MOST. Their studies revealed 48 periods from 10 h to 25 d, which they assigned to pulsations in both p-modes and g-modes.

---

[4] As an example, a value of $v_{\rm macro} = 80\,{\rm km\,s^{-1}}$ along with $v_{\rm rot} \sin i = 47\,{\rm km\,s^{-1}}$ is needed to fit the shape of the Si III lines of the B0 Ia supergiant star HD 89767, (see Figure 4 in Puls, 2008).

Especially the occurrence of g-modes in a post-main sequence massive supergiant star was surprising. The stability analysis of Saio et al. (2006) revealed that the existence of g-modes can be explained by the development of an intermediate convective zone (ICZ) connected with the hydrogen burning shell. This ICZ results from a semi-convection episode during the main-sequence evolution. At this convective zone selected g-modes can be reflected back towards the surface. The ICZ hence prevents the modes from penetrating the radiative damping core of the star and, therefore, supports the establishment of g-mode pulsations. But for this, the position of the ICZ within the envelope plays an important role. If it is located too close to the surface, oscillations cannot be excited, and if it is too close to the core, the excited oscillations will be significantly damped. Moreover, the presence of physical effects such as rotation (mixing) and magnetic fields, as well as the strength of mass-loss, semi-convection, and overshooting during the main-sequence evolution have been found to influence the evolution of massive stars and thus can favor or prevent the formation of the ICZ (see, e.g., Godart et al., 2009, 2014). In that respect it is worth mentioning that follow-up investigations of Daszyńska-Daszkiewicz et al. (2013) have shown that the detection of pulsations is not necessarily a proof for the existence of an ICZ, but only for the presence of *some* reflective layer, which might also have a different physical origin.

Saio et al. (2006) computed stellar models using the updated OPAL opacities (Iglesias & Rogers, 1996) for stars covering a range of initial masses of 7–20 $M_\odot$ from the main-sequence into the BSG domain. As in most stars, it is the κ-mechanism that excites the modes in BSGs. This mechanism acts due to the iron-opacity bump in the superficial layers. Their analysis revealed a new instability domain for g-mode pulsations, covering the loci of BSGs in the HR diagram. For the BSG star HD 163899 the frequencies of these pulsations were in fairly good agreement with the frequencies found from the photometric light curve. Follow-up studies of BSGs with known photometric variability, e.g. from HIPPARCOS light curves, were found to have stellar parameters that placed them into the newly identified instability domain and were hence considered as gravity-mode pulsators (Lefever et al., 2007).

With the knowledge of multiple g-mode pulsations acting in BSGs, Aerts et al. (2009) could show that the shapes of the metal line profiles of BSGs can be naturally explained by combining the broadening caused by the velocity of hundreds of low-amplitude, non-radial gravity-mode pulsations. This was the first firm proof that pulsations can significantly contribute to (if not completely explain) the "macro-turbulent" line broadening observed in BSGs. Besides g-mode pulsations as the cause for "macro-turbulence" other scenarios appeared in the literature and require further notice. One of them comprises stochastically excited oscillations caused by subsurface convection (Grassitelli et al., 2015), another one proposes convectively driven internal gravity waves (Aerts & Rogers, 2015). Which of them is really responsible for the "macro-turbulence" in BSGs needs to be further studied, and maybe the truth lies in the interplay of more than one effect.

2.3. Pulsation Behavior in the Different BSG Populations

The discovery of pulsations in BSGs and the identification of the new instability domain helped to explain the observed variabilities in a number of BSGs. However, those BSGs that were classified as α Cygni variables display variabilities that point towards multiple periods spreading over a large period range. These are not in agreement with what would be expected from pure non-radial g-mode oscillations. Especially the long periods are more likely connected to radial modes. To test this hypothesis, Saio et al. (2013) extended their calculations of pulsation instabilities and computed the pulsation patterns following the evolution of massive stars up to the red-supergiant (RSG) stage and beyond for stars with initial masses up to $25\,M_\odot$. They did that for the case of both non-rotating stars and stars rotating initially with 40% of their critical speed.

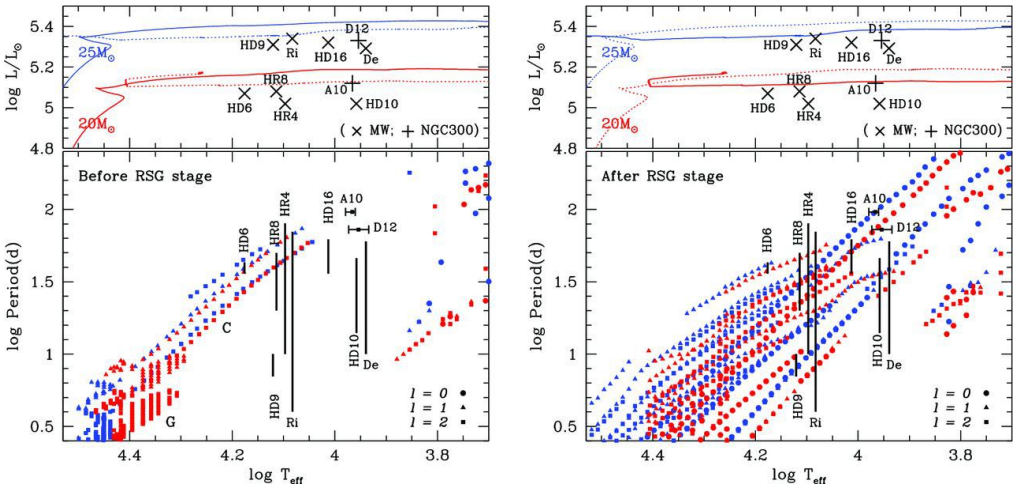

Figure 2. Evolutionary tracks (top) of stars with rotation and the excited pulsation periods in the models (bottom) during the pre- (left) and post-RSG (right) phase. For comparison, the period ranges of some α Cyg variables in the Milky Way and NGC 300 are included. Figure is taken from Saio et al. (2013) (their Figure 5).

As stellar evolution calculations of Ekström et al. (2012) have shown, rotating stars tend to evolve back to the blue side of the HR diagram after having passed through a cool, RSG phase, whereas non-rotating stars evolve only to the RSG stage and explode there as supernovae. Based on these latter models, the calculations of Saio et al. (2013) (see Figure 2) predict the excitation of radial pulsations only during the main-sequence and shortly after, and during their RSG state. In between, i.e. in the temperature regime from 20 000 K down to about 6 000 K where the α Cygni variables reside, no radial modes are excited.

For the stellar models with rotation, the situation with respect to the excitation of radial modes during the pre-RSG evolution is very similar to the non-rotating models, and the radial fundamental mode is only excited within the β Cephei instability region. Within the BSG domain only very few oscillatory convection modes are predicted which cannot explain the number and period

range of the observed oscillations in α Cygni variables. However, after the stars have passed through the RSG state, they develop a complex frequency behavior. They are capable to establish and maintain numerous pulsation modes spreading over a large period range, in agreement with the range of observed periods in the α Cygni variables.

Among the excited modes are several radial ones, including the so-called radial strange modes. These strange modes are particularly interesting, because they have been proposed to cause pulsation-driven time-variable mass-loss (Glatzel et al., 1999), leading to the interpretation of periodic variability of supergiants in terms of strange-mode instabilities (Glatzel & Kiriakidis, 1993). A prerequisite for their excitation is that the star needs to reach a luminosity over mass ratio of $L_*/M_* > 10^4\,\mathrm{L}_\odot/\mathrm{M}_\odot$ (Gautschy & Glatzel, 1990; Glatzel, 1994). Exceeding such a limit is no problem for massive stars that have passed through the RSG phase, during which they tend to loose a significant fraction of their mass via dense dust-driven winds thus increasing their L_*/M_* easily by a factor of 2 or more. Consequently, post-RSGs have much lower masses but similar luminosities than their younger pre-RSG counterparts, and present a completely different pulsation behavior. These differences can be used to pin down the evolutionary stage of BSGs by sorting them into pre- and post-RSGs, and to identify in such way possible supernova progenitors, for which the α Cygni variables seem to be suitable candidates.

2.4. Identification of Pulsations in BSGs

For the identification of stellar pulsations two types of observations are typically used: photometric light curves and spectroscopic time series.

Photometric Light Curves Photometric variability in BSGs has been detected based on light curves, especially from satellite missions such as HIPPARCOS and MOST as mentioned before. But also other satellites such as BRITE and TESS observed (and still observe) a number of them.

However, light curves of BSGs, especially when the band passes are optimized for the red, face two issues. Firstly, BSGs have stellar winds, which is obvious from P Cygni-type profiles of their Hα lines. These winds are not steady but vary in time as can be seen from the sample of Hα profile shapes of the BSG star 55 Cyg shown in Figure 3. But the variation is not periodic, as has been demonstrated by Kraus et al. (2015a). The wavelength range covering Hα is contained in the white-light filter of HIPPARCOS, and in both the red band pass of BRITE and the wide band pass of TESS. Therefore, any variability in the Hα line due to changes in the wind conditions will automatically imprint a variability signature on the stellar brightness measured by the photometric magnitude.

Second, depending on their density distribution, the winds of BSGs can alter the continuum flux. These winds have a radial velocity distribution that is usually described with the so-called β-law, defined by $v(r) = v_0 + (v_\infty - v_0)(1 - R_*/r)^\beta$, where v_∞ is the terminal wind velocity, v_0 is the velocity at the base of the wind, R_* is the stellar radius, and β describes the "steepness" of the velocity increase. Values of β for OB stars with line-driven winds are normally in the range 0.8-1.0, but for many BSGs, β has been proposed to take values of 3 or

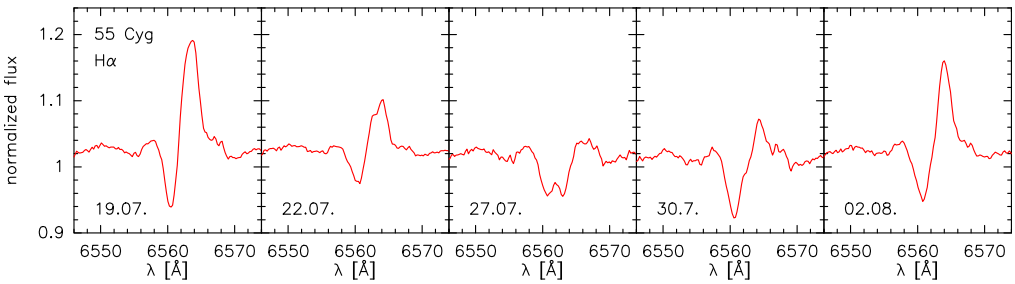

Figure 3. Snapshots of the Hα line of the BSG star 55 Cyg demonstrating the wind variability. The data were taken during a 14-day period in 2013 with the Perek 2-m telescope at Ondřejov Observatory.

even higher (e.g., Crowther et al., 2006). However, the higher the value of β, the higher is the density within the innermost wind region. As has been shown by Kraus et al. (2008), winds of BSGs with $\beta > 1$ significantly contribute with their free-free and free-bound emission to the total continuum emission, especially in the red part of the spectrum. Any variation in the wind thus produces an additional variability signal that influences and perturbs the measured stellar brightness and can (maybe severely) hamper the frequency analysis.

Considering these two effects, it is questionable whether photometric observations in broad-band filters or even in white light (such as TESS) can provide reliable insight into the pulsation behavior of those BSGs (such as the α Cygni variables), whose photometric fluxes are contaminated by variable wind emission due to significant changes in stellar mass-loss rates affecting both the red continuum and the Hα line profile.

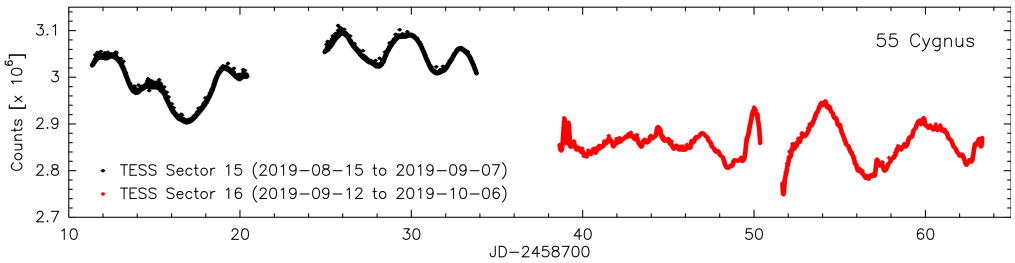

Figure 4. TESS example light curve of the α Cygni variable 55 Cygnus.

An example of a TESS light curve[5] of an α Cyg variable is shown in Figure 4. TESS has observed this star during two periods labeled as sectors 15 and 16. Obviously, the character of the variability has changed between the two observing runs. While it showed a smooth behavior during the first period, it appears more irregular and chaotic during the second one.

[5]The data described here may be obtained from the MAST archive at https://dx.doi.org/10.17909/t9-ncv5-bb52.

Spectroscopic Time Series Spectroscopic time series of high-quality (in both resolution and signal-to-noise level) provide an excellent tool to unveil whether the variability in the observed line profiles are due to pulsations, and to investigate whether the periodicities are strict such as for long-term coherent modes. This requires the monitoring of photospheric lines, typically of metals, which are not affected by superimposed emission from the stellar wind.

As has been discussed in a previous Chapter, pulsations cause changes in radial velocity and in the profile shape of the lines. To quantify these parameters, we make use of the so-called "velocity moments" of the lines, based on which a line profile is fully characterized (see, e.g., Aerts et al., 1992, 2010a; North & Paltani, 1994). Considering that a spectral line is a set of discrete measurements (λ_i, F_i), its moments are defined in the following way:

$$M_0 = \sum_{i=1}^{N}(1-F_i)\Delta x_i, \quad (1)$$

$$M_1 = \sum_{i=1}^{N}(1-F_i)(x_i-x_0)\Delta x_i, \quad (2)$$

$$M_2 = \sum_{i=1}^{N}(1-F_i)(x_i-x_0)^2\Delta x_i, \quad (3)$$

$$M_3 = \sum_{i=1}^{N}(1-F_i)(x_i-x_0)^3\Delta x_i, \quad (4)$$

with the normalized flux F_i measured at wavelength λ_i for pixel i, $\Delta x_i = x_i - x_{i-1}$ whereby x_i is the velocity corresponding to λ_i with respect to the laboratory wavelength of the line (λ_0), and x_0 is the relative motion of the star with respect to the Sun that needs to be corrected for to guarantee that the odd moments have an average of zero.

For practical purposes one utilizes the normalized moments, which are defined as $\langle v^j \rangle = M_j/M_0$ for $j = 1, 2, 3$. The units of these moments are $(\mathrm{km\,s^{-1}})^j$, and the first three of these normalized moments are connected to specific properties of the profile:

$\langle v^1 \rangle$ is the radial velocity, i.e., a measure for the center of gravity of the line,

$\langle v^2 \rangle$ provides a measure for the line width, and

$\langle v^3 \rangle$ measures the skewness, i.e. the asymmetry of the profile.

Each photospheric line forms over a certain range of depth in the atmosphere, and the actual velocity of motion is a function of stellar longitude, latitude, and depth. Moreover, we see the stellar surface only in its projection, and the radial velocity is inferred from the integration over that projected surface. Therefore, the first moment provides not any pulsation velocity, but it can be used to derive the periods of the pulsations.

The variations recorded in the moments can furthermore be used to separate pulsating stars from stars with other types of variability, such as stars with surface spots. Stellar spots are commonly seen in chemically peculiar stars, in which localized over- and under-abundances in specific elements cause surface inhomogeneities. Consequently, the variability in such stars is linked to the stellar rotation period, and different elements display diverse variabilities (see e.g., Briquet et al., 2004; Lehmann et al., 2006) in contrast to pulsating stars, in which the lines from different elements vary in phase. Moreover, theoretically generated profiles of pulsating stars have revealed that their first and third normalized moments vary in phase as well (de Pauw et al., 1993). This property is also useful to discriminate pulsating stars from objects with spots (e.g., Briquet et al., 2004).

Application of the moment method to spectroscopic time series of two BSG stars (σ Cyg and 55 Cyg) collected with the Perek 2-m telescope in the wavelength range $6250 - 6750$ Å with a spectral resolution of 13 000 and a signal-to-noise ratio of $S/N > 300$ resulted in interesting discoveries. For σ Cyg, a very short oscillation period of just 1.59 hours (Kraus et al., 2012) has been identified from several short-term time series of the photospheric Si II and He I lines (Figure 5).

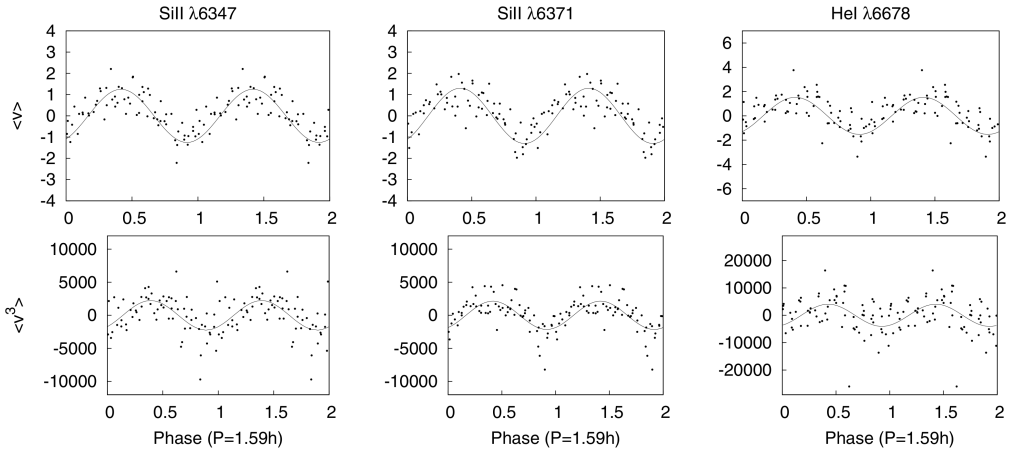

Figure 5. First and third moment of the photospheric Si II $\lambda\lambda$6347,6371 and the He I λ6678 lines of the BSG star σ Cyg. The spectroscopic time series were taken in 2010 and 2012. The oscillation character is deduced from the fact that both, the first and third moments of each element and the moments of different elements vary in phase. The data have been phased to the identified period of 1.59 h. Credit: Kraus et al. (2012), reproduced with permission ©ESO.

In the long-term spectroscopic time series of the BSG star 55 Cyg, a total of 19 periods have been found from the analysis of the radial velocity curve of the photospheric He I λ6678 line. These periods range from a few hours to 22.5 days, in agreement with their classification as p-modes, g-modes, and at least one radial strange mode (Kraus et al., 2015a). Moreover, the analysis of the

wind and stellar parameters of 55 Cyg based on computation of the Balmer, helium and silicon lines using the FASTWIND code (Puls et al., 2005) revealed that the star has a time-variable radius along with variable wind conditions, in agreement with cyclic phases of enhanced mass-loss. In particular, for the stellar parameters it has been found that the effective temperature, $T_{\rm eff}$, ranges from 18 570 K to 19 100 K, the stellar radius is $R_* = 57 \pm 1\,{\rm R}_\odot$ but varies from 52 to 65 ${\rm R}_\odot$, and the stellar luminosity is $\log L_*/L_\odot = 5.57 \pm 0.03$. With a spectroscopic mass of $34 \pm 4\,M_\odot$, $L_*/M_* > 10^4\,L_\odot/M_\odot$, which is the needed condition for the star to be able to excite strange mode pulsations. In addition, the line profiles revealed values for $v_{\rm rot} \sin i = 50 - 60\,{\rm km\,s^{-1}}$ and $v_{\rm macro} = 10 - 50\,{\rm km\,s^{-1}}$.

For the wind parameters of 55 Cyg it was found that $\dot{M}$ varies between 1.5×10^{-7} and $4.6 \times 10^{-7} M_\odot {\rm yr}^{-1}$, meaning that the change in mass loss occasionally exceeds a factor of 3. In addition, v_∞ varies between 230 and 350 ${\rm km\,s^{-1}}$, with exceptions of 600 and 700 ${\rm km\,s^{-1}}$ at times when also the mass-loss rates were increased. The large amount of detected periods including a radial strange mode resulted in the classification of 55 Cyg as a post-RSG object and hence as an α Cyg variable.

The findings of multiple pulsation periods in 55 Cyg have been confirmed by numerical non-linear simulations performed by Yadav & Glatzel (2016). Their calculations additionally unveiled that 55 Cyg undergoes strange-mode instabilities with triggered mass-loss, in agreement with the results derived from the observations.

Periodic mass-loss episodes related to a time-variable oscillation mode have also been found in the BSG star HD 50064 (Aerts et al., 2010b), and wind variability along with a pulsation–mass-loss relation was postulated for a sample of BSGs by Haucke et al. (2018). These results reinforce the need of in depth studies of the pulsation and mass-loss properties and their interrelation in these luminous objects.

3. Yellow Hypergiants

Stars falling into the category of yellow hypergiants (YHGs) reside in the temperature regime $T_{\rm eff} = 4000 - 9000\,{\rm K}$ and have luminosities of $L = 10^{5.3} - 10^{5.8}\,L_\odot$. These objects have evolved from progenitor stars with initial masses in the range $25 - 50\,M_\odot$. YHGs are rare objects, implying a short lifetime of this evolutionary transition phase. In total we currently know of ∼30 objects that are classified as YHGs or YHG candidates in the Milky Way and neighboring galaxies of the Local Group (e.g., de Jager, 1998; Clark et al., 2005; Kourniotis et al., 2017), and so far, only a handful of them have been thoroughly examined.

YHGs have been proposed to have passed through the RSG phase and evolve now back to the hot side of the HR diagram (de Jager, 1998). The structure of YHGs can best be approximated by a compact core that is surrounded by a huge inflated, low-density envelope. Due to this inflation, the surface gravity of YHGs is very small or can even approach a value of zero. This means, that even smallest perturbations within the atmosphere can initiate mass-loss from the star.

When the star reaches a surface temperature of $\sim 7000\,{\rm K}$, its atmosphere becomes dynamically unstable (Nieuwenhuijzen & de Jager, 1995; Lobel, 2001).

Strong mass loss sets in, creating what is called a pseudo-photosphere and veiling the central object. Such an outburst phase can last from a few months up to years during which the pseudo-photosphere mimics a much cooler temperature of the object. Only after the termination of the strongly enhanced mass-loss and when the released material has diluted, the star appears back at its real (hotter) temperature. This process repeats until the stellar atmosphere finally reaches again an equilibrium state. However, for a stable state, the star must reach an effective temperature of about 12000 K. This means that the star remains unstable until it has lost its complete outer layers, which is done most likely in a series of such outbursts. The temperature region of this instability domain, spreading from 7000 to 12000 K in the HR diagram, appears to be vacant of stars and was thus called the Yellow Void.

Because the star seems to move back and forwards in the HR diagram, YHGs are indicated in Figure 1 by connecting lines between the real (hot) position of the star and its position during outburst (cool). The multiple attempts of the star to pass through this temperature domain has been described as bouncing at the Yellow Void (de Jager, 1998) respectively Yellow Wall (Oudmaijer et al., 2009). As a consequence of this bouncing and the multiple mass ejection phases, the star might be surrounded by several distinct shells of gas and dust as is seen, e.g., around the star IRAS 17163-3907 dubbed as the fried-egg nebula (Lagadec et al., 2011).

Most famous for its outbursts is the Galactic YHG star ρ Cas (=HD 224014). This star has been monitored for more than a century. During that time, the star underwent several outbursts with major events in 1945–1947, 1985–1986, 2000–2001, and a most recent, shorter and less pronounced one in 2013 (Kraus et al., 2019). The outbursts can be traced by a strong decrease in brightness by more than 1 mag in V-band along with the development of spectroscopic signatures of molecules such as TiO and CO that form within the developing cool, massive wind (e.g., Lobel et al., 2003; Gorlova et al., 2006). The decrease in the time interval between individual outbursts might indicate that the star could be preparing for a major eruption that might help to catapult it out of the Yellow Void instability region and would finally allow the star to reach a new, hot equilibrium state.

In contrast to ρ Cas, the YHG star V509 Cas (=HD 217476, HR 8752) displayed a different behavior over the past $\sim$ 150 yr. It also underwent a number of material ejection events during which a pseudo-photosphere was produced and the temperature dropped. However, underneath these temperature fluctuations the star experienced a real increase in effective temperature from about 5000 K back in 1973 to 8000 K in 2001 (Nieuwenhuijzen et al., 2012). Since then, this development seems to have stopped (Aret et al., 2017). A similar trend with an increasing effective temperature has been reported for the YHG object IRC+10420. Spectroscopic monitoring of this object revealed that it has changed from spectral type F8 to a mid-A type, meaning that it heated up by more than 1000 K over the course of about 20 years (Oudmaijer et al., 1996; Oudmaijer, 1998), and then stabilized in the vicinity of the high-temperature boundary of the Yellow Void (Klochkova et al., 2016).

3.1. Indications for Pulsations in YHGs

Outside their outburst phases YHGs display both spectroscopic and photometric variability, that are reminiscent of pulsation activity.

Theoretical investigations by Fadeyev (2011) proposed that the κ-mechanism operating in the helium ionization zones can cause radial pulsations with periods up to 200 d. However, the observed light curves of YHGs display low-amplitude photometric variability which has quasi-periods that are much longer, reaching a few hundred days (e.g., Percy & Zsoldos, 1992; Arkhipova et al., 2009; Kraus et al., 2019). These quasi-periods can most likely be ascribed to semi-regular, non-radial pulsations (Lobel et al., 1994).

Spectroscopic monitoring reveals that the atmospheres of YHGs are highly dynamical, as has been proven by radial velocity measurements of a variety of atmospheric lines formed in different depths (e.g., Klochkova et al., 2014; Klochkova, 2019). These atmospheric motions also display a quasi-periodic variation in agreement with semi-regular pulsations, and it has been found that this pulsation activity increases, i.e. develops larger velocity amplitudes prior to outbursts (Lobel et al., 2003; Kraus et al., 2019). Such a behavior is commonly observed in relation to the excitation and development of strange mode instabilities. Alike the α Cygni variables YHGs have lost a significant amount of mass during their previous RSG evolution so that they fulfill the required criteria of a high luminosity to mass ratio for strange mode excitation, and detailed numerical investigations are badly needed and currently underway that will help to deepen our comprehension of pulsations in YHGs and their ability to trigger outbursts.

4. Conclusions

This Chapter was devoted to some intriguing post-main sequence phases through which a massive star may evolve and which have been reported to display pulsations. Among them were the BSGs, which can be either in a pre- or a post-RSG stage, the latter are also known as α Cygni variables. It has been shown that these two populations display divers pulsation properties. In particular, stars in the post-RSG phase typically display many more pulsation modes than their younger counterparts. Detailed pulsation analyses of BSGs can thus provide a meaningful tool to separate these two BSG populations. However, care should be taken with the choice of data for the analysis. The photometric light curves might be contaminated by the variable emission of their high-density winds, which can lead to false results.

A second group of objects, that has been presented, are comprised by the YHGs. Alike the α Cygni variables, YHGs are also massive stars in their post-RSG evolution, but these objects reside still within the cool, yellow domain of the HR diagram. YHGs perform long-term (several hundred days) quasi-periodic oscillations and undergo from time to time outbursts with strongly enhanced mass loss. These outbursts, which are also related to the formation of a pseudo-photosphere, lead to an apparent (much) cooler temperature of the object. Moreover, the objects display a strongly enhanced pulsation activity prior to the outbursts.

Both groups of stars, the α Cygni variables and the YHGs, provide ideal conditions for the excitation of strange-mode instabilities. Investigations of the properties of such strange modes revealed that these instabilities can lead to significant mass-loss, which can reach values comparable to or even in excess to those from the line-driven winds of these objects. Consequently, strange-mode pulsations might provide an important component to the observed wind variability and the formation of structures and density inhomogeneities in the winds of α Cygni variables. Moreover, they might be a suitable trigger for the outbursts observed in YHGs.

YHGs and α Cygni variables are cornerstone objects in the evolution of massive stars, because they constitute a link between the cool RSGs and the hot pre-supernova evolutionary stages such as Wolf-Rayet stars and Luminous Blue Variables. Detailed knowledge about the mass-loss behavior in these transition phases in stellar evolution is essential because the mass loss controls the fate of these fascinating objects.

Acknowledgments. I wish to thank the SOC and LOC for their fantastic job in organizing and implementing this interesting and pleasant Summer School. This paper includes data collected with the TESS mission, obtained from the MAST data archive at the Space Telescope Science Institute (STScI). Funding for the TESS mission is provided by the NASA Explorer Program. STScI is operated by the Association of Universities for Research in Astronomy, Inc., under NASA contract NAS 5-26555. The Astronomical Institute, Czech Academy of Sciences, is supported by the project RVO:67985815. This project has received funding from the Czech Science Foundation (GA ČR 20-00150S) and from the European Union's Framework Programme for Research and Innovation Horizon 2020 (2014-2020) under the Marie Skłodowska-Curie Grant Agreement No. 823734.

References

Aerts C., Christensen-Dalsgaard J., Kurtz D. W., 2010a, *Asteroseismology*

Aerts C., de Pauw M., Waelkens C., 1992, *A&A*, **266**, 294

Aerts C., Lefever K., Baglin A., Degroote P., Oreiro R., Vučković M., Smolders K., Acke B., Verhoelst T., Desmet M., Godart M., Noels A., Dupret M. A., Auvergne M., Baudin F., Catala C., Michel E., Samadi R., 2010b, *A&A*, **513**, L11

Aerts C., Puls J., Godart M., Dupret M. A., 2009, *A&A*, **508(1)**, 409

Aerts C., Rogers T. M., 2015, *ApJL*, **806(2)**, L33

Aret A., Kolka I., Kraus M., Maravelias G., 2017, A. Miroshnichenko, S. Zharikov, D. Korčáková, and M. Wolf (eds.), *The B[e] Phenomenon: Forty Years of Studies*, Vol. 508 of *Astronomical Society of the Pacific Conference Series*, p. 239

Arkhipova V. P., Esipov V. F., Ikonnikova N. P., Komissarova G. V., Tatarnikov A. M., Yudin B. F., 2009, *Astronomy Letters*, **35(11)**, 764

Briquet M., Aerts C., Lüftinger T., De Cat P., Piskunov N. E., Scuflaire R., 2004, *A&A*, **413**, 273

Castor J. I., Abbott D. C., Klein R. I., 1975, *ApJ*, **195**, 157

Clark J. S., Negueruela I., Crowther P. A., Goodwin S. P., 2005, *A&A*, **434(3)**, 949

Crowther P. A., 2007, *ARA&A*, **45(1)**, 177
Crowther P. A., Lennon D. J., Walborn N. R., 2006, *A&A*, **446(1)**, 279
Curé M., 2004, *ApJ*, **614(2)**, 929
Daszyńska-Daszkiewicz J., Ostrowski J., Pamyatnykh A. A., 2013, *MNRAS*, **432(4)**, 3153
de Jager C., 1998, *A&A Rev.*, **8(3)**, 145
de Pauw M., Aerts C., Waelkens C., 1993, *A&A*, **280(2)**, 493
Dufton P. L., Langer N., Dunstall P. R., Evans C. J., Brott I., de Mink S. E., Howarth I. D., Kennedy M., McEvoy C., Potter A. T., Ramírez-Agudelo O. H., Sana H., Simón-Díaz S., Taylor W., Vink J. S., 2013, *A&A*, **550**, A109
Ekström S., Georgy C., Eggenberger P., Meynet G., Mowlavi N., Wyttenbach A., Granada A., Decressin T., Hirschi R., Frischknecht U., Charbonnel C., Maeder A., 2012, *A&A*, **537**, A146
Fadeyev Y. A., 2011, *Astronomy Letters*, **37(6)**, 403
Gautschy A., Glatzel W., 1990, *MNRAS*, **245**, 597
Glatzel W., 1994, *MNRAS*, **271**, 66
Glatzel W., Kiriakidis M., 1993, *MNRAS*, **263**, 375
Glatzel W., Kiriakidis M., Chernigovskij S., Fricke K. J., 1999, *MNRAS*, **303(1)**, 116
Godart M., Grotsch-Noels A., Dupret M.-A., 2014, J. A. Guzik, W. J. Chaplin, G. Handler, and A. Pigulski (eds.), *Precision Asteroseismology*, Vol. 301 of *IAU Symposium*, pp 313–320
Godart M., Noels A., Dupret M. A., Lebreton Y., 2009, *MNRAS*, **396(4)**, 1833
Gorlova N., Lobel A., Burgasser A. J., Rieke G. H., Ilyin I., Stauffer J. R., 2006, *ApJ*, **651(2)**, 1130
Grassitelli L., Fossati L., Simón-Diáz S., Langer N., Castro N., Sanyal D., 2015, *ApJL*, **808(1)**, L31
Gray D. F., 2005, *The Observation and Analysis of Stellar Photospheres*
Haucke M., Cidale L. S., Venero R. O. J., Curé M., Kraus M., Kanaan S., Arcos C., 2018, *A&A*, **614**, A91
Iglesias C. A., Rogers F. J., 1996, *ApJ*, **464**, 943
Kaufer A., Stahl O., Wolf B., Fullerton A. W., Gaeng T., Gummersbach C. A., Jankovics I., Kovacs J., Mandel H., Peitz J., Rivinius T., Szeifert T., 1997, *A&A*, **320**, 273
Kaufer A., Stahl O., Wolf B., Gaeng T., Gummersbach C. A., Kovacs J., Mandel H., Szeifert T., 1996, *A&A*, **305**, 887
Klochkova V. G., 2019, *Astrophysical Bulletin*, **74(4)**, 475
Klochkova V. G., Chentsov E. L., Miroshnichenko A. S., Panchuk V. E., Yushkin M. V., 2016, *MNRAS*, **459(4)**, 4183
Klochkova V. G., Panchuk V. E., Tavolzhanskaya N. S., Usenko I. A., 2014, *Astronomy Reports*, **58(2)**, 101
Kourniotis M., Bonanos A. Z., Yuan W., Macri L. M., Garcia-Alvarez D., Lee C. H., 2017, *A&A*, **601**, A76
Kraus M., 2006, *A&A*, **456(1)**, 151
Kraus M., 2019, *Galaxies*, **7(4)**, 83
Kraus M., Cidale L. S., Arias M. L., Maravelias G., Nickeler D. H., Torres A. F., Borges Fernandes M., Aret A., Curé M., Vallverdú R., Barbá R. H., 2016, *A&A*, **593**, A112

Kraus M., Haucke M., Cidale L. S., Venero R. O. J., Nickeler D. H., Németh P., Niemczura E., Tomić S., Aret A., Kubát J., Kubátová B., Oksala M. E., Curé M., Kamiński K., Dimitrov W., Fagas M., Polińska M., 2015a, *A&A*, **581**, A75

Kraus M., Kolka I., Aret A., Nickeler D. H., Maravelias G., Eenmäe T., Lobel A., Klochkova V. G., 2019, *MNRAS*, **483(3)**, 3792

Kraus M., Kubát J., Krtička J., 2008, *A&A*, **481(2)**, 499

Kraus M., Oksala M. E., Cidale L. S., Arias M. L., Torres A. F., Borges Fernandes M., 2015b, *ApJL*, **800(2)**, L20

Kraus M., Tomić S., Oksala M. E., Smole M., 2012, *A&A*, **542**, L32

Lagadec E., Zijlstra A. A., Oudmaijer R. D., Verhoelst T., Cox N. L. J., Szczerba R., Mékarnia D., van Winckel H., 2011, *A&A*, **534**, L10

Lamers H. J. G. L. M., Cassinelli J. P., 1999, *Introduction to Stellar Winds*

Lefever K., Puls J., Aerts C., 2007, *A&A*, **463(3)**, 1093

Lehmann H., Tsymbal V., Mkrtichian D. E., Fraga L., 2006, *A&A*, **457(3)**, 1033

Lobel A., 2001, *ApJ*, **558(2)**, 780

Lobel A., de Jager C., Nieuwenhuijzen H., Smolinski J., Gesicki K., 1994, *A&A*, **291**, 226

Lobel A., Dupree A. K., Stefanik R. P., Torres G., Israelian G., Morrison N., de Jager C., Nieuwenhuijzen H., Ilyin I., Musaev F., 2003, *ApJ*, **583(2)**, 923

Maeder A., 2009, *Physics, Formation and Evolution of Rotating Stars*

Maeder A., Rufener F., 1972, *A&A*, **20**, 437

Maravelias G., Kraus M., Cidale L. S., Borges Fernand es M., Arias M. L., Curé M., Vasilopoulos G., 2018, *MNRAS*, **480(1)**, 320

Martins F., Palacios A., 2013, *A&A*, **560**, A16

Maryeva O., Viotti R. F., Koenigsberger G., Calabresi M., Rossi C., Gualandi R., 2019, *Galaxies*, **7(3)**, 79

Meynet G., Maeder A., 2000, *A&A*, **361**, 101

Nieuwenhuijzen H., de Jager C., 1995, *A&A*, **302**, 811

Nieuwenhuijzen H., De Jager C., Kolka I., Israelian G., Lobel A., Zsoldos E., Maeder A., Meynet G., 2012, *A&A*, **546**, A105

North P., Paltani S., 1994, *A&A*, **288**, 155

Oksala M. E., Kraus M., Arias M. L., Borges Fernand es M., Cidale L., Muratore M. F., Curé M., 2012, *MNRAS*, **426(1)**, L56

Oudmaijer R. D., 1998, *A&AS*, **129**, 541

Oudmaijer R. D., Davies B., de Wit W. J., Patel M., 2009, *Post-Red Supergiants*, Vol. 412 of *Astronomical Society of the Pacific Conference Series*, p. 17

Oudmaijer R. D., Groenewegen M. A. T., Matthews H. E., Blommaert J. A. D. L., Sahu K. C., 1996, *MNRAS*, **280(4)**, 1062

Pelupessy I., Lamers H. J. G. L. M., Vink J. S., 2000, *A&A*, **359**, 695

Percy J. R., Zsoldos E., 1992, *A&A*, **263**, 123

Puls J., 2008, F. Bresolin, P. A. Crowther, and J. Puls (eds.), *Massive Stars as Cosmic Engines*, Vol. 250 of *IAU Symposium*, pp 25–38

Puls J., Urbaneja M. A., Venero R., Repolust T., Springmann U., Jokuthy A., Mokiem M. R., 2005, *A&A*, **435(2)**, 669

Ramírez-Agudelo O. H., Simón-Díaz S., Sana H., de Koter A., Sabín-Sanjulían C., de Mink S. E., Dufton P. L., Gräfener G., Evans C. J., Herrero A., Langer N., Lennon D. J., Maíz Apellániz J., Markova N., Najarro F., Puls J., Taylor W. D., Vink J. S., 2013, *A&A*, **560**, A29

Rosendhal J. D., 1973, *ApJ*, **182**, 523
Saio H., Georgy C., Meynet G., 2013, *MNRAS*, **433(2)**, 1246
Saio H., Kuschnig R., Gautschy A., Cameron C., Walker G. A. H., Matthews J. M., Guenther D. B., Moffat A. F. J., Rucinski S. M., Sasselov D., Weiss W. W., 2006, *ApJ*, **650(2)**, 1111
Simón-Díaz S., Herrero A., 2007, *A&A*, **468(3)**, 1063
Simón-Díaz S., Herrero A., Uytterhoeven K., Castro N., Aerts C., Puls J., 2010, *ApJL*, **720(2)**, L174
Smith N., 2017, *Philosophical Transactions of the Royal Society of London Series A*, **375(2105)**, 20160268
Sterken C., 1977, *A&A*, **57**, 361
Torres A. F., Cidale L. S., Kraus M., Arias M. L., Barbá R. H., Maravelias G., Borges Fernandes M., 2018, *A&A*, **612**, A113
Waelkens C., Aerts C., Kestens E., Grenon M., Eyer L., 1998, *A&A*, **330**, 215
Weis K., 2011, C. Neiner, G. Wade, G. Meynet, and G. Peters (eds.), *Active OB Stars: Structure, Evolution, Mass Loss, and Critical Limits*, Vol. 272, pp 372–377
Weis K., Bomans D. J., 2020, *Galaxies*, **8(1)**, 20
West R. M., Lauberts A., Jorgensen H. E., Schuster H. E., 1987, *A&A*, **177**, L1
Yadav A. P., Glatzel W., 2016, *MNRAS*, **457(4)**, 4330

ISBN 978-987-24948-7-2